

High-resolution neurotransmitter receptor
mapping:
From in vitro autoradiography to in vivo PET

Thomas Funck

Doctor of Philosophy

Integrated Program for Neuroscience

McGill University

Montreal, Quebec

2019-12-15

A thesis submitted to McGill University in partial fulfillment of the requirements of
the degree of PhD in Neuroscience

©Thomas Funck, 2019

DEDICATION

To Gabrielle who started this journey with me in a windowless room in a run-down apartment and supported me through all the ups and downs. To Juliette who beat me to the academic finish line, fair and square. To my mother and father who, in true keeping to Montessori philosophy, always encouraged me to follow my interests even when the outcome wasn't so clear.

ACKNOWLEDGEMENTS

The work of this thesis was only possible thanks to many individuals. Thank you to my advisory committee, Dr. Louis Collins and Dr. Petra Schweinhardt, for their feedback and advice. Thank you to Claude Lepage and Paule-Joanne Toussaint for their invaluable mentorship. Thank you to Nicola Palomero-Gallagher and Karl Zilles. Lastly, for their guidance and support, my sincere thanks my supervisors Dr. Alexander Thiel and Dr. Alan C. Evans.

This work was funded in part by the Sievers family (Ann and Richard Sievers Neuroscience Award), the Jeanne Timmins Costello Fellowship, and LDI/TD Bank Studentship Award, in addition to the Canadian Institutes for Health Research (CIHR) and Fonds de Recherche du Quebec-Sante (FRQ-S).

ABSTRACT

Neurotransmitters and their corresponding receptors allow for the transmission of information between neurons and hence underpin all information processing in the brain. Creating maps that represent neurotransmitter receptor densities in the brain is therefore essential for characterizing human brain anatomy and function in both healthy and diseased states. Neurotransmitter receptor mapping can be accomplished at very high spatial resolution ($50\ \mu\text{m}$) using post-mortem imaging with autoradiography or in vivo at a lower spatial resolution ($\sim 2\text{-}3\ \text{mm}$) with positron emission tomography (PET). Creating canonical atlases of neurotransmitter receptor densities in different populations will require large datasets to account for the variance of receptor densities between individuals within populations. PET is better suited for large-scale receptor mapping than autoradiography because it can be used on living subjects and is relatively less expensive. An important challenge in using PET for creating brain atlases of neurotransmitter receptor distributions is that it is not clear at exactly what spatial resolution PET can be used to accurately quantify receptor densities. We investigated PET spatial resolution in a top-down approach using real clinical data from patients with ischemic stroke to determine if PET can detect changes in receptor density in a small ($3\ \text{mm}$) region around the infarct, related to delayed neuronal loss. We then performed a bottom-up investigation of PET resolution by reconstructing 2D autoradiographs into 3D and then used the reconstructed volume to perform Monte-Carlo PET simulation to create a highly realistic simulated PET image. In pursuing this objective we developed the first open-source PET image processing pipeline that includes all the steps necessary to perform high-resolution receptor mapping with PET.

ABRÉGÉ

Les neurotransmetteurs et leurs récepteurs correspondent permettent la transmission d'information entre neurones et ainsi sous-tend tout traitement d'information dans le cerveau. La création d'atlas qui représentent la distribution des densités de récepteurs de neurotransmetteurs est donc essentiel pour caractériser l'anatomie et la fonction des cerveaux en états sains et malades. La cartographie des récepteurs de neurotransmetteurs peut-être accompli a une très haute résolution ($50 \mu\text{m}$) avec l'imagerie post-mortem autoradiographique ou in vivo a une plus faible résolution spatiale ($\sim 2\text{-}3 \text{ mm}$) avec la tomographie d'émissions de positrons (TEP). La création d'atlas canonique des densités des récepteurs de neurotransmetteurs dans différentes populations requiert des grands ensembles de données pour refléter la variance des densités des récepteurs entre individu dans différentes populations. La TEP convient mieux pour la cartographie de récepteurs à grande échelle que l'autoradiographie parce que la TEP peut être utilisé dans des sujets vivant et est relativement moins cher. Un défis importants dans l'utilisation de la TEP pour la création d'atlas de distribution de récepteurs de neurotransmetteurs c'est qu'il n'est pas claire a exactement quelle résolution spatiale la TEP peut être utilisé pour précisément mesurer la densité des récepteurs. Nous avons utilisé deux approche pour étudier la résolution spatiale de la TEP. La première approche était d'utiliser des images TEP par venants de patients avec des accidents vasculaires cérébrales ischémique pour déterminer si la TEP pouvait détecter des changements dans la densité des récepteurs dans une petite regions (3 mm) autours d'un infarctus ischémique, reliez aux perds des neurones. Nous avons ensuite poursuivi une étude pour créer des images TEP simuler réaliste. Pour créer ces images réaliste nous avons reconstruit des images 2D autoradiographique en volume 3D et utiliser ce volume pour effectuer des simulations TEP Monte-Carlo. Dans la poursuite de ces objectifs nous avons développé le premier logiciel "open-source" pour automatiser tout le traitement d'image TEP nécessaire pour créer des images à haute résolution de récepteurs de neurotransmetteurs.

TABLE OF CONTENTS

DEDICATION		ii
ACKNOWLEDGEMENTS		iii
ABSTRACT		iv
ABRÉGÉ		v
LIST OF TABLES		vii
LIST OF FIGURES		viii
1 Introduction		1
1.1 Neurotransmitter receptor mapping		1
1.2 Imaging neurotransmitter receptors in the living human brain		3
1.3 Investigating PET resolution with phantom scans and simulation		5
1.4 Probing the limits of PET: the need for a gold standard		6
1.5 From single brains to large scale population based neuroreceptor maps		7
1.6 Objectives		7
1.7 Contribution to Original Knowledge		13
1.8 First Author Publications		14
2 Background		16
2.1 Positron Emission Tomography		16
2.2 In vivo imaging of neuronal loss in the human brain		22
2.3 Quantitative Receptor Autoradiography		27
2.4 Image Alignment		32
2.5 Monte-Carlo PET Simulation		36
3 Assessing Neuronal Density in Peri-Infarct Cortex With PET: Effects of Cortical Topology and Partial Volume Correction		39

3.1	Preamble	39
3.2	Abstract	40
3.3	Introduction	41
3.4	Methods	45
3.5	Results	55
3.6	Discussion	60
3.7	Conclusions	68
3.8	Contribution of Authors	69
4	APPIAN: Automated Pipeline for PET Image Analysis	71
4.1	Preamble	71
4.2	Abstract	73
4.3	Introduction	74
4.4	Materials and Methods	75
4.5	Results	86
4.6	Discussion	88
4.7	Conclusion	96
4.8	Contribution of Authors	96
5	Improving reproducibility of PET image analysis with automated quality control	98
5.1	Preamble	98
5.2	Abstract	99
5.3	Introduction	100
5.4	Methods	102
5.5	Results	112
5.6	Discussion	116
5.7	Author Contributions	125
6	3D reconstruction of multi-ligand autoradiography and application for Monte-Carlo PET simulation	126
6.1	Preamble	127
6.2	Abstract	128
6.3	Introduction	129
6.4	Methods	139
6.5	Results	166
6.6	Discussion	176

6.7	Conclusions	191
6.8	Contribution of Authors	191
7	Discussion	193
7.1	Discussion	193
7.2	Conclusion	200

LIST OF TABLES

<u>Table</u>	<u>page</u>
3-1 Demographic and clinical information for enrolled patients	46
3-2 2W-RM ANOVA testing the effect of PVC on BPND	60
3-3 2W-RM ANOVA testing effect of scanning session on cortical thickness (mm)	60
4-1 Accuracy is measured as the ratio of recovered to true radiotracer concentration or parameter value. APPIAN accurately recovers radiotracer concentrations and tracer kinetic parameters from the SORTEO simulated PET images.	88
4-2 Many different PET processing software exist with various features. . .	90
6-1 List of the 20 radioligands and associated neurotransmitter receptors. The autoradiographs were categorized into tiers based on the visual contrast of the images. The tiers were used in the initial section- to-section alignment so that autoradiographs were only aligned to images in the same tier or lower.	141
6-2 ANTs parameters used to align the autoradiographs to one another. .	150
6-3 ANTs parameters used to align the autoradiograph GM slab volume to the MRI GM volume.	155
6-4 ANTs parameters used to perform non-linear alignment between the autoradiograph GM slab volume and the MRI GM volume.	158
6-5 ANTs parameters used to perform a) non-linear alignment between the autoradiograph GM slab volume and the MRI GM volume and b) non-linear alignment between MRI GM sections.	163

LIST OF FIGURES

<u>Figure</u>	<u>page</u>
3-1 The infarcts were manually identified and drawn independently by two stroke neurologists on the FLAIR images.	51
3-2 (A) Volumetric masks were drawn by hand on flair MRI. (B) FMZ BPND parametric images show GABAA receptor density. (C) Infarct masks were intersected with surface representations of the cortical GM. (D) Distance maps were produced by calculating geodesic distances from the border of the infarct. (E) Illustrative comparison of distance maps. The Euclidean distance maps were calculated volumetrically, but interpolated onto the participant's cortical surface representation. Both B1/2 and C1/2 show that the Euclidean distance metric produces an inconsistent distance measure that does not increase monotonically. A1/2 show that the Euclidean distance metric underestimates distances compared to the geodesic metric.	52
3-3 Average BPND measured in affected and unaffected hemispheres for initial and follow-up images. BPND is reduced closer to the infarct and gradually increases to close to normal levels further away. '*': P<0.05; '**': P<0.01.	56
3-4 Using an Euclidean distance metric, BPND in the affected hemisphere is generally lower than in the unaffected hemisphere. However only in the 3 mm ring is there a statistically significant difference between hemispheres. '*': P < 0.05; '**': P < 0.01.	58
3-5 IHDBP is consistently larger with the geodesic masks, particularly in follow-up images.	59
3-6 IHDBP for PVC and uncorrected PET at initial and follow-up images. Without PVC, the inter-hemispheric difference in BPND appears to be underestimated.	61

4-1	APPIAN performs all processing steps necessary to obtain quantitative parameters from reconstructed PET images. Flexible definition of ROI allows use of APPIAN for a wide variety of experimental designs. Integrated QC helps ensure that the pipeline performs as expected.	76
4-2	Output images produced by APPIAN can be viewed via a web browser-based dashboard. Visual QC for the coregistration stage can be performed by viewing the MRI, PET, and the fusion images of the two.	82
4-3	Output from automated quality control (QC) allows users to assess the performance of major processing steps at a glance. Here the automated QC metrics for the coregistration processing stage are shown: CC, cross-correlation,gc MI, mutual information, FSE, feature-space entropy.	83
4-4	Illustrative example of the image volumes produced by APPIAN for the three major processing stages for FDG, FDOPA, and RCL. . .	87
4-5	Time-activity curves for each subject and each radiotracer. Blue points indicate the uncorrected PET radioactivity concentration after PET-MRI coregistration and green points show radioactivity concentration after PVC with the GTM method. PVC corrects for spill-over of radiotracer distribution and increases the measured radioactivity concentration.	89
4-6	Flowchart of the modules implemented in APPIAN. Green boxes indicate mandatory inputs, blue boxes indicate optional inputs, and tan boxes indicate the primary quantitative outputs of the pipeline.	95

5-1	A. Performance is defined as a quantitative measure of how closely the actual result produced by the pipeline coincides with the ideal result that should theoretically be produced by that processing stage. Each point represents an individual scan from a subject in the sample. If performance of a processing stage increases monotonically with the QC metric for that processing stage, then a single-tailed test is sufficient to identify anomalous QC metrics. The red point indicated QC metrics that would be identified as anomalous values. B. A two-tailed test is necessary to identify anomalous QC metrics when a higher QC metric does not necessarily reflect better performance of the processing stage.	105
5-2	Increasing misalignments were generated to evaluate the sensitivity of GRAD. GRAD showed high sensitivity in the coregistration and quantification processing stages with moderate sensitivity for the PVC processing stage.	114
5-3	GRAD was able to detect misregistered images across all processing stages for translation errors.	115
6-1	Example autoradiograph from each of the 20 neurotransmitter receptor binding sites illustrating the substantial heterogeneity in image intensities between the autoradiographs.	135
6-2	The donor brain was cut into slabs prior to freezing. The red lines show how cuts made at different angles create slabs of tissue that are then sectioned along different planes (shown in green). Note that this schema is only for illustrative purposes and does not represent the actual cuts that were made on the donor brain. . . .	137
6-3	A multistage (S_{1-7}) pipeline was devised for reconstructing 2D sections from multiple autoradiographs. The pipeline was applied independently to individual slabs. Transformations T_1, T_4, T_5 were applied to cropped autoradiographs to produce a receptor volume in autoradiograph space and transformation T_3^{-1} was applied to transform receptor slabs to the donor's MRI in MNI space[4]. . . .	145
6-4	Example of autoradiographs with multiple pieces of tissue and non-tissue objects: frames (A), fiducial triangles (B), and arrows (C) . . .	146

6–5	A simplified U-Net architecture was designed to identify non-tissue objects (i.e., frames, arrows, and triangles in the autoradiographs).	147
6–6	Autoradiographs were preprocessed before they could be reconstructed. A deep learning network was trained to identify frames in the autoradiographs and remove them. Computer vision techniques were then used to remove pieces of brain tissue other than the target brain tissue in the image.	149
6–7	An initial reconstructed autoradiograph volume was produced by aligning autoradiographs to its adjacent neighbour. The central autoradiograph ($N/2$) of each section was used as the reference to which the others were aligned. The alignment process was repeated iteratively to avoid misalignments.	151
6–8	Cortical surfaces were extracted from the donor’s MRI and used to derive a 250 μm MRI GM volume. The ANIMAL algorithm was used to create a binary GM volume for subcortical GM regions. . .	153
6–9	The autoradiograph slab volume was segmented to identify GM regions using the K-means algorithm. The segmentation facilitates the alignment to the MRI GM volume.	154
6–10	The position along the coronal axis for each autoradiograph GM slab was chosen based on the location that had the maximum weighted cross-correlation. This figure is for illustrative purposes and does not represent the actual alignment of the slabs or the corresponding cross-correlation.	156

6–11	Green bars L_0 and L_4 represent autoradiographs at positions 0 and 4. Grey bars represent coronally sliced GM mask at positions 0-4. Autoradiographs were non-linearly aligned to the corresponding MRI sections. The MRI sections at positions with corresponding autoradiographs were then non-linearly aligned in 2D to the positions with no autoradiographs. These two transformations were concatenated to directly transform the autoradiograph to a new position. The estimated autoradiograph at position 1 was thus calculated by applying transform T_{L_0,GM_1} to L_0 and applying transformation T_{L_4,GM_1} to L_4 . The two transformed autoradiographs from the anterior and posterior direction were averaged using linear, distance-weighted interpolation.	162
6–12	At iteration 0 the autoradiographs were stacked without performing any alignment. Gross anatomic structures can be seen after a single iteration of rigid alignment between sections, with smaller refinements in subsequent iterations.	167
6–13	GM volumes extracted from autoradiograph slabs were aligned to the donor’s MRI GM volume using affine transformations. The alignment appeared accurate, but required further non-linear deformation to improve the alignment.	168
6–14	An interpolation scheme for estimating missing autoradiographs was used to reconstruct a continuous 3D representation of $GABAA_{Benz.}$ receptor density. The green lines indicate the coronal sections where autoradiographs representing $GABAA_{Benz.}$ receptor density were acquired. The spaces in between the green lines represent the estimated $GABAA_{Benz.}$ receptor density.	169
6–15	The equivolumetric GM volume has a discrete label for each layer of the cortical GM. The middle image shows the result of interpolating the equivolumetric GM volume using only the coronal sections for which $GABAA_{Benz.}$ autoradiographs were acquired. Note that the interpolation scheme conserves the laminar distribution of voxel intensities across the cortical surface GM. The error volume was calculated by dividing the interpolated by the true equivolumetric GM volume. Error levels were consistent across the coronal axis. . .	171

6–16	The average error in each coronal section shows that the interpolation scheme works well when there was a small gap between acquired sections (0-6%), but increases substantially for larger gaps. The troughs in the error level indicate the positions where autoradiographs were acquired.	172
6–17	The alignment of the reconstructed $GABAA_{Benz.}$ autoradiograph volume in the prefrontal cortex and the donor’s MRI showed that the reconstruction pipeline produces volumes that accurately match the donor’s gross brain anatomy.	172
6–18	Alignment of the reconstructed $GABAA_{Benz.}$ autoradiograph volume shows good alignment in coronal axis, but illustrates the large gaps between some of the autoradiograph volumes.	173
6–19	The simulated PET image shows that in principle PET can recover laminar patterns in the neurotransmitter receptor distribution. The source radioactivity distribution was defined at $500\mu\text{m}$ and the simulated PET image was sampled at 1mm.	174
6–20	Local correlation (Kendall’s Tau) of the reconstructed autoradiograph volume and simulated PET image show that the accuracy of PET varied based on cortical folding and thickness.	175
6–21	Distance-weighted interpolation of a missing autoradiograph section from adjacent sections is biased if the sections are cut tangentially to curvature of cortical surface. Section C is tangential to the cortical surface and does not accurately represent the distribution of layers across the cortical surface. Hence if section B is interpolated based on sections A and C, section C will bias this estimate due to its misrepresentation of the laminar distribution of signal intensity across the surface.	184

CHAPTER 1

Introduction

1.1 Neurotransmitter receptor mapping

Neurotransmitters and their corresponding receptors mediate the transmission of electrical signals across the synaptic gap between neurons and hence underpin the brain's neural information processing capabilities. Quantitative mapping of neurotransmitter receptor densities in healthy and pathologic brains is therefore of interest for understanding normal and pathologic brain function and behaviour. Anatomic [1–4] and cytoarchitectonic [5–9] atlases of the human brain have been widely used for many decades, but similar atlases characterizing neurotransmitter receptor distribution have only just been generated and only for one neurotransmitter system [10]. We here investigate the possibility of generating high resolution quantitative atlases of neurotransmitter receptor distribution based on data acquired with in vivo PET.

There are two primary methods for quantifying neurotransmitter receptor densities in the brain: receptor autoradiography and positron emission tomography (PET). Both methods use a radioligand—also called a radiotracer—that is composed of a radioactive isotope attached to a biological ligand to image the distribution of the receptor to which the ligand binds in biological tissue. Receptor autoradiography can be conducted by allowing the radioligand to bind in the living animal or in vitro

[11]. With *ex vivo* autoradiography the radioligand is injected in a living animal after which it is sacrificed and the brain is sectioned. *In vitro* autoradiography is performed on slices of dead brain tissue incubated in a solution containing the radioligand. While *ex vivo* autoradiography can only be performed in animals, *in vitro* methods can also be applied to post-mortem human brain tissue.

PET is the only imaging modality that is currently available for creating high-resolution receptor atlases because it can be used *in vivo* to acquire large, representative data sets from target populations. However, creating receptor atlases with PET is limited by relatively poor spatial resolution of a few millimeters, depending upon scanner type, radioisotope, length of scan, patient motion etc. The so-called partial volume effect (PVE) refers to the contamination of PET signal in the neuratomical structure of interest from signal arising in adjacent structures. A variety of software “partial volume correction” (PVC) approaches, discussed later, have been employed to correct for this source of bias. As a consequence of these resolution-related factors, it is not clear up to what spatial resolution PET can be used to accurately map receptor distributions in the brain. Furthermore, a secondary limitation of using PET to produce receptor atlases is that it requires complex image analysis that is susceptible to subtle processing errors that can bias results.

The goal of this project has been to address these two limitations by developing a strategy to determine the maximum possible spatial resolution that can be obtained with PET and by facilitating the creation of standardized high-resolution receptor maps using PET. This investigation includes 1. development of a software package for

performing in vivo receptor mapping with PET, 2. a practical investigation into PET spatial resolution with real clinical data and 3. a simulation experiment based on an atlas of neurotransmitter receptor distribution acquired from gold-standard human post-mortem data. While these 3 branches of investigation are methodologically distinct, all three are necessary for creating in vivo receptor atlases at the maximum spatial resolution possible with PET. Together they provide researchers with the tools necessary to create novel receptor atlases and validate their spatial accuracy.

1.2 Imaging neurotransmitter receptors in the living human brain

PET is the primary non-invasive imaging modality for quantitative in vivo receptor mapping of the brain. The current generation PET scanners—such as the CTI-Siemens ECAT HRRT—have a spatial resolution of up to 2.4mm full-width at half maximum (FWHM) [12] and new scanners in development are designed to achieve 1.2mm [13] FWHM resolution. While the spatial resolution of PET is clearly not as high as with autoradiography, PET is the only method to study large, representative human population samples at many different stages in normal aging or disease progression. Therefore, the characterization of the spatial distribution of neurotransmitter receptors will have to depend primarily on PET.

The present work is concerned with the effective spatial resolution of PET and all references to PET spatial resolution should be taken to reflect both the intrinsic resolution of the PET system and the properties of the object being imaged. For example, the CTI-Siemens ECAT HRRT scanner has a maximum resolution of ~2.4mm FWHM at the center of the field of view (FOV) when measured using a

uniform cylindrical radioactivity source of 1mm diameter [12]. However, the cumulative impact of partial-volume effects (PVE), patient motion, and PET image reconstruction may degrade the effective spatial scale at which regions in the brain can be accurately quantified[14] and hence the spatial resolution obtainable with the CTI-Siemens ECAT HRRT may in practice be worse than 2.4mm. Alavi et al [15] echo this concern in the context of clinical PET, because clinicians may underestimate the risk of PVE by assuming that the scanner resolution measured in phantom studies accurately reflects the spatial resolution of PET images acquired from real patients in the clinic.

Algorithms for partial-volume correction (PVC) can potentially enhance PET spatial resolution and the quantitative accuracy of measured tissue radioactivity concentrations [16–18]. However, validation of PVC algorithms has depended on phantom PET studies or PET simulation studies that do not attempt to model biologically accurate receptor distributions. The lack of complete validation of PVC algorithms has practical consequences. For example, in their atlases for several serotonin receptor subtypes, Beliveau et al [10] opted not to use PVC even though it could in theory produce a higher resolution atlas. They were concerned that different PVC algorithms produce different results and hence that PVC may not be fully reliable [19].

It is therefore of interest to know to what extent PET, with and without PVC, can be used to measure neurotransmitter receptor densities from small anatomic regions such as the cortical grey matter layers, small GM structures such as the amygdala, or even smaller brain stem nuclei. For example, the cortical grey matter

in the brain is 3-7mm thick and hence is just within the maximum resolution of the CTI-Siemens ECAT HRRT PET scanner. A more thorough quantification of both native PET resolution and PV-corrected PET images would allow for better atlases of neurotransmitter receptor distribution and allow for a more accurate use of PET imaging more generally. Although the focus of this work is on research applications of PET, it is also important to note that PVE can have a significant impact on clinical PET. PVE can make it more difficult to identify cancerous tissue and can thereby lead to misdiagnosis [20].

1.3 Investigating PET resolution with phantom scans and simulation

Phantom PET studies are typically used to evaluate PET resolution and can also be used to validate PVC algorithms [16]. In phantom studies a glass object containing a solution with a known radioactivity concentration is scanned and the ensuing PET image is compared to the known source radioactivity concentration. While phantoms that model the human brain are available, such as the Hoffman phantom [21], the radioactivity distributions in these phantoms are not representative of the actual receptor distributions in the brain.

An alternative approach is to use digital Monte-Carlo PET simulations [17, 18]. Here a source radioactivity distribution is defined digitally and the physics involved in PET image acquisition are simulated using stochastic Monte-Carlo models. This allows for much more complex radioactivity source distributions that can more closely reflect actual receptor distributions. Whereas previous Monte-Carlo PET simulation studies [22] defined receptor distributions using large regions of interest

(ROI) with uniform receptor densities, we sought to perform PET simulation using a gold-standard high resolution map of actual receptor distributions in the human brain, summarized below and detailed in Chapter 6.

1.4 Probing the limits of PET: the need for a gold standard

Autoradiography provides the best available quantitative map of neurotransmitter receptor distributions. The advantage of autoradiography is its high spatial resolution of approximately $50 \mu\text{m}$. However, autoradiography is performed on 2D sections that are sliced from full 3D brain volumes and thus only give a series of 2D representations of the brain. Autoradiography for a full brain is expensive and time consuming because of the manual labour involved.

Autoradiography provides the ideal ground-truth for creating PET simulations because both modalities can be used to measure the same receptor distribution, only at a much higher spatial resolution with autoradiography. To perform 3D PET simulation with autoradiography, the 2D sections must be reconstructed into 3D. Once reconstructed the autoradiographs can serve as an input into a PET simulator to produce realistic simulated PET images based on actual neurotransmitter receptor distributions. It is then possible to characterize the quantitative performance of PET using 3D autoradiography as a gold-standard map of real human neurotransmitter receptor distributions.

1.5 From single brains to large scale population based neuroreceptor maps

If simulation studies can demonstrate conclusively what is the maximum spatial resolution that can be achieved with PET, and whether PVC helps in this, it will be important to have PET analysis software available that can effectively leverage this maximum spatial resolution to produce the best possible in vivo neurotransmitter receptor atlases.

Accurate receptor mapping with PET requires complex data analysis on large data sets. Indeed, creating an atlas that reflects receptor density with PET requires at least: 1) anatomic information from structural imaging; 2) the use of tracer kinetic analysis to create parametric images of receptor density; 3) transforming these parametric images into a common coordinate space; and 4) potentially the use of PVC to enhance the spatial resolution of the PET images. Furthermore, hundreds of images of individual brains are required to reflect the variability in a target population [10]. To make such large-scale data analysis more robust, it is necessary to perform quality control for each processing stage of each image that is analyzed. Providing open-source PET processing software that includes all of these processing stages would thus facilitate reproducible and robust high-resolution neurotransmitter receptor mapping with PET.

1.6 Objectives

1.6.1 Objective 1: Practical investigation with real clinical PET images

The practical spatial resolution of real PET images and the potential impact of PVC was evaluated on images from patients with acute cortical ischemic stroke.

In acute stroke, neurons die from ischemia in the core of the infarct within minutes to hours. Brain tissue surrounding this infarct core—called the peri-infarct cortex—survives but is subject to long-term selective neuronal loss [23]. PET radioligands, which bind specifically to the body of neurons (such as the $GABAA_{Benz.}$ receptor ligand [18-F]-Flumazenil) can be used as surrogate markers to measure changes in neuronal density and to measure delayed neuronal loss after stroke. The challenge lies in the fact that, based on histological studies, the extent of these small patches of neuronal loss are just at the limit of PET resolution [24–27]. PVEs are thus a particularly important confounder in detecting delayed neuronal death in stroke patients because a) the infarct is a region with very low radioligand binding, b) neuronal loss may have caused cortical atrophy, and c) the transition zone between the infarct and healthy tissue is susceptible to spill-in artefacts from radioactivity originating from the adjacent healthy tissue.

We examined if the regions of decreased $GABAA_{Benz.}$ around the infarct could be detected in the peri-infarct cortex with high-resolution PET, both with and without PVC. This tested two hypotheses:

H_1) high-resolution PET is capable of detecting a small region of neuronal loss surrounding the infarct that is predicted by histological studies of stroke, and

H_2) that PVC produces statistically different output measures than obtained from uncorrected PET images.

Using these advanced image processing methods to push the limits of PET resolution, it was indeed possible to detect small regions of delayed neuronal loss in peri-infarct cortex with longitudinal scans. However, given that we did not know the true receptor distribution in the patient’s brain, it was impossible to determine if PVC PET images provided more genuinely more accurate measurements. Furthermore, the question of how far the limits of PET resolution can be pushed with PVC, can neither be answered by analyzing real PET data sets nor by using phantoms which do not reflect the complex topology and layered distribution of neurotransmitter receptors in the human cortex.

1.6.2 Objective 2: Theoretical investigation with simulated PET images

Objective 2.1: Reconstructing 3D receptor atlases from 2D autoradiographs

To further elucidate the maximum possible spatial resolution of PET it was necessary to perform a theoretical investigation using simulated data. We developed a bottom-up approach to quantitatively evaluate PET by simulating PET images from real postmortem receptor autoradiographs which accurately represent the layered cytoarchitectonics and complex topology of the human cortex.

The autoradiographic data used in this study—provided by Karl Zilles and Nicola Palomero-Gallgher and described in Ref.[28]—are unique in that autoradiographs measuring 20 different neurotransmitter receptor binding sites were acquired at a resolution of 50 μm from 3 different donor human brains. These data are particularly rich, but suffer from numerous artefacts that had up to now prevented

reconstruction of these 2D autoradiographic sections into 3D digital datasets.

We therefore sought to create an image processing pipeline that could account for these artefacts and could be used to reconstruct 20 high-resolution receptor atlases for each of the 3 donor brains (Chapter 6). This tested the hypothesis that:

H_3) It is possible to correct the processing artefacts in the autoradiograph images to reconstruct them into 3D images; as a proof-of-principle, reconstruction was performed specifically for $GABAA_{Benz.}$ receptor.

The reconstruction process allows for the creation of a library of 20 3D whole brain neurotransmitter receptor maps at 50 μm resolution. We anticipate that this library, made available as open source data, will find many applications in neuroscience in the the years to come. Here, we describe the first 3D reconstruction of a $GABAA_{Benz.}$ receptor autoradiography data set of an entire human brain (see Fig.6–18).

Objective 2.2: Monte-Carlo PET simulation with 3D receptor atlas

The reconstructed autoradiograph volume was then used to model the source radioactivity distribution for a Monte-Carlo PET simulator with the software package GATE [29]. The simulated image allowed us to determine how accurately they corresponded to the true neurotransmitter receptor distribution. This allowed us to

determine, under ideal conditions, the spatial accuracy of PET. We thereby tested the hypothesis that:

H_4 : PET can in principle measure differences in radioactivity concentrations stemming from laminar distributions in neurotransmitter receptor density.

The combination of publicly available 3D receptor atlases in combination with Monte-Carlo simulation packages will allow researchers to determine the maximum effective spatial resolution of PET in their own specific use-cases.

1.6.3 Objective 3: Framework for high-resolution PET receptor atlas

Objective 3.1: Automated pipeline for PET image analysis

The second aim of this project was to create a software framework for producing atlases of neurotransmitter receptor distribution based on PET. Creating receptor atlases based on PET is challenging because it requires multiple steps of image processing and computational modelling. These steps can be subject to small errors that can introduce bias or distortions in the final maps of receptor distribution. Reliable and robust software are therefore necessary to produce PET atlases with the maximum spatial accuracy possible.

While several software packages exist, they do not include all of the processing steps that may be necessary to produce the in vivo atlases of receptor distribution at the highest possible spatial resolution. Specifically, to accomplish this it is necessary for the software package to include PET to MRI coregistration, quantitative modelling, alignment of receptor maps to a stereotaxic template, and may also require

some form of PVC to enhance PET spatial resolution. Moreover, it is preferable that such a software package be open-source and easily extendible so that it is available to the whole research community and so that the best available algorithms can be incorporated into the larger pipeline framework. We therefore developed a PET pipeline that incorporates all of the processing steps necessary to produce high-resolution neurotransmitter receptor atlases with PET (Chapter 4) and validated it on existing simulated PET data. This tested the hypothesis:

H_5 : An automated PET pipeline built with open-source tools can accurately recover parametric images based on simulated PET data.

Objective 3.2: Automated quality control

To limit the risk of subtle, but systematic errors (e.g., misregistration of the PET and MRI) that could bias PET quantitative accuracy we developed a novel automated quality control (QC) algorithm that detects and flags erroneous processing steps (Chapter 5). We therefore tested the hypothesis:

H_6 : An automated quality control algorithm can detect processing errors in automated PET image analysis.

Furthermore, because this form of automated QC is not yet perfectly reliable, we also included a graphical user interface to allow the user to perform visual QC.

The combination of the receptor atlas and simulation framework from Objective 2 and the PET processing software in Objective 3 will make it possible to produce

PET atlases at the highest resolution achievable with the currently existing PET scanner technology and computational algorithms.

1.7 Contribution to Original Knowledge

1. Novel algorithm for calculating geodesic distances on a surface and defining peri-infarct cortex.
2. The first report using in vivo imaging of a progressive decrease in neuronal density closer to infarct and long term decrease in neuronal density in the region surrounding the infarct.
3. Partial-volume correction increases sensitivity to neurotransmitter receptor density changes in peri-infarct cortex.
4. PET processing pipeline can recover accurate parametric values from simulated PET images
5. Automated quality control can detect errors in PET image processing and facilitate neurotransmitter receptor quantification on large data sets.
6. Serially sectioning autoradiographs of different types can be reconstructed into a 3D volume
7. The creation of the first ever high resolution 3D atlas of $GABAA_{Benz.}$ distribution in the human brain.
8. Quantification of PET resolution based on Monte-Carlo simulated PET and receptor autoradiography.

1.8 First Author Publications

1. Published: Funck, T., Al-Kuwaiti, M., Lepage, C., Zepper, P., Minuk, J., Schipper, H.M., Evans, A.C., Thiel, A., 2017. Assessing neuronal density in peri-infarct cortex with PET: Effects of cortical topology and partial volume correction. *Hum. Brain Mapp.* 38. doi:10.1002/hbm.23363
 - PET resolution and partial-volume correction was investigated in the peri-infarct cortex at 2 weeks and 6 months after ischemic stroke.
2. Published: Funck, T., Larcher, K., Toussaint, P.J., Evans, A.C., Thiel, A., 2018. APPIAN: Automated Pipeline for PET Image Analysis. *Front. Neuroinform.* 12.
 - Novel open-source pipeline for automating PET image analysis called APPIAN.
3. Prepared: Funck, T., Larcher, K., Toussaint, P.J., Hoge, R., Dagher, A., Evans, A.C., Thiel, A. 2019. Improving reproducibility of PET image analysis with automated quality control
 - Validation of automated quality control algorithm implemented in APPIAN using simulated misalignment between PET and MRI volumes.
4. Prepared: Funck, T., Palomero-Gallagher, N., Wagstyl, K., Omidyeganeh, M., Lepage, C., Thiel, A., Zilles, K., Evans, A.C. 3D reconstruction of multi-ligand autoradiography.
 - Automated pipeline for automated reconstruction of 2D autoradiography into 3D receptor atlases.

5. Prepared: Funck, T., Palomero-Gallagher, Zilles, K., Evans, A.C., Thiel, A.
Monte-Carlo PET simulation of 3D autoradiograph receptor atlas.
- Evaluation of PET resolution based on Monte-Carlo simulation and high-resolution receptor atlas.

CHAPTER 2 Background

2.1 Positron Emission Tomography

2.1.1 PET Physics

Radioactive decay and positron emission

Imaging with PET is based on the radioactive decay of a radioisotope that is injected into a living human or non-human animal. The radioisotope can be attached to a biological ligand so that the radioisotope accumulates in regions with greater density of the target receptor to which the ligand binds. The nucleus of a radioisotope contains a greater number of protons versus neutrons. This ratio of protons to neutrons is unstable and, by progressively converting protons to neutrons, tends to a more stable configuration.

The conversion causes the emission of a positron and a neutrino from the nucleus [30]. The positron follows a random trajectory over which its energy gradually decreases. The positron eventually collides with an electron for a very brief period of time, approximately 10^{-10} s. This collision results in annihilation of the positron and electron and the emission of two gamma photons, which are detected by the detectors in the PET camera. The detectors of the PET camera cannot measure the distance that the positron travels before it joins an electron. This distance depends on the energy of the positron and imposes an intrinsic physical limitation to PET

resolution. Radioisotopes with lower energy emit positrons that lose their energy more quickly and hence travel a shorter distance before combining with an electron [31]. Images using lower energy radioisotopes tend to produce images with better spatial resolution.

Detecting the photons

The combined positron and electron annihilate and emit 2 photons with an energy of 511-KeV along paths at approximately 180° [30]. The photons are recorded by a pair of scintillation detectors and the location of the annihilation is assumed to have occurred on the line of response (LOR) between the 2 detectors. If, however, the positron has residual energy when it annihilates, the angle between the paths of the photons may not be exactly 180° . The angle is instead randomly distributed around 180° according to a normal distribution [32]. This phenomenon is termed non-collinearity and it constitutes another fundamental physical limitation to PET spatial resolution.

Non-collinearity degrades PET spatial resolution because the LOR recorded by the scanner does not cover the true location of the annihilation event. To complicate matters further, the impact of non-collinearity depends on the location of the annihilation event within the field of view (FOV) of the scanner as well as the size and geometry of the scanner. The closer non-collinear photons are emitted to the center of the FOV of the scanner, the further they travel before reaching a detector and the further the recorded LOR is from where the true LOR would have been.

In a vacuum the photons travel along a straight path from the point of annihilation. In a dense medium like the brain it is possible that the trajectory of the

rays will be altered through interactions with surrounding atoms. One important interaction is the photoelectric effect [33]. This occurs when a photon imparts its entire energy to a bound electron that is also soon absorbed. Thus the photon would not reach the detector. The remaining photon of the pair, which does not interact with the surrounding tissue, may still be detected by the scanner within the same coincidence window as another, unrelated photon. These events are called "randoms" and contribute noise to the image by adding spurious counts along LOR that do not reflect true annihilation events. The second most common form of interaction between photons and surrounding tissue is called Compton scattering [34]. Here a photon only imparts a portion of its energy to a free or loosely bound electron and is diverted as a result. This introduces noise and ultimately degrades PET spatial resolution. Unlike positron travel and photon non-collinearity, photon attenuation and scatter can at least partially be accounted for with correction algorithms [35, 36].

Scintillation detector crystals of bismuth germanate (BGO) or lutetium oxyorthosilicate (LSO) transform the photons into light waves. They are arranged around the FOV usually in a circle or octagonal geometry [37]. Pairs of detectors detect photons within a coincidence time window such that a pair of photons is detected within this time window are taken to have been produced by the same annihilation event. This method is imperfect and can introduce noise when photons from different annihilation events, i.e., single photons, are detected within the coincidence window and are assumed to reflect a true photon pair. These misidentified photon pairs are termed "randoms" in contrast to true photon pairs.

Detectors can be made of continuous or discrete crystals. For discrete detectors, the surface area of the detectors is important for determining the resolution of the PET image, where smaller detectors result in higher resolution images. An important source of loss in PET resolution comes from "depth of interaction" effects. These occur when a photon hits a detector at an oblique angle, is not stopped by that detector, and passes through to an adjacent detector [38]. In this case the location of the photon would thus be misattributed and thus the recorded LOR would be incorrect.

Another important source of artefacts in PET image generation stems from the fact that there are more pairs of LORs between detector pairs that pass through the center of the FOV than its borders. This means that the PET system is more likely to detect photon pairs closer to the center of the FOV than further away from the center and hence would overrepresent objects at the center of the FOV. Normalization algorithms that take into account the scanner geometry are used to increase the number of counts measured proportional to their distance from the center of the FOV.

Partial volume effects

Partial-volume effects (PVE) are imaging artefacts that result in a loss of spatial resolution in the acquired PET image[39]. PVE have been a subject of interest since the early period of PET research in the late 1970s because they can result in the misestimation of the measured radioactivity concentrations within a given region [39, 40]. While spatial resolution of modern PET scanners has increased significantly

since the first PET systems, the problem of PVE remains because improved spatial resolution leads researchers to seek to resolve smaller objects.

PVEs can be categorized in two groups [41]. The first are tissue-fraction effects that result from the multiple tissue types being confounded together within the minimal volume unit (voxel) of a PET image. That is, a single voxel in a PET image may contain several distinct tissue regions, e.g., white matter and grey matter (GM), that each have different levels of radioligand binding. This then makes it difficult to quantify the amount of radioligand binding that is attributable to these distinct regions.

PVE also result from spill-over effects, where the point-spread function, or blur, induced by the PET system results in the mixing of radioactivity concentrations from distinct regions. Spill-over effects in PET are in part a function of factors that are independent of the particular object being scanned. These factors include the intrinsic physics involved in PET, e.g., the energy of emitted positron, and the characteristics of the scanner, e.g., the surface area of the detectors. These factors determine the blur of the scanned object induced by the PET system.

While the point-spread function of the PET system is independent of the object being measured the quantitative accuracy of PET does depend on the object in the scanner. This was originally demonstrated in a seminal series of studies on PET quantitation including Hoffman et al [39] and Mazziotta et al [40]. Along these lines, Hoffman and Phelps [14] distinguish between the intrinsic resolution of the PET system and the practical resolution at which the anatomical objects can reliably be measured. For instance, blurring between two adjacent regions has a negligible effect

if these regions have similar radioactivity concentrations, but a large one if they have very different radioactivity concentrations. Hence the size, shape, and contrast of the object during image acquisition has a significant impact on the spatial scale at which PET can accurately recover radioactivity concentrations in vivo. Movement of the object during the scan can also have an important impact on the effective spatial resolution of PET.

PVE are therefore the result of multiple physical phenomena and limitations in PET scanner design. The limitations to spatial resolution imposed by positron travel and non-collinearity are fundamental and cannot be overcome even with perfect instrumentation. While photon attenuation and scatter also result from physical phenomena, reliable algorithms have been designed to account for these. Other technical limitations, such as depth of interaction effects and detector surface area, are topics of ongoing research and continue to be improved upon [13]. The net effect of these artefacts is a decrease in the quantitative accuracy of the measured radioactivity concentrations.

Many important regions of the brain are susceptible to PVE that result from the properties of the object being imaged. In particular, PVE can be exacerbated by sharp gradients in radioligand binding and by morphological atrophy. Given that the cortical GM is already relatively thin compared to PET spatial resolution, PVE in this region are particularly aggravated by the cortical atrophy that accompanies both normal aging and is made worse by neurological disorders like Alzheimer's disease. The loss in spatial resolution due to PVE is also prominent when measuring from a small region of low radioligand binding that is located near adjacent regions

with high binding. Neuronal loss in the surviving cortex following ischemic stroke is a particularly good test case for investigating PET resolution because this region is surrounded by healthy tissue likely to have high radioligand binding and is also subject to cortical thinning.

Realistic simulation studies are necessary to fully characterize PET resolution. Although assessing PET resolution on real images is useful, the true radioactivity distribution that gives rise to the acquired PET image is fundamentally unknowable. Simulation studies allow for the comparison between the true radioactivity distribution and that is measured by the PET system. Simulations therefore provide a complementary method for determining the spatial scale at which PET can accurately measure receptor densities.

2.2 In vivo imaging of neuronal loss in the human brain

2.2.1 Stroke as a Model for Selective Neuronal Loss in humans

Occlusion of the arteries providing blood-flow to the brain results in ischemic stroke. Prolonged loss of blood-flow below the minimum viability threshold necessary to sustain cell metabolism leads rapidly to necrotic cell death in the brain regions supplied. This results in a region of infarcted tissue. In the brain region surrounding the infarct, cerebral blood flow may still be above the viability threshold and sufficient for neurons to survive but below the functional threshold necessary to sustain neuronal function [42]. This region is at risk of infarction, if blood flow is not rapidly restored within hours.

Even if blood flow to this viable but non-functional brain tissue is rapidly restored with reperfusion therapies like intravenous thrombolysis or endovascular thrombectomy, there is substantial evidence for delayed selective neuronal loss of initially surviving neurons in these brain regions surrounding the infarct [43] (see Ref.[23] for a review). This surrounding region is called the peri-infarct cortex and describes a histologically defined area around the infarct with decreased neuronal density [26]. This was found both in rodent models as well as in humans that suffered ischemic stroke [24–27]. While the transition between the infarct and adjacent healthy cortex is histologically well defined, there is a ring of tissue with decreased neuronal density extending typically from 3-5 mm, and occasionally up to 10mm from the infarct border into morphologically intact cortex. Assessing these changes in human stroke is of potential clinical interest because such delayed neuronal loss may impact stroke recovery and may play a role in the development of post-stroke cognitive decline.

2.2.2 Flumazenil as radioligand to measure neuronal density

Neuronal loss in the cortex results in a reduction of neuronal density that can be measured with $GABAA_{Benz.}$ receptor as a surrogate marker. While single neurons cannot be directly visualized in the living human brain, neurotransmitter receptors on the cell body surface can serve as surrogate markers for the neurons. One such neurotransmitter receptor is the benzodiazepine receptor complex which is co-localized with the GABA-A receptor on the cell somata and dendrites of cortical neurons,

where they form synapses with interneurons [44]. Interneurons make up 20% of cortical neurons, and so their corresponding $GABAA_{Benz.}$ receptors are densely, and generally evenly, spread throughout the cortical mantle [45, 46]. Using flumazenil either labeled with 11-C or 18-F radioisotope, it has been shown that variations in $GABAA_{Benz.}$ density is related to differences in neuronal density in healthy humans and potentially reflect differences in the underlying cortical cytoarchitectonics [47]. In acute stroke, GABA-receptors from dying neurons are rapidly degraded and PET with flumazenil performed within hours of stroke onset can delineate infarcted from non-infarcted brain tissue [43, 48].

Evidence from autoradiography [49, 50] and PET [43, 51, 52] with flumazenil-based studies in animals suggests that decreased $GABAA_{Benz.}$ receptor density can also be detected in the peri-infarct cortex. However, it should be noted that not all groups have found a decrease in flumazenil binding after ischemic stroke with in vitro autoradiography [53]. Decreases in $GABAA_{Benz.}$ in the peri-infarct cortex have also been found in humans with iomazenil single-photon emission computed tomography (SPECT) [54, 55] and flumazenil PET [56–58].

2.2.3 The challenges of PET with Flumazenil in human stroke

Studying the peri-infarct cortex with PET is made difficult by its limited spatial resolution. Healthy cortex is between 3-7mm thick and may be subject to atrophy as a result of ischemia. Moreover, based on histological studies the peri-infarct region appears to be 3-5mm in width. Not only is the peri-infarct cortex small, it is also particularly subject to PVE. This is because it is, by definition, located

between regions of low and normal radioactivity concentrations in the infarct and surrounding healthy tissue. It is therefore at the very edge of PET resolution and therefore provides an ideal candidate for assessing whether PET, with and without PVC, can be used to detect changes in receptor densities in small regions subject to substantial PVE.

Most previous PET studies in human stroke have detected reduced GABA-A receptor densities in the peri-infarct cortex in small cross-sectional case series without accounting for related morphological changes in the cortex. An important exception to this is Guadagno et al. [57] and Zepper et al. [58], both of which used PVC to correct for potential PVE stemming from cortical atrophy. The PVC method used by Guadagno et al [57] does not, however, account for PVE within the cortical GM [59], which may be an important source of confounding error in the case of the peri-infarct cortex. PVC is essential because it allows one to disambiguate whether the cause of decreased flumazenil binding is due to cortical atrophy versus decreased neuronal density. It should be noted that receptor downregulation is also a potential cause of a decrease in flumazenil binding. However, while temporary downregulation of GABAA receptors has been shown in gerbils in the hours after transient ischemic stroke [60], to our knowledge there is no clear evidence for long-term downregulation of GABAA receptors in humans.

While PET studies of the peri-infarct cortex have been performed in the past, we wished to specifically determine if PET could measure small spatial changes in receptor density in the peri-infarct cortex consistent with delayed neuronal loss. This requires defining a space along which receptor densities are measured longitudinally.

Previous PET studies of the peri-infarct cortex have used an Euclidean distance to define the distance from the infarct border. This is problematic because the cerebral vasculature does not travel along straight lines through the cortex. Defining the peri-infarct cortex using Euclidean distances is particularly inappropriate in cortical stroke because the cortical vasculature generally follows the cortical surface. It is therefore necessary to use an anatomically plausible measure of distances from the infarct border and thereby identify the peri-infarct cortex. In contrast to Euclidean distance, a geodesic distance refers to the minimum distance measured over a manifold. If the manifold is flat, then the Euclidean and geodesic distances are equivalent. In Chapter 3 we describe how geodesic distances provided just such an anatomically plausible method and use it to quantify $GABAA_{Benz.}$ density in the peri-infarct cortex. This made it possible to determine whether PET was able to detect small changes in $GABAA_{Benz.}$ density along the cortical surface and whether PVC significantly affected the measured receptor density.

The use of high-resolution PET systems and advanced image processing algorithms can allow for accurate measurements from small regions subject to significant PVE. However, the question of how far the limits of PET spatial resolution can be pushed remains and cannot be answered by using non-invasive in vivo imaging modalities because it is impossible to determine how accurately the acquired and PV-corrected PET images reflect the true radioactivity distribution. PET simulation allows for an alternative approach to assess PET resolution by making it possible to compare the source radioactivity distribution with the acquired PET image. However, given that simulators which accurately model the physics of PET acquisition

are readily available, realistic PET simulation is only as good as the source radioactivity distribution that is used as input for the simulation. The source radioactivity distribution should ideally accurately reflect the real distribution of a given radioligand and corresponding receptor in human brains. Such information can only be derived from in vitro autoradiography but is not without its challenges, including the inherently 2D nature of autoradiographic images.

2.3 Quantitative Receptor Autoradiography

Autoradiography is an imaging modality that uses a radioligand, or simply a radioisotope, that binds to biological tissue and measures the particles emitted during radioactive decay. A radio-sensitive film is used to record the emitted radioactive particles. The film is composed of a layer of silver halide crystals, or grains, that are organized into a lattice. Radioactive β particles that hit the lattice cause the release of free electrons. These electrons migrate along the lattice to locations where they form silver ions [61]. The latent images produced by the silver ions decay with time and must be developed to create permanent images of the radioligand distribution.

Early autoradiography studies were used to measure receptor binding in the brain. The earliest techniques for quantification of receptor density involved the injection of a radioligand in an animal and, after sacrificing the animal, placing solubilized brain regions in scintillation vials from which radioactivity counts were measured [62–64]. However this approach only yields average regional radioactivity

concentrations and not actual images representing the spatial radioactivity distribution. In vivo autoradiographic techniques were applied to receptor mapping with autoradiography to map muscarinic and opiate receptor distributions in rats [65–68].

In the late 1970s, Young and Kuhar pioneered a then novel technique for performing autoradiography [69]. Instead of in vivo injection of the radioligand and then sectioning the brain, they first sectioned the brain and then incubated the sections in a solution of the radioligand. Hence this method was called in vitro autoradiography. In vitro autoradiography presented important advantages over in vivo autoradiography for receptor mapping, because it makes it possible to incubate adjacent sections with different radioligands. Hence in vitro autoradiography makes it possible to visualize multiple receptors within the same brain. It is also possible to use radioligands that do not cross the blood brain barrier and hence cannot be used in vivo.

A broadly standardized approach to in vitro autoradiography for neurotransmitter receptors was arrived at in the 1980s and 1990s [70–77]. According to this method brains are extracted post-mortem from the donor cadaver and are shock frozen and stored between -50 and -70 C. Brains are not fixed because fixation can modify the configuration of the proteins that make up receptors [78].

Frozen brains are sectioned with a cryostat microtome at $20\mu\text{m}$. Thicker sections require shorter exposure time because of the increased radioisotope concentration in the section but have lower resolution. If the angle at which the electron particle emitted by the decaying radioisotope is not perpendicular to the film, an electron emitted in a thicker section would travel further away from its point of emission before reaching the emulsion. Sections of $20\mu\text{m}$ provide a good tradeoff between exposure

time versus spatial resolution [79]. Additionally, prior to sectioning, photographs of the sections, called block-face images, may be acquired and used as a reference during 3D reconstruction of the 2D sections.

After sectioning, the sections are thaw mounted onto a glass slide and freeze-dried. The slides must then be rehydrated and rinsed to remove any endogenous ligand in the section. The sections are then ready to be incubated in a buffer solution either with just the titrated ligand or the ligand in addition to another displacer molecule that also binds to the target receptor. A displacer molecule is used to create autoradiographs of non-specific binding. A second rinsing step is required to remove the extra ligand as well as salts from the buffer. The sections are then exposed to a film that is sensitive to the β particles emitted by the radioisotope in the section.

After the film is developed, the autoradiographs are digitized with charge-coupled device (CCD) camera. The digital autoradiographs have 8-bit pixel intensity resolution, i.e., pixel values from 0 to 255. The pixel intensities of the autoradiographs themselves do not reveal the actual radioactivity concentrations but merely pixel intensities that are produced by these concentrations. The pixel intensities must be converted to radioactivity concentrations by using radioactivity standards. These standards are small cubes with a known radioactivity concentration and are placed next to the tissue section on the glass slides. Therefore the standards are co-exposed to the β -sensitive film alongside the tissue section that has been incubated in the radioligand. The standards are hence visible on the autoradiographs and have unique pixel intensities. Given that the true radioactivity concentration for

the standard is known, it is possible to plot the acquired pixel intensities versus the corresponding radioactivity concentration. This calibration curve is interpolated to convert the pixel intensities of the raw autoradiographs to radioactivity concentrations. These images, are then converted into images with pixel values representing the concentration of the receptor density in fmol/mg protein [80, 81].

The analysis of autoradiographs has generally been performed in 2D. This is problematic because these sections cannot accurately represent the complex 3D, folded topology of the cortical grey matter. That is, the cortical grey matter in the brain is organized into a series of layers that are oriented orthogonally to the curvature of the cortical gray matter. Sections which cut through the surface at an angle other than that is orthogonal to the curvature of the surface misrepresent the extent of these layers. To illustrate this, imagine cutting a multi-tiered cake at angle of 90° versus 75° . In the latter case, certain layers appear longer than they would in the former case. The problem is that the surface of the brain, unlike a rectangular cake, cannot be cut such that each section is at a perpendicular, or even at a consistent angle, relative to the cortical surface. Algorithms have been developed that are capable of reconstructing 2D brain sections into 3D and thereby create a more accurate representation of the brain's true anatomy and is discussed in the following sections.

Although many methods have been proposed for 3D reconstruction, these methods remain useful largely for the datasets similar to the specific use case for which they were developed. While certain portions of these methods could be borrowed

and incorporated into new reconstruction methods, there is no generalized 3D reconstruction algorithm that applies to all datasets. The data used in this study are unique and make it particularly difficult to apply existing techniques. The particularities of this dataset include the diversity of receptors imaged, the large number of missing sections, the large gaps between autoradiographs of the same receptor, and the significant non-linear deformations in the autoradiographs. The combination of these challenges made it necessary to develop a novel reconstruction pipeline. To avoid developing an entirely new set of tools, a software package for generic image alignment was used as a key component to this new reconstruction pipeline.

2.4 Image Alignment

2.4.1 Overview

Generic image alignment algorithms provide a useful tool for developing a novel 3D reconstruction method for the autoradiographic data used in this study. This section describes the general principles of image alignment and describes the SyN (symmetric normalization) algorithm implemented in the ANTs¹ software package. SyN is a particularly robust and well-validated generic image alignment algorithm that can be used on images from virtually any modality and can be applied in 2D, 3D, and even 4D. While ANTs has been employed in 3D reconstruction of histological data [82], it has not to our knowledge been applied to autoradiographic data. It plays a crucial role in the reconstruction pipeline described in Chapter 6.

¹ ANTs is derived from the name of its author Brian Avants

An image can be thought of as a function that maps a vector of spatial coordinates to a scalar value in the case of grayscale images or a vector of dimension 3 for an RGB color images. Here we only consider grayscale images. The range of the image can be a binary value (0 or 1), an integer, or a real number, depending on the type of image. The domain of the image is usually of 2 or 3 dimensions, which correspond to a 2D image or a 3D image volume. In the case of a 2D image a coordinate point denotes the center of a pixel while a 3D coordinate point denotes the center of a volumetric pixel or "voxel".

Image registration is the process by which the coordinates of one image, termed the "moving" image, is spatially transformed so that it is aligned to a second "fixed" or "target" image. There are many types of transformations that may be applied to the moving image to align it to the target image. Transformations can be divided into 2 classes: linear and non-linear transformations. Whereas linear transformations apply global changes to each dimension of the coordinate grid of an image, non-linear transformations allow for local deformations to a subset of the image's coordinate grid.

There are many algorithms that have been developed for automated image registration[83], but these can almost universally be understood in terms of 3 components: a similarity metric, a transformation, and an optimizer. The similarity metric serves as a cost-function that quantifies how similar 2 images are to one another. The transformation defines the model that is used to modify the coordinate points of an image. The optimizer finds the best, or at least satisfactory, transformation as defined by the similarity metric.

2.4.2 Non-linear image alignment with ANTs SyN

Hundreds of methods have been proposed for aligning spatial images with non-linear transforms [83]. A full description of all existing approaches to non-linear image alignment is beyond the scope of the overview given here and is not necessary for understanding the techniques used in this work.

In a comparison of 14 non-linear alignment methods on 4 MRI data sets, Klein, et al. [84] found that 4 algorithms that consistently provided the most accurate alignment across all 4 data sets: ART, SyN, DARTEL, and IRTK. Among these, SyN and ART were consistently the most accurate. We describe SyN because it is part of a popular image alignment software package, ANTs, and is used extensively in Chapter 6.

SyN is based on framework based on diffeomorphisms. A diffeomorphism is a mapping between 2 manifolds that is smooth, invertible and is also differentiable. Because of these features, diffeomorphisms have the significant benefit that they guarantee to preserve topology, which is not always the case with other methods of image alignment. Moreover, the fact that diffeomorphisms are differentiable and invertible is particularly important because it means that if there exists a diffeomorphic non-linear deformation that maps the moving image to the fixed image, then a mapping from the fixed image to the moving image also exists. The typical formulation for a diffeomorphic transformation is of the form [85] :

$$v = \operatorname{argmin} \int_0^1 \|Lv(x, t)\|^2 dt + \lambda \int M(I_m, I_f) \quad (2.1)$$

where L is a differential operator applied to the vector field, v , M is a similarity metric, and λ is a parameter modulating the weight of the similarity metric. The integral with respect to time represents the summation over the vector field that maps the moving image to the fixed image over unit time. The first component $\|Lv(x, t)\|^2$ serves to enforce smoothness by penalizing vector fields with large derivatives. The second component calculates the similarity metric between the moving and fixed image over the image domain.

SyN takes advantage of the fact that the diffeomorphism can be split into 2 components, one that calculates the deformation field from 0 to 0.5 time units and one calculates the deformation field from 1 to 0.5 time units. Hence the equation 2.1 is reformulated as :

$$v = \operatorname{argmin} \int_0^{0.5} \|Lv_1(x, t)\|^2 dt + \int_{0.5}^1 \|Lv_2(x, t)\|^2 dt + \lambda \int M(I_m \dot{\phi}_1, I_f \dot{\phi}_2) \quad (2.2)$$

where v_1 and v_2 represent the velocity fields that transform I_m and I_f to a midpoint at 0.5 time units. SyN therefore changes the traditional approach to alignment. Instead of calculating the similarity of the moving image transformed to the fixed image, both the moving and fixed images are transformed to a midpoint. Given that diffeomorphisms are composable, once the separate diffeomorphisms are calculated the separate velocity fields can be joined to transform the moving to fixed image and vice versa. According to Avants et al. [86] this guarantees that the diffeomorphic transformation calculated by SyN is not just invertible in theory, but that SyN actually produces the transforms to and from the moving and fixed image, respectively.

ANTs in particular was therefore a natural choice to develop a novel reconstruction pipeline because it is well validated on diverse data, produces invertible transformations, and is publicly available. ANTs has not seem to have been used to align autoradiographs and it was therefore not obvious whether ANTs would be capable of overcoming the challenges posed by our autoradiographic data. The implementation of this pipeline is described in detail in Chapter 6.

2.5 Monte-Carlo PET Simulation

The purpose of simulating PET scanners is to obtain an image that reflects the characteristics of a real PET image but is produced from an a priori defined source distribution of radioactivity in an object. There are 2 important factors that determine the realism of the simulation. The accuracy of the physics that are modelled by the simulator determines if the characteristics of the simulated PET image reflects the actual process by which a real PET image is acquired. To assess the accuracy of PET for the particular use case of neurotransmitter receptor mapping, it is necessary to also define a radioactivity distribution that reflects actual neurotransmitter receptor distribution in the brain. Simulation is useful because it allows for a direct comparison between the source radioactivity—which is usually inaccessible in the case of real PET scans—and the simulated image.

The most realistic method for PET simulation is Monte-Carlo simulation. Monte-Carlo simulations are characterized by their use of random sampling methods to model stochastic processes. PET Monte-Carlo simulations involve the modeling of the behaviour of individual particles in real-time according to probabilistic physical

models [87]. This has the advantage of closely modeling the probabilistic nature of radioactive decay. This physical realism comes at the cost of significant computation time.

Several Monte-Carlo PET simulators are available with different degrees of computational speed, accuracy and usability. The most accurate simulators, and consequently the slowest, model each aspect of the physical processes involved in positron emission, annihilation, and detection of photons as Monte-Carlo processes, i.e. by generating random numbers. The most accurate of these simulators are GEANT4[88] and PENELOPE [89], both of which are general purpose Monte-Carlo particle physics simulators. GEANT4 and PENELOPE are designed for performing a wide range of particle simulations, of which PET is just one application. This makes it difficult to use GEANT4 or PENELOPE, and as such, versions of these have been tailored specifically for modeling PET.

To overcome the limitations of high accuracy Monte-Carlo simulators with respect to computational speed and usability, several alternative simulators have been proposed. GATE is an open-source PET/SPECT simulator based on the GEANT4 code-base and is actively maintained by an international community of scientists [29]. Due to the extensive use of Monte-Carlo sampling, GATE is an accurate but relatively slow simulator. GATE has been validated in empirical studies against phantom PET simulations and produces nearly identical results [29].

Multiple PET and SPECT simulators have been implemented for GATE, including the Siemens HR+ and CTI-Siemens ECAT HRRT scanners. PeneloPET [90], based on the PenelopePET code-base, and PET SORTEO [22] are attempts to

improve the speed of simulation with minimal cost to accuracy by modeling certain aspects of the simulator with analytic functions. While PeneloPET has been shown to be many times faster than GATE and to differ from it by only 5% in counts of annihilation events measured between detector pairs, only small animal PET scanners have been implemented for PeneloPET [90]. Similarly, images from PET SORTEO have been shown to be in good agreement with real PET images acquired from PET phantoms [22]. However, the code-base for PET SORTEO is not publicly available and it has not been implemented for the CTI-Siemens ECAT HRRT. GATE is open-source, user friendly, accurate, and has been validated for the CTI-Siemens ECAT HRRT [91]. It therefore is an ideal simulator for producing realistic CTI-Siemens ECAT HRRT PET images based on an anatomically derived radioligand distribution. Chapter 6 describes the use of a 3D neurotransmitter receptor atlas derived using autoradiography as a radioactivity source distribution for Monte-Carlo PET simulation with GATE.

CHAPTER 3

Assessing Neuronal Density in Peri-Infarct Cortex With PET: Effects of Cortical Topology and Partial Volume Correction

Thomas Funck^{1,2}, Mohammed Al-Kuwaiti^{1,2}, Claude Lepage¹, Peter Zepper³, Jeffrey Minuk², Hyman M. Schipper², Alan C. Evans¹ and Alexander Thiel^{1,2}

¹ Montreal Neurological Institute, McGill University, Montreal, Canada

² Jewish General Hospital, Lady Davis Institute, Montreal, Canada

³ Department of Neurology, Technische Universitat Munchen, Munich, Germany

Published: Funck, T., Al-Kuwaiti, M., Lepage, C., Zepper, P., Minuk, J., Schipper, H.M., Evans, A.C., Thiel, A., 2017. Assessing neuronal density in peri-infarct cortex with PET: Effects of cortical topology and partial volume correction. Hum. Brain Mapp. 38. doi:10.1002/hbm.23363

3.1 Preamble

The aim of this study was to use PET with 18F-FMZ to detect small changes in neuroreceptor density in patients with subacute stroke. These areas are thought to represent small patches of delayed neuronal loss in the morphologically normal appearing brain tissue surrounding the infarct which are just at the limit of PET

resolution. PVEs are thus expected to be particularly important limitation for detecting these changes.

Using a novel method to define the peri-infarct cortex based on geodesic distances, we demonstrate that these small regions of decreased $GABAA_{Benz}$ around the infarct can be resolved with high-resolution PET, both with and without PVC and that PVC produces statistically significant different outcome measures than obtained in uncorrected PET. In addition, results obtained with geodesic distances were different than those obtained with Euclidean distance metrics. Euclidean distance metrics are not anatomically realistic when measuring the peri-infarct cortex in the case of ischemic stroke because the cerebral vasculature does not run through cortical sulci. More broadly, this also suggests that when analyses are conducted on the basis of a distance from some region in the brain, e.g., distance from a tumor or epileptic foci, the distance metric used should reflect the brain's anatomy.

The fact that decreases in BPnd became more prominent over 6 months and were present after PVC for atrophy effects, suggests that a delayed loss of neurons can be detected with such sophisticated methods pushing the limits of neuroreceptor PET.

3.2 Abstract

Abstract: The peri-infarct cortex (PIC) is the site of long-term physiologic changes after ischemic stroke. Traditional methods for delineating the peri-infarct gray matter (GM) have used a volumetric Euclidean distance metric to define its extent around the infarct. This metric has limitations in the case of cortical stroke, i.e.,

those where ischemia leads to infarction in the cortical GM, because the vascularization of the cerebral cortex follows the complex, folded topology of the cortical surface. Instead, we used a geodesic distance metric along the cortical surface to subdivide the PIC into equidistant rings emanating from the infarct border and compared this new approach to a Euclidean distance metric definition. This was done in 11 patients with [F-18]-Flumazenil ([18-F]-FMZ) positron emission tomography (PET) scans at 2 weeks post-stroke and at 6 month follow-up. FMZ is a PET radiotracer with specific binding to the alpha subunits of the type A g-aminobutyric acid (GABAA) receptor. Additionally, we used partial-volume correction (PVC) of the PET images to compensate for potential cortical thinning and long-term neuronal loss in follow-up images. The difference in non-displaceable binding potential (BPND) between the stroke unaffected and affected hemispheres was 35% larger in the geodesic versus the Euclidean peri-infarct models in initial PET images and 48% larger in follow-up PET images. The inter-hemispheric BPND difference was approximately 17–20% larger after PVC when compared to uncorrected PET images. PET studies of peri-infarct GM in cortical strokes should use a geodesic model and include PVC as a preprocessing step. Key words: PET; partial-volume effects; receptor mapping; ischemic stroke; neuronal density

3.3 Introduction

Long-term physiologic changes occur after ischemic stroke in morphologically preserved gray matter (GM) surrounding the core of ischemic brain parenchyma, termed peri-infarct cortex (PIC). This region can be defined along morphologic or

physiologic criteria. When using a physiologic definition of the PIC, it is typically termed the “penumbra” and refers to cortex where cerebral blood flow is reduced below the level necessary for neuronal function, but above that needed for maintaining neuronal integrity [42]. However, the PIC can also be defined as cortex that has undergone morphologic change resulting from the stroke. Changes in the PIC are various, depending on the location of the infarct, time post-stroke and the patient’s use of rehabilitative therapy [92–94]. Whereas some of the physiologic changes in the PIC are adaptative, others are deleterious to the patient. An infarct in the somatosensory cortex results in an adaptive remapping of the body representation in this region through a decrease in the number of dendritic spines and an increase in axonal sprouting [94–100]. Similarly, gene expression related to axonal sprouting is up regulated in the PIC [101]. Other studies have demonstrated neuroinflammatory changes in the PIC post-stroke [102–104] and argued that this persistent neuroinflammation may be related to the development of post-stroke cognitive impairment [105, 106]. Changes in the PIC can develop over several months post-stroke in both rat models and humans [58, 93, 107, 108]. Previous studies have shown evidence of neuronal loss outside of the infarct core, both in post mortem studies [24–27] and in-vivo [54, 55, 57, 58].

The PIC may be useful for predicting patient outcomes, monitoring the evolution of the infarct, and may be an important site for post-stroke therapy. Decreased FMZ binding in the PIC has been shown to correlate with decreased oxygen consumption and eventual infarction [48]. An accurate measure of the extent of the PIC may be useful for predicting the patient’s outcome and defining the region around the

infarct that would benefit from therapeutic intervention. The size of penumbral PIC appears to be inversely correlated with functional outcome [109]. For stroke therapy, electrical stimulation of PIC in nonhuman primates resulted in improved motor performance [110].

When the PIC is taken as the region surrounding the infarct that is morphologically preserved after ischemia, it is typically defined by delineating a region surrounding the infarct using an Euclidean distance metric [43, 58, 103, 111–113]. An Euclidean-based PIC is limited when defining PIC in cortical infarcts, because the vascularization of the cerebral cortex follows the complex, folded topology of the cortical surface. That is, two points on neighbouring gyri may be close together in 3D space, but much further from one another when measuring the geodesic distance along the 2D cortical surface. We therefore propose a new method that uses the geodesic distance along a 2D representation of the cortical mantle to define the PIC. Our method allows the PIC to be segmented into rings based on the distance from the infarct and at the same time to study the effect of ischemia at regular intervals outwards from the infarct core.

In positron emission tomography (PET), regions that are less than approximately twice the resolution of the scanner are subject to partial-volume effects (PVE) [39]. In regions of high radiotracer concentration, PVE result in a decrease in the measured radiotracer concentration because a portion of the signal “spills-out” to neighboring regions. Cortical thickness is generally between 3–4 mm and thus tends to be less than or, in the case of high resolution PET scanners [12], just on the cusp of what the PET scanner can measure without spill-out effects. Thus radiotracer

concentrations in the cortical surface may be underestimated due to PVE resulting from cortical atrophy. PVE may also be increased by particularly low radiotracer binding in the infarct. The PIC may also be subject to important “spill-in” PVE because reduced radiotracer binding in the PIC may lead an increased proportion in signal from adjacent healthy tissue spilling-in.

PVC is of particular concern in the case of acute focal ischemia, because this has been shown to lead to selective neuronal loss [23, 24, 26, 43, 55, 57, 114–116] and may result in decreased cortical thickness [117]. Using a GM representation extracted from MRI it is possible to perform PVC for potential spill-out from the cortical GM.

It is the aim of this study to test the hypothesis that geodesic distances, which are based on more theoretically sound assumptions of cortical vasculature, provide significantly different results than obtained with an Euclidean distance metric for defining the PIC. Distance profiles of BPND of [18-F]-FMZ were created on PET images from patients with ischemic stroke using both metrics. [18-F]-FMZ was used because it binds to g-aminobutyric acid (GABAA) receptors that are found in large and uniform quantities in the cortical GM and thus serves as a surrogate marker for neuronal loss [48]. To assess if there was any difference between the BPND distance profiles, we compared the sensitivity of each method to detect a difference between the stroke affected and unaffected hemispheres. The BPND distance profiles produced with both metrics were also compared directly to see if they were significantly different from one another. Additionally, we evaluated the effect of PVC on the BPND measured within the PIC using anatomic information extracted from MRI.

Cortical thickness maps were calculated to determine if there was significant cortical atrophy between initial and follow-up images and evaluate its effect on PVC.

3.4 Methods

Subjects

All participants were prospectively recruited from the Jewish General Hospital and Montreal General Hospital acute stroke units between March 2012 to October 2014. This study was approved by McGill Faculty of Medicine Institutional Review Board. All participants were enrolled after informed consent in accordance with regulations for human participant's studies.

Eleven participants were enrolled if they presented with first ever anterior circulation ischemic stroke within 31 days post stroke onset, had a neurological deficit defined on National Institutes of Health Stroke Scale (NIHSS) score 5 upon entry to the study, were between 40 and 90 years of age and able to speak either English or French (Table 3-1). Patients were excluded if there was evidence of alcoholism or psychoactive drug use, benzodiazepine use 24 hour prior to the PET study, if they were unable to complete the initial MRI or PET studies or had a history of either epilepsy, psychiatric or neurodegenerative diseases. One participant withdrew from the study after the initial scan and was excluded from analysis when initial and follow up PET images were compared directly.

Enrolled patients were evaluated in the sub-acute phase of their stroke and on 6 months follow-up images using a clinical assessment battery for motor and cognitive

Table 3–1: Demographic and clinical information for enrolled patients

Patient	Age	Sex	Affected vascular territory	Initial scan time (Days)	F/U scan time (Months)	Initial infarct volume (cm ³)	F/U infarct volume (cm ³)
1	66	M	MCA	21	5.53	65	75
2	87	M	MCA	13	5.63	0.46	0.36
3	71	M	MCA	18	5.93	4.6	4
4	63	F	MCA	14	6.16	3.7	3.8
5	54	M	ACA	10	5.93	109	104
6	62	M	MCA	21	5.93	5	2.3
7	53	M	MCA	27	6.83	2.5	1.4
8	50	M	MCA	15	6.03	3.8	3
9	69	F	MCA	27	5.93	99.6	82.5
10	72	F	MCA	17	NA	20.2	NA
11	55	F	MCA	31	7	6.5	5.5

recovery, and with both MRI and PET scans to measure the peri-infarct cortical thickness and estimate the neuronal cell density changes, respectively.

T1 and Flair MR Acquisition

All MR images were acquired on a Siemens MAGNETOM TrioTim syngo MR B17. The Fluid attenuated inversion recovery (FLAIR)—a T2 weighted MR image with attenuated CSF signal—sequence used a TR of 9000 ms, TE of 75 ms and TI of 2500 ms with a flip angle of 150° to acquire 60 transaxial slices with thickness of 2 mm and a base resolution of 192 3 192 voxels in plane. The T1-weighted data set for surface extraction was acquired using a MPRAGE sequence with TR 2300 ms, TE 2.98 ms, TI 9 ms and 9 degree flip angle comprising 160 sagittal slices with isotropic 1mm voxels and 256 3 256 voxels in plane resolution.

The FLAIR image was upsampled to the resolution of the T1 image using linear interpolation and blurred with a 2 mm FWHM Gaussian kernel to attenuate noise.

CIVET

CIVET is an image processing pipeline that generates mesh representations of the cortical GM from T1 MR images. CIVET uses the non-parametric N3 method to correct MR field non-uniformity [118]. The MRI is then transformed to MNI stereotaxic space of the ICBM 152 6th generation non-linear brain atlas [4], using a 12 parameter affine transformation [2]. Spatially normalized images are then segmented into three tissue classes: GM, WM and cerebral spinal fluid using INSECT [119], a discrete classifier, as well as a probabilistic classifier [120]. The Constrained Laplacian Anatomic Segmentation using Proximity algorithm generates a mesh representation of the cortical GM using two deformable mesh models consisting of 81924 vertices connected to form triangles. Cortical thickness is measured by taking the distance between the mesh fitted to the WM-GM boundary and that fitted to the GM-pia boundary. Volumetric cortical GM binary images were created from the WM-GM and GM-Pia mater surface meshes using a ray-tracing algorithm to identify the voxels that lie between the two surface meshes [121]. The GM masks and WM were transformed from MNI stereotaxic space to T1 native using nearest-neighbor interpolation.

PET Acquisition

[18-F]-FMZ scans were obtained for all participants with an ECAT HRRT PET scanner in list mode (Siemens Medical Solutions, Knoxville, TN, USA) [12]. The ECAT HRRT is a dedicated full 3D high resolution brain scanner, with a field view

of 25.2 cm (axially) and 31.2 cm (diameter), and has a spatial resolution of between 2.3 mm and 2.8 mm FWHM and enables data acquisition with high spatial resolution combined with high sensitivity. In addition, the use of two crystal layers (LSO/LYSO) permits photon detection with depth-of-interaction information. After a transmission scan for attenuation correction (^{137}Cs -source), approximately 370 MBq ^{18}F -FMZ were injected intravenously as a slow bolus over 60 s. The list mode data were acquired for 60 min after injection and were subsequently binned into 2209 sinograms (each of size 256 radial bins 3 288 azimuthal bins) using span 9 compression for a total of 17 time frames (40s, 20s, 2 330s, 360 s, 4 350s, 3 3300s, and 3 3600s), resulting in images with a voxel size of $1.22 \times 1.22 \times 1.22\text{mm}^3$. Fully 3D FBP by 3D reprojection (3D RP) was carried out with a Hamming windowed Colsher filter (alpha 5 0.5, cut off at the Nyquist frequency). The PET image was co-registered and resampled using linear interpolation to the native T1 using a six parameter rigid transformation.

Partial-Volume Correction

PET images were partial-volume corrected using the idSURF algorithm [121]. IdSURF is an iterative algorithm based on Lucy-Richardson deconvolution and attempts to make subsequently better guesses of the true tracer-distribution [122, 123]. The algorithm proceeds by filtering an estimate of the true tracer-distribution, initially the PET image itself, with a model of the PET scanner point-spread function; in this case a Gaussian filter (FWHM 2.5). The difference between the original PET image and the filtered test image is used to update the estimate of the true

tracer distribution. Anatomically constrained filtering is performed by taking the local mean of voxels within predefined anatomic regions. Whereas traditional linear filtering, e.g., Gaussian smoothing, are effective at removing noise, they also smooth between anatomic regions and thus increase PVE. By constraining the filtering to within anatomic regions, idSURF controls for noise while preserving edges between these regions. The infarct core, GM and WM were treated as separate anatomic regions for this analysis. Both the uncorrected PET and idSURF corrected images were compared to evaluate the effect of PVC on measured radiotracer concentrations in the PIC.

Tracer Kinetic Analysis

Tracer kinetic analysis was used to quantify specific tracer binding across patients. We computed the BPND maps from the PET images. BPND of a reversibly binding radioligand is related to the maximum available concentration of its receptor (Bmax) accounting for the binding affinity of the tracer and the fraction of non-displaceable binding (i.e., tracer irreversibly bound to other molecules than the receptor) in the tissue. Parametric images of BPND were created using the Logan plot method [124], with a white matter (WM) reference region ¹ and a start time of

¹ The WM was used as reference region because it is believed to have negligible $GABAA_{Benz.}$ density [125] and has been shown to produce similar results to using the pons as a reference region [126]. It is also larger than the pons, making it less susceptible to noise.

300 seconds for the linear regression. To avoid any potential spill-over signal between the WM and GM, the WM reference region was eroded by 4 voxels, i.e., 4 mm.

Surface Infarct ROI

Volumetric ROIs were drawn on the FLAIR MR images acquired for each participant for both initial and follow-up scans and independently verified by two stroke neurologists (Fig. 3-1). Initial surface infarct masks were produced by nearest neighbour interpolation of the volumetric infarct ROI with the mid-surface produced using CIVET (Fig. 3-2C). The surface ROIs were then defragmented to remove isolated points outside, as well as holes within, the main infarct. All regions smaller than 25% of the largest ROI were removed.

Geodesic Peri-Infarct Rings

Geodesic distances were calculated from the border of the infarct ROI. This produces a surface map where the value at each surface vertex is the minimum distance from the vertex to the border of the infarct (Fig. 3-2D). Distance maps were created using in-house software that calculates the minimum distances by expanding a closed region outwards along the edges of a surface mesh. The distance maps were segmented into five rings of 3 mm, from 0 to 15 mm from the infarct. The rings were named such that the 3 mm contains vertices from 0 to 3 mm and the 6 mm ring contains vertices from 3 mm to 6 mm from the infarct core, and so forth for the other rings.

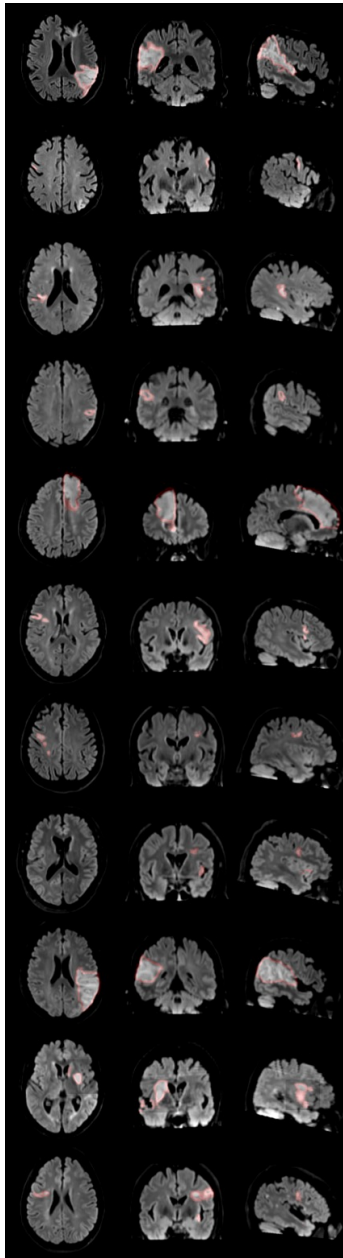


Figure 3-1: The infarcts were manually identified and drawn independently by two stroke neurologists on the FLAIR images.

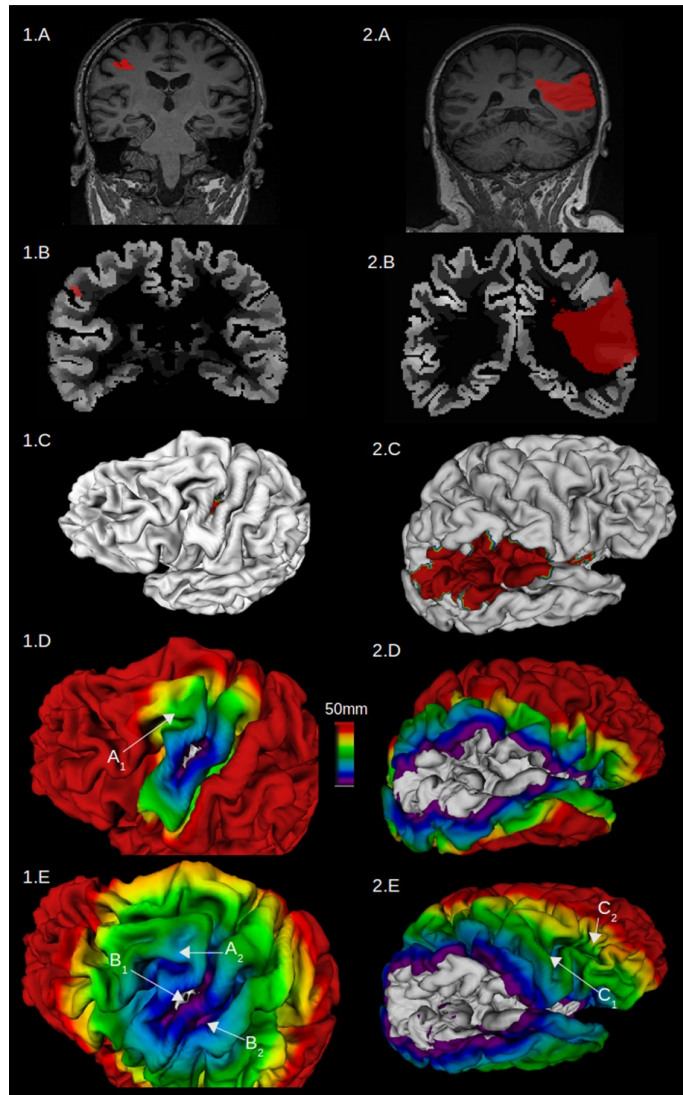


Figure 3-2: (A) Volumetric masks were drawn by hand on flair MRI. (B) FMZ BPND parametric images show GABAA receptor density. (C) Infarct masks were intersected with surface representations of the cortical GM. (D) Distance maps were produced by calculating geodesic distances from the border of the infarct. (E) Illustrative comparison of distance maps. The Euclidean distance maps were calculated volumetrically, but interpolated onto the participant's cortical surface representation. Both B1/2 and C1/2 show that the Euclidean distance metric produces an inconsistent distance measure that does not increase monotonically. A1/2 show that the Euclidean distance metric underestimates distances compared to the geodesic metric.

The PIC ring width of 3 mm was chosen because this approaches the spatial resolution of 2.5 mm FWHM of the HRRT [12]. Histological studies have shown decreased neuronal density up to 10 mm from the infarct core [27]. Hence the 9–12 mm PIC ring was the maximum distance at which BPND was expected to be reduced in the affected hemisphere. The maximum distance of 15 mm was therefore chosen to include a 12–15 mm PIC ring that would, presumably, include healthy tissue.

Geodesic PIC rings for the contralateral hemisphere were produced by reflecting the surface mesh along the midline of the x axis. The reflected surface mesh was then intersected with the infarct ROI to produce a surface ROI of the infarct in the contralateral hemisphere. Geodesic distances were calculated from the infarct reflected onto the unaffected hemisphere ROI and segmented to produce contralateral PIC rings.

Euclidean Peri-Infarct Rings

Whereas the geodesic PIC rings were defined on a surface, the Euclidean PIC rings were volumetric and produced in a similar manner as [58]. The first step was to intersect the infarct and GM ROI. Euclidean distance maps from the GM infarct were then calculated. As with the geodesic peri-infarct rings, the Euclidean distance maps were segmented into five rings of 3 mm, from 0 to 15 mm from the infarct. These rings were then intersected with a binary GM image to eliminate voxels outside of the GM. Euclidean PIC rings for homologous regions in the unaffected hemisphere were created by reflecting the infarct ROI along the x-axis and intersecting it with a

volumetric binary image of the GM. Euclidean distances were then calculated in the unaffected hemisphere and segmented into Euclidean PIC rings.

Statistical Methods

The effect of the ischemic insult on the PIC was measured by subtracting BPND in the unaffected hemisphere by that of the affected hemisphere to give the inter-hemispheric difference of BPND ($IHDBP = BPND_{Unaffected} - BPND_{Affected}$). In all but one of the two-way repeated measures (2RM) ANOVA described below, the geodesic PIC rings were used as one of the two factors.

The following tests were performed on initial and follow-up images separately. The effect on BPND of (1) PIC ring and (2) cerebral hemisphere (i.e., unaffected vs ischemia affected) was tested using a 2RM ANOVA. For the purpose of comparison, this same test was performed with the Euclidean peri-infarct rings. To determine that the two distance metrics produced different results, the 2RM ANOVA used (1) PIC ring and (2) distance metric (i.e., Euclidean vs. geodesic) as factors. Lastly, to evaluate the effect of PVC on IHDBP we performed a 2RM ANOVA with (1) PIC ring and (2) PVC method (i.e., uncorrected vs idSURF) as factors.

To determine if there was a change in the IHDBP between initial and follow-up images, a 2RM ANOVA was performed with (1) PIC ring and (2) scanning session as factors. This same test was also performed for the cortical thickness values extracted from the initial and follow-up MRI.

If the interaction effect of the 2RM ANOVA reached significance at the 5% level, post-hoc tests were performed on each PIC ring to test if there was a significant

difference in the measured response variable between the two-levels of the factor. The purpose of the post-hoc testing was to determine which PIC rings contributed to the significant interaction effect of the ANOVA. This was done using Wilcoxon signed-rank [127], with P-values adjusted for multiple comparisons with Hochberg’s method [128]. The correction for multiple comparisons was performed independently for each set of ANOVA, because these tests asking conceptually independent questions about the data and do not use the same set of response variables.

3.5 Results

3.5.1 Surface Geodesic Distances Show Decreased BPND Closer to Infarct

The results of the surface PIC analysis indicate first that BPND is lower in the affected hemisphere compared to the unaffected hemisphere in both the initial and follow-up images. The difference in BPND between hemispheres was significant both in the main effect of hemisphere (Initial: $P < 0.01$, $F = 16.15$, Follow-Up: $P < 0.001$, $F = 20.98$) and in the interaction between hemisphere and PIC ring in both initial and follow-up images (Initial: $P < 0.001$, $F = 18.78$, Follow-Up: $P < 0.001$, $F = 20.34$). Post-hoc testing revealed that the difference in BPND between hemispheres is significant from 0 mm to 6 mm in the initial images and 0 mm to 15 mm in the follow-up images (Fig. 3–3).

There appears to have been a significant increase in IHDBP from initial PET images to follow-up. The 2RM ANOVA showed an overall significant difference in IHDBP in the PIC rings between initial and follow-up images ($P < 0.01$, $F = 4.88$). However, using the Wilcoxon signed rank test for post-hoc testing, none of

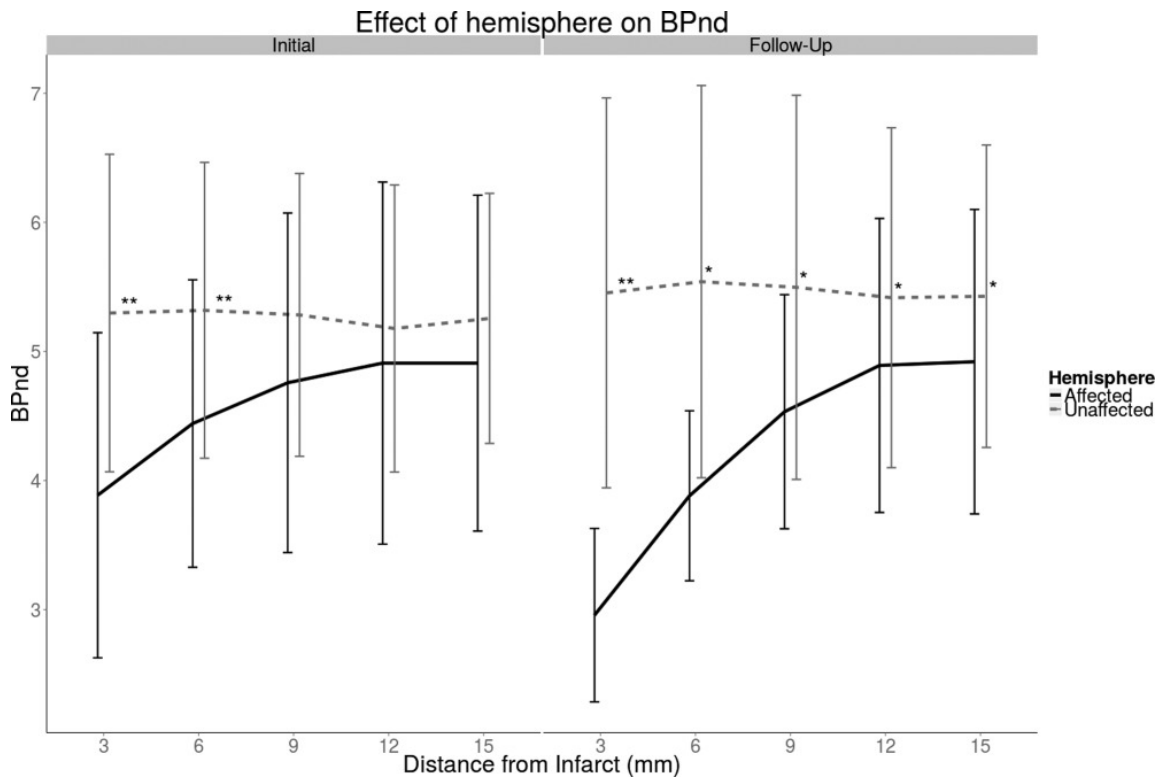


Figure 3-3: Average BPND measured in affected and unaffected hemispheres for initial and follow-up images. BPND is reduced closer to the infarct and gradually increases to close to normal levels further away. ‘*’: $P < 0.05$; ‘**’: $P < 0.01$.

the individual PIC were significantly different in IHDBP between initial and follow-up images.

3.5.2 Geodesic and Euclidean Distances Produce Different Results

The distance profiles produced with the Euclidean PIC rings do not show the gradual increase in BPND in the stroke affected hemisphere that was observed with the geodesic profiles (Fig. 3–4). In the main effect of hemisphere, the difference in BPND between hemispheres was trending towards significant in the initial scanning session and significant in the follow-up session (Initial: $P < 0.1$, $F = 4.59$, Follow-Up: $P < 0.01$, $F = 11.7$). There was a significant interaction effect between hemisphere and PIC ring in both initial and follow-up images (Initial: $P < 0.001$, $F = 15.06$, Follow-Up: $P < 0.001$, $F = 19.95$). In post-hoc testing, however, the difference between hemispheres was only significant in the 0–3 mm PIC rings.

We compared the Euclidean IHDBP profiles to the IHDBP profiles produced with a geodesic distance metric (Fig. 3–5, see Fig. 3–2 for visual example). In the initial and follow-up scans, there was a significant difference in IHDBP due to the main effect of distance metric (Initial: $P < 0.05$, $F = 6.45$, $P < 0.01$, $F = 13.09$), but no significant interaction effect between distance metric and peri-infarct ring. The area under the geodesic IHDBP profile was 35% larger than that under the Euclidean IHDBP profile in the initial images and 48% larger in follow-up images.

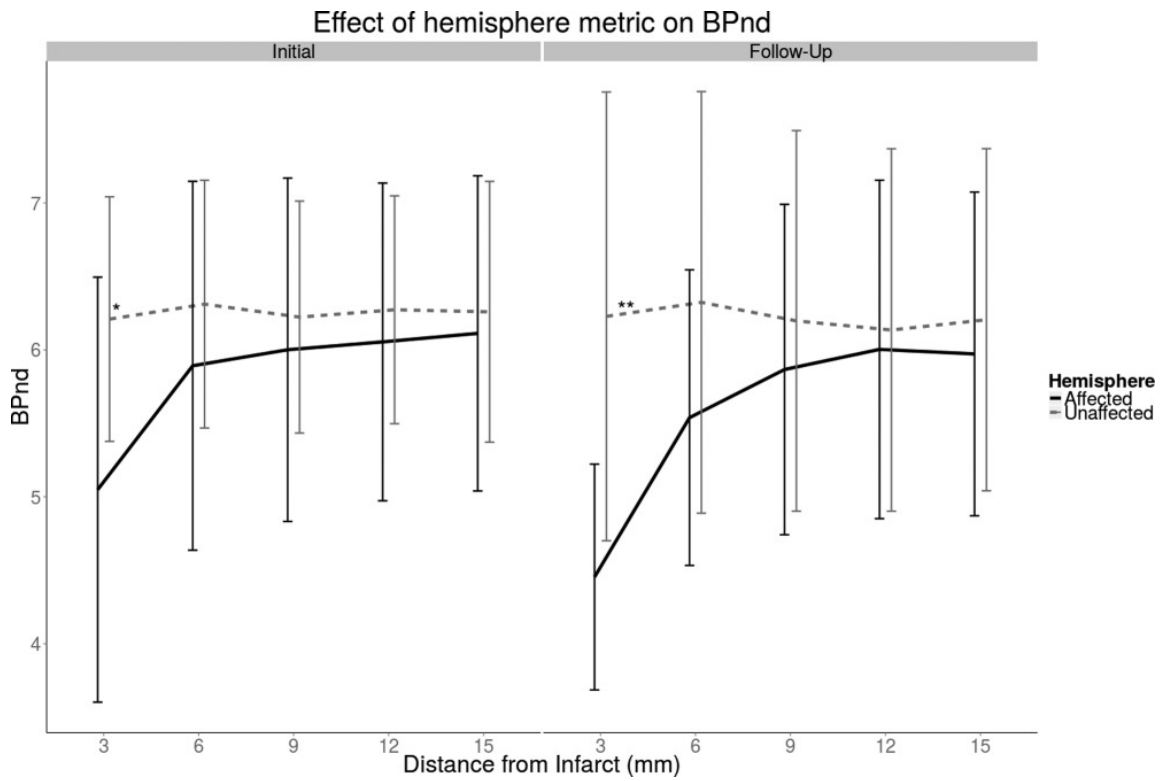


Figure 3-4: Using an Euclidean distance metric, BPND in the affected hemisphere is generally lower than in the unaffected hemisphere. However only in the 3 mm ring is there a statistically significant difference between hemispheres. '*': $P < 0.05$; '**': $P < 0.01$.

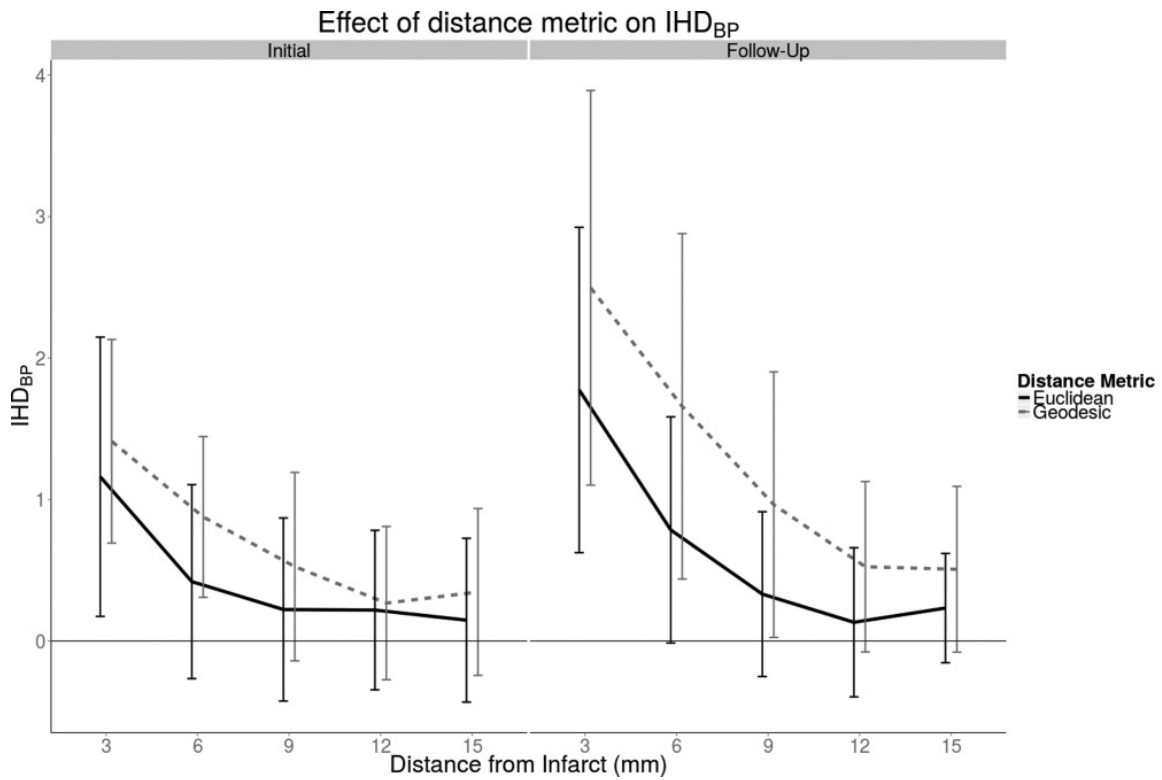


Figure 3-5: IHD_{BP} is consistently larger with the geodesic masks, particularly in follow-up images.

Table 3–2: 2W-RM ANOVA testing the effect of PVC on BPND

	Response Variable	Main effect 1	Main effect 2	Interaction effect
<i>Scanning Session</i>				
Initial	BP _{ND}	PIC ring $P < 0.001, F = 19.75$	PVC $P < 0.05, F = 10.35$	PIC ring \times PVC N.S. ($P < 0.1$), $F = 2.28$
Follow-up	BP _{ND}	PIC ring $P < 0.001, F = 26.01$	PVC $P < 0.05, F = 5.45$	PIC ring \times PVC $P < 0.01, F = 4.61$

“N.S.”: Not significant.

3.5.3 Partial-Volume Correction Increases BPIDH

PVC produces larger IHDBP than observed in uncorrected PET images (Table 3–2). However, only in follow-up images was there a significant interaction effect between PIC ring and PVC. In post-hoc testing, the only significant difference between PVC and uncorrected images was in follow-up images in the 3 mm PIC ring, but this did not survive correction for multiple comparisons (Fig. 3–6). PVC IHD BP was found to be 17% larger than uncorrected IHDBP in the initial images and 20% larger in the follow-up images.

3.5.4 Cortical Thickness Is Reduced in Follow-up Scans

The difference in cortical thickness between affected and unaffected hemispheres was only trending towards significance in the initial cortical thickness maps and was found to be significant in the follow-up maps (Table 3–3). The interaction effect between PIC rings and hemisphere was significant in the follow-up images, but this was not attributable to any specific PIC ring.

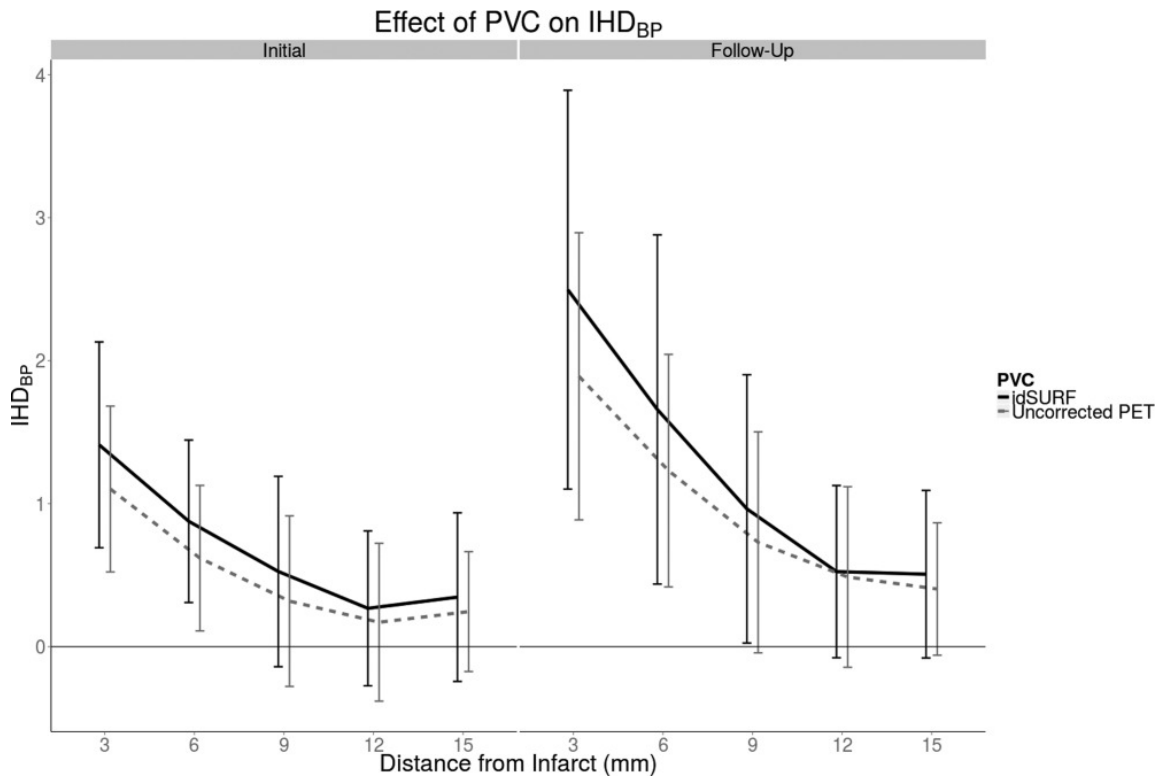


Figure 3–6: IHDBP for PVC and uncorrected PET at initial and follow-up images. Without PVC, the inter-hemispheric difference in BPND appears to be underestimated.

Table 3–3: 2W-RM ANOVA testing effect of scanning session on cortical thickness (mm)

	Response variable	Main effect 1	Main effect 2	Interaction effect
<i>Scanning Session</i>		PIC ring	Hemisphere	PIC ring × Hemisphere
Initial	Cortical thickness (mm)	N.S., $F = 1.12$	N.S. ($P < 0.1$), $F = 4.86$	N.S., $F = 0.63$
Follow-up	Cortical thickness (mm)	$P < 0.05$, $F = 2.99$	$P < 0.05$, $F = 7.32$	N.S., $F = 1.57$

“N.S.”: Not significant.

3.6 Discussion

The PIC is the site of important physiologic changes after ischemic stroke in initially viable cortex and is often defined using a Euclidean distance metric to measure distances from the infarct. We developed a new PIC model that uses geodesic distances measured along a surface model of the cortical GM and used it to analyze [18-F]-FMZ PET images of stroke patients. Using the geodesic method results in IHDBP that is 35–48% larger than that obtained with a traditional Euclidean method and is 17–20% larger with PVC.

3.6.1 IHDBP Measured with Geodesic PIC Rings Show Long-Term Neuronal Cell Loss

Distances measured relative to the cortical vasculature are better modeled with a geodesic distance metric than an Euclidean metric, because the former does not cut across the folds of the cortical surface. Defining the PIC using a geodesic distance metric allows for a more anatomically realistic measurement of changes in BPND along the cortical surface. There was a significant reduction of BPND in the PIC in the affected hemisphere compared to the unaffected hemisphere and this difference was larger closer to the infarct core. This suggests that the effect of the stroke on viable cortex does not have a sharp boundary and should be studied at regular distance intervals from the infarct border rather than in a single region.

IHDBP was significantly larger at follow-up than in the initial images. [18-F]-FMZ binds to GABAA receptors on cortical neurons and is used as a surrogate marker of neuronal density [47, 129]. The increase in IHDBP between initial and follow-up is consistent with long-term neuronal cell death in the peri infarct grey

matter after ischemic stroke. This interpretation is consistent with findings from post-mortem histological studies of humans with ischemic infarcts [24, 25, 27]. In these participants, a transition zone of decreased neuronal density from 0–5 mm (and up to 10 mm in some patients) around the infarct border was observed. It should be noted that these histological studies measured distance from the infarct by projecting distances along the cortical surface onto the outside surface of the brain, excluding the sulcal depths. This distance metric will produce uniformly larger distances than the geodesic distance metric. In the initial PET images we found a decrease in BPND in the affected hemisphere from 0 mm to 6 mm, which was consistent with previous results from histological studies. In the follow-up images, however, the decrease in BPND in the affected hemisphere extended up to 15 mm, suggesting a larger and more gradual transition zone between infarct ed and healthy tissue.

In vivo evidence has also been found for selective neuronal loss in the non-infarcted penumbra both in FMZ PET [56–58] and [123-I]-Iomazenil SPECT [54, 55]; for a review, see [23]. The limitation of these methods is that they define the PIC as a single, uniform region and do not reveal changes in BPND within the PIC. The current findings suggest that the PIC is not homogeneous and may vary as a function of the distance from the infarct core.

Previous studies of the effect of stroke on cortical thickness have also reported changes in cortical thickness. Some studies have also reported increases in cortical thickness in regions associated with functional remapping in both acute [130] and chronic stroke [131]. A study of sub-cortical infarcts from cerebral small vessel disease

found long-term cortical thinning in GM regions connected via WM tracts to the infarct [132].

3.6.2 Euclidean PIC Rings Are Less Sensitive to IHDBP

The PIC can be defined morphologically by measuring the distance from the border of the infarct to the surrounding tissue. Traditional approaches have delineated the PIC using a Euclidean distance metric [103, 107, 111–113]. These methods start by defining a volumetric ROI of the infarct. The PIC is then defined by identifying points that are within a given distance from the infarct, where the distance is measured as a straight line in 3D space. This is typically done by performing a pixel or voxel-wise dilation of the infarct to produce PIC rings or spheres. Dilations of the infarct implicitly use a Euclidean metric by assuming that all voxels contained within a dilation are equally far from the infarct.

The geodesic and Euclidean PIC rings produced different BPND profiles. With the Euclidean peri-infarct rings, unlike the geodesic IHDBP profiles, there was little difference between the stroke affected and unaffected hemispheres beyond the 3 mm ring. The difference between geodesic and Euclidean IHDBP was larger in follow-up images. The reason for this appears to be that the BPND profiles produced with Euclidean and geodesic PIC rings differ in how they relate to the topology of the cortical surface and its vasculature.

The Euclidean metric measures distances in the PIC as a straight line to the border of the infarct. The limitation of this method is that it cuts across folds in the cortical surface (Fig. 3–21.E and 3–2.2.E), and thus underestimates the true

distance traveled by the vasculature (Fig. 3–2.1.D and 3–2.2.D). The result of this underestimation is that beyond 3 mm, where the geodesic and Euclidean rings sample approximately the same voxels, the Euclidean PIC rings include regions that are relatively unaffected by the stroke and thus have normal BPND. Hence, beyond the 3 mm PIC rings, the Euclidean PIC rings exhibited no difference in BPND between the unaffected and stroke affected hemispheres in both initial and follow-up images.

The surface-fitting used by CIVET depends on a sharp WM-GM gradient, which may be eroded or eliminated by the infarction caused by acute ischemia. Visual inspection of the CIVET surfaces revealed that they closely followed the cortical mantle outside of the infarct where the WM GM border was preserved. The surfaces did not follow the cortical mantle inside of the infarct, but this region was not used in the present analysis.

3.6.3 Partial-Volume Correction Results in Higher Sensitivity to Long-Term Neuronal Cell Loss

In the initial and follow-up PET images there was significant difference between uncorrected and PVC IHDBP. However, at follow-up there was a significant interaction between PVC and PIC ring. This suggests that PVEs are a more important confounds in PET-images acquired 6 months after the stroke.

Despite these concerns, PVC has not been widely implemented in studies involving the PIC and may be a source of bias in results. For example, several PET and SPECT studies have reported decreased binding to GABAA receptors [43, 54–56, 108] at several weeks to months post-stroke. Without PVC it is difficult to conclude

whether their results are consistent with those reported here, because it remains possible that their reported decrease in radiotracer binding to GABAA was the result of a change in cortical thickness and not a change in the availability of GABAA receptors.

While PVC is not widely used in studies of the PIC, some studies have used simple PVC algorithms that compensate for spill-out effects [57, 58]. In the present study we found that spill-in PVE were particularly important because small but significant changes in radiotracer binding within a region can be obscured by spill-in radiotracer concentration from adjacent regions.

There are a multitude of factors that come into play when determining whether or not PVC be important in PET images of stroke patients: size of the infarct, presence of cortical thinning, the gradient of radiotracer concentration between the infarct and healthy tissue. It is difficult to know a priori how these will come into play. The use of PVC methods that correct for both spill-in and spill-out effects in the analysis may thus reduce the risk of overlooking significant results due to PVE and should be considered in standard data analysis procedures. The aforementioned studies of GABAA with PET and SPECT use mismatch between an image of the initial hypoperfusion, e.g., from perfusion CT, with the an image of the final infarct, e.g., from FLAIR MRI, and thereby define one large peri-infarct region [43, 54–57, 108]. Our geodesic PIC method is compatible with this approach because the image of the initial hypoperfusion can be mapped onto a surface representation of the cortical GM and used to constrain the spatial extent of the PIC rings. This would

ensure that the PIC rings only sample from tissue that is known to be hypoperfused and improve the signal-to noise ratio of the BPND distance profiles.

3.6.4 Limitations

One limitation of the present study was the use of the contra-lateral hemispheres instead as comparator. Kim et al. [108] have reported both widespread bilateral decrease in GABAA receptor density in human stroke patients as well as some localized increase in GABAA receptor density in the contralateral peri-infarct. A global decrease however should not affect the results presented here, because the difference between the hemispheres remains the same given a global reduction in both hemispheres. Moreover, if the peri infarct rings of the unaffected hemisphere in this study do include regions with increased GABAA receptor density, then the results would only tend to underestimate the true difference in BPIHD and would only introduce a bias into the conservative direction.²

Infarction causes a local reduction in the gradient of the MRI signal between the WM and GM and thus interferes with the definition of a WM-GM surface mesh. Without a reliable WM-GM surface mesh, it is impossible to accurately

² Disruption of the blood-brain-barrier could theoretically have caused an un-specific influx of the radioligand and thus an overestimation of BPND in the initial scans in the subacute phase. The effect of BBB disruption is however considered to be low because by definition the PIC is morphologically normal tissue (BBB-disruption mainly occurs in the infarct). Even if the BPND would have been overestimated, this would have introduced a bias into the conservative direction because it would have led to a decreased of the interhemispheric difference in BPND.

measure cortical thickness. Visual inspection of the surface meshes revealed that the distortion of the mesh is limited to the infarct and thus had no visible effect on the surrounding PIC.

The most important limitation is the high variability of the size, shape and location of the stroke volumes. The only way to account for this variability would be to use the size or location of the stroke as an additional factor in the statistical analysis. A complex statistical analysis such as this would require additional participants and was not possible in the present study.

3.7 Conclusions

In cortical strokes, a geodesic distance metric provides an anatomically realistic method for modeling the PIC because it conforms more closely to the anatomy of the vasculature than traditional, Euclidean distance metric. PVC may be important in the context of cortical ischemic stroke because it gives a more anatomically realistic estimate of BPND and controls for long-term changes in cortical thickness due to the ischemic insult.

3.7.1 Acknowledgements

This study was funded by the Canadian Institutes for Health Research (CIHR) grant MOP-115107 to AT and support from Fonds de Recherche du Québec-Santé (FRQ-S) to AT.

3.8 Contribution of Authors

Thomas Funck designed the data analysis, co-developed the geodesic distance algorithm, wrote all of the software used for the data analysis, and was the primary author of the manuscript.

Mohamed Al-Kuwaiti created the manual labels for the infarct.

Claude Lepage co-developed the geodesic distance algorithm and helped edit the paper.

Peter Zepper provided ideas for the data analysis; specifically, it was his idea to study changes in the cortex based on Euclidean distance from the infarct.

Jeffrey Minuk was involved in identifying patients for enrollment in the study.

Hyman M. Schipper was involved in identifying patients for enrollment in the study.

Alan C. Evans provided conceptual guidance for conducting the data analysis.

Alexander Thiel was the principal investigator, designed the study, identified patients for enrollment in the study, provided conceptual guidance for the data analysis, and edited the manuscript.

References

2. Collins, D. L., Neelin, P., Peters, T. & Evans, A. Automatic 3D intersubject Registration fo MR Volumetric Data in Standardized Talairach Space. *Journal of Computer Assisted Tomography* **10**, 192–205. ISSN: 10538119 (1994).
4. Mazziotta, J. *et al.* A probabilistic atlas and reference system for the human brain: International Consortium for Brain Mapping (ICBM). *Philosophical Transactions of the Royal Society B: Biological Sciences* **356**, 1293–1322. ISSN: 0962-8436 (Aug. 2001).
12. Wienhard, K. *et al.* The ECAT HRRT: performance and first clinical application of the new high resolution research tomograph. *IEEE Transactions on Nuclear Science* **49**, 104–110. ISSN: 0018-9499 (Feb. 2002).
23. Baron, J.-C., Yamauchi, H., Fujioka, M. & Endres, M. Selective neuronal loss in ischemic stroke and cerebrovascular disease. *Journal of cerebral blood flow and metabolism : official journal of the International Society of Cerebral Blood Flow and Metabolism* **34**, 2–18. ISSN: 1559-7016 (2014).
24. Nedergaard, M., Astrup, J. & Klinken, L. Cell density and cortex thickness in the border zone surrounding old infarcts in the human brain. *Stroke; a journal of cerebral circulation* **15**, 1033–9. ISSN: 0039-2499 (Jan. 1984).

25. Nedergaard, M., Vorstrup, S. & Astrup, J. Cell density in the border zone around old small human brain infarcts. *Stroke* **17**, 1129–1137. ISSN: 0039-2499 (Nov. 1986).
26. Nedergaard, M. Neuronal injury in the infarct border: a neuropathological study in the rat. *Acta*, 267–274 (1987).
27. Torvik, A. & Svindland, A. Is there a transitional zone between brain infarcts and the surrounding brain? A histological study. *Acta neurologica Scandinavica* **74**, 365–370. ISSN: 0001-6314 (Nov. 1986).
39. Hoffman, E. J., Huang, S. C. & Phelps, M. E. *Quantitation in positron emission computed tomography: 1. Effect of object size*. 1979.
42. Astrup, J., Siesjo, B. & Symon, L. Thresholds in Cerebral Ischemia. *Stroke* **12**, 723–725 (1981).
43. Sette, G. *et al.* In vivo mapping of brain benzodiazepine receptor changes by positron emission tomography after focal ischemia in the anesthetized baboon. *Stroke; a journal of cerebral circulation* **24**, 2046–57, discussion 2057–8. ISSN: 0039-2499 (1993).
47. La Fougère, C. *et al.* Where in-vivo imaging meets cytoarchitectonics: the relationship between cortical thickness and neuronal density measured with high-resolution [18F]flumazenil-PET. *NeuroImage* **56**, 951–60. ISSN: 1095-9572 (June 2011).
48. Heiss, W. D. *et al.* Repeat positron emission tomographic studies in transient middle cerebral artery occlusion in cats: residual perfusion and efficacy of

- postischemic reperfusion. *Journal of cerebral blood flow and metabolism : official journal of the International Society of Cerebral Blood Flow and Metabolism* **17**, 388–400. ISSN: 0271-678X (1997).
54. Nakagawara, J., Sperling, B. & Lassen, N. A. Incomplete Brain Infarction of Reperfused Cortex May Be Quantitated With Iomazenil. *Stroke* **28**, 124–132. ISSN: 0039-2499 (Jan. 1997).
55. Saur, D., Buchert, R., Knab, R., Weiller, C. & Röther, J. Iomazenil-single-photon emission computed tomography reveals selective neuronal loss in magnetic resonance-defined mismatch areas. *Stroke* **37**, 2713–2719. ISSN: 00392499 (2006).
56. Carrera, E. *et al.* Is neural activation within the rescued penumbra impeded by selective neuronal loss? *Brain* **136**, 1816–1829. ISSN: 00068950 (2013).
57. Guadagno, J. V. *et al.* Selective neuronal loss in rescued penumbra relates to initial hypoperfusion. *Brain : a journal of neurology* **131**, 2666–78. ISSN: 1460-2156 (Oct. 2008).
58. Zepper, P. *et al.* Imaging delayed cell death in subacute stroke with high-resolution 18F-Flumazenil. *Society of Nuclear Medicine Annual Meeting Abstracts* **53**, 37 (May 2012).
92. Jones, T. A. *et al.* Remodeling the brain with behavioral experience after stroke. *Stroke* **40**, S136–S139. ISSN: 00392499 (2009).
93. Nudo, R. J. Postinfarct cortical plasticity and behavioral recovery. *Stroke* **38**, 840–845. ISSN: 00392499 (2007).

94. Nudo, R. J. & Milliken, G. W. Reorganization of movement representations in primary motor cortex following focal ischemic infarcts in adult squirrel monkeys. *Journal of neurophysiology* **75**, 2144–2149. ISSN: 0022-3077 (1996).
95. Brown, C. E., Aminoltejadi, K., Erb, H., Winship, I. R. & Murphy, T. H. In vivo voltage-sensitive dye imaging in adult mice reveals that somatosensory maps lost to stroke are replaced over weeks by new structural and functional circuits with prolonged modes of activation within both the peri-infarct zone and distant sites. *The Journal of neuroscience : the official journal of the Society for Neuroscience* **29**, 1719–1734. ISSN: 0270-6474 (2009).
96. Carmichael, S. T., Wei, L., Rovainen, C. M. & Woolsey, T. A. New patterns of intracortical projections after focal cortical stroke. *Neurobiology of disease* **8**, 910–922. ISSN: 0969-9961 (2001).
97. Florence, S. L., Taub, H. B. & Kaas, J. H. Large-scale sprouting of cortical connections after peripheral injury in adult macaque monkeys. *Science (New York, N.Y.)* **282**, 1117–1121. ISSN: 0036-8075 (1998).
98. Murphy, T. H. & Corbett, D. Plasticity during stroke recovery: from synapse to behaviour. *Nature reviews. Neuroscience* **10**, 861–872. ISSN: 1471-003X (2009).
99. Stroemer, R. P., Kent, T. a., Hulsebosch, C. E. & Feeney, D. M. Enhanced Neocortical Neural Sprouting, Synaptogenesis, and Behavioural Recovery With D -Amphetamine Therapy. *Stroke* **29**, 2381–2395 (1998).
100. Ueno, Y. *et al.* Axonal outgrowth and dendritic plasticity in the cortical peri-infarct area after experimental stroke. *Stroke* **43**, 2221–2228. ISSN: 00392499 (2012).

101. Carmichael, S. T. *et al.* Growth-associated gene expression after stroke: evidence for a growth-promoting region in peri-infarct cortex. *Experimental neurology* **193**, 291–311. ISSN: 0014-4886 (June 2005).
102. Gulyás, B. *et al.* Evolution of microglial activation in ischaemic core and peri-infarct regions after stroke: A PET study with the TSPO molecular imaging biomarker [11C]vinpocetine. *Journal of the Neurological Sciences* **320**, 110–117. ISSN: 0022510X (2012).
103. Price, C. J. S. *et al.* Intrinsic activated microglia map to the peri-infarct zone in the subacute phase of ischemic stroke. *Stroke* **37**, 1749–1753. ISSN: 00392499 (2006).
104. Schroeter, M. *et al.* Neuroinflammation extends brain tissue at risk to vital peri-infarct tissue: a double tracer [11C]PK11195- and [18F]FDG-PET study. *Journal of cerebral blood flow and metabolism : official journal of the International Society of Cerebral Blood Flow and Metabolism* **29**, 1216–1225. ISSN: 0271-678X (2009).
105. Ceulemans, A.-G. *et al.* The dual role of the neuroinflammatory response after ischemic stroke: modulatory effects of hypothermia. *Journal of neuroinflammation* **7**, 74. ISSN: 1742-2094 (Jan. 2010).
106. Thiel, A., Cechetto, D. F., Heiss, W. D., Hachinski, V. & Whitehead, S. N. Amyloid burden, neuroinflammation, and links to cognitive decline after ischemic stroke. *Stroke*, 2825–2829. ISSN: 00392499 (2014).
107. Fink, G. R., Herholz, K., Pietrzyk, U., Huber, M. & Heiss, W.-D. Peri-Infarct perfusion in human ischemia: Its relation to tissue metabolism, morphology,

- and clinical outcome. *Journal of Stroke and Cerebrovascular Diseases* **3**, 123–131. ISSN: 10523057 (1993).
108. Kim, Y. K., Yang, E. J., Cho, K., Lim, J. Y. & Paik, N.-J. Functional Recovery After Ischemic Stroke Is Associated With Reduced GABAergic Inhibition in the Cerebral Cortex: A GABA PET Study. *Neurorehabilitation and neural repair* **28**, 576–583. ISSN: 1552-6844 (2014).
109. Furlan, M., Marchal, G., Viader, F., Derlon, J. M. & Baron, J. C. Spontaneous neurological recovery after stroke and the fate of the ischemic penumbra. *Annals of neurology* **40**, 216–226. ISSN: 0364-5134 (1996).
110. Plautz, E. J. *et al.* Post-infarct cortical plasticity and behavioral recovery using concurrent cortical stimulation and rehabilitative training: A feasibility study in primates. *Neurological Research* **25**, 801–810. ISSN: 0161-6412 (Dec. 2003).
111. Cramer, S. C., Shah, R., Juranek, J., Crafton, K. R. & Le, V. Activity in the peri-infarct rim in relation to recovery from stroke. *Stroke* **37**, 111–115. ISSN: 00392499 (2006).
112. Heiss, W. D. *et al.* Progressive derangement of periinfarct viable tissue in ischemic stroke. *Journal of cerebral blood flow and metabolism : official journal of the International Society of Cerebral Blood Flow and Metabolism* **12**, 193–203. ISSN: 0271-678X (1992).
113. Markus, R. *et al.* Topography and Temporal Evolution of Hypoxic Viable Tissue Identified by ¹⁸F-Fluoromisonidazole Positron Emission Tomography in Humans After Ischemic Stroke. *Stroke* **34**, 2646–2652. ISSN: 00392499 (2003).

114. Carrera, E. *et al.* The vascular mean transit time: a surrogate for the penumbra flow threshold? *Journal of cerebral blood flow and metabolism : official journal of the International Society of Cerebral Blood Flow and Metabolism* **31**, 1027–35. ISSN: 1559-7016 (Apr. 2011).
115. Hatazawa, J. *et al.* Evaluation of cerebral infarction with iodine 123-iomazenil SPECT. *Journal of nuclear medicine : official publication, Society of Nuclear Medicine* **36**, 2154–2161. ISSN: 0161-5505 (1995).
116. Sasaki, M. *et al.* Benzodiazepine receptors in chronic cerebrovascular disease: comparison with blood flow and metabolism. *Journal of nuclear medicine : official publication, Society of Nuclear Medicine* **38**, 1693–1698. ISSN: 01615505 (1997).
117. Li, Q. *et al.* Cortical thickness estimation in longitudinal stroke studies: A comparison of 3 measurement methods. *NeuroImage: Clinical*. ISSN: 22131582. doi:10.1016/j.nicl.2014.08.017 (2014).
118. Sled, J. G., Zijdenbos, A. P. & Evans, A. C. A nonparametric method for automatic correction of intensity nonuniformity in MRI data. English. *IEEE transactions on medical imaging* **17**, 87–97. ISSN: 0278-0062 (Feb. 1998).
119. Zijdenbos, A. P., Forghani, R. & Evans, A. C. *Automatic Quantification of MS Lesions in 3D MRI Brain Data Sets: Validation of INSECT in MICCAI '98 Proceedings of the First International Conference on Medical Image Computing and Computer-Assisted Intervention* (Springer-Verlag, Oct. 1998), 439–448. ISBN: 3-540-65136-5. <http://dl.acm.org/citation.cfm?id=646921.709333>.

120. Tohka, J., Zijdenbos, A. & Evans, A. Fast and robust parameter estimation for statistical partial volume models in brain MRI. *NeuroImage* **23**, 84–97. ISSN: 1053-8119 (Sept. 2004).
121. Funck, T., Paquette, C., Evans, A. & Thiel, A. Surface-based partial-volume correction for high-resolution PET. *NeuroImage* **102**, 674–87. ISSN: 1095-9572 (Nov. 2014).
122. Lucy, L. B. An iterative technique for the rectification of observed distributions. en. *The Astronomical Journal* **79**, 745. ISSN: 00046256 (June 1974).
123. Richardson, W. H. Bayesian-Based Iterative Method of Image Restoration. EN. *Journal of the Optical Society of America* **62**, 55. ISSN: 0030-3941 (Jan. 1972).
124. Logan, J. *et al.* Distribution Volume Ratios Without Blood Sampling from Graphical Analysis of PET Data. *Journal of Cerebral Blood Flow & Metabolism* **16**, 834–840. ISSN: 0271-678X (Sept. 1996).
125. Savic, I. *et al.* in-Vivo Demonstration of Reduced Benzodiazepine Receptor Binding in Human Epileptic Foci. *The Lancet* **332**, 863–866. ISSN: 01406736 (Oct. 1988).
126. Salmi, E. *et al.* Measurement of GABAA receptor binding in vivo with [11C]flumazenil: a test-retest study in healthy subjects. *NeuroImage* **41**, 260–9. ISSN: 1053-8119 (June 2008).
127. Wilcoxon, F. Individual Comparisons by Ranking Methods. *Biometrics Bulletin* **1**, 80–83 (1945).

128. Hochberg, Y. A Sharper Bonferroni Procedure for Multiple Tests of Significance. *Biometrika* **75**, 800–802 (1988).
129. Heiss, W. D. *et al.* Permanent cortical damage detected by flumazenil positron emission tomography in acute stroke. *Stroke; a journal of cerebral circulation* **29**, 454–461. ISSN: 0039-2499 (1998).
130. Schaechter, J. D., Moore, C. I., Connell, B. D., Rosen, B. R. & Dijkhuizen, R. M. Structural and functional plasticity in the somatosensory cortex of chronic stroke patients. *Brain : a journal of neurology* **129**, 2722–2733. ISSN: 1460-2156 (Oct. 2006).
131. Brodtmann, A. *et al.* Changes in regional brain volume three months after stroke. *Journal of the Neurological Sciences* **322**, 122–128. ISSN: 0022510X (2012).
132. Duering, M. *et al.* Incident subcortical infarcts induce focal thinning in connected cortical regions. *Neurology* **79**, 2025–2028. ISSN: 0028-3878 (Nov. 2012).

CHAPTER 4

APPIAN: Automated Pipeline for PET Image Analysis

Thomas Funck^{1, 2*}, Kevin Larcher³, Paule-Joanne Toussaint¹, Alan C. Evans^{1,3,4}
and Alexander Thiel^{2,4}

¹ Montreal Neurological Institute, McGill University, Montreal, QC, Canada

² Jewish General Hospital and Lady Davis Institute for Medical Research, Montreal, QC, Canada

³ Biospective, Inc., Montreal, QC, Canada ⁴ Department of Neurology and Neurosurgery, McGill University, Montreal, QC, Canada

Published: Funck, T., Larcher, K., Toussaint, P.J., Evans, A.C., Thiel, A., 2018. APPIAN: Automated Pipeline for PET Image Analysis. Front. Neuroinform. 12.

4.1 Preamble

In this chapter we present a novel software package, APPIAN (Automated Pipeline for PET Image ANlysis) to facilitate and improve the state of neurotransmitter receptor mapping with PET by making it more robust and reproducible. The challenge of neurotransmitter receptor mapping with PET is that it requires several image processing stages in order to produce the desired quantitative values representing radioligand binding densities. While researchers have a wide variety of algorithms to choose from, it is often not clear which algorithm offers the best solution for the

specific task. Another problem is that at each stage there is a potential for errors that may be difficult for the user to notice, but that can subtly bias the final results.

While there exists a software package that handles most of the needs of researchers, it is not open-source and is prohibitively expensive for smaller research groups. By making the software package presented here open-source, we hope to encourage the PET research community to participate in the development of this software by contributing preferred algorithms. This will allow easy comparison between different algorithms on a wide variety of different data sets and promote the adoption of consensus image processing methods. In this study, APPIAN was not directly compared to existing pipelines on the same datasets. In the future a comparison would ideally be performed versus PMOD as this is currently considered the gold-standard data set.

In the following manuscript a comparison is made between existing PET processing pipelines. Two important software packages were not included in the manuscript, one of which had not yet been released at time of publication, but are important to include in a discussion of competing PET pipelines. PETSurfer [19, 133] is a suite of individual tools that can be used to perform post-reconstruction PET motion correction, PET-MRI coregistration, PVC, and quantification with tracer kinetic analysis. Magia is another recent PET pipeline and includes: post-reconstruction PET motion correction, PET-MRI coregistration, quantification with tracer kinetic analysis [134].

In addition to the criteria which are used in the manuscript to distinguish these pipelines, there are a few additional considerations for differentiating them: the ability to use arterial input functions, use the subject's MRI, and motion correction.

Of the reviewed pipelines the ones that allow the use of arterial input functions are: APPIAN, MIAKAT, and PMOD. Post-reconstruction motion correction can be an important preprocessing step in PET imaging and is implemented in : MIAKAT, PMOD, PETSurfer, and Magia. All described software packages except CapAIBL can be used with the subject's MRI.

To demonstrate that this software package, which is based on freely available PET processing tools, can accurately recover parametric values, such as radioligand binding potential, from raw PET image, we evaluate its accuracy on Monte-Carlo simulated PET data.

4.2 Abstract

APPIAN is an automated pipeline for user-friendly and reproducible analysis of positron emission tomography (PET) images with the aim of automating all processing steps up to the statistical analysis of measures derived from the final output images. The three primary processing steps are coregistration of PET images to T1-weighted magnetic resonance (MR) images, partial-volume correction (PVC), and quantification with tracer kinetic modeling. While there are alternate open-source PET pipelines, none offers all of the features necessary for making automated PET analysis as reliably, flexibly and easily extendible as possible. To this end, a novel method for automated quality control (QC) has been designed to facilitate reliable, reproducible research by helping users verify that each processing stage has been performed as expected. Additionally, a web browser-based GUI has been implemented to allow both the 3D visualization of the output images, as well as plots describing

the quantitative results of the analyses performed by the pipeline. APPIAN also uses flexible region of interest (ROI) definition— with both volumetric and, optionally, surface-based ROI—to allow users to analyze data from a wide variety of experimental paradigms, e.g., longitudinal lesion studies, large cross-sectional population studies, multi-factorial experimental designs, etc. Finally, APPIAN is designed to be modular so that users can easily test new algorithms for PVC or quantification or add entirely new analyses to the basic pipeline. We validate the accuracy of APPIAN against the Monte-Carlo simulated SORTEO database and show that, after PVC, APPIAN recovers radiotracer concentrations within 93–100% accuracy.

4.3 Introduction

The increasing availability of large brain imaging data sets makes automated analysis essential. Not only is automated analysis important for saving time, but it also increases the reproducibility of research. No existing post-reconstruction positron emission tomography (PET) software package satisfies all the needs of researchers, specifically code that is free, open-source, language agnostic, easily extendible, deployable on web platforms as well as locally, and including all necessary processing steps prior to statistical analysis. We therefore present APPIAN (Automated Pipeline for PET Image Analysis) a new open-source pipeline based on NiPype [135] for performing automated PET data analysis. The starting point for APPIAN are reconstructed PET images on which all necessary processing steps are performed to obtain quantitative measures from the original PET images (Figure 4–1). In conjunction with the reconstructed PET image, APPIAN uses T1-weighted

MR images to define regions of interest (ROI) that are used at multiple processing stages. Briefly, APPIAN (1) coregisters the T1 MR image with the PET image, (2) defines ROI necessary for later processing steps, (3) performs partial-volume correction (PVC), (4) calculates quantitative parameters, (5) produces a report of the results, and finally, (6) performs QC on the results (see Figure 4–1 for a schema of APPIAN, and Discussion section for a detailed description of the pipeline, complete with flowchart).

4.4 Materials and Methods

4.4.1 Pipeline Overview

Coregistration

Positron emission tomography images are coregistered to the corresponding non-uniformity corrected [118] T1 MR-images using a six parameter linear fitting algorithm that minimizes normalized mutual information. The algorithm is based on `minctracc`¹ and proceeds hierarchically by performing iterative coregistration at progressively finer spatial scales [2]. Coregistration is performed in two stages, the first using a binary mask for the PET and the T1 MR images, respectively, to obtain a coarse coregistration. This is followed by a second registration step to refine the initial fit between the PET and T1 MR images without the use of the binary images.

¹ <https://github.com/BIC-MNI/minc-toolkit-v2>

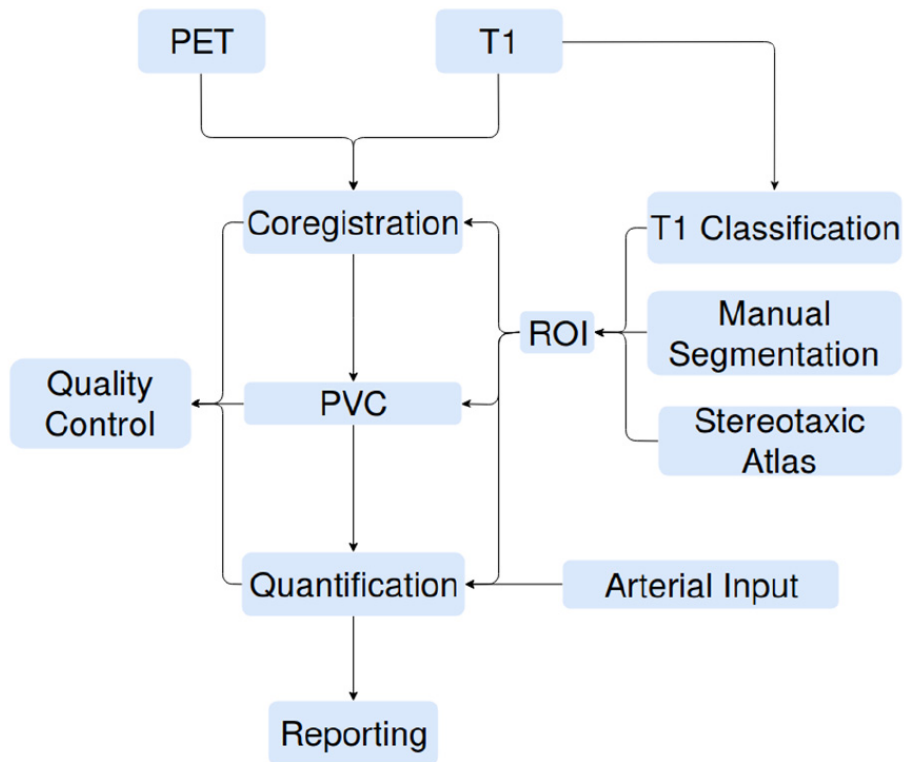


Figure 4-1: APPIAN performs all processing steps necessary to obtain quantitative parameters from reconstructed PET images. Flexible definition of ROI allows use of APPIAN for a wide variety of experimental designs. Integrated QC helps ensure that the pipeline performs as expected.

MR Image Processing

T1 structural preprocessing is performed if the user does not provide a binary brain mask volume and a transformation file that maps the T1 MR image into stereotaxic space. If these inputs are not provided, APPIAN will automatically coregister the T1 MR image to stereotaxic space. By default, the stereotaxic space is defined on the ICBM 152 6th generation non-linear brain atlas [4], but users can provide their own stereotaxic template if desired. Coregistration is performed using an iterative implementation of minctracc [2]. Brain tissue extraction is performed in stereotaxic space using BEaST [136]. In addition, tissue segmentation can also be performed on the normalized T1 MR image. Currently, only ANTs Atropos package [137] has been implemented for T1 tissue segmentation but this can be extended based on user needs.

Regions of Interest

Regions of interest have an important role in three of the processing steps in APPIAN: PVC, quantification, and reporting of results. ROIs are used in PVC algorithms to define anatomical constraints. When no arterial input is available for quantification, a reference ROI is placed in a brain region devoid of specific tracer binding. Finally, when reporting results from APPIAN, ROIs are needed to define the brain areas from which average parameters are calculated for final statistical analysis. ROIs for each of these processing steps can be defined from one of three sources. The simplest ROI are those derived from a classification of the T1 MR image, e.g., using ANIMAL [4], prior to using APPIAN. Users can also use tissue classification software

implemented in APPIAN to classify their T1 MR images, thereby eliminating the need to run a strictly MR image-based pipeline prior to using APPIAN.

Regions of interest can also be defined on a stereotaxic atlas, e.g., AAL [138], with a corresponding template image. In this case, the template image is non-linearly coregistered to the T1 MR image in native space, and subsequently aligned to the native PET space of the subject. Finally, it is frequently necessary to manually define ROI on each individual MR image, for instance when segmenting focal brain pathologies such as a tumor or ischemic infarct. This option is also implemented in APPIAN.

Partial-Volume Correction

In PET, partial-volume effects result from the presence of multiple tissue types within a single voxel and the blurring of the true radiotracer concentrations. PVC of PET images is thus necessary to accurately recover the true radiotracer distribution and, for example, differentiate between true neuronal loss from cortical thinning. Several methods have been proposed to perform PVC, many of which are implemented in PETPVC [139]. In addition, we have also implemented idSURF [121], a voxel-wise iterative deconvolution that uses anatomically constrained smoothing to control for noise amplification while limiting the amount of spill-over between distinct anatomical regions. APPIAN thus allows the user to select the appropriate PVC method based on their needs and their data. If the desired PVC method is not implemented in APPIAN, it can be easily included in the pipeline by creating a file describing the inputs and outputs of the method.

Quantification

In PET images, quantitative biological or physiological parameters—such as non-displaceable binding potential or cerebral blood flow—are often calculated from the measured temporal change of tissue radiotracer concentration, so-called time activity curves (TACs), within voxels or ROIs. Many models exist for performing quantification depending on the type of radiotracer, parameter of interest, and time frames acquired. The quantification methods available in APPIAN are from the Turku PET Centre tools² [140]. Currently, the implemented models are: the Logan Plot [141], Patlak–Gjedde Plot [142, 143], Simplified Reference Tissue Model [144], and standardized uptake value [145]. APPIAN implements both voxel-based and ROI-based quantification methods. It can also process arterial input functions as well as input functions from reference regions devoid of specific binding. Arterial inputs are in the “.dft” format described by the Turku PET Centre.

Results Report

The ROI defined in “MR Image Processing” section are used to calculate regional mean values for the parameter of interest from the output images after coregistration, PVC and quantification processing steps. Additionally, if cortical surface meshes are provided by the user, the output images can be interpolated on these meshes and be used to derive surface-based parameter estimates. Regional mean parameter

² http://www.turkupetcentre.net/petanalysis/format_tpc_dft.html

values are saved in wide format ‘.csv’ files in the so-called ‘vertical format’ (i.e., the output measure from each subject and each region is saved in a single column). This standardized data format simplifies subsequent analysis with statistical software, such as R (R Core Team, 2016 or scikit-learn [146]).

APPIAN also calculates group-level descriptive statistics obtained from the output images. The group-level statistics that are provided exploit the BIDS³ naming convention which requires that file names include the subject ID, the task or condition, and the scanning session. APPIAN thus provides users with summary statistics for the subjects, tasks, and sessions. Descriptive statistics are plotted and displayed in a web browser-based GUI to allow simple and easy visualization of the results.

Quality Control and Visualization

APPIAN includes both visual and automated quality control. Visual quality control is facilitated by the incorporation of BrainBrowser—a 3D/4D brain volume viewer [147]—in the web browser-based GUI (Figure 4-2). This makes it possible to visualize the output images of the coregistration, PVC and quantification processing stages without the need for additional software.

While visual inspection remains the gold-standard method for verifying the accuracy of PET coregistration [148–152], automated QC can be useful in guiding the user to potentially failed processing steps. The first stage of the automated QC is to define a QC metric that quantifies the performance of a given processing step. For

³ Brain Imaging Data Structure

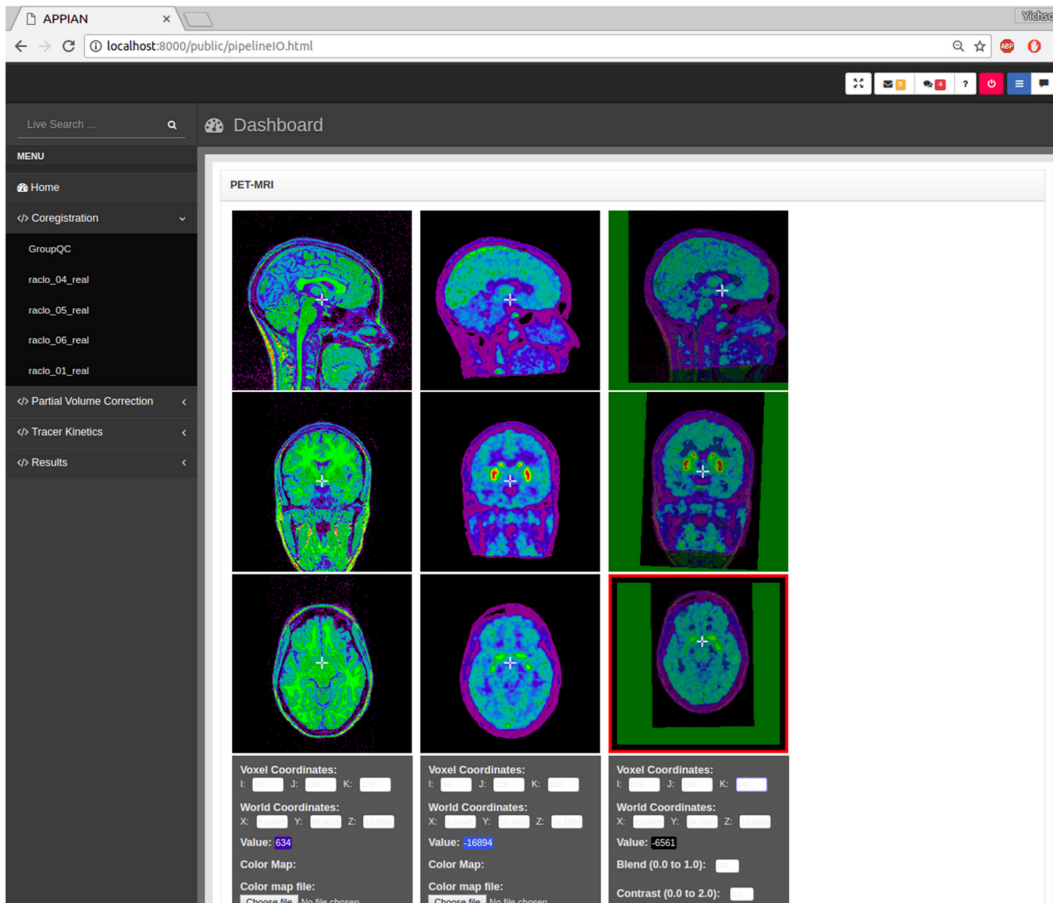


Figure 4–2: Output images produced by APPIAN can be viewed via a web browser-based dashboard. Visual QC for the coregistration stage can be performed by viewing the MRI, PET, and the fusion images of the two.

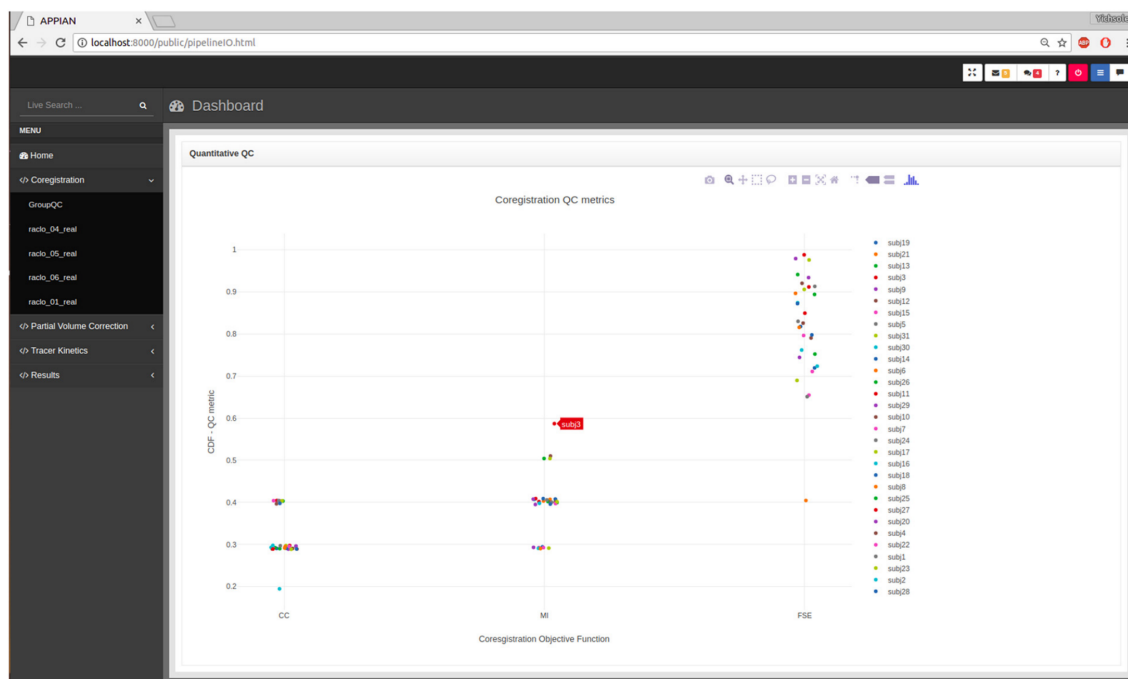


Figure 4-3: Output from automated quality control (QC) allows users to assess the performance of major processing steps at a glance. Here the automated QC metrics for the coregistration processing stage are shown: CC, cross-correlation, MI, mutual information, FSE, feature-space entropy.

example, in the case of PET-MRI coregistration the relevant QC metric is the similarity metric that quantifies the joint-dependence of spatial signal intensity distribution of the PET and MR images. By itself a single metric is insufficient to determine whether the processing step has been performed correctly. However, by calculating the distribution of several QC metrics for all subjects, it is possible to identify potential anomalies. Kernel density estimation is used to calculate the probability of observing a given QC metric under the empirical distribution of the entire set of QC metrics. The results are displayed in an interactive plot in the web browser-based dashboard (Figure 4-3).

File Formats

Input files for APPIAN are organized following the Brain Imaging Data Structure (BIDS) specifications [153], which uses the Nifti format. In addition, APPIAN also supports input files in the MINC file format [10], which are also organized according to the BIDS specifications but with the MINC file extension.

High Performance Computing

APPIAN is optimized for high performance computing in two ways. APPIAN is distributed in a Docker container⁴ that contains all the software necessary to run APPIAN on any computing platform supporting such containers (i.e., where Docker or Singularity has been installed). APPIAN can therefore be run identically across a wide variety of computing environments. This not only facilitates the reproducibility of results, but also allows APPIAN to be deployed simultaneously across multiple computing nodes to analyze subjects in parallel. Additionally, APPIAN supports multithread processing via NiPype and can therefore be run in parallel on multiple CPUs on a given computing platform, e.g., a personal workstation or a processing node on a server.

APPIAN also follows the specification of the BIDS apps in being capable of running subject-level and group-level analyses independently. This means that an instance of APPIAN can be run for each subject in parallel across the available

⁴ <https://www.docker.com/>

computing resources. Once the individual processing steps have been completed and stored in the same location, the group-level analyses can then be run, e.g., automated QC and reporting of group-level descriptive statistics. Thus, a given data set can be processed with APPIAN at different times and on different computing platforms.

The ability to process large data sets in an easy, fast, and reproducible manner is essential, particularly in cases where parameters for a given algorithm need to be optimized or where the performance of different algorithms at a given processing stage is being compared.

Accuracy of APPIAN

The accuracy of the APPIAN pipeline was evaluated using the SORTEO Monte-Carlo simulated PET data set [22]. These data consist of 15 subjects with a real T1 MR image segmented into anatomical defined ROIs derived from these images. From each of these anatomically segmented images, three sets of simulated PET images were produced by assigning empirically derived TACs of radiotracer concentrations of [11- C]-raclopride (RCL), [18-F]-fluorodeoxyglucose (FDG), and [18-F]-fluorodopa (FDOPA) into each segmented ROI. The PET images were simulated using the SORTEO Monte-Carlo PET simulator for the Siemens ECAT HR+ scanner [154].

Magnetic resonance images were processed using CIVET. CIVET uses the non-parametric N3 method to correct MR field non-uniformity [118]. The MR image is then transformed to MNI stereotaxic space of the ICBM 152 6th generation non-linear brain atlas [4], using a 12 parameter affine transformation [2]. Spatially normalized images are then segmented into gross anatomical regions with ANIMAL

(Collins and Evans, 1997). Thus all ROI images used in the subsequent analysis were derived using CIVET prior to running APPIAN.

The accuracy of the APPIAN was verified by comparing the results of the three central processing stages (coregistration, PVC, quantification) to the true radiotracer concentration TACs or the parametric values derived from them. For the coregistration and PVC stages, the integral of the TAC recovered from the processed images was compared to the integral of the true radiotracer concentration TACs. Parameter values were obtained by calculating the K_i , BP_{nd} , and $SUVR$ for the FDOPA, RCL, and FDG images, respectively, and compared to the same values calculated from the true radiotracer concentration TACs. The accuracy for each processing stage was calculated by dividing the results from APPIAN by the true radiotracer concentration or parametric values. This calculation was performed for a specific ROI for each radiotracer: cortical GM for FDG, the putamen for FDOPA, and the caudate nucleus for RCL. PVC was performed using the GTM method with a point spread function of 6.5 mm full-width half-maximum [155]. The cerebellum was used as a reference region for the calculation of parametric values in the quantification stage.

4.5 Results

APPIAN was able to recover accurate values at each major processing stage (Table 4-1), see Figure 4-4 for illustrative example from one subject. The recovered values for the coregistration and PVC were the integral of the regional TACs. For the quantification stage the recovered values were the parametric values as described in section “Accuracy of APPIAN”. The accuracy of the coregistration stage was between

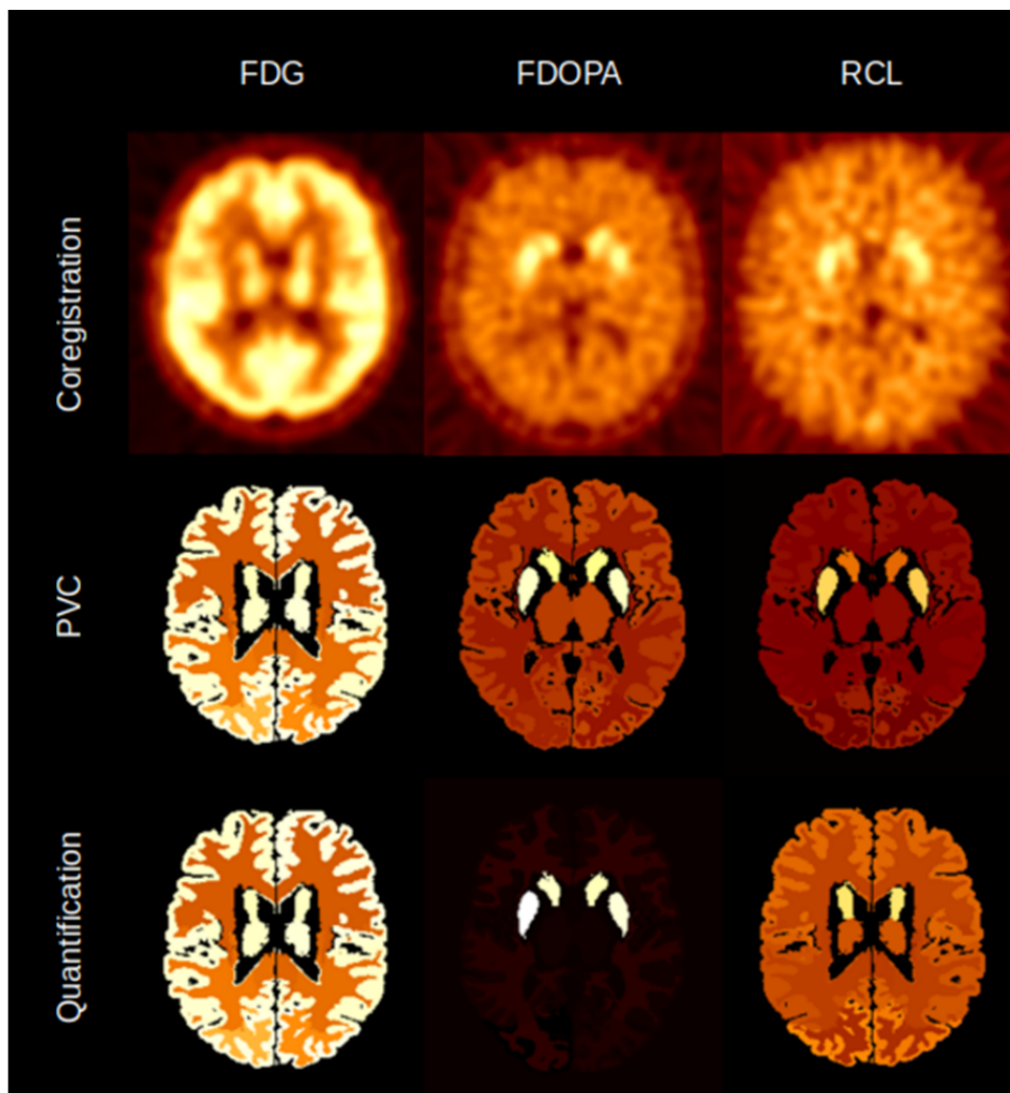


Figure 4-4: Illustrative example of the image volumes produced by APPIAN for the three major processing stages for FDG, FDOPA, and RCL.

Table 4–1: Accuracy is measured as the ratio of recovered to true radiotracer concentration or parameter value. APPIAN accurately recovers radiotracer concentrations and tracer kinetic parameters from the SORTEO simulated PET images.

Radiotracer	ROI	PVE	Analysis	Metric	Accuracy
FDG	GM	Uncorrected	Coregistration	integral	0.66 ± 0.006
FDG	GM	Corrected	PVC	integral	0.93 ± 0.025
FDG	GM	Corrected	Quantification	SUVR	0.94 ± 0.048
FDOPA	Putamen	Uncorrected	Coregistration	integral	0.69 ± 0.03
FDOPA	Putamen	Corrected	PVC	integral	1 ± 0.055
FDOPA	Putamen	Corrected	Quantification	Ki	0.83 ± 0.238
RCL	Caudate Nucleus	Uncorrected	Coregistration	integral	0.77 ± 0.016
RCL	Caudate Nucleus	Corrected	PVC	integral	1.05 ± 0.035
RCL	Caudate Nucleus	Corrected	Quantification	BPnd	1.03 ± 0.042

0.66 and 0.77, which represented an underestimation of the radiotracer distribution due to partial-volume effects. The accuracy was significantly improved by PVC, ranging between 0.93 and 1.05. The effect of PVC on the uncorrected radioactivity concentration for each radiotracer is shown in Figure 4–5. The PVC led to a slight overestimation in the caudate nucleus with RCL, but near perfect accuracy in the putamen with FDOPA. The final output parametric values were very accurate for RCL (1.02) and FDG (0.94), and lower in the case of FDOPA (0.83).

4.6 Discussion

4.6.1 Accuracy of APPIAN

APPIAN recovered accurate values for each of the three major processing steps on the SORTEO simulated PET data set. Not surprisingly, the accuracy of the recovered parameters was initially low (0.65–0.77), because of partial-volume effects. This improved significantly after PVC with the GTM method (0.93–1.05). For RCL and FDG, the parametric values resulting from the quantification processing stage maintained a similar level of accuracy to that of the PVC radiotracer concentrations.

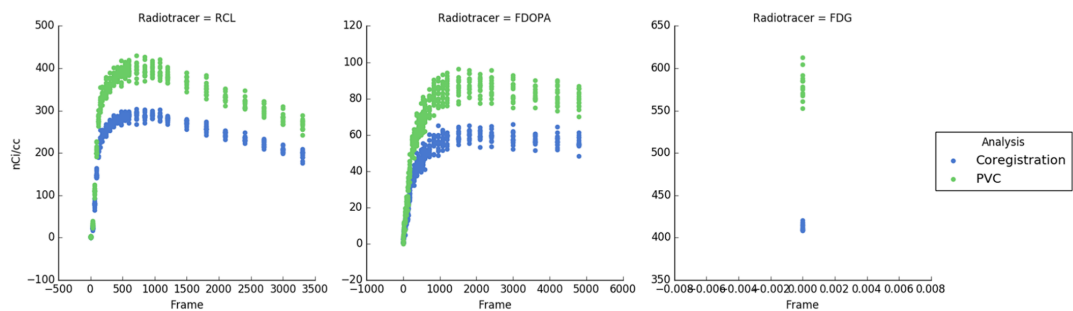


Figure 4–5: Time-activity curves for each subject and each radiotracer. Blue points indicate the uncorrected PET radioactivity concentration after PET-MRI coregistration and green points show radioactivity concentration after PVC with the GTM method. PVC corrects for spill-over of radiotracer distribution and increases the measured radioactivity concentration.

This was not the case with FDOPA where the accuracy decreased from 1 to 0.83. The decrease in accuracy was due to noise in the radiotracer concentrations that were measured in the caudate nucleus, which led to errors in the calculation of the integrals used by the Patlak plot to determine K_i .

For each radiotracer, the validation of APPIAN’s accuracy was performed with differing ROI and using different methods for calculating parametric values. These differences mean that it is not possible to quantitatively compare APPIAN’s accuracy for each radiotracer. The choice of ROI and algorithms for deriving parametric values were chosen to reflect analysis procedures that are widely used by researchers for each of the three radiotracers. It should be noted that the cerebellum is not typically used as a reference region for calculating SUVR or K_i for FDG and FDOPA, respectively. However, while the specific location of the reference region is of utmost

Table 4–2: Many different PET processing software exist with various features.

Feature	MIAKAT	PMOD	Pypes	CapAIBL	NiftyPET	APPIAN
Cost	Free	2,970–14,850\$	Free	Free	Free	Free
Open-source	Yes	No	Yes	No	Yes	Yes
Language	MATLAB	Java	Agnostic*	C++	Python	Agnostic*
Quantification	Yes	Yes	No	SUVR	No	Yes
PVC	No	No	Yes	No	Yes	Yes
Structural imaging	Yes	Optional	Yes	No	Yes	Required
Cloud-based processing	No	DICOM server	No	Yes	Maybe	Yes
Local processing	Yes	Yes	Yes	No	Yes	Yes
Visualization	GUI	GUI	Result plots	3D surfaces	No	Dashboard
Surface-based	No	No	No	Yes	No	Yes
Reconstruction	No	No	No	No	Yes	No

importance when performing true PET quantification, it is not relevant for verifying the computational accuracy of the algorithms in the APPIAN pipeline.

4.6.2 Comparison to Existing Pipelines

Several PET processing pipelines have been presented in recent years. We here briefly describe them to highlight their relative strengths (Table 4–2) and discuss how APPIAN compares to these. There are other PET pipelines that carry out at least three of the six steps performed by APPIAN, they are: PMOD [156], CapAIBL [157], MIAKAT [158], Pypes [159], and NiftyPET [160].

PMOD

PMOD [156] is the gold-standard software for quantification of PET images and is distributed in modules that perform specific aspects of PET analysis. PKIN includes an exhaustive list of quantification models and preprocessing methods for blood and plasma activity curves for analyzing regional PET data, while PXMOD performs the same analyses at the pixel level. PMOD also has modules that perform

analysis and PVC (PBAS), and image registration (PFUS). All these modules can be used interactively using a graphical user interface (GUI) but can also be linked together in a pipeline to automate the analysis of large data sets. A particularly useful feature is the option to add a QC step after each processing stage. PMOD thus includes all the preprocessing and analysis methods needed for automated PET analysis. As a commercial software solution however, the PMOD code is not open-source and thus imposes limitations on the user community with respect to flexible development and implementation of new image processing and analytical methods.

CapAIBL

CapAIBL [157] is a surface-based PET processing pipeline that is available through an online platform. It spatially normalizes PET images to cortical surface templates for the surface-based analysis and visualization of PET data without the need for structural imaging. Cortical surfaces are derived from a standardized template, thus subcortical structures such as the basal ganglia are not included in the analysis. A purely surface-based approach is also limited to images from structurally intact brains and may thus be difficult to apply to datasets with focal brain lesions. Nonetheless, CapAIBL provides a highly original method for performing automated PET analysis that is useful for the study of the cerebral cortex in cases where no structural image has been acquired alongside the PET image. Dore et al. [161] have shown a close correspondence in PET quantification across a wide range of radiotracers with coregistered PET and MR images and using CapAIBL, i.e., without coregistration.

Pypes

A recent multi-modal pipeline, Pypes [159], combines PET analysis with structural, diffusion, and functional MR images. This pipeline is free, open-source, and it is also written using NiPype [135]. Pypes leverages several brain imaging software packages—including SPM12 [162], FSL [163], and AFNI [164]—to provide multi-modal workflows. While Pypes does incorporate PVC, it does not incorporate tracer kinetic analysis, flexible ROI definition, or automated QC.

MIAKAT

MIAKAT [156] is the most complete, open- source PET processing pipeline. In addition to featuring many tracer-kinetic models, MIAKAT also includes motion-correction, a feature that is not currently implemented in APPIAN. One of MIAKAT’s most important features is its user-friendly GUI. This makes MIAKAT easy to use for users not familiar with the command-line interface. In addition to analyzing PET images, MIAKAT also includes the option to include structural images which are used to define regions of interest (ROI). MIAKAT has been recently extended for use on non-brain PET image analysis and for application to species other than humans [165].

One limitation of MIAKAT is that it does not include PVC, although this could potentially be added to the pipeline. More importantly, it is built using MATLAB, which restricts MIAKAT to a single, proprietary language with licensing restrictions.

NiftyPET

NiftyPET is another open-source, Python-based PET processing pipeline that implements Graphical Processing Unit-processing for massively parallel processing [160]. It is the only PET processing pipeline to reconstruct PET images from sinograms and to perform PVC [166]. It should be noted that the authors of NiftyPET use the term “quantification” to refer to quantification of radioactivity concentrations, whereas this term is here used to refer to the quantification of underlying biological or physiological parameters. NiftyPET therefore does not include parametric quantification.

APPIAN

There are a wide variety of PET pipelines presently available, each satisfying a different niche. APPIAN provides a highly flexible framework for processing large PET data sets, see Figure 4–6 for a detailed flowchart of APPIAN. One important feature is that APPIAN allows the user to define ROI from a variety of sources and is therefore compatible with a wide variety of experimental designs. Whereas lesion studies frequently use a binary lesion image defined on each subject’s respective structural image in its native coordinate space, it may be necessary for some studies (e.g., investigating lesion effects on functional systems as in aphasia post stroke) to use a common brain atlas in MNI-space. On the other hand, PET studies of, e.g., microglial inflammation may identify ROI based on the subjects’ respective tracer binding pattern in PET images in their native space. Quantification of PET images also requires users to be able to use either ROI to define a reference region without

specific binding of the radiotracer or TAC measured from arterial blood samples. APPIAN is therefore suited for a wide variety of experimental contexts because of its flexible system for ROI definition.

APPIAN is also modular and easily extendable so that users can either test new algorithms, e.g., a new PVC method, or add entirely new analyses to the pipeline. Moreover APPIAN, like Pypes, is written with NiPype and can thus use any program that can be run in a Bash shell environment. Users therefore do not need to rewrite their software in, e.g., Python if they wish to implement it in APPIAN. Also, given that descriptive statistics for ROI are automatically generated in the reporting stage, it is easy to extend APPIAN to perform sophisticated group-wise analyses. For example, investigators interested in implementing graph theoretical analyses can append their analysis to the group-level processing and input the descriptive statistics that are collected at the reports stage to their analysis.

Finally, APPIAN implements automated and visual QC to facilitate the analysis of large data sets. This is essential because as multiple processing stages are linked together into increasingly sophisticated pipelines, it is important that users be able to easily and reliably confirm that each processing stage has been performed correctly.

Using APPIAN

APPIAN is available for both local use and cloud-based use. The source code for APPIAN is freely available⁵ . While the code-base will be maintained by the

⁵ www.github.com/APPIAN-PET/APPIAN

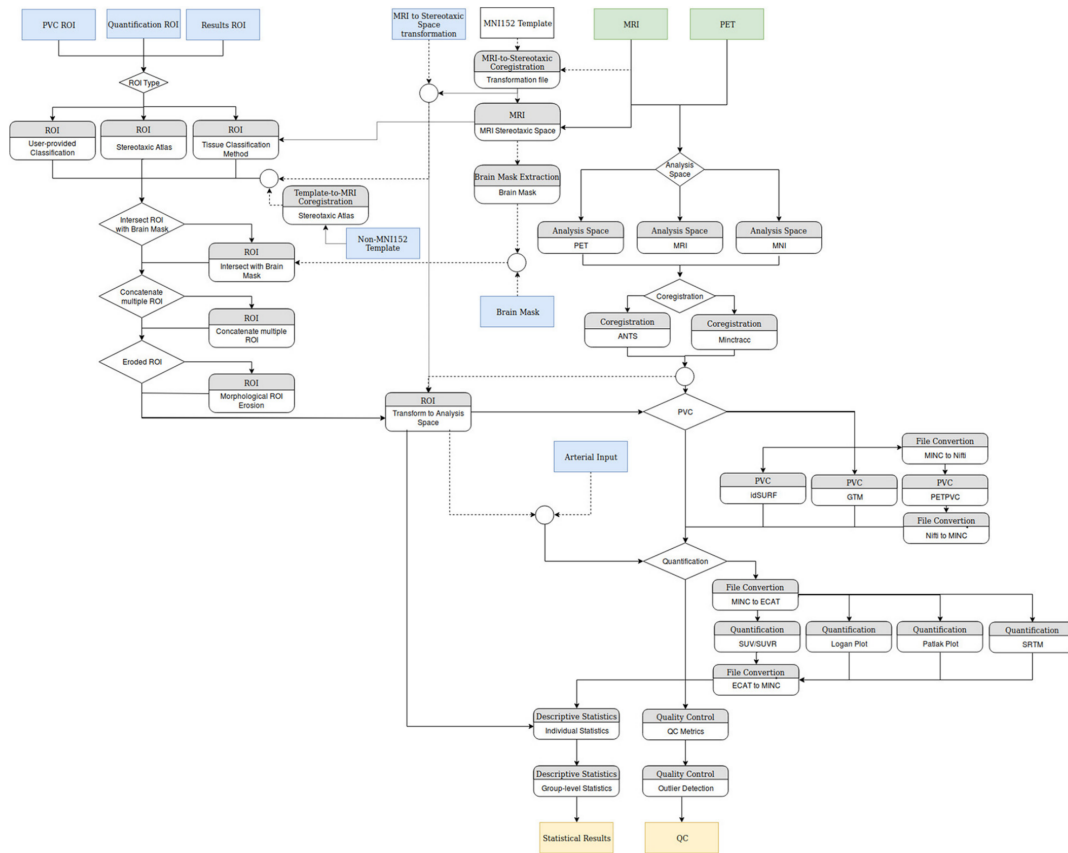


Figure 4–6: Flowchart of the modules implemented in APPIAN. Green boxes indicate mandatory inputs, blue boxes indicate optional inputs, and tan boxes indicate the primary quantitative outputs of the pipeline.

authors, we hope to create a community of developers to support the project in the long-term. Changes to APPIAN will be validated against the open CIMBI PET data⁶ [10]. APPIAN is provided via a Docker (see footnote 3) image and can be easily downloaded from Docker hub under `tffunck/appian:latest`. Cloud-based APPIAN is available via the CBRAIN platform⁷.

4.7 Conclusion

APPIAN is a novel PET processing pipeline that seeks to automate the processing of reconstructed PET images for a wide variety of experimental designs. It is therefore flexible and easily extendable. In order to ensure that each processing step is performed as expected, visual and automated QC are implemented. Our results on Monte-Carlo simulated PET data have shown that APPIAN accurately recovers radiotracer concentration and parametric values. Future work will focus on increasing the sensitivity of the automated QC and implementing more algorithms for coregistration, PVC, and quantification.

4.8 Contribution of Authors

Thomas Funck is the primary author of the manuscript, developed the APPIAN code.

⁶ <https://openneuro.org/datasets/ds001421>

⁷ portal.cbrain.mcgill.ca

Kevin Larcher developed the APPIAN code.

Paule-Joanne Toussaint is the advisor for designing APPIAN, edited the manuscript, and ongoing development of new PET quantification models.

Alexander Thiel (principal investigator) and Alan C. Evans (co-principal investigator) provided conceptual guidance and edited the manuscript.

FUNDING This work was supported by the Canadian Institutes of Health Research (CIHR) grants MOP-115107 (AT) and MOP-37754 (AE), and by the National Institutes of Health (NIH) operating grant 248216 (AE).

References

2. Collins, D. L., Neelin, P., Peters, T. & Evans, A. Automatic 3D intersubject Registration fo MR Volumetric Data in Standardized Talairach Space. *Journal of Computer Assisted Tomography* **10**, 192–205. ISSN: 10538119 (1994).
4. Mazziotta, J. *et al.* A probabilistic atlas and reference system for the human brain: International Consortium for Brain Mapping (ICBM). *Philosophical Transactions of the Royal Society B: Biological Sciences* **356**, 1293–1322. ISSN: 0962-8436 (Aug. 2001).
10. Beliveau, V. *et al.* A high-resolution in vivo atlas of the human brain’s serotonin system. *Journal of Neuroscience* **37**, 120–128. ISSN: 15292401 (Jan. 2017).

19. Greve, D. N. *et al.* Different partial volume correction methods lead to different conclusions: An 18F-FDG-PET study of aging. *NeuroImage* **132**, 334–343. ISSN: 10538119 (May 2016).
22. Reilhac, A. *et al.* PET-SORTEO: Validation and development of database of simulated PET volumes. *IEEE Transactions on Nuclear Science* **52**, 1321–1328. ISSN: 00189499 (Oct. 2005).
118. Sled, J. G., Zijdenbos, A. P. & Evans, A. C. A nonparametric method for automatic correction of intensity nonuniformity in MRI data. English. *IEEE transactions on medical imaging* **17**, 87–97. ISSN: 0278-0062 (Feb. 1998).
121. Funck, T., Paquette, C., Evans, A. & Thiel, A. Surface-based partial-volume correction for high-resolution PET. *NeuroImage* **102**, 674–87. ISSN: 1095-9572 (Nov. 2014).
133. Greve, D. N. *et al.* Cortical surface-based analysis reduces bias and variance in kinetic modeling of brain PET data. *NeuroImage* **92**, 225–236. ISSN: 10959572 (May 2014).
134. Karjalainen, T. *et al.* Magia: Robust Automated Image Processing and Kinetic Modeling Toolbox for PET Neuroinformatics. *Frontiers in Neuroinformatics* **14**, 3. ISSN: 1662-5196 (Feb. 2020).
135. Gorgolewski, K. *et al.* Nipype: A Flexible, Lightweight and Extensible Neuroimaging Data Processing Framework in Python. *Frontiers in Neuroinformatics* **5**, 13. ISSN: 1662-5196 (2011).
136. Eskildsen, S. F. *et al.* BEaST: Brain extraction based on nonlocal segmentation technique. *NeuroImage* **59**, 2362–2373. ISSN: 10538119 (Feb. 2012).

137. Avants, B. B. *et al.* A reproducible evaluation of ANTs similarity metric performance in brain image registration. *NeuroImage* **54**, 2033–2044. ISSN: 10538119 (2011).
138. Tzourio-Mazoyer, N. *et al.* Automated Anatomical Labeling of Activations in SPM Using a Macroscopic Anatomical Parcellation of the MNI MRI Single-Subject Brain. *NeuroImage* **15**, 273–289 (2002).
139. Thomas, B. A. *et al.* PETPVC: A toolbox for performing partial volume correction techniques in positron emission tomography. *Physics in Medicine and Biology* **61**, 7975–7993. ISSN: 13616560 (Nov. 2016).
140. Oikonen, V. *Software for positron emission tomography* 2017. http://www.turkupetcentre.net/petanalysis/sw%7B%5C_%7Dpet.html.
141. Logan, J. *et al.* Graphical analysis of reversible radioligand binding from time-activity measurements applied to [N-11C-methyl]-(-)-cocaine PET studies in human subjects. *Journal of cerebral blood flow and metabolism : official journal of the International Society of Cerebral Blood Flow and Metabolism* **10**, 740–7. ISSN: 0271-678X (Sept. 1990).
142. Gjedde, A. Calculation of cerebral glucose phosphorylation from brain uptake of glucose analogs in vivo: A re-examination. *Brain Research Reviews* **4**, 237–274. ISSN: 0165-0173 (June 1982).
143. Patlak, C. S., Blasberg, R. G. & Fenstermacher, J. D. Graphical evaluation of blood-to-brain transfer constants from multiple-time uptake data. *Journal of cerebral blood flow and metabolism : official journal of the International*

- Society of Cerebral Blood Flow and Metabolism* **3**, 1–7. ISSN: 0271-678X (Mar. 1983).
144. Gunn, R. N., Lammertsma, A. A., Hume, S. P. & Cunningham, V. J. Parametric imaging of ligand-receptor binding in PET using a simplified reference region model. *NeuroImage* **6**, 279–287. ISSN: 10538119 (1997).
145. Sokoloff, L. *et al.* the [14C]Deoxyglucose Method for the Measurement of Local Cerebral Glucose Utilization: Theory, Procedure, and Normal Values in the Conscious and Anesthetized Albino Rat. *Journal of Neurochemistry* **28**, 897–916. ISSN: 14714159 (May 1977).
146. Pedregosa, F. *et al.* *Scikit-learn: Machine Learning in Python* 2825–2830. <http://dl.acm.org/citation.cfm?id=2078195> (MIT Press, 2001).
147. Sherif, T., Kassis, N., Rousseau, M.-E., Adalat, R. & Evans, A. C. Brain-Browser: distributed, web-based neurological data visualization. *Frontiers in Neuroinformatics* **8**, 89. ISSN: 1662-5196 (Jan. 2015).
148. Ge, Y. *et al.* Retrospective registration of pet and mr brain images: An algorithm and its stereotactic validation. *Journal of Computer Assisted Tomography* **18**, 800–810. ISSN: 15323145 (1994).
149. Andersson, J. L. R., Sundin, A. & Valind, S. A method for coregistration of PET and MR brain images. *Journal of Nuclear Medicine* **36**, 1307–1315. ISSN: 01615505 (July 1995).
150. Alpert, N., Berdichevsky, D., Levin, Z., Morris, E. & Fischman, A. Improved Methods for Image Registration. *NeuroImage* **3**, 10–18. ISSN: 1053-8119 (Feb. 1996).

151. Mutic, S. *et al.* Multimodality image registration quality assurance for conformal three-dimensional treatment planning. *International Journal of Radiation Oncology Biology Physics* **51**, 255–260. ISSN: 03603016 (Sept. 2001).
152. DeLorenzo, C. *et al.* A new method for assessing PET-MRI coregistration in *Proceedings of SPIE* (eds Plum, J. P. W. & Dawant, B. M.) **7259** (International Society for Optics and Photonics, Feb. 2009), 72592W–72592W–8. ISBN: 9780819475107. doi:10.1117/12.812170. <http://link.aip.org/link/PSISDG/v7259/i1/p72592W/s1%7B%5C%7DAgg=doi>.
153. Gorgolewski, K. J. *et al.* The brain imaging data structure, a format for organizing and describing outputs of neuroimaging experiments. *Scientific Data* **3**, 160044. ISSN: 20524463 (June 2016).
154. Adam, L.-E. *et al.* Performance evaluation of the whole-body PET scanner ECAT EXACT HR/sup +/- following the IEC standard. *IEEE Transactions on Nuclear Science* **44**, 1172–1179. ISSN: 00189499 (June 1997).
155. Rousset, O. G., Ma, Y. & Evans, A. C. Correction for partial volume effects in PET: Principle and validation. *Journal of Nuclear Medicine* **39**, 904–911. ISSN: 01615505 (May 1998).
156. Mikolajczyk, K., Szabatin, M., Rudnicki, P., Grodzki, M. & Burger, C. A JAVA environment for medical image data analysis: Initial application for brain PET quantitation in *Medical Informatics* **23** (Taylor & Francis, Jan. 1998), 207–214. doi:10.3109/14639239809001400. <http://www.tandfonline.com/doi/full/10.3109/14639239809001400>.

157. Bourgeat, P. *et al.* *Computational analysis of PET by AIBL (CapAIBL): a cloud-based processing pipeline for the quantification of PET images* in (eds Ourselin, S. & Styner, M. A.) (International Society for Optics and Photonics, Mar. 2015), 94132V. doi:10.1117/12.2082492. <http://proceedings.spiedigitallibrary.org/proceeding.aspx?doi=10.1117/12.2082492>.
158. Gunn, R. N., Coello, C. & Searle, G. E. Molecular Imaging And Kinetic Analysis Toolbox (MIAKAT) - A Quantitative Software Package for the Analysis of PET Neuroimaging Data. *Journal of Nuclear Medicine* **57**, 1928 (2016).
159. Savio, A. M., Schutte, M., Graña, M. & Yakushev, I. Pypes: Workflows for Processing Multimodal Neuroimaging Data. *Frontiers in Neuroinformatics* **11**, 25. ISSN: 1662-5196 (Apr. 2017).
160. Markiewicz, P. J. *et al.* NiftyPET: a High-throughput Software Platform for High Quantitative Accuracy and Precision PET Imaging and Analysis. *Neuroinformatics* **16**, 95–115. ISSN: 15392791 (Jan. 2018).
161. Dore, V. *et al.* in *Patch-Based Techniques in Medical Imaging: Second International Workshop, Patch-MI 2016, Held in Conjunction with MICCAI 2016, Athens, Greece, October 17, 2016, Proceedings* (eds Wu, G., Coupé, P., Zhan, Y., Munsell, B. C. & Rueckert, D.) 109–116 (Springer International Publishing, Cham, 2016). ISBN: 978-3-319-47118-1. doi:10.1007/978-3-319-47118-1_14. https://doi.org/10.1007/978-3-319-47118-1%7B%5C_%7D14.
162. Ashburner, J. *SPM: A history* Aug. 2012. doi:10.1016/j.neuroimage.2011.10.025. <https://www.sciencedirect.com/science/article/pii/S1053811911011888?via%7B%5C%7D3Dihub>.

163. Kriegeskorte, N. *et al.* Greater Neural Pattern Similarity Across Repetitions Is Associated with Better Memory {\textemdash} Greater Neural Pattern Similarity Across Repetitions Is Associated with Better Memory {\textemdash} Supporting Online Material. *NeuroImage* **10**, 97–102. ISSN: 10538119 (Aug. 2006).
164. Cox, R. W. *AFNI: What a long strange trip it's been* Aug. 2012. doi:10.1016/j.neuroimage.2011.08.056. <https://www.sciencedirect.com/science/article/pii/S1053811911009736?via%7B%5C%7D3Dihub>.
165. Searle, G., Coello, C. & Gunn, R. *Extension of the MIAKAT analysis software package to non-brain and pre-clinical PET analysis* **supplement 1**, 1305–1305. <http://jnm.snmjournals.org/content/58/supplement%7B%5C%7D1/1305.short> (Society of Nuclear Medicine, May 2017).
166. Yang, J., Huang, S. C., Mega, M. & Lin, K. P. Investigation of partial volume correction methods for brain fdg pet studies. *IEEE Transactions on Nuclear Science* **43**, 3322–3327. ISSN: 00189499 (1996).

CHAPTER 5
**Improving reproducibility of PET image analysis with automated
quality control**

Thomas Funck^{1,2}, Kevin Larcher¹, Paule-Joanne Toussaint¹, Richard Hoge^{1,3}
Alain Dagher^{1,3} Alan C. Evans^{1,3} Alexander Thiel^{2,3}

¹ Montreal Neurological Institute, McGill University, Montreal, QC, Canada

² Jewish General Hospital and Lady Davis Institute for Medical Research, Mon-
treal, QC, Canada

³ Department of Neurology & Neurosurgery, McGill University, Montreal, QC,
Canada

5.1 Preamble

In chapter 3 we presented a software package called APPIAN for automating PET image analysis. This software package includes a novel algorithm, called GRAD, for performing automated QC. This algorithm can, in principle, be used to perform QC for any automated image processing. The only necessary condition is that the success of a processing stage can be quantified on a continuous scale. Given the generality of GRAD, it is important to determine how well it works in the particular

case of PET image processing. The work described in this chapter is aimed at validating the ability of GRAD to detect processing errors in APPIAN. We used a set of real PET images and systematically applied misregistrations between the PET and MRI to determine how reliably GRAD would detect such misalignments.

5.2 Abstract

Automated quality control (QC) is necessary when analyzing large PET-data sets using processing pipelines to ensure that each processing stage has been performed correctly and hence improve reproducibility of the analysis. We designed a new algorithm for performing automated QC via a framework we call GRoupwise Anomaly Detection (GRAD). For a given processing stage, automated QC is performed by first calculating image-derived metrics that quantify the performance of the processing stage for all images acquired within a study cohort. The empirical distribution of the QC metrics is then estimated using Gaussian kernel density estimation and used to identify images with anomalous values in the chosen metric. While GRAD can in principle be used to perform automated QC for any imaging modality, we have implemented and validated it in the context of positron emission tomography (PET). GRAD was validated by simulating misalignments between PET and magnetic resonance (MR) images and testing how accurately GRAD could identify misaligned images in the coregistration, partial-volume correction (PVC), and quantification stages of PET image processing. The results showed that the AUC for GRAD's error detection ROC was 0.7-0.97 for images that were rotated by

more than 6° or translated by more than 6mm. GRAD was therefore able to detect moderate to large errors in coregistration with high sensitivity and specificity.

5.3 Introduction

The increasing availability of large brain imaging data sets has made automated pipelines essential for reproducible and robust image processing and analysis. However, automated pipelines require rigorous quality control (QC) to ensure that each processing step has been performed as expected. While manual QC based on visual inspection is still the most commonly used and gold-standard method for performing QC [148–152], it requires significant time and labor on the part of investigators. Manual QC also suffers from inter- and intra-rater variability [167]. We therefore propose a general framework for performing automated QC based on groupwise anomaly detection (GRAD) and demonstrate its application to the automated QC of PET image analysis.

Within the field of brain imaging, automated QC algorithms fall into one of two conceptual frameworks: reference range approaches and group comparison approaches

The first approach identifies a reference range for image-derived metrics from a set of manually quality controlled images [167–169]. A classifier is then trained on the reference set of image-derived metrics to determine which images should pass QC. Automated QC is then performed by applying the trained classifier to a new set of images.

In the simplest case the classifier can be a threshold criterion which a metric must exceed in order to pass QC. This criterion is determined by visual inspection of the set of metrics obtained from manual quality controlled data [168]. More sophisticated classifiers may also be used. Esteban, et al.[167] implement both a support vector machine and random forest classifier to obtain an MR image classification based on a set of image metrics. Similarly, Oguz, et al. [169] use entropy measures from a set of artefact-free diffusion MR images to identify directional artefacts.

The fundamental assumption of the reference range approach is the generalizability of the metrics' reference range from a reference data set to new scans from different individuals. This assumption may not hold for imaging modalities with a high degree of variability in the image-derived metrics. For example, an [18-F]-FDG PET scan acquired on the CTI-Siemens ECAT HRRT and [18-F]-flumazenil PET scan acquired on the Siemens ECAT HR+ will have very different image-derived metrics that make it difficult to use a single reference range.

The second conceptual framework for performing automated QC is to compare the image-derived metrics for the images acquired within a given study. Group comparison of QC metrics may be evaluated visually [167, 170] or by a quantitative algorithm that automatically detects outliers, e.g., k-means clustering [171].

We have implemented a novel technique for groupwise automated quality control, which we term GRAD (GRoupwise Anomaly Detection). The overall approach of automated QC is to define a metric that quantifies the performance of a given processing step. For example, in the case of coregistration this would be a similarity metric, e.g., mutual information, between the PET and T1-weighted MR images. By

itself, a metric for a single image is insufficient to determine whether that processing step was performed correctly. Instead, an outlier detection algorithm is applied to the empirical distribution of the QC metrics and outliers are identified based on a user-defined threshold.

While GRAD can in principle be applied to any automated pipeline where meaningful QC metrics can be defined, we evaluate GRAD in the context of PET-MRI coregistration. Coregistration is the first of the 3 major processing stages that are regularly performed in PET analysis. This step is usually followed by partial-volume correction (PVC), and quantification by tracer kinetic analysis. Coregistration is also a frequent source of error and can have a significant impact on downstream analyses [17, 152, 166, 172–174]. We therefore evaluate the sensitivity and specificity of GRAD for detecting errors resulting from misregistration in the coregistration, PVC, and quantification stages.

5.4 Methods

5.4.1 Groupwise anomaly detection

GRAD was devised to assist the user in performing visual QC. While visual inspection remains the gold-standard QC method [148–152], automated QC can be useful in guiding the user to images that have potentially failed a processing stage. The first stage of GRAD is to define a QC metric that quantifies the performance of a given processing step.

The empirical distribution of QC metrics is calculated from all coregistered image data sets from all subjects in the cohort using kernel density estimation (KDE), E , with a gaussian kernel, G , and a bandwidth, h , of 0.2:

$$E(x) = \frac{1}{nh} \sum_{i=0}^{i < n} G\left(\frac{x - x_i}{h}\right) \quad (5.1)$$

QC metrics are standardized and centered around 0 to simplify calculations. This empirical distribution is therefore calculated on a cohort of subjects whose PET images have been acquired under similar conditions, e.g., a set of subjects acquired with the same experimental protocol for a particular study. Anomalous values are those whose probability of being observed falls below a predefined tolerance limit.

The probability of observing a given metric can be defined using either a single- or two-tailed test (Fig.5-1). Certain QC metrics can be defined such that the performance of the processing stage theoretically increases monotonically as a function of the QC metric (Fig.5-1A), e.g., the mutual information between the PET and MR images increases as the fit between the two improves. In this case, abnormally large QC metrics do not need to be considered in the anomaly detection because they are assumed to reflect an unusually good performance of the processing stage. Therefore, only the probability of observing a QC metric value that is less than or equal to the observed QC metric, i.e., a single-tailed test, needs to be calculated.

There are also instances where the performance does not monotonically increase with the QC metric (Fig. 5-1B). In this case, anomalous QC metrics are detected by calculating the probability of observing a QC metric that is larger than the absolute value of the observed QC metric, i.e., a two-tailed test. Single-tail anomaly detection

has higher specificity because it ignores positive outliers that represent abnormally successful QC metrics. Distinguishing between QC metrics requiring single- and two-tailed tests is therefore useful because it increases the overall specificity of the automated QC.

QC metric for coregistration

The QC metric for the PET to MRI coregistration is defined as the image similarity between the PET and MR images. Increasing similarity between the PET and T1-weighted MR image implies better performance and thus anomaly detection may be performed by calculating the single tailed probability of observing a value less than or equal to the QC metric. In practice many metrics exist for evaluating similarity between images, including mutual information (MI)(Eq.5.2) , feature-space entropy (FSE)(Eq.5.3), and cross correlation (CC)(Eq.5.4):

$$MI(x, y) = \frac{1}{n} \sum_{i=0}^{i < n} p(x, y) \log\left(\frac{p(x, y)}{p(x)p(y)}\right) \quad (5.2)$$

$$FSE(x, y) = \frac{1}{n} \sum_{i=0}^{i < n} p(x, y) \log(p(x, y)) \quad (5.3)$$

$$CC(x, y) = \frac{\sum_{i=0}^{i < n} (x_i - \hat{x})(y_i - \hat{y})}{\sum_{i=0}^{i < n} (x_i - \hat{x}) \sum_{i=0}^{i < n} (y_i - \hat{y})} \quad (5.4)$$

where x and y are the 2 images being compared, i.e., the PET and MRI.

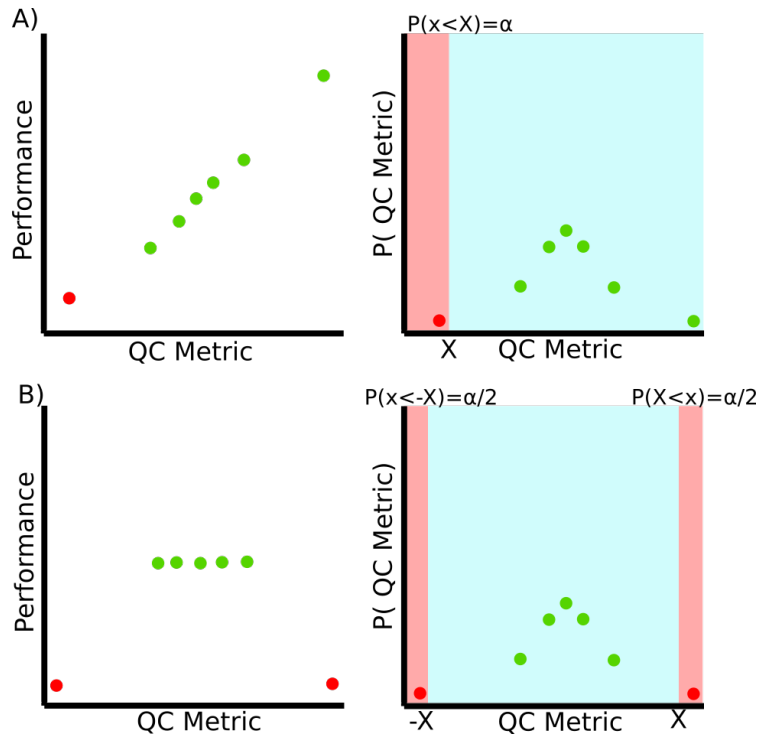


Figure 5-1: A. Performance is defined as a quantitative measure of how closely the actual result produced by the pipeline coincides with the ideal result that should theoretically be produced by that processing stage. Each point represents an individual scan from a subject in the sample. If performance of a processing stage increases monotonically with the QC metric for that processing stage, then a single-tailed test is sufficient to identify anomalous QC metrics. The red point indicated QC metrics that would be identified as anomalous values. B. A two-tailed test is necessary to identify anomalous QC metrics when a higher QC metric does not necessarily reflect better performance of the processing stage.

QC metric for PVC

The QC metric that was devised to detect errors at the PVC stage was based on the standard mathematical formulation of image acquisition is $O = P \otimes R_{True} + n$, where O is the observed PET image, R_{True} is the true radioactivity distribution, P is the scanner point-spread function, and n is noise. In principle, PVC therefore attempts to estimate the source radioactivity distribution, $R_{Est.}$, in the object by removing the blurring effect of the scanner point-spread function, P . The QC metric for PVC should be defined so that it is, in theory, maximized when the PV-corrected image, $R_{Est.}$ approaches R_{True} . The QC metric for PVC used here was defined as the negative mean-squared error (MSE) between the observed PET image, O , and the PV-corrected PET image convolved with the approximation of the point-spread function of the PET scanner used to acquire the image, $P \otimes T_{Est.}$ (Eq.5.5). A better fit of the PVC algorithm between the observed and PV-corrected images leads to larger, i.e., less negative, values for the QC metric. A singled tailed test of the PVC QC metrics is therefore performed to identify potential anomalies. The strong assumption underlying this approach is that the point-spread function of the PET scanner can accurately be represented using a simpler model like a gaussian function.

$$QC_{PVC} = -\frac{1}{n} \sum_{i=0}^{i < n} (PET_i - [P \otimes T_{Est.}]_i)^2 \quad (5.5)$$

QC metric for quantification

Whereas the previous 2 processing stages can be characterized in terms of a QC metric that monotonously increases with processing performance, this is not the

case for the quantification stage. The quantification stage includes the application of models to calculate quantitative or semi-quantitative values from the PET images, e.g., BPnd. The quantification stage therefore includes tracer-kinetic analysis as well as simpler models such as SUVR. The QC metric for the quantification stage is therefore the average parametric value within the user-defined ROI (Eq.5.6). Regardless of whether the user has selected to calculate quantitative parameters on a voxel or ROI basis, mean regional values are calculated using the ROI for the results stage. Outliers from the quantification stage are then calculated using a two-tailed test for outliers on the empirical probability density function (PDF) of the regional average values.

The QC metric for the quantification stage is simply the average parametric value within the set of user-defined ROIs :

$$QC_{TKA(r)} = \frac{1}{n_r} \sum_{i \in r} PET_i^{TKA} \quad (5.6)$$

where i is an element of a set of voxel coordinates in a user-defined ROI, r ; n is the number of voxels in the ROI; and PET TKA is the parametric image derived with the chosen quantification method.

5.4.2 Evaluation of GRAD

PET images

Brain PET images with three different radioligands [18-F]-flumazenil, (FMZ), [18-F]-fluorodeoxyglucose (FDG), and [C-11]-raclopride (RCL) and corresponding T1-weighted MR images were acquired. 46 FMZ images were acquired with an

injected dose of 370MBq [175]. 31 FDG images were acquired with an injected dose of 185MBq and 27 RCL images [176] with an injected dose of 296-370MBq.

All PET scans were performed on the CTI-Siemens ECAT HRRT scanner in list mode (SiemensMedical Solutions, Knoxville, TN, USA) [12]. The ECAT CTI-Siemens ECAT HRRT is a dedicated full 3D high resolution brain scanner, with a field view of 25.2 cm (axially) and 31.2 cm (diameter) and has a spatial resolution of between 2.3 and 3.4mm FWHM, allowing data acquisition with high spatial resolution and high sensitivity. In addition, the use of two crystal layers (LSO/LYSO) permits photon detection with depth-of-interaction information. The list mode data were binned into 2209 sinograms (each of size 256 radial bins \times 288 azimuthal bins) using span 9 compression, resulting in images with a voxel size of $1.22 \times 1.22 \times 1.22\text{mm}^3$.

FMZ images were reconstructed using fully 3D FBP by 3D reprojection (3D RP) carried out with a Hamming windowed Colsher filter (alpha=0.5, cut off at the Nyquist frequency). RCL and FDG images were reconstructed with 3D ordinary Poisson OSEM [177].

MR images

The T1 MR images were acquired on a Siemens Magnetom TrioTim syngo MR B17 using a MPRAGE sequence (repetition time (TR) 2300 ms, echo time (TE) 2.98 ms, TI 9 ms and flip angle = 9° matrix size = $160 \times 256 \times 256$). The T1 MRI corresponding to the RCL images were acquired on the Siemens Sonata 1.5T system,

using a gradient echo pulse sequence (TR = 22 ms, TE = 9.2 ms, flip angle = 30° and matrix size 176 × 256 × 256).

CIVET

All MR images were processed using CIVET on the CBRAIN platform (<https://mcinim.ca/technology/cbrain/>). CIVET uses the non-parametric N3 method to correct MR field non-uniformity [118]. The MR image is then transformed to MNI stereotaxic space of the ICBM 152 6th generation non-linear brain atlas [4], using a 12 parameter affine transformation [2]. Spatially normalized images are then segmented into GM, WM and cerebrospinal fluid [178]. Additionally, a stereotaxic atlas of the basal ganglia defined on the ICBM 153 template [4] was non-linearly co-registered onto the subject MRI in MNI stereotaxic space.

Additionally, CIVET uses the ANIMAL and INSECT segmentation algorithms to classify the T1 MR images into gross anatomical regions. ANIMAL produces a classification of the cerebral lobes and subcortical grey matter regions [179]. The INSECT algorithm is used to segment T1 MR images into regions composed of gray matter, white matter and cerebrospinal fluid [180]. Finally, the results of ANIMAL and INSECT are combined (ANIMAL+INSECT) to create an image consisting of a lobular segmentation of the cortical gray matter and white matter in addition to subcortical grey matter regions [178].

APPIAN

All PET image processing steps were performed with APPIAN. APPIAN (Automated Pipeline for PET Image Analysis) [181] an open-source pipeline based on NiPype [135] for performing automated PET data analysis. APPIAN begins with reconstructed PET images and performs all processing steps necessary to extract quantitative measures from the PET images on which users will perform the statistical analysis. In conjunction with the reconstructed PET image, APPIAN uses a T1-weighted MR-image to define regions of interest (ROI) that are used at multiple processing stages. Briefly, APPIAN 1) coregisters the T1 MR and PET images, 2) defines ROI necessary for later processing steps, 3) performs PVC, and 4) PET quantification, 5) produces a report of the results, and finally, 6) performs automated QC.

PVC was performed using the geometric transfer matrix method (GTM)[155]. The regions of interest used for PVC were the segmented images produced by ANIMAL+INSECT. For the FMZ and RCL tracers, PET quantification was performed with the Logan plot [124]. A white matter reference region was used to calculate non-displaceable binding potential and were defined on classification of the T1 MR image with INSECT. 6 morphological erosions were applied to the reference region mask to avoid any contamination from the cortical gray matter. The Patlak-Gjedde plot method was used to calculate K_i , i.e., the net uptake rate for the radioligand, for the FDG images using arterial input sampling [142, 143].

Simulated misalignment

A set of correctly – as determined based on visual inspection - coregistered PET and MR images were generated by running APPIAN on each of the three sets of PET images. For each of the correctly coregistered PET images, a series of transformations were applied to systematically misalign them relative to the MR image. The misalignments comprised rotations of 2, 4, 6, 12, 18, 24 degrees and translations of 2, 4, 6, 12, 18, 24 mm in the axial plane, respectively.

The performance of GRAD was evaluated for the three major image processing stages included in APPIAN: coregistration, PVC, and quantification. Three QC metrics were used to measure the performance of the coregistration processing stage: cross-correlation (CC), mutual information (MI), and feature-space entropy (FSE) [182]. A synthetic similarity metric, "All" was also used and was defined as the Euclidean norm of the standardized CC, MI, and FSE metrics. For the PVC and quantification stages, the QC metrics were defined as described in Eq.5.5 and Eq.5.6, respectively. The automated QC for the quantification stage is performed for specific, user-defined ROI. For FMZ and FDG PET images, the cortical GM was used for automated QC of the quantification stage. Automated QC of the quantification stage for the RCL PET images on the putamen as defined using the basal ganglia atlas that was co-registered to each subject's MR image in MNI space.

Outliers were detected as described above (section 2.2). ROC curves were calculated from the probability values generated by GRAD. The area under the curve (AUC) of the ROC curves was used to compare the performance of the groupwise outlier detection algorithm at various levels of misregistration.

5.5 Results

5.5.1 Evaluation of automated QC

The results from the simulated PET to MR image misalignment indicated that the automated outlier detection was able to detect errors due to misaligned PET images with good sensitivity in all three image processing stages. For the detection of rotation errors in the coregistration stage (Fig.5–2, first row) the GRAD algorithm performed only slightly better than chance (AUC=0.5-0.6) for small errors (2° rotation). This increases to an AUC of 0.7-0.9 for moderate errors (6- 16° rotation). The sensitivity of GRAD depended both on the type of radioligand and the QC metric used to quantify the performance of coregistration. With respect to rotation errors, MI was generally the most robust single QC metric across all radioligands, although anomaly detection with CC and FSE appeared to be more sensitive for FMZ and FDG, respectively. Anomaly detection with the Euclidean norm of the three individual coregistration QC metrics (“All”) was most sensitive for RCL and FMZ, and similar to results with MI for FDG.

Although the sensitivity of anomaly detection at the PVC stage (Fig.5–2, second row) was lower than for coregistration, GRAD was nonetheless able to detect anomalies with higher than chance probability (AUC=0.7-0.8 for 20° rotation). The performance of GRAD for the quantification processing stage was dependent on the radioligand used. The best performance was obtained with RCL and FMZ (AUC=0.95 for 6° rotation), while the performance with FDG (AUC=0.75 for 20° rotation) was lower.

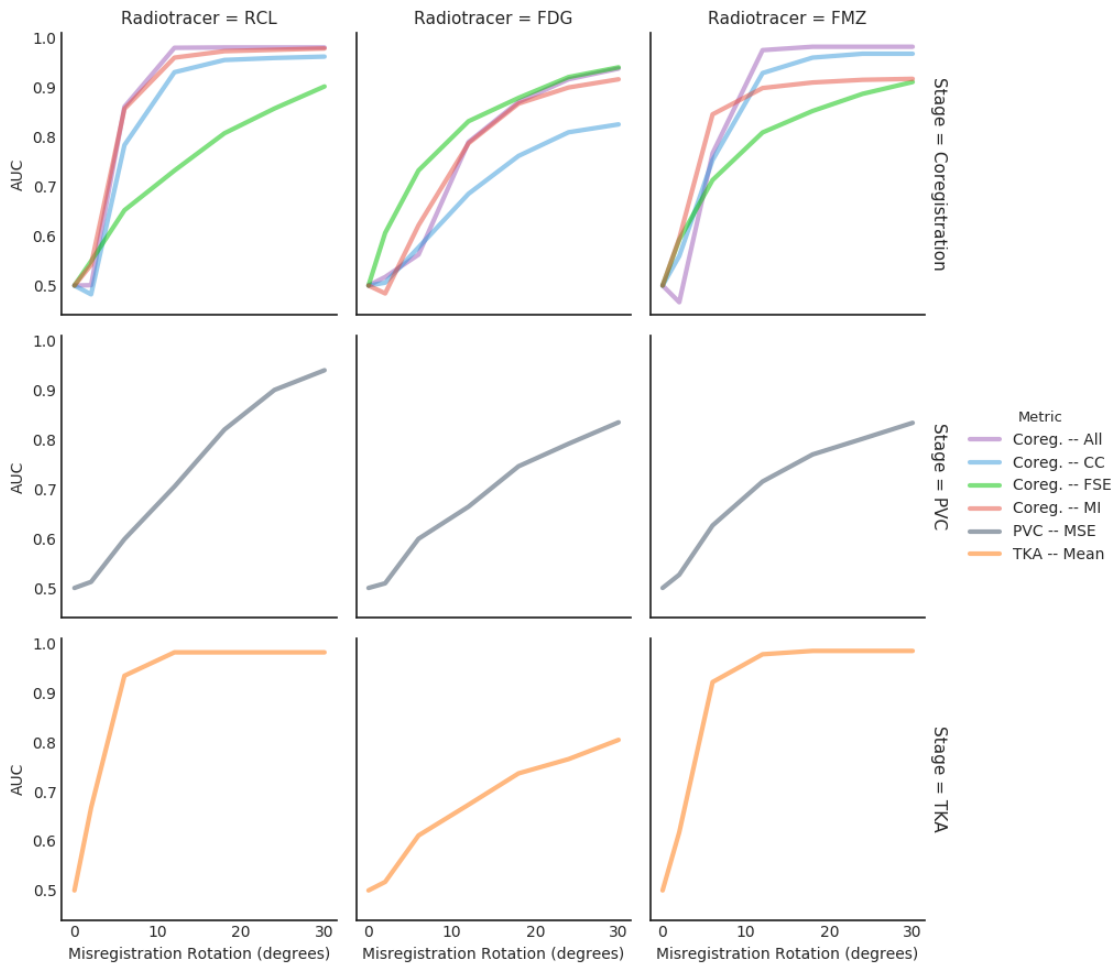


Figure 5-2: Increasing misalignments were generated to evaluate the sensitivity of GRAD. GRAD showed high sensitivity in the coregistration and quantification processing stages with moderate sensitivity for the PVC processing stage.

For rotation error in the coregistration stage, FSE was the most robust single QC metric with an AUC of approximately 0.8 for FDG and FMZ for a rotation error of 6° but was lower for RCL with an AUC of 0.65 for this error level (Fig.5–2). CC and MI did not have monotonically increasing AUC with increased translation error for all 3 radioligands (Fig.5–3). However, the mean of the Euclidean norm of the QC metrics had the best sensitivity for anomaly detection for FMZ and RCL, and a similar performance to FSE for FDG.

GRAD had a similar level of sensitivity for translation misregistration error in the PVC stage across all 3 radioligands (AUC=.85-.95 for translation errors of 12mm). A similar sensitivity was achieved for the quantification processing stage for FMZ and RCL (AUC=0.90-0.95 for translation errors of 6mm). The sensitivity of GRAD in the quantification stage was lower for FDG (AUC=0.68 for translation errors of 6mm).

5.6 Discussion

5.6.1 Overview

The analysis of large imaging data sets makes the automation of image analysis imperative. Rigorous QC is essential to ensure that each processing step has been performed as expected. We have therefore created an automated QC method based on identifying anomalous images within a given data set. We systematically misregistered the PET images relative to the MR images to evaluate GRAD’s ability to detect errors propagated from the simulated misregistration at the major processing stages of PET analysis: coregistration, PVC, and quantification. GRAD was

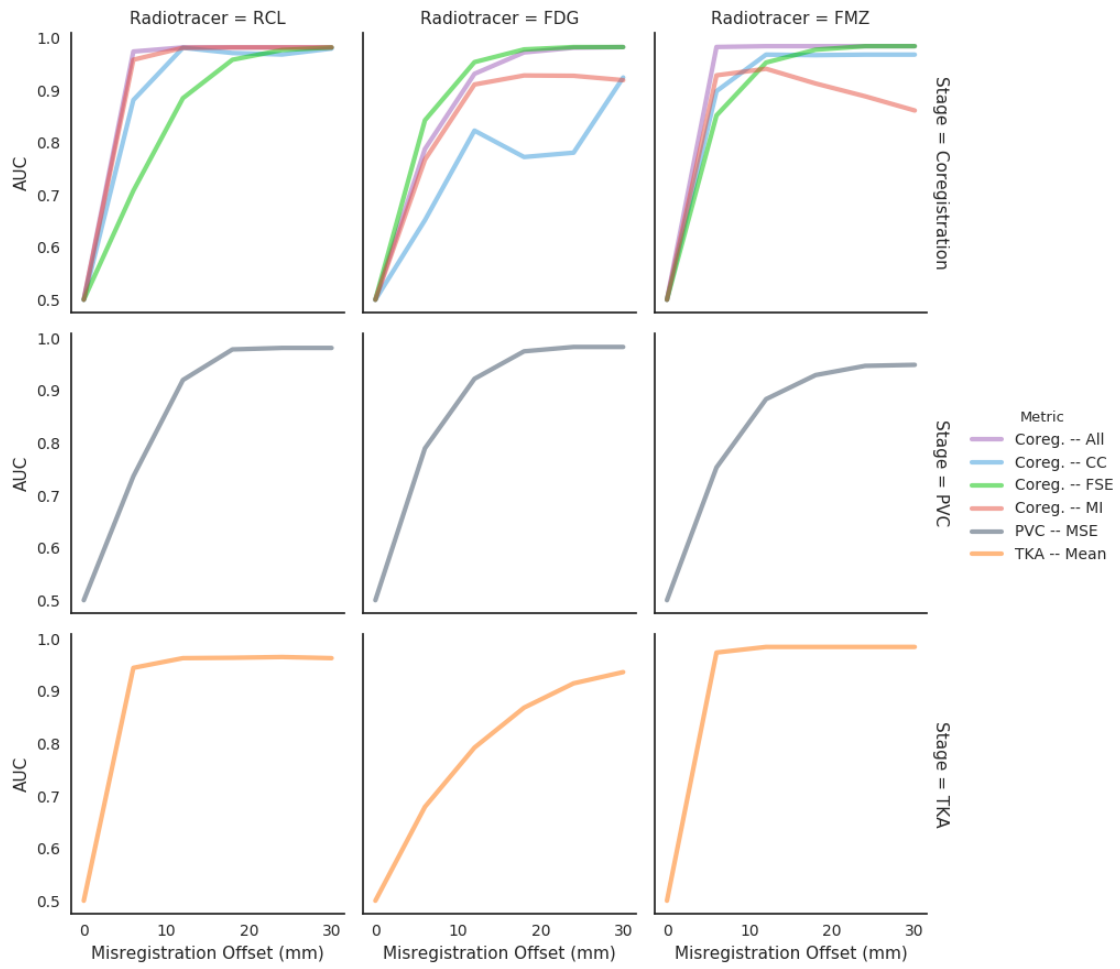


Figure 5-3: GRAD was able to detect misregistered images across all processing stages for translation errors.

successfully able to detect moderate to large misregistration errors at each of the 3 processing stages, for all 3 radioligand types and both for translation and rotation alignment errors.

5.6.2 Evaluation of GRAD

The results indicated that the algorithm could detect moderate to large misregistration errors. The outlier detection was only slightly better than chance for small errors (2mm or 2°). This is not surprising given that such small errors are difficult to detect even for a human observer. Alpert, et al. [150] validated their coregistration algorithm against human visual QC and found that human raters had 80% accuracy in successfully identifying 2mm misregistrations between PET and MRI. While this level of performance exceeds that of GRAD at present, it highlights the fact that human observers are imperfect and may benefit from the development of automated QC algorithms.

The performance of GRAD was worse for the PVC stage across all 3 radiotracers, indicating that the QC metric may not be sensitive enough to identify failed PVC. A limitation of the PVC QC metric is that it assumes that convolving the PVC PET image with the scanner point-spread function produces an image that resembles the original PET image. This assumption is likely too simplistic given that the point-spread function varies from the center to the periphery of the field-of-view of the scanner. Moreover this PVC QC metric is better suited to voxel-wise instead of ROI-based PVC, because the latter produces potentially large regions of homogenous radioactivity concentrations. A more robust choice of PVC QC metric may need to be

devised. An example of an alternate PVC QC metric would be the average difference in radioactivity concentration before and after PVC. That is, by comparing the effect of PVC within a set of ROI, it may be possible to determine if there was an abnormal change for a given subject and region that would be indicative of a processing error.

Performance of GRAD

The performance of GRAD for the coregistration stage was highly dependent on the choice of distance metric, the radioligand, and the type of error. Overall, for coregistration the most robust QC metric was the Euclidean norm of the three individual QC metrics, with good performance for both translation and rotation errors. However, it was not consistently the most accurate metric, e.g., FSE outperformed the mean of the QC metrics for FDG for rotation errors.

In the coregistration stage, not all QC metrics increased monotonically with increasing error. Specifically, for simulated translation errors the CC and MI metrics exhibited a decrease in AUC for FDG and FMZ images, respectively. The decrease in AUC is likely due to a spurious match between anatomical structures in the PET and MR images that result in an erroneous increase in the QC metrics. That is, QC metrics like CC and MI are imperfect in that they may not improve alignment between the PET and MR image. When this occurs, a worse alignment results in a better QC metric and thereby affects the accuracy of GRAD. This illustrates that QC metrics which should theoretically increase only as a result of improved performance of the processing stage may in practice be susceptible to artefacts that result in the violation of this assumption of monotonicity.

Notably, the violation of the monotonicity assumption by some QC metrics did not appear to significantly impact the performance of the Euclidean norm of the QC metrics. A synthetic metric that combines information from multiple individual metrics is therefore potentially robust against the failure of any one of its composite metrics. The superior performance of the synthetic metric suggests that the performance of GRAD may be improved by evaluating methods for combining the metrics and a larger set of metrics.

The results of GRAD for the PVC stage were uniformly worse across all the radioligands for rotation versus translation errors. It is not clear why PVC was so distinctly affected by the difference in misregistration error. By contrast, the performance of GRAD for the quantification stage was substantially similar for both error types for FMZ and RCL, with a larger improvement in error detection from rotation to translation errors for FDG.

The variability in performance between the three radioligands is due to the extent to which each radioligand distribution in the PET images is similar to the signal intensity distribution in the MRI. The more the radioligand's spatial distribution and contrast resembles the anatomic structures represented in the MR image, the more the QC metrics is affected by a mismatch between the PET and MR images and, hence, the better the performance of the automated QC. FDG, for example, has significant radioligand binding in both GM and WM. This means that a misalignment of the FDG image has less impact on the misaligned QC metrics than for a radioligand with high GM-WM contrast, such as FMZ.

The correspondence of the PET radioligand distribution to the MR image also explains the difference in the performance of GRAD between the translation and rotation error. Up to relatively large angles, rotations preserve a greater overlap between the PET and the MR image.

Only rotations in the axial plane and translations in the coronal plane were tested, because of the computational cost of performing exhaustive simulations across all axes for both error types. Earlier studies from 2D PET scanners are inconclusive as to whether differences in coregistration errors between dimensions are significant [148, 149]. Andersson, et al. found that the extent of the difference in misalignment in the 3 dimensions varied greatly between the FDG, RCL, and nomifenisine [149]. This supports the hypothesis that investigations on PET coregistration are difficult to generalize across radioligands. More exhaustive investigations in high-resolution 3D PET are required to establish whether there is indeed a differential likelihood of misregistration in the 3 imaging planes and how this affects different radioligands. The ability to simulate misalignments as described here is included in APPIAN so that users can evaluate the accuracy of the automated QC for other radioligands than the ones tested here.

Studies of automated PET coregistration have reported misalignment with real and simulated PET that is within the range of what we have classified as small to moderate error levels. A study with simulated FDG PET has shown misregistration errors of between 1-8mm, depending on the coregistration algorithm being used [183]. Another study of FDG PET to MRI coregistration found an average of 2-4mm and 0-7° misalignment errors [148]. Other studies have demonstrated slightly smaller

average misregistration errors of 2-3mm and with errors as high as 7.4mm [149, 184]. In their retrospective analysis of the accuracy of existing PET-MRI coregistration algorithms, West, et al. [185] report a misregistration error range of between 2-4mm for the 12 methods tested.

It should be noted that these studies use an older generation of 2D PET scanners [148, 184, 185], i.e., Siemens ECAT 933 scanner, with a FWHM spatial resolution of approximately 6.5mm [186]. Similarly, the simulated images from Anderson, et al. [149] were generated to have a FWHM spatial resolution of 7mm. Although these PET images have a generally lower spatial resolution than can be acquired with high-resolution PET scanners like the CTI-Siemens ECAT HRRT [12], they have a similar in-plane spatial resolution to the ECAT HR+ scanner [154], which is still actively used for PET imaging. The results of coregistration studies from earlier generations of PET scanners are therefore still relevant for understanding misregistration errors in the context of more modern PET scanners.

Comparison of GRAD to existing QC methods

Training a classifier on a data set of manually quality controlled images is likely an excellent approach to performing QC on MRI, but it is less applicable in the case of PET. Not only do PET images vary across sites, but PET image statistics are highly dependent on several other factors, such as radioligand, the specific activity of the injected radioligand, injected radioligand dose, scanner, reconstruction method, patient genotype, and patient population. Esteban, et al. [167] note that the site of image acquisition presents an important challenge in training their classifier. Given

the greater potential for variability in PET image statistics versus MR images, an approach to automated QC like that of MRIQC is all the more difficult to apply to PET.

Automated QC based on the spread of QC metrics as implemented by GRAD suffers from two potential limitations. First, GRAD would be unable to detect images that failed a given processing stage if all the images for that stage had performed poorly. For example, the MI value of a misaligned PET image from one subject does not appear anomalous if those of all the subjects were also misaligned and had correspondingly low MI values. However, such a systematic error is more likely to be detected by the user than a small subset of failed images and is thus less of a concern.¹

Groupwise QC also requires a sufficient sample size to have a representative spread of the QC metrics. However, GRAD was designed specifically to process large datasets where visual QC is highly demanding and where it is therefore plausible to assume a suitably large data set. Here the smallest data set, that of RCL PET images, had only 27 images. GRAD, therefore, can perform well for data sets that fall within the range of sample sizes that are regularly acquired in PET studies.

¹ An additional limitation that should be noted is that the effect of post-reconstruction motion correction and filtering may have a larger impact on the outcome measures of a study than misregistration [187]. GRAD could be extended to use for detecting errors in post-reconstruction motion correction by, for example, averaging similarity metrics calculated between time frames in the PET image.

It is important to stress that automated QC cannot yet replace diligent visual QC. Visual QC is the primary method for verifying the accuracy of novel PET-MRI coregistration algorithms on images that have been acquired in vivo [148–152]. Thus, visual QC remains the gold standard method for confirming coregistration accuracy and cannot yet be easily replaced. Visual QC in all imaging domains is, however, subject to intra- and inter-observer variability, and it is therefore useful for the user to be directed to potentially problematic images that should be treated with particular attention. Automated QC is therefore intended as a complement to visual QC and not yet as replacement. To this end, we have implemented a simple dashboard GUI in APPIAN that allows users to navigate through co-registered images as 3D volumes. In addition, the QC metric is also represented graphically so that the user can easily see how the QC metric of a particular image compares to the overall distribution of that image.

Limitations

This work to validate GRAD was focused only on misregistration between the PET and MR image as error source for each of the processing stages. Misregistration was chosen because it is a common source of error in PET processing that can easily be parametrized in terms of rotation and translation. Indeed, perfect registration is often cited as an important underlying assumption for PVC [41, 188]. Moreover, misregistration is a source of error that can be applied universally regardless of the type of PET image or the type of algorithm that is being used to analyze the image.

The error induced by misregistration is similar to what would be expected from other common other sources of error like erroneous segmentation or patient head movement because misregistration, like erroneous segmentation and patient head movement, results in the mixing of radioactivity concentrations from different regions into a distinct ROI. Contamination of ROI is important because most PVC methods use ROI to define regions of uniform, or at least similar, radioactivity concentrations and many quantification methods use an ROI to define a reference region with no specific binding of the radioligand. Misregistration thus results in contamination of these ROI with radioactivity concentrations from neighbouring regions and hence reflects to some degree the errors that would be expected from these other sources.

While alternate sources of erroneous processing may provide useful ways of evaluating the performance of GRAD for the PVC and quantification stages, it is difficult to identify error sources that are common and would provide generalizable results. Consider erroneous segmentation of the MR image. The problem with using erroneous segmentation is that it depends entirely on the regions being segmented, e.g., the entire GM versus the supplementary motor area of the GM, and which algorithm is using the segmented image. For example, a 10% segmentation error of the entire GM would have a modest effect on a voxel-wise PVC algorithm, but a 10% segmentation error of the thalamus would likely have a significant impact on ROI-based PVC of sub-cortical GM areas with the GTM. Hence the results of evaluating GRAD for detecting segmentation errors would be difficult to generalize.

5.6.3 Conclusion

GRAD is a novel automated QC algorithm that seeks to automate the processing of reconstructed PET images for a wide variety of experimental protocols to facilitate robust and reproducible analysis. Our results have shown GRAD is accurate and is capable of assisting users in detecting moderate to large errors in processing. While the desiderata of a reliable, fully automated QC remain elusive, GRAD provides a general framework for automated QC of image processing software pipelines. Future work will focus on developing better QC metrics that allow for more sensitive anomaly detection.

5.7 Author Contributions

Thomas Funck is the primary author of the manuscript, developed the code used in this chapter, designed and performed the data analysis.

Kevin Larcher is a co-developer of the APPIAN code.

Paule-Joanne Toussaint is an advisor for designing APPIAN, edited the manuscript.

Alain Dagher provided raclopride PET data.

Richard Hoge provided FDG PET data.

Alexander Thiel (principal investigator) and AE (co-principal investigator) provided conceptual guidance and edited the manuscript.

References

2. Collins, D. L., Neelin, P., Peters, T. & Evans, A. Automatic 3D intersubject Registration fo MR Volumetric Data in Standardized Talairach Space. *Journal of Computer Assisted Tomography* **10**, 192–205. ISSN: 10538119 (1994).
4. Mazziotta, J. *et al.* A probabilistic atlas and reference system for the human brain: International Consortium for Brain Mapping (ICBM). *Philosophical Transactions of the Royal Society B: Biological Sciences* **356**, 1293–1322. ISSN: 0962-8436 (Aug. 2001).
12. Wienhard, K. *et al.* The ECAT HRRT: performance and first clinical application of the new high resolution research tomograph. *IEEE Transactions on Nuclear Science* **49**, 104–110. ISSN: 0018-9499 (Feb. 2002).
17. Hutton, B. F. *et al.* What approach to brain partial volume correction is best for PET/MRI? *Nuclear Instruments and Methods in Physics Research, Section A: Accelerators, Spectrometers, Detectors and Associated Equipment* **702**, 29–33. ISSN: 01689002 (Feb. 2013).
41. Rousset, O., Rahmim, A., Alavi, A. & Zaidi, H. Partial Volume Correction Strategies in PET. *PET Clinics* **2**, 235–249. ISSN: 15568598 (Apr. 2007).
118. Sled, J. G., Zijdenbos, A. P. & Evans, A. C. A nonparametric method for automatic correction of intensity nonuniformity in MRI data. English. *IEEE transactions on medical imaging* **17**, 87–97. ISSN: 0278-0062 (Feb. 1998).

124. Logan, J. *et al.* Distribution Volume Ratios Without Blood Sampling from Graphical Analysis of PET Data. *Journal of Cerebral Blood Flow & Metabolism* **16**, 834–840. ISSN: 0271-678X (Sept. 1996).
135. Gorgolewski, K. *et al.* Nipype: A Flexible, Lightweight and Extensible Neuroimaging Data Processing Framework in Python. *Frontiers in Neuroinformatics* **5**, 13. ISSN: 1662-5196 (2011).
142. Gjedde, A. Calculation of cerebral glucose phosphorylation from brain uptake of glucose analogs in vivo: A re-examination. *Brain Research Reviews* **4**, 237–274. ISSN: 0165-0173 (June 1982).
143. Patlak, C. S., Blasberg, R. G. & Fenstermacher, J. D. Graphical evaluation of blood-to-brain transfer constants from multiple-time uptake data. *Journal of cerebral blood flow and metabolism : official journal of the International Society of Cerebral Blood Flow and Metabolism* **3**, 1–7. ISSN: 0271-678X (Mar. 1983).
148. Ge, Y. *et al.* Retrospective registration of pet and mr brain images: An algorithm and its stereotactic validation. *Journal of Computer Assisted Tomography* **18**, 800–810. ISSN: 15323145 (1994).
149. Andersson, J. L. R., Sundin, A. & Valind, S. A method for coregistration of PET and MR brain images. *Journal of Nuclear Medicine* **36**, 1307–1315. ISSN: 01615505 (July 1995).
150. Alpert, N., Berdichevsky, D., Levin, Z., Morris, E. & Fischman, A. Improved Methods for Image Registration. *NeuroImage* **3**, 10–18. ISSN: 1053-8119 (Feb. 1996).

151. Mutic, S. *et al.* Multimodality image registration quality assurance for conformal three-dimensional treatment planning. *International Journal of Radiation Oncology Biology Physics* **51**, 255–260. ISSN: 03603016 (Sept. 2001).
152. DeLorenzo, C. *et al.* A new method for assessing PET-MRI coregistration in *Proceedings of SPIE* (eds Plum, J. P. W. & Dawant, B. M.) **7259** (International Society for Optics and Photonics, Feb. 2009), 72592W–72592W–8. ISBN: 9780819475107. doi:10.1117/12.812170. <http://link.aip.org/link/PSISDG/v7259/i1/p72592W/s1%7B%5C%7DAgg=doi>.
154. Adam, L.-E. *et al.* Performance evaluation of the whole-body PET scanner ECAT EXACT HR/sup +/- following the IEC standard. *IEEE Transactions on Nuclear Science* **44**, 1172–1179. ISSN: 00189499 (June 1997).
155. Rousset, O. G., Ma, Y. & Evans, A. C. Correction for partial volume effects in PET: Principle and validation. *Journal of Nuclear Medicine* **39**, 904–911. ISSN: 01615505 (May 1998).
166. Yang, J., Huang, S. C., Mega, M. & Lin, K. P. Investigation of partial volume correction methods for brain fdg pet studies. *IEEE Transactions on Nuclear Science* **43**, 3322–3327. ISSN: 00189499 (1996).
167. Esteban, O. *et al.* MRIQC: Predicting Quality in Manual MRI Assessment Protocols Using No-Reference Image Quality Measures. *bioRxiv*. doi:10.1101/111294. <http://biorxiv.org/content/early/2017/02/24/111294> (2017).
168. Gedamu, E. L., Collins, D. & Arnold, D. L. Automated quality control of brain MR images. *Journal of Magnetic Resonance Imaging* **28**, 308–319. ISSN: 10531807 (Aug. 2008).

169. Oguz, I. *et al.* DTIPrep: quality control of diffusion-weighted images. doi:10.3389/fninf.2014.00004. <https://www.ncbi.nlm.nih.gov/pmc/articles/PMC3906573/pdf/fninf-08-00004.pdf> (2014).
170. Panta, S. R. *et al.* A Tool for Interactive Data Visualization: Application to Over 10,000 Brain Imaging and Phantom MRI Data Sets. *Frontiers in Neuroinformatics* **10**, 9. ISSN: 1662-5196 (Mar. 2016).
171. Christodoulou, A. G. *et al.* A quality control method for detecting and suppressing uncorrected residual motion in fMRI studies. *Magnetic Resonance Imaging* **31**, 707–717. ISSN: 0730725X (June 2013).
172. Frouin, V., Comtat, C., Reilhac, A. & Grégoire, M. C. Correction of partial-volume effect for PET striatal imaging: Fast implementation and study of robustness. *Journal of Nuclear Medicine* **43**, 1715–1726. ISSN: 01615505 (Dec. 2002).
173. Meltzer, C. C. *et al.* Comparative evaluation of MR-based partial-volume correction schemes for PET. *Journal of nuclear medicine : official publication, Society of Nuclear Medicine* **40**, 2053–65. ISSN: 0161-5505 (1999).
174. Quarantelli, M. *et al.* Integrated software for the analysis of brain PET/SPECT studies with partial-volume-effect correction. *Journal of Nuclear Medicine* **45**, 192–201. ISSN: 01615505 (Feb. 2004).
175. Funk, T. *et al.* Assessing neuronal density in peri-infarct cortex with PET: Effects of cortical topology and partial volume correction. *Human Brain Mapping* **38**, 326–338. ISSN: 10659471 (Jan. 2017).

176. Cox, S. M. *et al.* Striatal D1 and D2 signaling differentially predict learning from positive and negative outcomes. *NeuroImage* **109**, 95–101. ISSN: 10959572 (Apr. 2015).
177. Comtat, C. *et al.* *OSEM-3D reconstruction strategies for the ECAT HRRT in IEEE Symposium Conference Record Nuclear Science 2004*. **6** (IEEE, 2004), 3492–3496. ISBN: 0-7803-8701-5. doi:10.1109/NSSMIC.2004.1466639. <http://ieeexplore.ieee.org/document/1466639/>.
178. Collins, D. L. *et al.* in *Information Processing In Medical Imaging, Proceedings* 210–223 (Springer, Berlin, Heidelberg, 1999). ISBN: 978-3-540-66167-2. doi:10.1007/3-540-48714-X. <http://apps.webofknowledge.com/InboundService.do?SID=V1Mh6do0Hnf4594ppeI%7B%5C%7Dproduct=WOS%7B%5C%7DUT=000170515200016%7B%5C%7DsrcApp=Papers%7B%5C%7DDestFail=http://www.webofknowledge.com%7B%5C%7DInit=Yes%7B%5C%7Daction=retrieve%7B%5C%7DFunc=Frame%7B%5C%7DcustomersID=mekentosj%7B%5C%7DsrcAuth=mekentosj%7B%5C%7DIsProductC%7B%5C%7D5Cnhttp://a>.
179. Collins, D. L. & Evans, A. C. Animal: Validation and Applications of Nonlinear Registration-Based Segmentation. *International Journal of Pattern Recognition and Artificial Intelligence* **11**, 1271–1294. ISSN: 0218-0014 (Dec. 1997).
180. Zijdenbos, A. *et al.* in *Lecture Notes in Computer Science (including subseries Lecture Notes in Artificial Intelligence and Lecture Notes in Bioinformatics)* 439–448 (Springer, Berlin, Heidelberg, 1996). ISBN: 3540616497. doi:10.1007/bfb0046984. <http://link.springer.com/10.1007/BFb0046984>.

181. Funck, T., Larcher, K., Toussaint, P. J., Evans, A. C. & Thiel, A. APPIAN: Automated Pipeline for PET Image Analysis. *Frontiers in Neuroinformatics* **12**. ISSN: 16625196. doi:10.3389/fninf.2018.00064. <https://www.frontiersin.org/article/10.3389/fninf.2018.00064/full> (Sept. 2018).
182. Studholme, C., Hill, D. L. & Hawkes, D. J. Automated three-dimensional registration of magnetic resonance and positron emission tomography brain images by multiresolution optimization of voxel similarity measures. *Medical Physics* **24**, 25–35. ISSN: 00942405 (Jan. 1997).
183. Strother, S. C. *et al.* Quantitative comparisons of image registration techniques based on high-resolution MRI of the brain. *Journal of computer assisted tomography* **18**, 954–62. ISSN: 0363-8715 (1994).
184. Ashburner, J. & Friston, K. Multimodal image coregistration and partitioning - A unified framework. *NeuroImage* **6**, 209–217. ISSN: 10538119 (Oct. 1997).
185. West, J. *et al.* Comparison and evaluation of retrospective intermodality brain image registration techniques. *Journal of Computer Assisted Tomography* **21**, 554–566. ISSN: 03638715 (1997).
186. Delbeke, D., Patton, J. A., Martin, W. H. & Sandler, M. P. FDG PET and dual-head gamma camera positron coincidence detection imaging of suspected malignancies and brain disorders. *Journal of Nuclear Medicine* **40**, 110–117. ISSN: 01615505 (Jan. 1999).
187. Nørgaard, M. *et al.* Optimization of preprocessing strategies in Positron Emission Tomography (PET) neuroimaging: A [11C]DASB PET study. *NeuroImage* **199**, 466–479. ISSN: 10959572 (Oct. 2019).

188. Rousset, O. & Zaidi, P. Correction for partial volume effects in emission tomography. *Quantitative Analysis in Nuclear Medicine ...* http://link.springer.com/chapter/10.1007/0-387-25444-7%7B%5C_%7D8 (2006).

CHAPTER 6
**3D reconstruction of multi-ligand autoradiography and application for
Monte-Carlo PET simulation**

Thomas Funck,^{1,2} Nicola Palomero-Gallagher^{4,5}, Konrad Wagstyl³, Mona Omidyeganeh²,
Claude Lepage², Alexander Thiel¹, Karl Zilles⁴, Alan C. Evans²

¹ Lady Davis Institute, Jewish General Hospital, McGill University, Montreal,
Quebec, Canada

² Montreal Neurological Institute, McGill University, Montreal, Quebec, Canada

³ Wellcome Trust Center, University College London, London, United Kingdom

⁴ Institute of Neuroscience and Medicine INM-1, Research Centre Jülich, Jülich,
Germany

⁵ Department of Psychiatry, Psychotherapy and Psychosomatics, Medical Fac-
ulty, RWTH Aachen, University, Aachen

6.1 Preamble

Neurotransmitter receptor mapping can be conducted at many spatial scales, from 50 μm resolution with autoradiography to $\sim 2\text{-}3$ mm with PET. While the work in Chapter 3 was an investigation into using novel image processing methods to optimize the spatial information that can be obtained from PET neurotransmitter receptor mapping studies, the work in this chapter attempts to go in the opposite direction. The limitation of using real images to study PET resolution is that it is impossible to know the true source radioactivity distribution corresponding to that measured in the image. Simulation and phantom studies are two common methods for evaluating PET resolution, but the source radioactivity distributions used in these approaches are too simplistic.

Autoradiography typically provides a high resolution 2D map of neurotransmitter receptor distribution that can in principle be used to define a source radioactivity distribution and perform realistic PET simulation. This has not been done in part because of the expense and technical difficulty involved in acquiring autoradiographs across the entire human brain. There are also technical challenges that must be overcome before autoradiography can be used to define a source radioactivity concentration for PET simulation, the first being to reconstruct the 2D autoradiographs into a 3D volume. To this end we developed a pipeline to perform 3D reconstruction and used it to produce a 3D high resolution atlas of $GABAA_{Benz.}$ receptor distribution in the brain. This in and of itself is an important novel contribution because it is the first ever such 3D autoradiography atlas for the whole human brain.

Monte-Carlo PET simulation was then performed using the 3D volume of $GABAA_{Benz.}$ as a source radioactivity distribution. The accuracy of PET imaging for high-resolution receptor mapping was evaluated by comparing the simulated PET images to the source volume. It is important to note that the particular neurotransmitter receptor used to create a simulated PET image, $GABAA_{Benz.}$, and the PET scanner that was modelled, i.e., CTI-Siemens ECAT HRRT, are both the same as were used for in vivo PET in Chapter 3. We hope therefore to provide complementary insights into receptor mapping from the perspective of real in vivo PET and from simulation based on autoradiography.

6.2 Abstract

Neurotransmitter receptor mapping is typically conducted either at high resolution (50 μm) in 2D with autoradiography or at lower resolution (in the order of millimeters) with positron emission tomography (PET). While PET is less expensive than autoradiography, it is not clear what is the maximum spatial resolution at which PET can accurately measure receptor densities. To address this problem we have developed a pipeline that can reconstruct a 3D volume from 2D autoradiographs for 20 different neurotransmitter binding site densities obtained from a serially sectioned post-mortem human brain. A validation study using synthetic data was used to evaluate the interpolation error for estimating missing autoradiographs in the reconstruction pipeline and showed that the error level was generally between 0-6%. The reconstructed volume was then used to define a source radioactivity distribution for Monte-Carlo PET simulation using the Geant4 Application for Emission

Tomography (GATE). A simulated PET image for the radioligand [18-F]-flumazenil was produced based on the actual distribution of the $GABAA_{Benz.}$ receptor distribution from the donor brain. The reconstruction of the receptor density volume for $GABAA_{Benz.}$ receptor was visually compared to the donor's MRI. The simulated PET image showed that under ideal conditions, PET was able to measure radioactivity concentrations related to laminar receptor densities in the cortical GM and had an average local correlation of 0.71 over the GM. We also found that partial-volume effects (PVE) were highly dependent on cortical morphology, with greater PVE and decreased correlation ($\sim 0.5-0.65$) on abutting sulcal walls. The results suggest that PET can potentially be used to perform neurotransmitter mapping at near laminar spatial resolution. The reconstruction pipeline in conjunction with Monte-Carlo PET simulation allows for the creation of a database of high resolution neurotransmitter receptor atlases and corresponding simulated PET images, which can serve as reference standard for the validation of PET algorithms and help the design of next generation PET cameras.

6.3 Introduction

Three dimensional digital brain atlases are important both for (i) neuroscience, e.g., characterizing the heterogeneity of brain anatomy or function within a given population, and (ii) the analysis of brain images, e.g., as a prior for brain image registration or segmentation [189]. As of yet, high resolution atlases of human neurotransmitter receptors have not been available. The lack of neurotransmitter receptor

atlases is particularly unfortunate given that neurotransmitters and their corresponding receptors underpin all synaptic transmission and hence all information processing in the brain.

While atlases based on in vivo neurotransmitter receptor imaging using PET have recently been created [10], PET suffers from relatively poor spatial resolution when compared to the spatial distribution of neurotransmitter receptors. Despite its limitations, at present PET offers the only realistic approach to creating atlases of neurotransmitter receptor density for a wide range of populations with a sample size sufficient to capture the variability within these populations. While many studies have been performed to evaluate PET resolution, these typically use geometric or simple anatomic phantoms [12, 39, 190]. Given that the receptor distributions measured with PET are more complex than those modeled in phantom scans, it is not clear how accurately and at what scale PET can quantify receptor densities in practice.

We have developed a method for creating a 3D 50 μm neurotransmitter receptor atlas from autoradiographs measuring 20 different neurotransmitter receptor binding sites. We furthermore show how this reconstructed atlas can be used to derive highly realistic simulated PET images. These simulated PET images can then be used to assess the spatial resolution obtainable with PET versus the true source radioactivity distribution.

6.3.1 3D reconstruction from 2D post-mortem brain sections

Autoradiography is limited by sectioning artefacts which result in a biased representation of the complex cortical topology of the brain. Correcting these artefacts represents a major challenge to accurately recovering the 3D representation of the true receptor distribution in the brain.

Many approaches have been devised for reconstructing histological or autoradiographic sections into 3D. Thorough literature reviews have already been written by Dubois [191] and Pichat et al [192]. We therefore only briefly describe previous techniques for 3D reconstruction of histological and autoradiographic data to contrast how these relate to the autoradiographic data described in our work. While many 3D reconstruction algorithms have been proposed, none of these methods are adapted for reconstruction of the autoradiography data obtained with multiple radioligands in the same brain [28]. This data poses specific challenges such as the relatively sparse sampling rate, large non-linear artefacts, and the cutting of the brains into non-orthogonal slabs, which have not been addressed by existing autoradiography reconstruction methods.

To accurately reconstruct 2D sections into 3D, there are two major types of corrections that must be applied to the 2D sections, which, according to the terminology of Dauguet [193], are called "primary" and "secondary" artefacts. Primary artefacts are global errors that apply to the overall 3D shape of the object being reconstructed and secondary artefacts pertaining to individual 2D sections.

Perhaps counter-intuitively, secondary artefacts must be understood and dealt with first. Secondary artefacts apply to individual 2D sections such as tearing, shearing, stretching, etc.

Primary artefacts affect the overall 3D shape of the object being reconstructed and precede secondary artefacts in that they affect the brain before being sectioned. Primary artefacts include global deformations of the brain or challenges involved in recovering the 3D shape of the brain. One particularly important instance of a primary artefact is termed the "banana effect". This refers to the fact that if a sectioned banana was reconstructed by only aligning the sections to one another, the reconstructed banana would be straight and would have lost its natural curvature. There is not enough information in the 2D sections to correct for the banana effect. Additional imaging that captures the overall shape of the object prior to sectioning is required.

Three dimensional reconstruction techniques can be categorized along several criteria, including: the level of manual intervention required, the imaging modality, and the artefacts that were corrected by the reconstruction method. While the first reconstruction methods were either entirely manual or semi-automated, more recent algorithms have attempted to provide fully automated approaches [191, 192]. Reconstruction techniques can also be categorized based on the imaging modality, e.g., histology or autoradiography, along with the complementary imaging modalities that were used to provide additional information about the shape of the brain, e.g., MRI or blockface imaging.

Semi-automated methods included the placement of fiducial markers in the brain prior to sectioning so that the sections have easily identifiable physical landmarks [194–196]. An alternative approach that did not require physical manipulation of the brains was to manually identify anatomical landmarks on adjacent sections [197, 198].

The earlier automated reconstruction techniques focused on correcting for secondary artefacts. Automated reconstruction can be performed with only the 2D sections themselves using principal-axes transforms[199], intensity or frequency-based cross-correlation [200, 201], sum of squared error [202], discrepancy matching optical flow [203], edge-based point matching [204]. The main drawback of these methods was that misalignment errors were propagated to all subsequently coregistered sections. Methods have been developed to help address this problem and produce more robust alignments [205–208].

Additional imaging of the brain is required to correct for primary artefacts. A common approach is to use blockface imaging as an intermediate step, where the 2D sections are aligned to the blockface image and then the latter is aligned to the MRI [209–211]. If no blockface imaging has been acquired, an alternative approach is to perform an initial section-to-section reconstruction followed by alignment of this first reconstruction to the donor’s MRI in 3D, and then refine the alignment of the reconstructed volume to the MRI using 2D alignments of the sections [212, 213]. A recent and particularly innovative approach to 2D alignment of histological and corresponding MRI sections involved using Bayesian methods to simultaneously align

the histological section and the MRI section while transforming the pixel intensities of the former to resemble the latter [214].

Despite the existence of many reconstruction algorithms, these tend to be particular to the data sets they were designed for and hence cannot be straightforwardly be applied to reconstructing the dataset used in this study.

6.3.2 Challenges

The 3D autoradiograph data set from Zilles et al [28] combines many of the aforementioned challenges as well as several unique ones, which are elaborated below.

Non-orthogonal slabs

The brains were cut coronally into slabs prior to freezing and sectioning. However, the cuts were not parallel to one another, hence producing slabs that were not sectioned along an orthogonal plane (see Fig.6–2 for schematic illustration). This means that each slab has a different plane of sectioning and as such the coronal axis for each slab was oriented at a slightly different angle. Resampling the autoradiographs to a common coordinate grid would require resampling and interpolating the autoradiographs onto this common space. Because the autoradiographs are not densely sampled, i.e., there are significant gaps between acquired sections, interpolating these onto a new coordinate grid risks introducing interpolation errors by averaging between autoradiographs and empty regions where no section was acquired. The 3D reconstruction pipeline must therefore be applied separately for each slab. Additionally, there are gaps between the slabs therefore even if the slabs were put

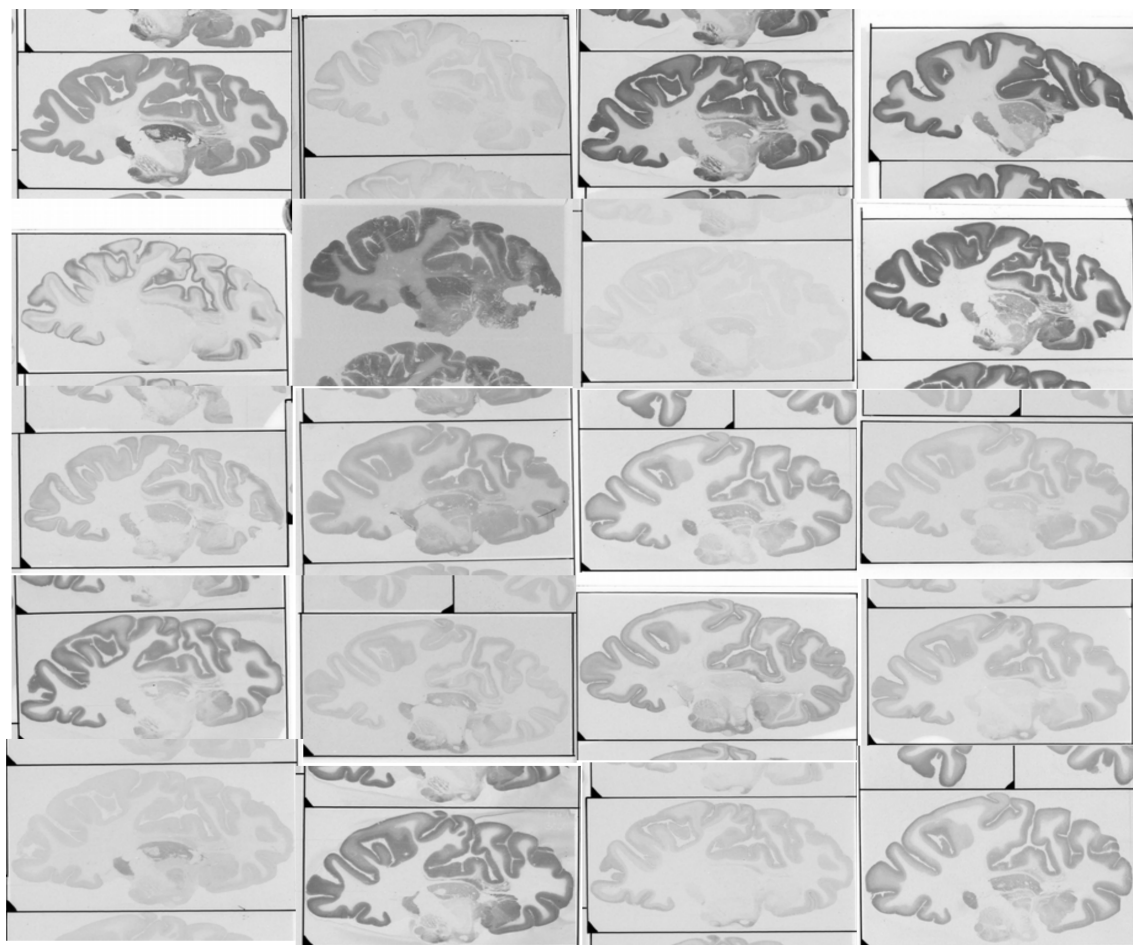


Figure 6-1: Example autoradiograph from each of the 20 neurotransmitter receptor binding sites illustrating the substantial heterogeneity in image intensities between the autoradiographs.

into a common space, it is not clear how far apart and at which angle the slabs should be positioned relative to one another.

Finally, the ends of the slabs frequently do not contain a full coronal section of brain tissue, thus making alignment of these incomplete sections difficult.

3D non-linear warping

Significant non-linear warping resulted from the brains not being fixed prior to removal from the cranial cavity. These non-linear deformities included compression and expansion both in and out of plane of sectioning. Warping could also result from collapse of the ventricles. These warping artefacts cannot be corrected without use of external reference. While this is common to autoradiography, what makes it particularly challenging in this case is that the entire human brain was being sectioned. Because the human brain is a relatively large organ, it is difficult to freeze uniformly and nearly instantaneously. To avoid freezing artefacts, the brain was cut into slabs of tissue along the coronal axis. However this introduces non-linear warping artefacts to each individual slab—a problem that is not commonly encountered in other data sets—and which further complicates the reconstruction.

Missing sections within slabs

Ideally, sections for a particular type of neurotransmitter would be acquired in equidistant sections every $400\mu\text{m}$. However mechanical processing errors or the use of some slices for other histological staining result in significant gaps between some of the acquired autoradiographs.

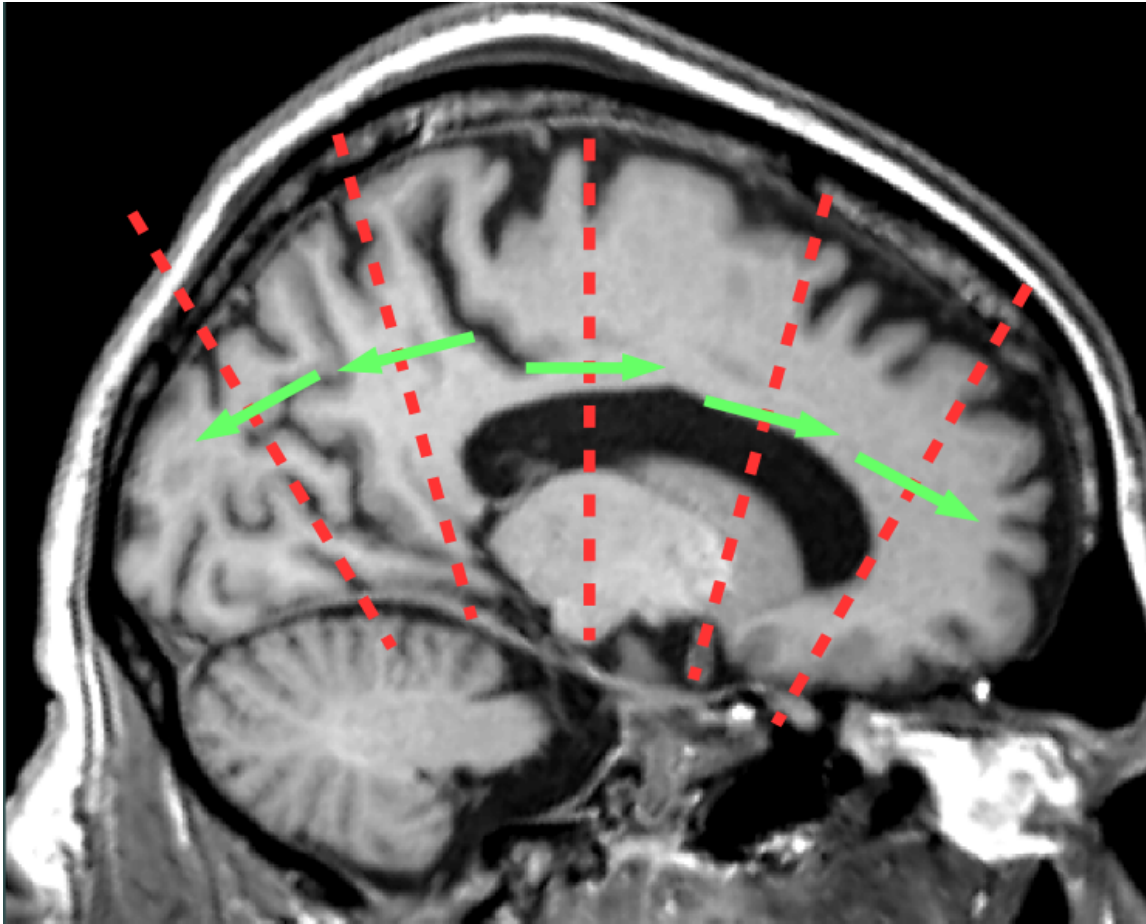


Figure 6-2: The donor brain was cut into slabs prior to freezing. The red lines show how cuts made at different angles create slabs of tissue that are then sectioned along different planes (shown in green). Note that this schema is only for illustrative purposes and does not represent the actual cuts that were made on the donor brain.

Variability in neurotransmitter receptor intensity

One of the most important obstacles for 3D reconstruction of the present data was the degree of variability in the distributions of neurotransmitter receptors. This is illustrated in Fig.6–1 where the autoradiographs represent very different receptor distributions and overall image contrast. In order to make a fully-automated pipeline, each step of the pipeline should perform equally well for the various ligands and hence must perform robustly given the diversity of intensity distributions in the autoradiographs.

Variability in autoradiograph acquisition protocol

After sectioning, brain sections were placed onto the same photographic film such that the raw autoradiographs contain multiple tissue slices that were incubated with the same ligand. This requires an automated processing step to identify the target piece of brain tissue from each autoradiograph and remove extraneous pieces of brain tissue from the image.

In addition, non-tissue objects, such as frames, arrows, and fiducial triangles, were placed on the autoradiographs prior to digitization. These also need to be removed so that they do not interfere with the reconstruction process. These artefacts are particularly challenging because they greatly impact the autoradiograph's histogram of pixel intensities.

6.3.3 Reconstruction pipeline overview

Previous methods have typically focused on reconstructing up to 3 different types of 2D images. Those methods that have attempted to reconstruct multiple types of sections into 3D have benefitted from blockface images. For example, Schubert, et al 2016 reconstructed polarized light images, histology, and autoradiographs of M2 muscarinic neurotransmitter receptor distribution in rat brains using blockface imaging [211]. To address the unique challenges presented by the data acquired by Zilles et al [28], we have developed a fully automated pipeline that systematically accounts for each of these issues to successfully perform reconstruction.

6.4 Methods

6.4.1 Data Acquisition

Although 3 brains were acquired at autopsy from donors (45-77 years), only one single (male) brain was used in the present study. The brain was acquired 8-13 h post-mortem without chemical fixation. A T1w MRI was acquired from the donor after they were declared deceased by the attending physician. The MRI was acquired on a Siemens Magnetom Sonata scanner with an MPRAGE acquisition protocol (2.2s TR, 1.2s TE, 15° flip angle).

The brains were then cut into slabs of tissue of approximately 2-3 cm to facilitate the even freezing of the brain tissue. Each slab was shock frozen between -40 and -50 C in N-methylbutane.

Slabs were sectioned at -20C into 20 μm thick sections of brain tissue with a cryostat microtome and placed on a gelatin-coated glass slide. Sections were freeze-dried overnight prior to incubation. Sections were first preincubated for rehydration and to eliminate any endogenous substances that may bind to the target receptor. Brain sections were then incubated in one of two ways for between 40-60min. For sections imaged for specific binding of the ligand to the target receptor, sections were incubated in a solution containing the titrated radiolabeled ligand. Alternatively, a subset of sections were imaged for non-specific binding by incubating the sections in a solution containing the radioligand as well as an unlabeled displacer that binds to 1 of 20 neurotransmitter receptors. The measured neurotransmitter receptors covered some of the most common neurotransmitter systems : glutamate, GABA, acetylcholine, dopamine, serotonin, noradrenaline, and adenosine (see Table.6-1 for detailed list). Sections were incubated sequentially with a specific radioligand such that there were at least 19 sections of brain tissue between any two sections incubated with the same radioligand. Lastly, the sections were rinsed to remove excess radioligand and stop additional binding. No blockface images were acquired.

Plastic titrated standards (Microscales[®], Amersham) with known radioactivity concentrations were also placed on the sheets alongside the brain sections and were co-exposed along with them. These standards allow pixel intensities to be converted to actual radioactivity concentrations.

Incubated sections were exposed to a β sensitive film (Hyperfilm, Amersham, Braunschweig, Germany). The autoradiographs were digitized with a CCD-camera on the Axiovision (Zeiss, Germany) imaging and processing system.

Table 6–1: List of the 20 radioligands and associated neurotransmitter receptors. The autoradiographs were categorized into tiers based on the visual contrast of the images. The tiers were used in the initial section-to-section alignment so that autoradiographs were only aligned to images in the same tier or lower.

Radioligand	Receptor	Transmitter	Contrast Tier
AMPA	AMPA	Glutamate	2
Kainate	Kainate	Glutamate	2
MK-801	NMDA	Glutamate	2
LY 341,495	mGluR2/3	Glutamate	2
Muscimol	GABAA (agonist)	GABA	1
SR95531	GABAA (antagonist)	GABA	1
CGP 54626	GABAB	GABA	1
Flumazenil	<i>GABAA_{Benzodiazepine}</i>	GABA	1
Pirenzepine	Muscarinic M_1	Acetylcholine	1
Oxotremorine-M	Muscarinic M_2 (agonist)	Acetylcholine	3
AF-DX384	Muscarinic M_2 (antagonist)	Acetylcholine	1
4-DAMP	Muscarinic M_3	Acetylcholine	2
Epibatidine	Nicotinic $\alpha_4\beta_2$	Acetylcholine	4
Prazosin	α_1	Noradrenalin	1
UK-14,304	α_2 (agonist)	Noradrenalin	2
RX 821002	α_2 (antagonist)	Noradrenalin	2
8-OH-DPAT	5 – HT_{1A}	Serotonin	2
Ketanserin	5 – HT_2	Serotonin	1
SCH 23390	D_1	Dopamine	2
DPCPX+Gpp(NH)	Adenosine 1	Adenosine	1

Radioactivity concentrations were calculated using standards. The pixel intensities of these standards were plotted against their respective radioactivity concentrations and a calibration curve was fit to these points. Radioactivity concentrations of pixel intensities were interpolated from the calibration curve.

Finally, binding densities, C_b (fmol/mg protein), were calculated by multiplying the radioactivity concentrations with a scaling factor according to :

$$C_b = \frac{R}{EBW_b S_a} \times \frac{K_D + L}{L} \quad (6.1)$$

where R is the measured radioactivity concentration interpolated from the calibration curve, E is the efficiency of the scintillation detector, B is a constant for the amount of radioactivity decays per unit time (Ci/min), W_b is the protein weight of a standard (mg), and S_a is the specific activity of the ligand (Ci/mmol), K_D is the dissociation constant (nM) and L is the free concentration of ligand during incubation (nM).

6.4.2 Pipeline Overview

The details of the pipeline are explained in the following sections, but it is useful to first give a broad overview. The overall framework used by the pipeline was to calculate a series of transformations that would transform each of the 2D autoradiographs to the correct position on the donor's MRI (see Fig.6-3). The purpose of this approach was to minimize the number of manipulations applied to the raw autoradiographs. Thus while many manipulations were performed on the autoradiographs at the various stages of the pipeline, the final reconstructed volume

was produced by applying only two transformations to the autoradiographs: (i) a composite 2D transformation applied to individual autoradiographs, and (ii) a non-linear 3D transformation applied to autoradiograph volumes.

As a proof-of-principle for the efficacy of our reconstruction pipeline, a single volume of $GABAA_{Benz.}$ receptors was reconstructed for the right hemisphere of 1 of the 3 donor brains.

Stages of autoradiograph reconstruction

Enumerated stages 1-7 correspond to S_{1-7} in Fig.6-3.

Stage 1: Automated cropping to isolate target brain tissue

- Automated cropping of the autoradiographs used to isolate the target piece of brain tissue from the raw image.

Stage 2: 2D rigid inter-autoradiograph alignment

- An initial 3D autoradiograph volume was reconstructed by aligning autoradiographs to one another.

Stage 3: Binary GM volume for autoradiograph volumes and MRI

- GM masks were extracted for the MRI (S_{3A}) and autoradiograph volumes (S_{3B}).
- This was done to facilitate subsequent alignments.

Stage 4: 3D alignment of autoradiograph volumes to MRI

- 3D linear alignment of autoradiograph GM volumes to find corresponding regions in MRI GM volume ($S_{4.1}$).

- 3D non-linear alignment of the MRI volume to each of the autoradiograph GM volumes ($S_{4.2}$).
- Creates a transformed versions of the MRI in coordinate space of the autoradiograph slabs.

Stage 5: 2D refinement of autoradiograph alignment to MRI

- 2D alignment of coronal sections in autoradiograph GM volume to corresponding coronal sections in MRI GM volumes.
- Refines the alignment between the autoradiographs and the MRI volume by correcting deformations in coronal axis.

Stage 6: Interpolation of missing autoradiographs

- MRI sections corresponding to autoradiograph sections were aligned to MRI sections where autoradiographs are missing ($S_{6.1}$).
- 3D receptor volume was produced for a given receptor using a distance-weighted interpolation scheme ($S_{6.2}$).

Stage 7: Transformation of receptor volumes to MRI coordinate space

- Slabs are transformed to donor's MRI in MNI coordinate space by inverting transform T_3 from $S_{4.2}$.

6.4.3 Stage 1: Automated cropping to isolate target brain tissue

The raw autoradiographs contained 3 components: the target section of brain tissue, extraneous pieces of brain tissue, and non-tissue objects (see Fig.6-4). The first step was to remove the extraneous pieces of brain tissue and non-tissue objects in the autoradiographs. To increase the computational speed of subsequent image

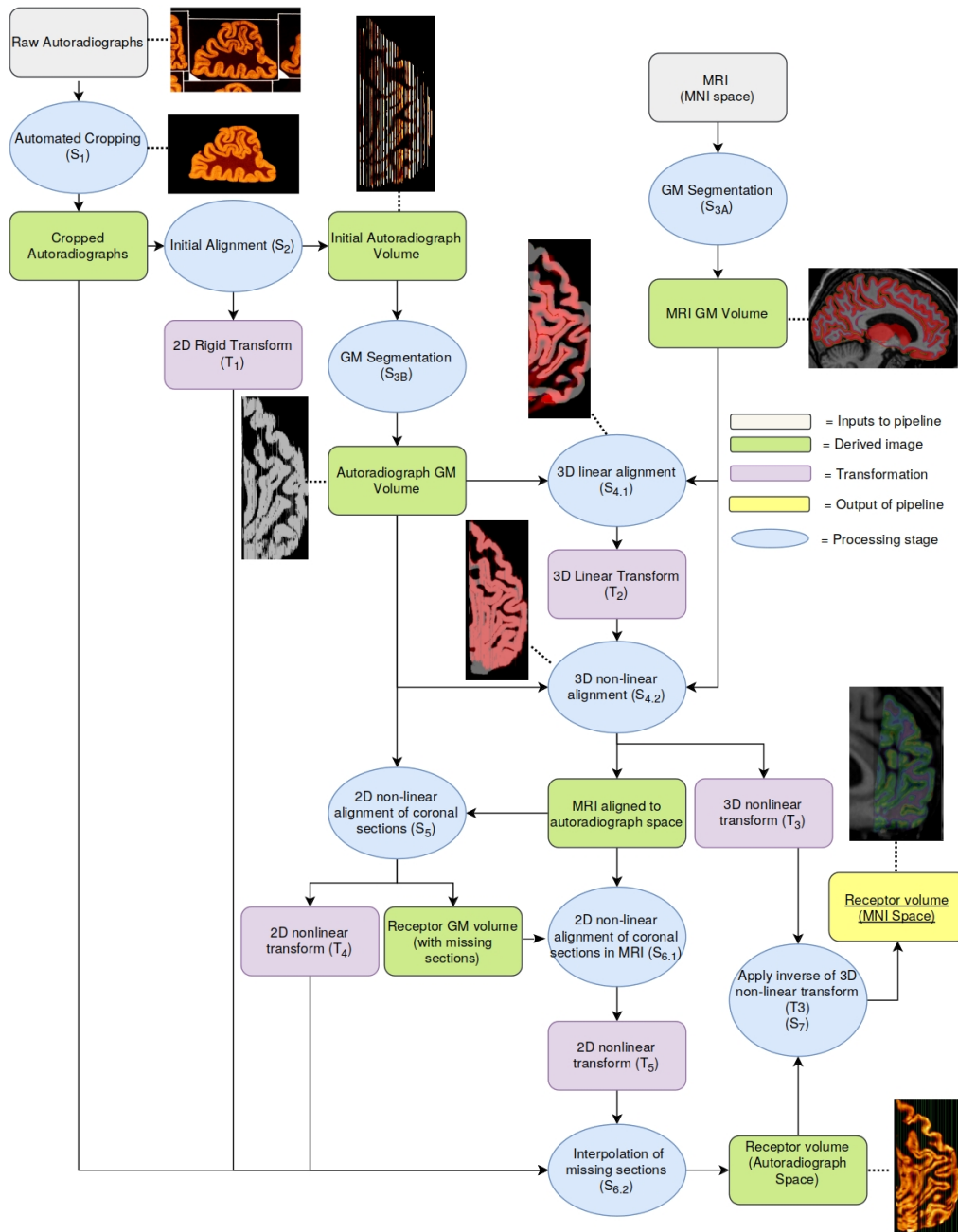


Figure 6–3: A multistage (S_{1-7}) pipeline was devised for reconstructing 2D sections from multiple autoradiographs. The pipeline was applied independently to individual slabs. Transformations T_1 , T_4 , T_5 were applied to cropped autoradiographs to produce a receptor volume in autoradiograph space and transformation T_3^{-1} was applied to transform receptor slabs to the donor's MRI in MNI space[4].

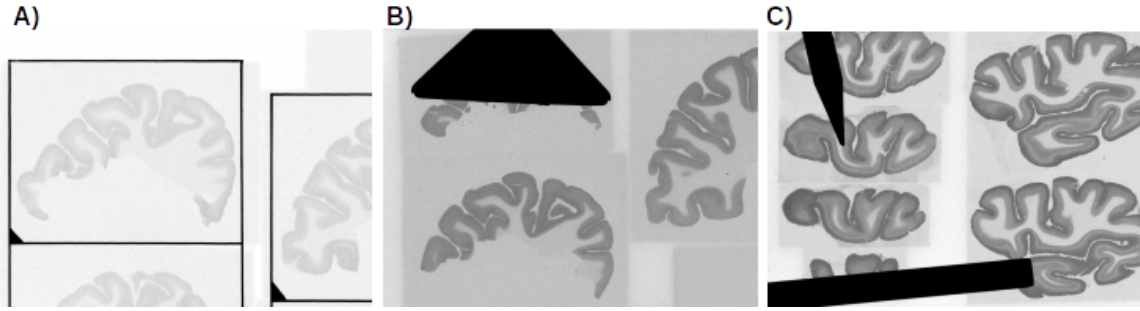


Figure 6-4: Example of autoradiographs with multiple pieces of tissue and non-tissue objects: frames (A), fiducial triangles (B), and arrows (C)

processing, the autoradiographs were downsampled from $20 \times 20 \mu\text{m}$ to a resolution to $200 \times 200 \mu\text{m}$.

The non-tissue objects were removed using a deep convolutional neural network based on the U-Net architecture [215]. Training data were created by manually thresholding a subset of the raw autoradiographs to isolate the frames, arrows, and triangular shapes, and then manually removing any thresholded pixels that were not part of the non-tissue objects. A simplified U-Net was then trained on these data using a binary cross-entropy and the architecture shown in Fig.6-5. Given the relatively small amount of training data, a simplified U-Net architecture was chosen instead of the full U-Net architecture. This was done to limit the number of parameters used by the network. The non-tissue objects were removed by replacing intensities within the objects with random intensity values sampled from the pixels within 3 pixels of the border of the non-tissue objects.

After removing the non-tissue objects from the autoradiographs, further processing was used to remove the extraneous pieces of tissue (see Fig.6-6 for illustrative

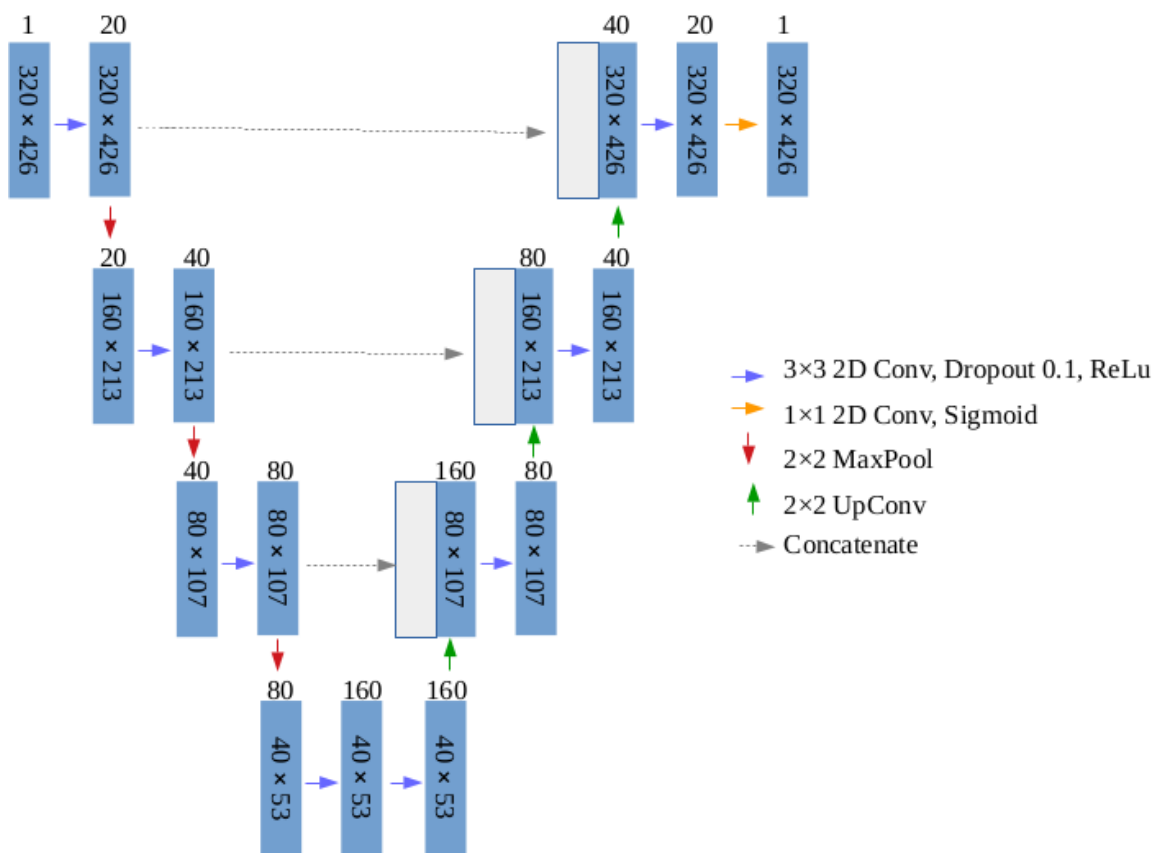


Figure 6–5: A simplified U-Net architecture was designed to identify non-tissue objects (i.e., frames, arrows, and triangles in the autoradiographs).

example of automated cropping). A multi-resolution approach to separating the foreground from background was implemented to limit the impact of background noise while attempting to preserve high-frequency spatial features. The autoradiographs were smoothed with gaussian filters at 0, 2, and 4 standard deviations and each one of the smoothed autoradiographs were thresholded into binary images with Otsu histogram thresholding [216]. The 3 thresholded images were then averaged (yielding an image between 0 and 1) and thresholded at 0.5 to create a binary image where pixels of 1 represented brain tissue and 0 represented background.

Foreground pixels were segmented into discrete connected regions and pixels in each tissue region were assigned a unique integer value for each region. Tissue regions that overlapped with either the border of the autoradiograph or with the non-tissue objects identified by the U-Net were discarded. This removed most of the extraneous pieces of tissue in the autoradiographs, but there were sometimes small islands of regions identified as tissue that needed to be removed. These could include both background pixels erroneously identified as tissue regions or small regions of detached extraneous tissue. To remove remaining extraneous tissue regions, the number of pixels in each tissue region was calculated and any region that was less than 5% of the size of the largest tissue region was removed. Finally, 3 series of morphological erosions followed by 3 morphological dilations was used to denoise the images.

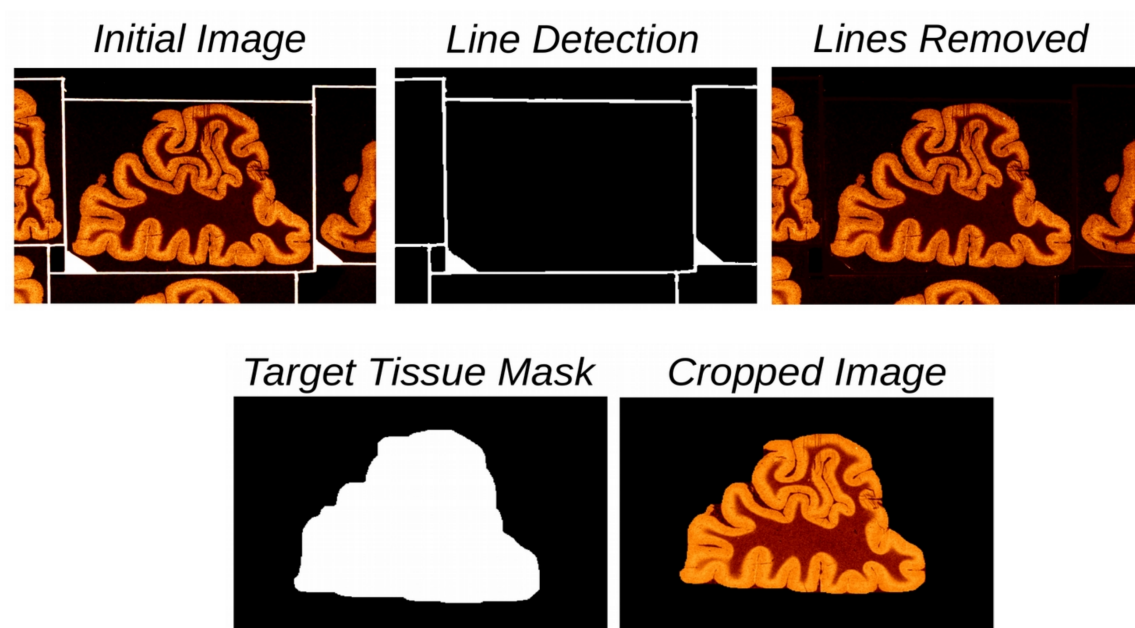


Figure 6–6: Autoradiographs were preprocessed before they could be reconstructed. A deep learning network was trained to identify frames in the autoradiographs and remove them. Computer vision techniques were then used to remove pieces of brain tissue other than the target brain tissue in the image.

Table 6–2: ANTs parameters used to align the autoradiographs to one another.

Transform	Iterations	Smoothing	Downsample Factor	Metric
Rigid	2100	3	6	Mattes MI
Rigid	1200	2	4	Mattes MI
Rigid	1200	1	2	Mattes MI
Rigid	10	0	1	Mattes MI

6.4.4 Stage 2: 2D rigid inter-autoradiograph alignment

The initial step of 3D reconstruction consisted in aligning the cropped autoradiographs to one another using 2D rigid body transformations (see Table.6–2 for parameters). As is seen in Fig.6–1, certain ligands produced autoradiographs with much greater image contrast than others. To limit the impact of autoradiographs with low contrast, the autoradiographs were also categorized into tiers based on visual evaluation of their image contrast (see Table.6–1). Autoradiographs with ligands in lower tiers were considered to have better image contrast. Each section was aligned to its nearest neighbour in the same tier or lower. This means that sections were only aligned to an image with a similar or better image contrast. To limit the possibility of systematic misalignments between adjacent sections, the entire alignment procedure was applied iteratively. The initial alignment was performed on the cropped autoradiographs that had been downsampled to 200 x 200 μm .

Due to the gap between the slabs and the different planes of sectioning for each slab, 2D autoradiograph alignment was only performed within each slab. The sections were aligned to the central section of the slab to limit the impact of incomplete sections at the ends of slabs.

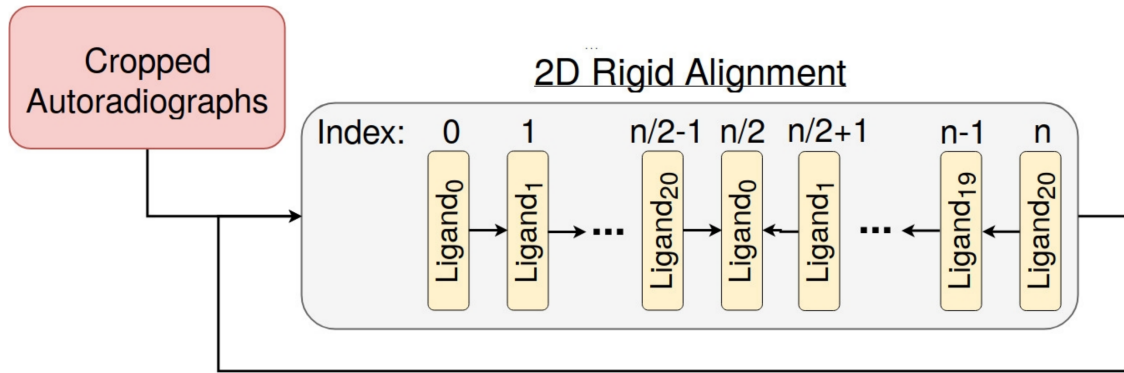


Figure 6–7: An initial reconstructed autoradiograph volume was produced by aligning autoradiographs to its adjacent neighbour. The central autoradiograph ($N/2$) of each section was used as the reference to which the others were aligned. The alignment process was repeated iteratively to avoid misalignments.

Once the autoradiographs were aligned to one another, they were reconstructed into an initial 3D autoradiograph volume for each slab, respectively. Therefore 6 initial autoradiograph volumes were produced, one for each slab. Each reconstructed autoradiograph volume had a resolution of $200 \times 20 \times 200 \mu\text{m}$ because the downsampled autoradiographs have a voxel spacing of $200 \times 200 \mu\text{m}$ and each section was $20 \mu\text{m}$ thick along the coronal axis. The 2D rigid transforms produced for each autoradiograph in a slab correspond to transform T_1 in Fig.6–3.

6.4.5 Stage 3: Binary GM volume for autoradiograph volumes and MRI

Aligning the autoradiograph volumes to the MRI volume directly was very challenging given the relatively sparse sampling of the autoradiographs and their heterogeneous intensity values. Instead, the alignment was performed between binary GM volumes derived from the initial autoradiograph volumes and the MRI volume.

The problem of multi-modal alignment is then simplified to mono-modal alignment between GM masks.

Extracting GM mask from MRI volume ($S_{3.A}$)

A binary MRI GM volume was extracted from the donor’s MRI using a mesh representation of the cortical surface (Fig.6–8). Cortical surface meshes were obtained from the MRI using the CIVET pipeline [217]. A super-resolution cortical GM mask at $250\ \mu\text{m}$ was obtained from these cortical surface meshes by sampling points between the inner white-matter and outer GM surface meshes[121]. A segmentation of the donor’s subcortical GM was then generated using ANIMAL [218], upsampled to $250\mu\text{m}$ using nearest neighbour interpolation, and added to the super-resolution cortical GM.

Extracting GM mask from autoradiograph volume ($S_{3.B}$)

A GM binary volume was generated for the initial autoradiograph volumes for each slab using a 3-class K-means [219] clustering to segment each 2D autoradiograph into background, white matter, and GM (Fig.6–9). The 3 classes for the K-means algorithms were initialized with the image maximum, the mean of non-zero voxels, and the minimum voxel value. The autoradiograph GM volume was downsampled from a voxel size of $200\times 20\times 200\mu\text{m}$ to $250\mu\text{m}$ isotropic resolution with an order 5 spline interpolation. This was done to facilitate alignment with the MRI GM volume.

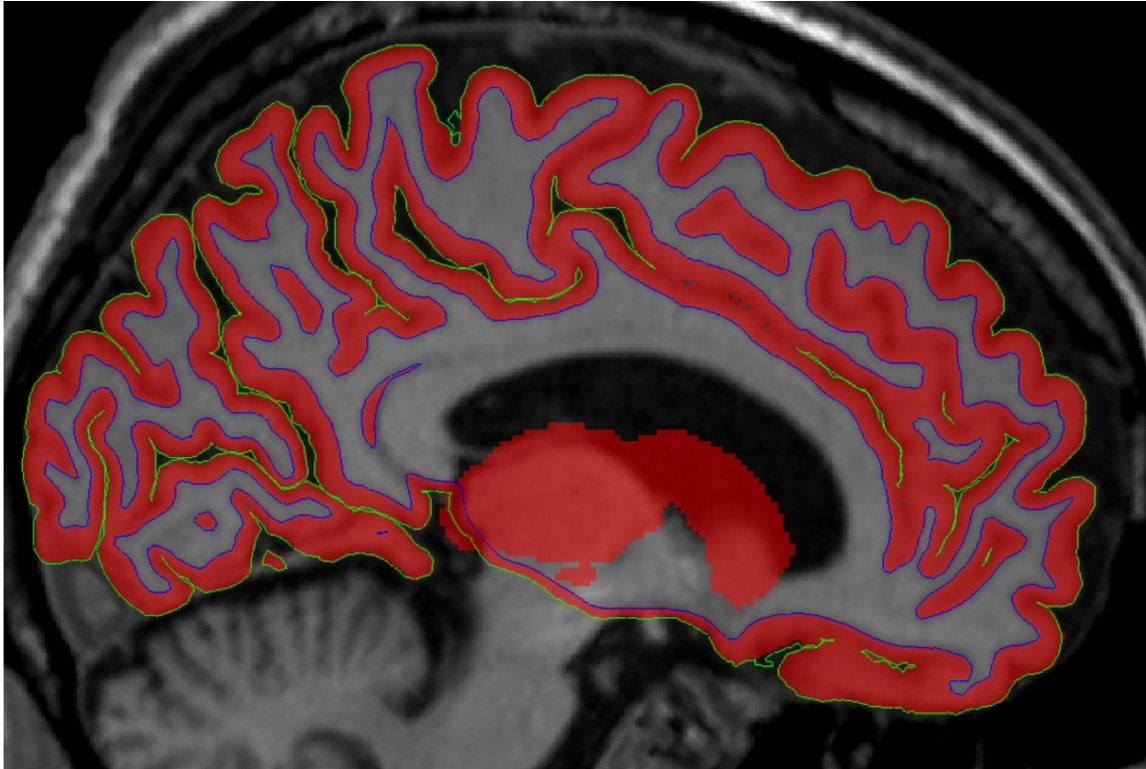


Figure 6–8: Cortical surfaces were extracted from the donor’s MRI and used to derive a 250 μm MRI GM volume. The ANIMAL algorithm was used to create a binary GM volume for subcortical GM regions.

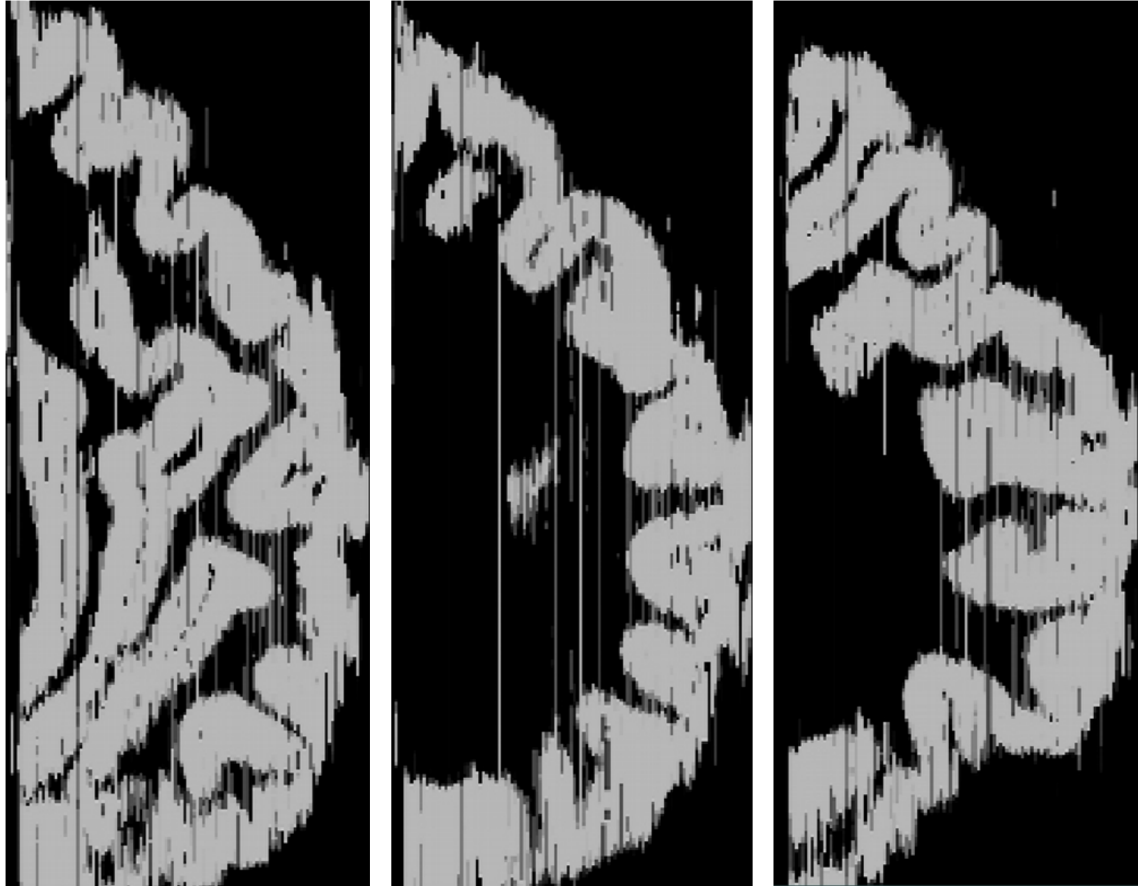


Figure 6-9: The autoradiograph slab volume was segmented to identify GM regions using the K-means algorithm. The segmentation facilitates the alignment to the MRI GM volume.

Table 6–3: ANTs parameters used to align the autoradiograph GM slab volume to the MRI GM volume.

Transform	Iterations	Smoothing	Downsample Factor	Metric
Rigid	1500	1	2	Global CC
Rigid	1000	0	1	Global CC
Affine	1500	1	2	Global CC
Affine	1500	0	1	Global CC

6.4.6 Stage 4: 3D alignment of autoradiograph volumes to MRI

Coregistration of the autoradiograph volume to the donor’s postmortem MRI was used to correct for deformations in the autoradiographs resulting from the brains not being fixed prior to sectioning and freezing. Coregistration was performed independently for each slab.

Finding MRI section corresponding to autoradiograph slabs ($S_{4.1}$)

An algorithm was developed based on Yang et al [213] to find the position in the MRI that corresponds to the receptor slab volume (Fig.6–10). Instead of a rigid, i.e. 6 parameter, transformation between volumes of histological tissue and the acquired MRI, we used a 12 parameter affine transformation to account for some of the deformations in the autoradiograph slab volumes. Prior to alignment, the autoradiograph and MRI GM volumes were blurred with a gaussian kernel with 0.75 mm standard deviation and downsampled to 1 mm using nearest neighbour interpolation. The alignment was calculated between the autoradiograph GM volumes and the MRI GM volume with ANTs [86] (see Table.6–3 for parameters).

The extra parameters of a full affine versus a rigid transformation increase the likelihood of misalignments resulting from local minima in the similarity metric. To

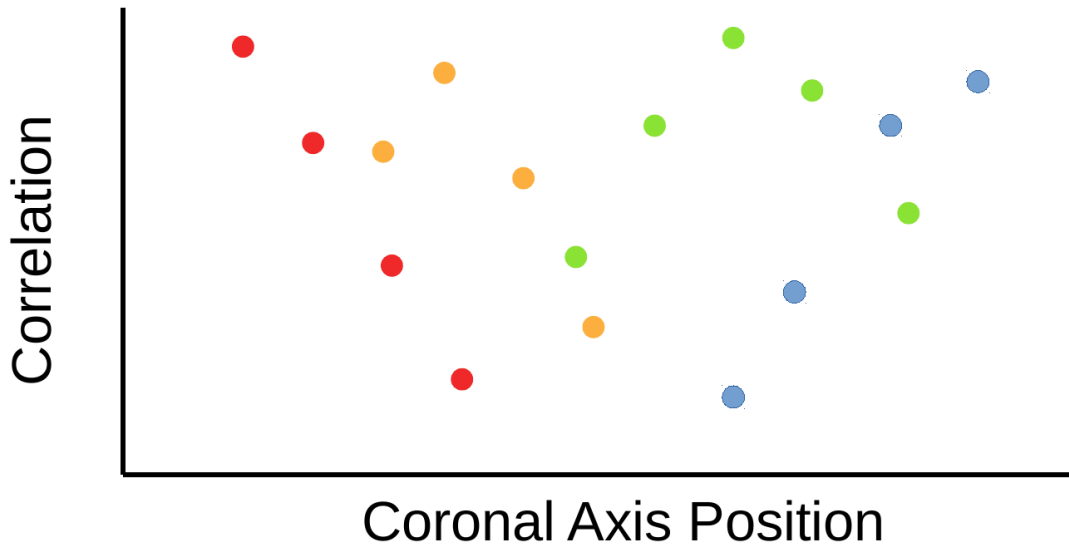
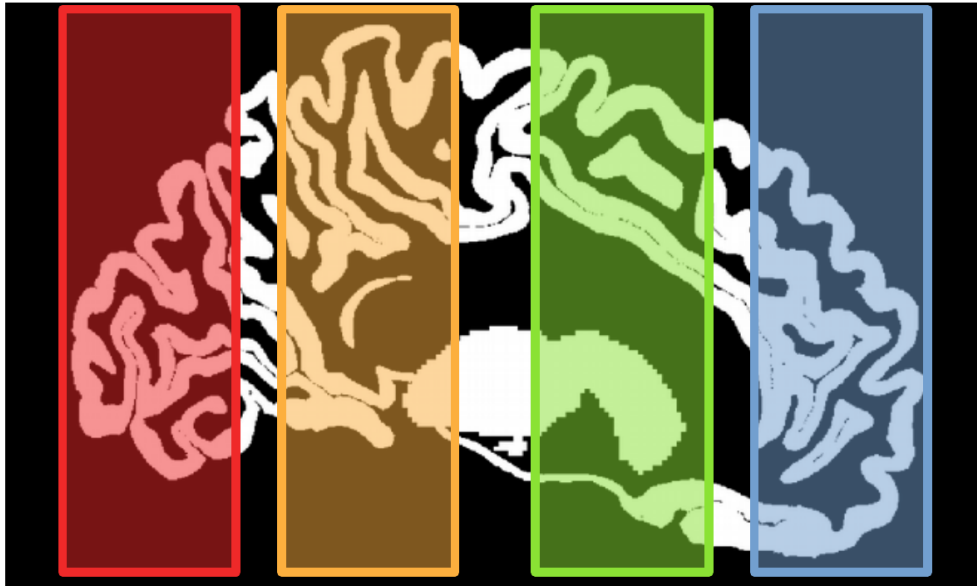


Figure 6–10: The position along the coronal axis for each autoradiograph GM slab was chosen based on the location that had the maximum weighted cross-correlation. This figure is for illustrative purposes and does not represent the actual alignment of the slabs or the corresponding cross-correlation.

limit the possibility of a misalignment we devised a pseudo-probability distribution for the probability of autoradiograph's position along the coronal axis of the MRI. The width of each brain slab, i.e., its extent along the coronal axis, was calculated based on the acquired autoradiograph sections in each slab. The expected location of the slabs was calculated by first placing the anterior and posterior slabs at the corresponding ends of the MRI. The position of the intermediate slabs was calculated based on their respective widths and assuming equal spacing between them. The pseudo-probability distribution was generated for each slab by convolving an impulse function at the expected slab position with a gaussian function. The gaussian had a standard deviation equal to 1.5 times the width of the slab. This pseudo-probability distribution was largest at the position closest to the expected slab position and dropped towards 0 further away from this position.

Starting from the most anterior position in the brain, the first slab volume was aligned to the MRI volume using an affine transform. The cross-correlation was calculated at the position of optimal fit and was weighted by multiplying it by the probability of a correct alignment at this position. Hence alignments further away from the expected position were penalized. The slab was then shifted by 5mm and the same process was repeated. To save computational time, positions that had a probability of less than half of the maximum of the pseudo-probability distribution were not considered. This process was repeated for each of the slabs in the hemisphere, alternating between slabs closest to the anterior and posterior poles of the brain. For each slab, the position with the highest weighted cross-correlation was taken to be the correct position of that slab relative to the MRI.

Table 6–4: ANTs parameters used to perform non-linear alignment between the autoradiograph GM slab volume and the MRI GM volume.

Transform	Iterations	Smoothing	Downsample Factor	Metric
SyN	1500	8	4	Global CC
SyN	1000	4	2	Global CC
SyN	500	2	1	Global CC

The 3D linear transformation for aligning the autoradiograph GM volumes for each slab to the donor’s MRI correspond to transform T_2 in Fig.6–3.

3D warping of MRI to autoradiograph volumes ($S_{4.2}$)

The inverse affine transformation from the autoradiograph GM volume to the MRI GM volume (this would correspond to the inverse of T_2 in Fig.6–3, i.e., T_2^{-1}) was used to initialize a further non-linear alignments of the MRI GM volume to the autoradiograph GM volumes for each slab (see Table.6–4 for parameters). The alignment thus produced an MRI GM mask aligned to the autoradiograph GM mask for each slab. This yielded a 3D non-linear transform that corresponds to T_3 in Fig.6–3.

Although the MRI GM volume was transformed to the coordinate space for each autoradiograph volume, it had to be resampled to the same resolution as the autoradiograph GM volumes at $200 \times 20 \times 200 \mu\text{m}$. This was done so that each coronal section in the transformed MRI GM volume would be aligned to a corresponding section in the autoradiograph GM volume.

6.4.7 Stage 5: 2D refinement of autoradiograph alignment to MRI

Whereas the initial autoradiograph was composed of all the acquired autoradiographs, the ultimate aim of the reconstruction pipeline was to create volumes for each of the 20 measured neurotransmitter receptors. The first step in creating a volume for a specific neurotransmitter receptor was to refine the alignment of the 2D autoradiograph sections to the transformed MRI GM volume. Coronal sections of the autoradiograph GM volumes for a given receptor were non-linearly aligned in 2D to corresponding coronal sections in the transformed MRI GM volume. The result of this processing stage was therefore to find transformations, for each slab, that mapped the autoradiographs for a single receptor to the donor's MRI in autoradiograph space. These transforms correspond to T_4 in Fig.6-3. ANTs was used to calculate these transformations [86] with the parameters listed in Table.6-5.

6.4.8 Stage 6: Interpolation of missing autoradiographs

2D alignment of MRI sections to estimate morphology of missing autoradiograph ($S_{6.1}$)

Autoradiographs for a specific neurotransmitter receptor were acquired with a minimum gap of $400\mu\text{m}$ between acquired slices. This means that ligand binding densities had to be estimated for positions between autoradiographs acquired for a particular receptor type. Estimates of missing autoradiographs were generated based on the neighbouring autoradiographs in the posterior and anterior direction along the coronal axis. By missing autoradiographs, we mean not only sections where no autoradiograph was acquired at all, but also autoradiographs that were not acquired for the particular receptor being reconstructed into a 3D volume.

While the receptor distribution of the missing autoradiograph is unknown, its morphology is characterized—if at a coarser spatial resolution—by the MRI. The neighbouring autoradiographs were used to estimate missing autoradiographs by warping them so that their morphology would resemble that of MRI at the coronal position of the missing section. This was done using the composition of two transformations (see Fig.6–11). The first transformation was described in the previous section, S_5 , and is the mapping of a coronal section from the the autoradiograph GM volume to the corresponding MRI section, i.e., T_4 in Fig.6–3. The second transformation was obtained by using a 2D non-linear transformation from sections in the MRI GM volume corresponding to the acquired autoradiographs to adjacent sections in the MRI GM volume where the autoradiograph was missing (transformation parameters listed in Table.6–5). This second transformation corresponds to T_5 in Fig.6–3.

Distance-weighted interpolation of missing autoradiograph ($S_{6.2}$)

Once the anterior and posterior autoradiographs were warped to the coronal section in the MRI GM volume corresponding to the missing section, these two images could be averaged to arrive at an estimate of the missing autoradiograph. The averaging was done so that missing sections closer to the anterior or posterior autoradiograph would be more heavily weighted towards the receptor distribution represented in that autoradiograph. A linear distance-weighted interpolation method was used to estimate missing autoradiographs based on neighbouring autoradiographs (see Fig.6–11 for details).

A reconstructed receptor volume could therefore be generated by applying a series of 2D transformations to the cropped autoradiographs and using distance-weighted interpolation for those sections for which no autoradiographs were acquired for a given receptor. For coronal sections in the reconstructed receptor volume where an autoradiograph was acquired, the cropped autoradiographs were transformed using the composite transform of $T_4 \times T_1$. In effect this meant applying the initial 2D rigid transform that brought the autoradiograph into initial alignment, T_1 , and the 2D non-linear transformation to align it to the MRI volume in autoradiograph space, T_4 .

For coronal sections where autoradiographs for a given receptor type were not acquired, the neighbouring autoradiographs were transformed by the composite transform of $T_5 \times T_4 \times T_1$. The additional transform, T_5 , served to transform the cropped autoradiograph so that it would match the morphology of the MRI at a section where no autoradiograph for the given receptor was acquired. Distance-weighted interpolation was then used to average neighbouring autoradiographs in the posterior and anterior direction.

Receptor volumes in autoradiograph space could therefore be created by applying composite transformations directly to the cropped autoradiographs, thus limiting the amount of manipulations applied to the images.

6.4.9 Stage 7: Transformation of receptor volumes to MRI coordinate space

The pipeline for 3D reconstruction operates on the basis of individual slabs. The last step of the pipeline was to combine the receptor volumes for each slab into a

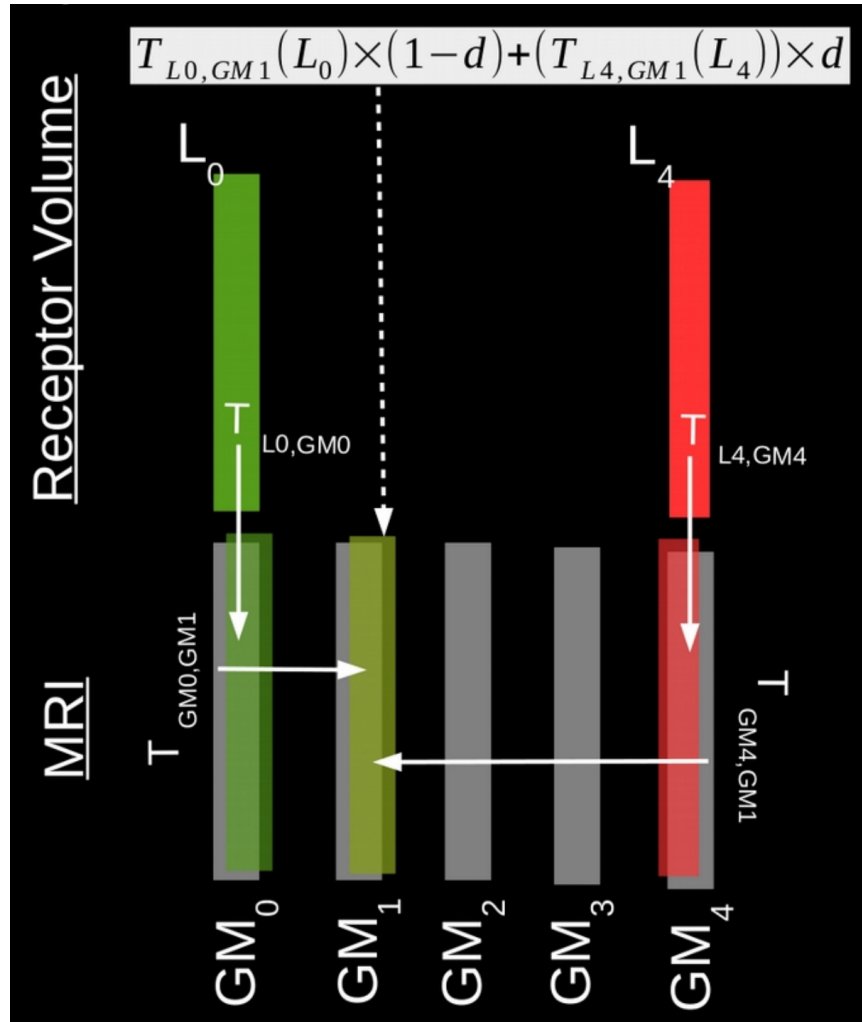


Figure 6–11: Green bars L_0 and L_4 represent autoradiographs at positions 0 and 4. Grey bars represent coronally sliced GM mask at positions 0-4. Autoradiographs were non-linearly aligned to the corresponding MRI sections. The MRI sections at positions with corresponding autoradiographs were then non-linearly aligned in 2D to the positions with no autoradiographs. These two transformations were concatenated to directly transform the autoradiograph to a new position. The estimated autoradiograph at position 1 was thus calculated by applying transform T_{L_0, GM_1} to L_0 and applying transformation T_{L_4, GM_1} to L_4 . The two transformed autoradiographs from the anterior and posterior direction were averaged using linear, distance-weighted interpolation.

Table 6–5: ANTs parameters used to perform a) non-linear alignment between the autoradiograph GM slab volume and the MRI GM volume and b) non-linear alignment between MRI GM sections.

Transform	Iterations	Smoothing	Downsample Factor	Metric
SyN	2100	3	6	Global CC
SyN	1200	2	4	Global CC
SyN	1200	1	2	Global CC
SyN	10	0	1	Global CC

common coordinate space. This was done by transforming the receptor volumes for each slab to the donor’s MRI in MNI space[4]. This was accomplished by applying the inverse of the transformation from the MRI GM mask to the autoradiograph GM volume for each slab, respectively (this corresponds to the inverse of T_3 Fig.6–3). All slabs were therefore mapped onto the donor MRI and were summed together to create a single volume for a given neurotransmitter receptor type.

The autoradiograph volume was downsampled to 500 μm and then was transformed into the MNI coordinate space [4] by inverting the 3D transformation of the donor’s MRI GM volume to the autoradiograph GM volume. The image was downsampled before transformation because the amount of RAM required to transform the receptor volumes was in excess of the resources available. Furthermore, a higher resolution receptor volume was not needed for the subsequent analyses described below.

6.4.10 Experiments

Validation of distance-weighted interpolation

To validate the interpolation scheme presented here, we applied the interpolation method to a synthetically generated receptor volume. An algorithm for calculating equivolumetric surfaces [220] was applied to the donor's MRI GM subdividing it into 6 layers. Values from 0 to 1 were assigned to the voxels based on the distance from the pial surface to the white matter. In the equivolumetric GM layer volume, the same sections for which $GABAA_{Benz.}$ autoradiographs were acquired were used to interpolate the missing $GABAA_{Benz.}$ sections. The interpolated values were compared to the true values in the equivolumetric GM layer volume by dividing the former by the latter.

Monte-Carlo PET Simulation

The first slab, covering the prefrontal cortex, of the reconstructed $GABAA_{Benz.}$ autoradiograph volume was used for Monte-Carlo PET simulation with GATE [29]. The source radioactivity distribution for performing PET simulation was based on the receptor binding densities at each voxel of the $GABAA_{Benz.}$. The binding densities in the autoradiograph volume were taken to represent radioactivity concentrations in Bq. GATE, however, requires that the source radioactivity distribution be defined with an integer valued volume, where each integer represents a region with a uniform radioactivity concentration. These regions of homogenous radioactivity do not need to be contiguous. To accommodate the input requirements of GATE, the autoradiograph volume was subdivided into 100 regions using the K-means algorithm

[219]. The mean regional value for each of these 100 regions was calculated from the $GABAA_{Benz.}$ autoradiograph volume. The input to GATE therefore consisted of the autoradiograph volume classified into 100 discrete regions and a text file that specifies the average radioactivity concentration (Bq) in each of these regions.

An attenuation map was generated from the donor's MRI by using a brain mask derived using CIVET [217] and used a skull mask produced by the FSL Brain Extraction Tool (BET) [221].

The scanner modelled in the simulation was the CTI-Siemens ECAT HRRT [91] and the total simulation time was 30 s.

The results of the simulation were not reconstructed according to traditional PET reconstruction algorithms. Instead the locations of the annihilation events were binned into a grid of 1x1x1 mm voxels. PET does not directly measure the location of an annihilation but rather the line of response (LOR) from two photons that are detected by the scanner within a given time window. To accurately reflect this fact in the binning, the locations of the annihilation events were projected onto the nearest point on their LOR. For random coincidences, where unrelated annihilation events are detected by the scanner, the mean of the locations of the two annihilation events was calculated and projected onto the LOR.

The simulated PET images were compared to the input radioactivity distribution by calculating the local-cross correlation between the two volumes. The window for the local cross-correlation was 5x5x5 voxels and Kendall's tau was used to calculate the correlation [222].

6.5 Results

The initial reconstruction between the cropped autoradiographs showed that the alignment algorithm was able to restore the gross anatomy of the donor's brain (Fig.6–12). Based on visual inspection, a major improvement in alignment could be observed between the first and second iterations and overall four iterations were sufficient for a satisfactory convergence. By the fourth iteration of the alignment algorithm, sulci and gyri were clearly visible. However, some sulci appear fused together. This also illustrates that a generic alignment algorithm like ANTs, with a mutual information cost function, was able to perform accurate alignment between autoradiographs of different receptors.

The algorithm to align the autoradiograph slabs to the MRI appeared to generally place the slabs at the correct locations (Fig.6–13). There were substantial gaps between these aligned slabs, particularly between the 4th and 5th slab from the anterior pole.

The interpolation of coronal sections where no $GABAA_{Benz.}$ autoradiographs were acquired is shown in Fig.6–14. The interpolation resulted in continuous distributions of synthetic neurotransmitter receptor densities across the cortical GM.

The interpolation scheme provided accurate estimates on the equivolumetric volume. As can be seen in Fig.6–15, the interpolated volume closely matched the synthetic volume. This was confirmed quantitatively in the error volume in Fig.6–15 which showed similar error magnitudes across the coronal axis. The average error in each coronal section was calculated and is shown in Fig.6–16. Error magnitudes

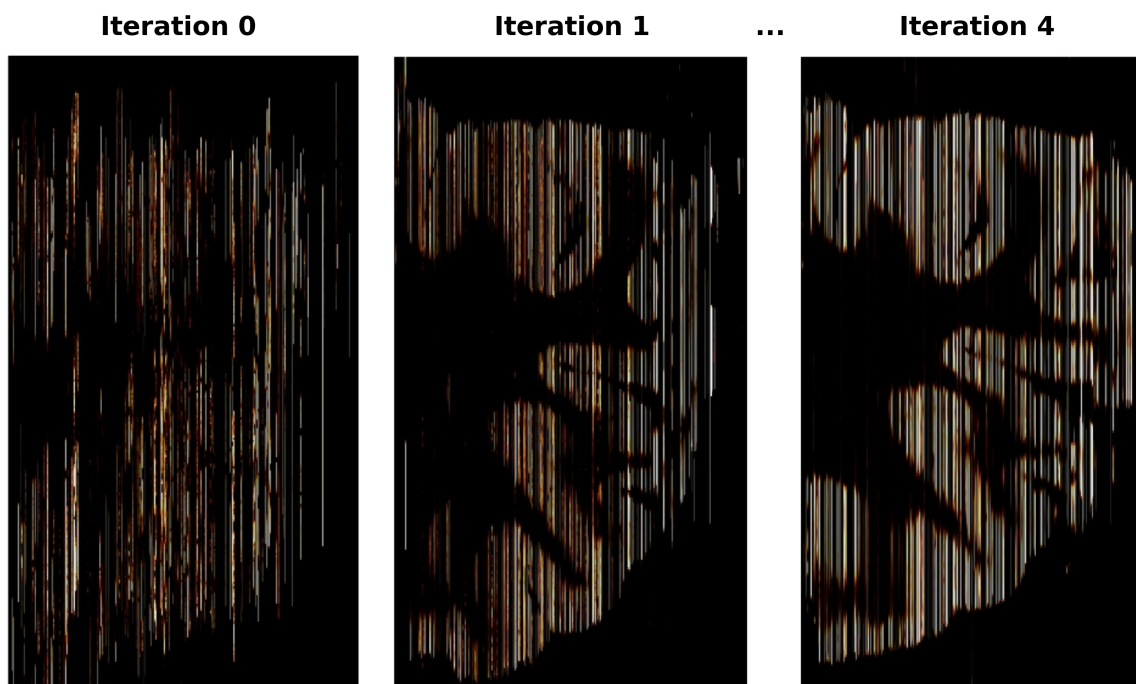


Figure 6–12: At iteration 0 the autoradiographs were stacked without performing any alignment. Gross anatomic structures can be seen after a single iteration of rigid alignment between sections, with smaller refinements in subsequent iterations.

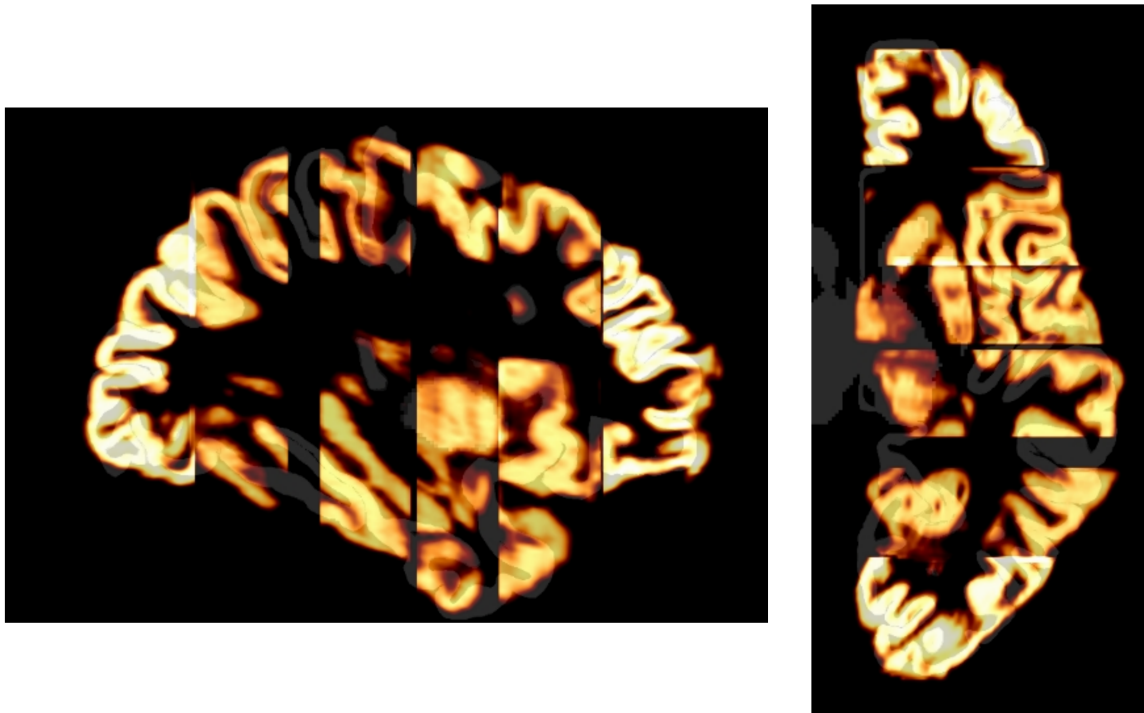


Figure 6–13: GM volumes extracted from autoradiograph slabs were aligned to the donor's MRI GM volume using affine transformations. The alignment appeared accurate, but required further non-linear deformation to improve the alignment.

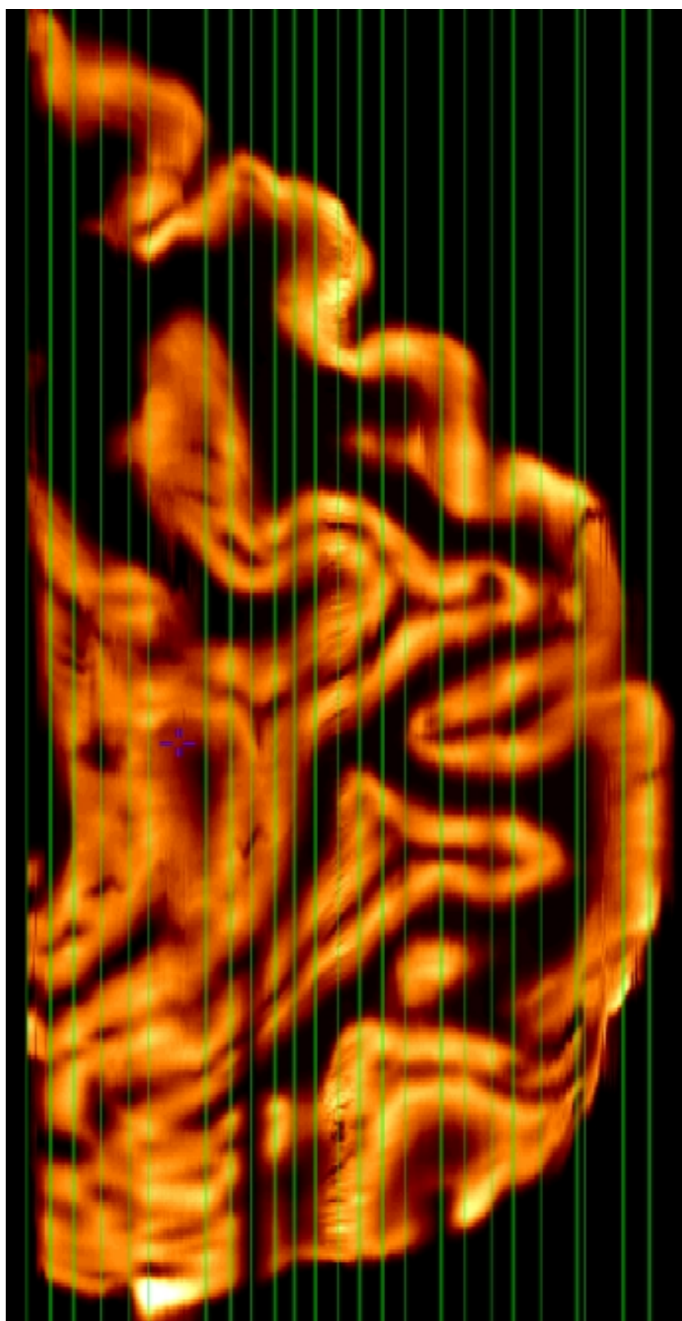


Figure 6-14: An interpolation scheme for estimating missing autoradiographs was used to reconstruct a continuous 3D representation of $GABAA_{Benz.}$ receptor density. The green lines indicate the coronal sections where autoradiographs representing $GABAA_{Benz.}$ receptor density were acquired. The spaces in between the green lines represent the estimated $GABAA_{Benz.}$ receptor density.

were generally between 0-6%, except for one particularly large gap between acquired sections where the error level reached 10%.

The results of the reconstruction pipeline are shown in Fig.6–17 for the first slab and for the entire hemisphere Fig.6–18. The reconstruction resulted in a 3D image of $GABAA_{Benz.}$ binding densities in the brain that closely resembles the donor’s MRI. While the correspondence between the reconstructed autoradiograph volume and the MRI was generally good, the temporal lobe in Fig.6–18 showed that the alignment was not perfect.

During the GATE simulation, a total of 10,153,400 counts were acquired during the 30 s simulation. The simulated PET image in Fig.6–19 showed that the simulated PET recovered some degree of the laminar neurotransmitter receptor distribution seen in the source radioactivity distribution. There was a clear difference in the intensity of the simulated PET image more dorsally due to non-uniformity artefacts.

The local correlation between the reconstructed autoradiograph volume and the simulated PET image indicates that the spatial accuracy of PET was not uniform throughout the cortex Fig.6–20. The correlation between the two images tended to be lower (0.5-0.65) in the abutting cortex in sulcal folds and was higher towards the edge of the cortex (0.75-0.83). Averaging the local correlation across the cortex gave a correlation of 0.71 ± 0.89 .

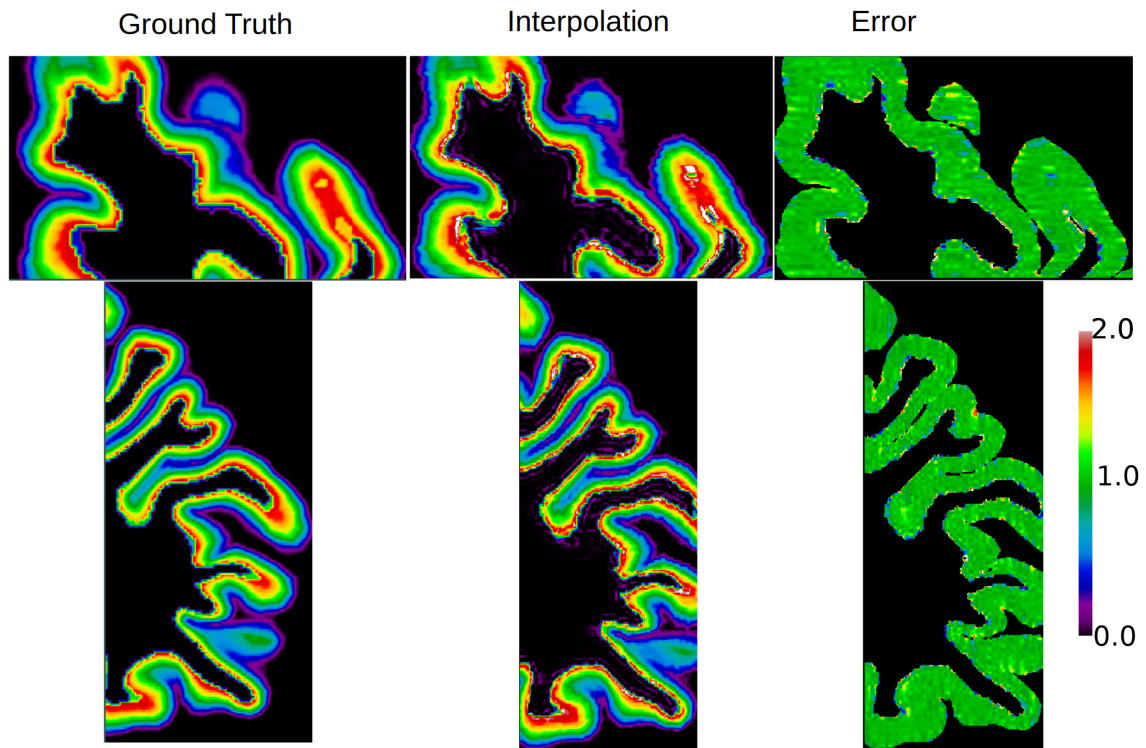


Figure 6–15: The equivolumetric GM volume has a discrete label for each layer of the cortical GM. The middle image shows the result of interpolating the equivolumetric GM volume using only the coronal sections for which $GABA_{Benz}$ autoradiographs were acquired. Note that the interpolation scheme conserves the laminar distribution of voxel intensities across the cortical surface GM. The error volume was calculated by dividing the interpolated by the true equivolumetric GM volume. Error levels were consistent across the coronal axis.

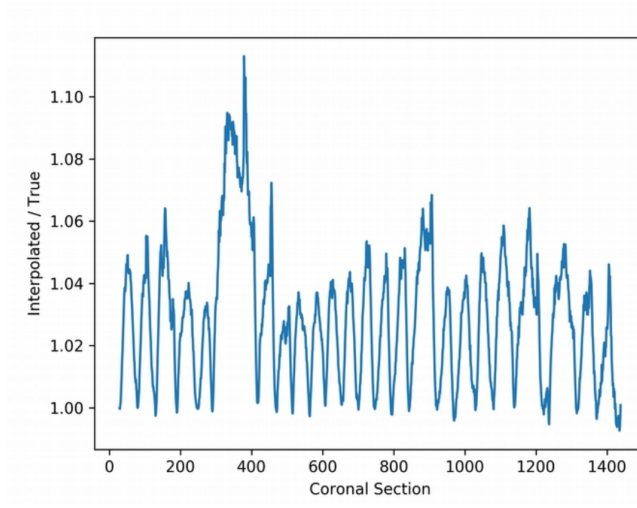


Figure 6–16: The average error in each coronal section shows that the interpolation scheme works well when there was a small gap between acquired sections (0-6%), but increases substantially for larger gaps. The troughs in the error level indicate the positions where autoradiographs were acquired.

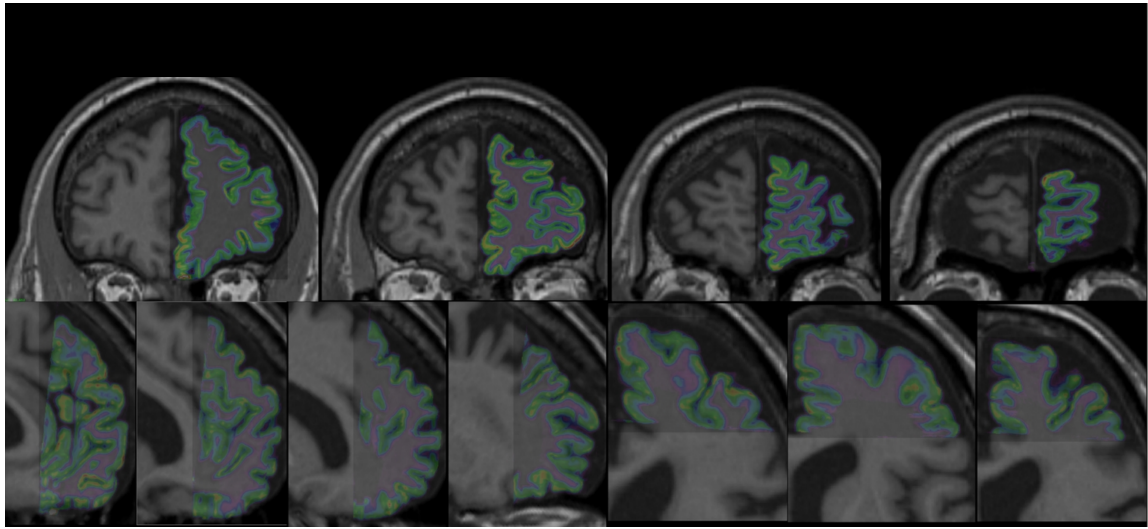


Figure 6–17: The alignment of the reconstructed $GABAA_{Benz.}$ autoradiograph volume in the prefrontal cortex and the donor’s MRI showed that the reconstruction pipeline produces volumes that accurately match the donor’s gross brain anatomy.

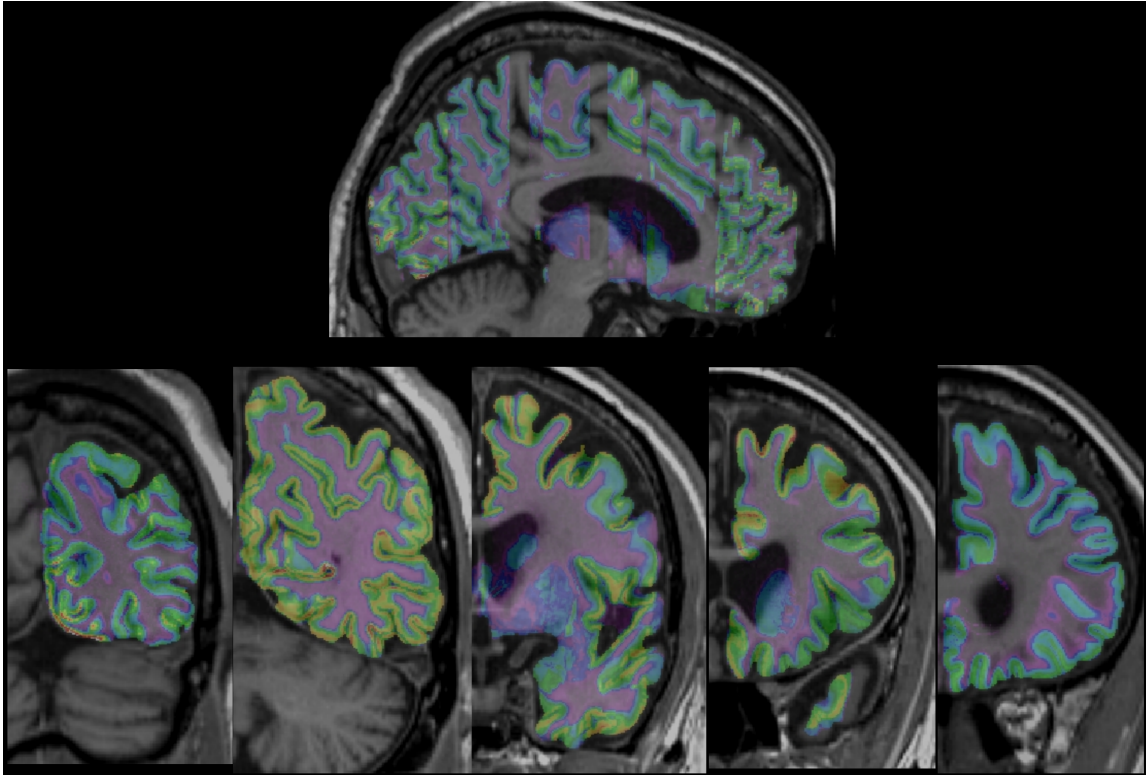


Figure 6-18: Alignment of the reconstructed $GABA_A$ Benz. autoradiograph volume shows good alignment in coronal axis, but illustrates the large gaps between some of the autoradiograph volumes.

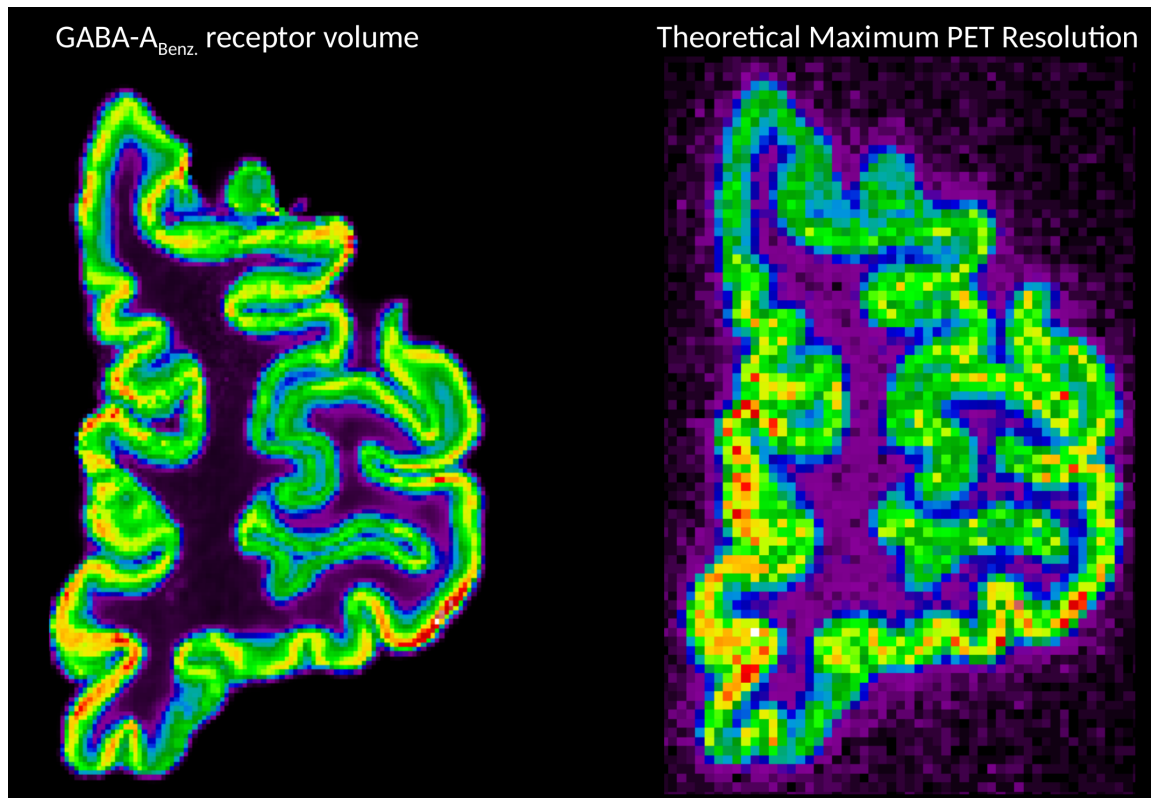


Figure 6-19: The simulated PET image shows that in principle PET can recover laminar patterns in the neurotransmitter receptor distribution. The source radioactivity distribution was defined at $500\mu\text{m}$ and the simulated PET image was sampled at 1mm .

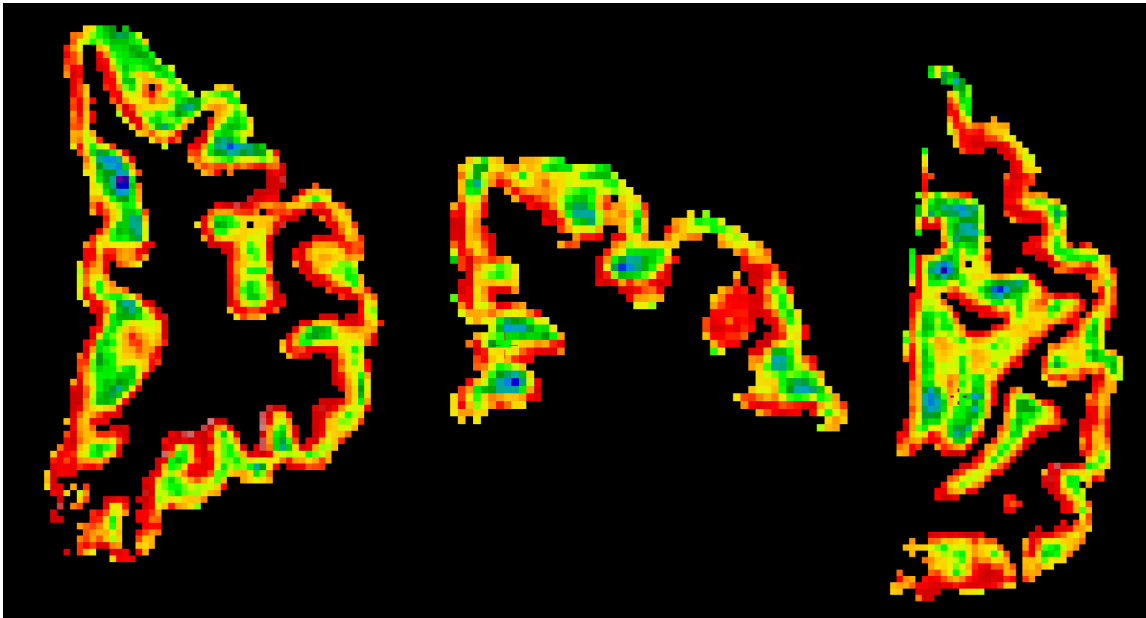


Figure 6–20: Local correlation (Kendall’s Tau) of the reconstructed autoradiograph volume and simulated PET image show that the accuracy of PET varied based on cortical folding and thickness.

6.6 Discussion

We have created a fully-automated pipeline that can successfully reconstruct 3D autoradiographic volumes of ligand binding densities for 20 different neurotransmitter receptors and demonstrated its application for the $GABAA_{Benz.}$ receptor. We then used this reconstructed autoradiograph volume to perform realistic PET simulation. To recapitulate briefly, the pipeline began by preprocessing the data to isolate target brain regions from raw autoradiographs. The preprocessed autoradiographs were aligned to one another using rigid transformations to create an initial 3D autoradiograph volume. Each autoradiograph in the initial reconstruction was then segmented to create an autoradiograph GM volume. A GM volume extracted from the donor's MRI was then non-linearly aligned in 3D to the autoradiograph volume. The 2D sections of the autoradiograph 3D volume were then non-linearly aligned in 2D to the resampled MRI GM volume. Finally, a volume for 1 of the 20 measured neurotransmitter receptors was created using a linear distance-weighted interpolation scheme. A reconstructed slab of $GABAA_{Benz.}$ receptor density was used as the radioactivity distribution for Monte-Carlo PET simulation. The results in Fig.6–18 showed that the pipeline was able to accurately reconstruct gross anatomic features although more work was needed to perfect the reconstruction. The simulated image showed that under ideal conditions, PET shows a strong correlation to the source radioactivity distribution and appeared able to recover some gradients in neurotransmitter receptor density stemming from the laminar distribution of the receptor.

6.6.1 3D reconstruction of 2D autoradiographs

Accuracy of reconstructed $GABA_{Benz.}$ atlas

Visual observations indicate that the reconstruction pipeline can accurately recover the 3D anatomy of the donor’s brain from the 2D autoradiographic sections. This was seen in both coronal sections as well as sagittal sections (see Fig.6–17 6–18). However, the anatomic accuracy was not perfect. In Fig.6–18 subcortical GM structures were overlapping with the ventricles and the temporal lobe was also not perfectly aligned. This imperfect alignment was due to imperfect processing at multiple steps of the pipeline and are addressed in the following sections.

Initial autoradiograph alignment

One particularly important potential source of error in the reconstruction pipeline comes from the inter-autoradiograph alignment algorithm that we developed. Imperfections in the initial reconstruction obscure anatomic landmarks and negatively impact all downstream stages of the pipeline. While the alignment of 2D biological sections, whether from histology or autoradiography, is a problem that has been solved many times for different data sets, these methods were not well adapted for the present data.

A method for creating robust reconstructions from 2D sections was proposed by Cifor et al [207]. They attempted to maximize smoothness of anatomic regions through axial cuts in the reconstructed image to limit the impact of individual misregistrations. However, their approach requires the same anatomic structures to be

present across sections and may not work well with the significant amount of missing sections in the present data set.

Similarly, the network-based approach to image alignment of Pichat et al [208] considered sections to be nodes in a graph and the similarity metric, e.g., mutual information, between two histological sections to be edge length between the sections. For example if the alignment between histological sections i and $i+1$, is poor but the alignment between section $i-1$ and $i+1$ is good, then, instead of transforming section i to section $i+1$ directly, it may be more effective to use the transformation from i to $i-1$ and then from $i-1$ to $i+1$. This is more robust than the method used here because it allows one to circumvent misalignments by considering alternate paths between sections. However, this method is unlikely to work in our context because the similarity metric between pairs of autoradiographs representing different receptor densities may not be directly comparable.

The block-matching alignment scheme of Ourselin et al. [205] was designed to align neighbouring histological sections even in cases where sections have suffered significant damage. Using their method on the current data set may not lead to good alignment because their method uses the cross-correlation between small 2D blocks in adjacent sections. Cross-correlation is not well suited to images with different intensity distributions. A simple solution to make their method more applicable to our data would be to replace cross-correlation with mutual information. The method of Ourselin et al[205] was not used here because, except at the edge of slabs, the sections were largely intact and because ANTs with Mattes mutual information was found to be sufficient for reliable alignment. Nonetheless it may be the case

that a modified block-matching strategy may provide better alignment in the few cases where ANTs was unsuccessful and may constitute a potential avenue for future development.

Another method for robust section alignment was created by Chakraverty et al. [206] for cases where no reference data was available. For a given section, they averaged the distortion fields for the alignment with the adjacent posterior and anterior sections, respectively, and repeated the alignment of all sections over several iterations. While this method does decrease the likelihood of misalignments by repeatedly reinitializing the alignment process, it is best suited to cases where no reference is available and where sections have to be non-linearly warped to one another.

A similar scheme was used by both Malandain et al [212] and Amunts et al [9] to reconstruct histological and autoradiograph volumes in 3D. Generally speaking this scheme iterates between two steps, where first the donor MRI is aligned in 3D to an autoradiograph stack and the autoradiographs are aligned in 2D to the transformed MRI. The difficulty in applying this method to our data is that the warping in the autoradiographs is so large that aligning autoradiographs to their corresponding sections in the MRI volume constitutes a significantly ill-posed problem. That is, there are many potential transformations that can align the autoradiograph section to the corresponding MRI section. For example, one autoradiograph may be better aligned in the dorsal portion of the cortex and poorly aligned in the ventral portion of the cortex, but the opposite may be the case for its neighbour. Thus when, during the development of the reconstruction pipeline, we attempted to implement a 2D linear alignment of all the autoradiographs sections to their corresponding MRI

sections, this led to a worse alignment between the autoradiographs than in the initial reconstruction where autoradiographs were aligned to one another.

Autoradiograph grey matter segmentation

Another important limitation in our reconstruction pipeline was the segmentation of GM in the autoradiographs. Poor segmentations led to a loss of anatomic information, especially when sulcal walls were fused. There were also instances where the entire cortex, including both white matter and GM, in the image was attributed to GM.

The K-means algorithm is a simple algorithm that suffers from significant limitations in the present context. It only takes into account the image intensities and does not include information about the spatial structure of the images. K-means also assumes that intensities follow a spherical distribution around their means. Therefore, while the 3 class K-means algorithm presented here worked well with high-contrast radioligands like flumazenil, it performed poorly with lower contrast radioligands, like pirenzepine.

The limitations of the GM segmentation with K-means poses two problems for autoradiograph reconstruction. The first is that it limits the spatial resolution and anatomic accuracy of the 3D autoradiograph GM volume which, in turn, limits the accuracy of the alignment of the autoradiograph and MRI volume. Improving the autoradiograph segmentation would produce a more anatomically accurate 3D GM volume that would, for example, have more clearly preserved sulci.

A further problem is that because 3 class K-means does not work well consistently for low contrast radioligands, the 2D non-linear alignment of the autoradiograph GM volume to the MRI GM volume in autoradiograph space is likely to be poor. While it is possible to align autoradiographs to corresponding MRI using information theoretic distance metrics, this may require fine-tuning parameters for each neurotransmitter receptor.

The heterogeneity of the imaged receptor distributions and in the acquisition protocol for the autoradiographs makes it difficult to use a single algorithm to segment all of the acquired autoradiographs. A more robust approach would be to use a deep neural network to perform the autoradiograph GM segmentation based on manually drawn labels. While this approach is time-consuming, it would provide a general autoradiograph GM classifier that could potentially be applied to other data sets.

3D alignment of MR to autoradiograph volume

Many reconstruction methods accomplish the alignment of the 2D sections to a reference MRI by iterating between 3D and 2D alignments between the reconstructed and MRI volumes, often through the use of intermediate blockface images [9, 209–212, 214]. While 2D alignments between reconstructed and MRI volumes were used in our pipeline, the initial alignment of these two volumes was performed in 3D. As mentioned above, this was because the particularly significant deformations in the autoradiographs and the lack of blockface images made it difficult to directly align the 2D sections to the MRI volume.

The errors in alignment of the reconstructed autoradiograph volume versus the donor's MRI may be improved by ensuring a better non-linear alignment between the autoradiograph GM slab volume and the MRI GM volume. Besides improving the initial inter-autoradiograph alignment and autoradiograph GM segmentation, another way of improving the overall reconstruction would be to improve the 3D non-linear alignment between the autoradiograph and MRI GM volumes. The fact that the subcortical GM structures in Fig.6–18 appear to be in the correct coronal plane suggests that the affine transformation that grossly aligns the volumes is correct, but that further deformation is needed to align these structures. This is also the case for the temporal lobe because in the raw autoradiographs it appears to be compressed against the frontal and parietal lobes. Increasing the amount of warping of the MRI GM volume when aligning it to the autoradiograph GM volume would therefore likely improve the alignment of the subcortical GM structures. Another way to improve the non-linear alignment may be to use local instead of global cross-correlation as a similarity metric for image alignment because the former is more sensitive to local misalignments.

Interpolation of Missing Sections

The diversity of neurotransmitter receptors that were measured in this dataset also means that there was a gap between acquired neurotransmitter receptors of at least $400\mu\text{m}$. This is a fundamental limitation of the dataset that cannot be improved on with the data at hand. An interpolation algorithm was devised to

provide an estimate of the missing receptor densities based on the nearest available sections.

An important theoretical limitation with the interpolation method presented here is that it assumes that each section for a particular autoradiograph cuts through the cortex orthogonally and therefore accurately represents the laminar distribution of the neurotransmitter receptor. Our distance-weighted interpolation method assumes that a middle section between acquired posterior and anterior sections can be accurately estimated as an average of the two acquired sections. A problem occurs if one, or both, of the acquired sections have been cut at an angle that is not orthogonal to the folding of the cortex(see Fig.6-21 for an illustration of this problem). In that case the acquired section may be missing particular laminae and the laminae may be distorted based on the cutting angle. Misrepresentation of the laminar receptor distribution will then bias the laminar receptor distribution in the interpolated missing section.

This problem could be overcome by using anatomic information from the MRI to constrain the interpolation to within receptor layers and hence avoid contaminating binding densities from different layers of the cortex[223]. This is a major avenue for future work and refinement of the method described here.

In practice tangential sectioning appears to have a modest impact of the interpolated values. The interpolation method was applied to a synthetically generated equivolumetric laminar volume [220]. This showed that the interpolation algorithm was accurate to within 0-6% except when the gap between acquired autoradiographs

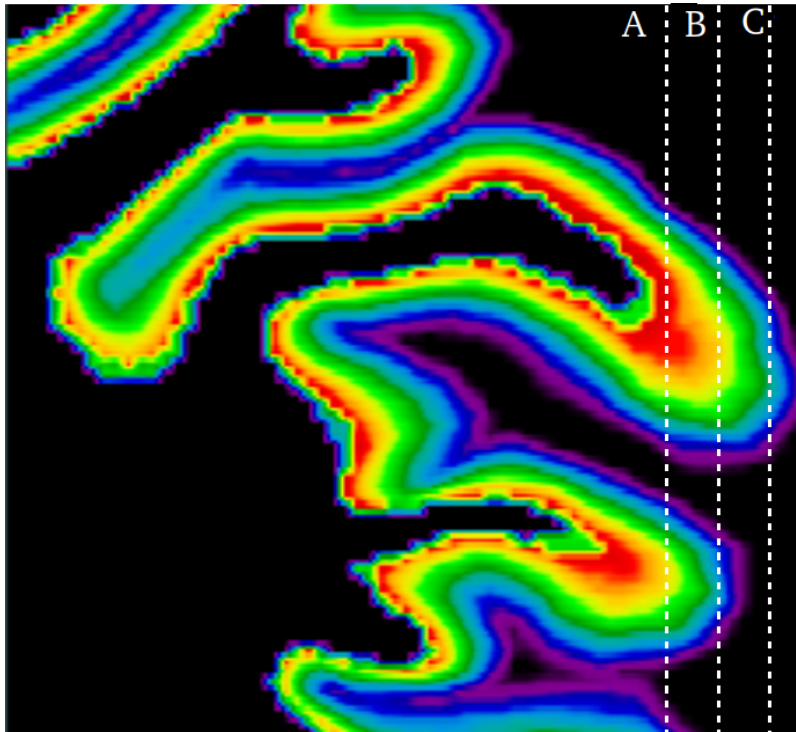


Figure 6-21: Distance-weighted interpolation of a missing autoradiograph section from adjacent sections is biased if the sections are cut tangentially to curvature of cortical surface. Section C is tangential to the cortical surface and does not accurately represent the distribution of layers across the cortical surface. Hence if section B is interpolated based on sections A and C, section C will bias this estimate due to its misrepresentation of the laminar distribution of signal intensity across the surface.

was large. Based on visual inspection of the volume produced using our interpolation method, it is clear that the latter preserves the laminar distribution seen in the equivolumetric laminar volume.

The distance-weighted interpolation scheme assumes that neurotransmitter receptor densities change linearly between the acquired sections and the missing section. This is not strictly biologically valid because there may be sharp boundaries between cytoarchitectonic areas [28] which would be obscured by our interpolation method. It does not appear possible to devise an interpolation method that could reproduce such sharp regional boundaries without additional information.

Another limitation of the work presented here was that the receptor volume was reconstructed on the basis of autoradiographs that had been cropped and downsampled. It is possible that interpolation errors were introduced by this downsampling process. This was done to minimize the computational time of reconstruction. However, in the future the receptor volume can be reconstructed by applying the final transformations produced by the pipeline directly to the raw autoradiographs, producing a receptor volume with voxels of $20 \times 20 \times 20 \mu\text{m}$.

Quantitative accuracy of autoradiography

An important underlying assumption in the creation of atlases of neurotransmitter receptor density based on autoradiography is that post-mortem *in vitro* radioligand binding reflects *in vivo* neuroreceptor distribution. The available evidence suggests that prolonged freezing of brain tissue did not affect receptor binding sites [224–227]. The quantitative accuracy of autoradiography was, however, affected by

the delay elapsed between the donor's time of death and the freezing of the brain. For example, NMDA, GABA, muscarinic M_1 , D2, and 5-HT2 receptor binding sites were stable for up to ~75 hours post-mortem [226, 228–231]. Other neurotransmitter receptor densities increased post-mortem before freezing, e.g., D1 and 5-HT 1A receptor binding sites [230]. Somewhat surprisingly, and most problematically for the present work, the $GABAA_{Benz.}$ receptor binding sites increased by 150% within a 48h post-mortem delay [224].

The brain used in the present study was frozen within 24h post-mortem. It is not clear if the increase in $GABAA_{Benz.}$ receptor binding sites post-mortem is uniform throughout the brain. If the effect is uniform, then the relative distribution of receptor binding sites will be correct and should not substantially impact the reconstructed atlas. However further studies would have to be conducted to determine the precise time course of changes to $GABAA_{Benz.}$ receptor binding sites post-mortem.

6.6.2 Monte-Carlo PET simulation with 3D reconstructed autoradiography

The results of the Monte-Carlo PET simulation showed that PET can in principle be used to image near laminar differences in neurotransmitter receptor densities. This can be observed visually and was measured quantitatively using the local cross-correlation (0.71 ± 0.89).

The spatial accuracy of PET was not uniform throughout the cortex, but varies based on morphology. The spatial variability of PET accuracy was seen in the local cross correlation volume of the simulated PET volume and reconstructed $GABAA_{Benz.}$ receptor density volume. The pattern of cross-correlation in this volume indicated

that PET is less able to recover the distribution of receptors towards the center of the cortex and on abutting sulcal walls. The latter was not surprising because abutting sulcal walls may be physically close in space but can have very different neurotransmitter receptor distributions. Hence PVE in these locations cause cross-contamination of radioactivity concentrations from very different regions.

The spatial pattern of PET accuracy highlights the importance of using source radioactivity distributions that reflect the real distribution of the receptor targeted by the radioligand. Traditional methods for performing PET simulation have typically used large ROI with homogenous radioactivity concentrations [22, 232]. The limitation of this approach is that it does not reflect the complex pattern of neurotransmitter receptor distribution. Moreover, using a source radioactivity distribution based on gross anatomic regions, it would not have been possible to observe the relationship between cortical morphology and PVE. Another approach to PET simulation is to derive a voxel-based radioactivity source distribution from a PET image [233]. This approach is limited in that it can never be used to assess the spatial resolution of PET because it, by definition, uses a radioactivity source that is at PET resolution and cannot represent source radioactivity concentrations below the millimeter scale.

Realism of PET Simulation

The Monte-Carlo simulation with GATE aimed to produce a simulated image that was as similar as possible to the image that would have been obtained if the

donor had been injected with [18-F]-flumazenil and scanned with an actual CTI-Siemens ECAT HRRT. There are important limitations to the realism of the simulated PET image generated in this study. One of the most important limitations is that in practice, there are many potential sources of radioligand binding other than specific binding to the target receptor. Depending on the radioligand, there can be significant non-specific binding, off-target binding, free radioligand in the blood and in the interstitial space. Non-specific binding can be accounted for in the present reconstruction and simulation framework by including the autoradiographs of non-specific binding which were also acquired as a part of the dataset used here.

Patient head movement is also another factor that affects real PET simulation and decreases spatial resolution. GATE allows for movement of the radioactivity source during the simulation and this could be used to model the effect of patient head movement on PET spatial resolution.

Another limitation concerns the proposed method for binning the location of annihilation events into a 3D grid. This binning approach does not include several standard correction algorithms that are implemented during PET reconstruction to improve the accuracy of the measured radioactivity concentration. These include non-uniformity correction, scatter correction, and attenuation correction. The effect of these correction algorithms is not taken into account in our binning method and would be likely to significantly affect that reconstructed simulated image.

The number of counts acquired in this experiment were also relatively low compared to real PET scans. A total 10,153,400 counts were acquired as opposed to 16 billion counts for whole brain simulations of 10 minutes in Ref.[22]. This relatively

low number of counts was chosen because GATE is computationally intensive, which results in long processing times and the number of acquired counts was sufficient to create a representation of the radioactivity source distribution. A lower number of counts will tend to produce a noisy image with poorer resolution and so the relatively low number of counts acquired here will only bias our results in a conservative direction. Nonetheless, in order to produce images that are as similar to real PET scans as possible, more counts should be acquired in future simulations.

The ideal way to validate the effective spatial resolution of PET would be by performing a direct comparison of in vivo PET versus in vitro autoradiography in the same subjects. One such study has been performed but only on 2D autoradiograph sections in the hippocampus for a clinical population [Koeppel1998]. Given that the effective resolution of PET will vary based on the ligand, radioisotope, scanner, and measured region, it is not currently feasible to perform a PET scan and subsequent full brain autoradiographic imaging to evaluate the effect on effective spatial resolution for each of these variables. Not only are the costs to full-brain autoradiography prohibitive, but there are also enormous logistical challenges and ethical concerns to performing a PET scan followed by post-mortem autoradiography in humans.

Future Work

Improving the realism of the PET simulation will be a central aim of future work on using 3D autoradiograph reconstruction for PET simulation. As mentioned in the preceding section, this will include reconstructing the non-specific binding images and adding these to the radioactivity source distribution for GATE. It will also

be important to perform simulations with higher count rates that more accurately reflect the quantities acquired in real PET scans. While it is useful to consider the theoretical maximum spatial resolution of PET, it is also of interest to assess PET resolution after reconstruction with a traditional algorithm, such as ordered-subset expectation maximization (OSEM).

Finally, several of the autoradiographs for other receptor binding sites could be used for PET simulation. The same radioligand is used to image the dopamine D1 receptor in both PET and autoradiography. This makes it particularly straightforward to use for PET simulation as the distribution of radioligand would be similar in both PET and autoradiography. For several other radioligands there are different radioligand for PET and autoradiography that nonetheless bind to the same receptor. These include the receptor binding sites for serotonin $5HT_{1A}$ and $5HT_2$, *nicotinic* $_4\beta_2$, and the AMPA. In these cases it would be necessary to account for differences in non-specific binding between the radioligand used in autoradiography and PET.

6.7 Conclusions

We have created an image processing pipeline for reconstructing 2D autoradiographs into 3D volumes and used one such reconstructed volume to perform Monte-Carlo PET simulation. Using this pipeline it will be possible to create a set of canonical high-resolution, 50 μm atlases of neurotransmitter receptor distribution based on 3 human brains. We have furthermore shown how these atlases can be used to create a new set of realistic simulated PET images. This data set will allow

us to investigate PET spatial resolution and serve as a gold-standard data set for validating PET algorithms for image analysis, reconstruction and correction.

6.8 Contribution of Authors

Thomas Funck: Designed and implemented the algorithms described in this chapter and performed all data analysis. Primary author of chapter.

Nicola Palomero-Gallagher : Acquired data used in this chapter and provided conceptual guidance.

Mona Omidyeganeh : Created an initial version for automated cropping of autoradiographs that provided inspiration for algorithm that was eventually used and which is described here.

Konrad Wagstyl : Created the equivolumetric volume used to validate interpolation scheme. Provided conceptual advice for interpolation scheme.

Claude Lepage : Processed donor MRI with CIVET and provided conceptual advice.

Alexander Thiel : Provided conceptual guidance and edited chapter.

Karl Zilles : Acquired the data used in this chapter.

Alan C. Evans : Provided conceptual guidance.

References

4. Mazziotta, J. *et al.* A probabilistic atlas and reference system for the human brain: International Consortium for Brain Mapping (ICBM). *Philosophical Transactions of the Royal Society B: Biological Sciences* **356**, 1293–1322. ISSN: 0962-8436 (Aug. 2001).
9. Amunts, K. *et al.* BigBrain: an ultrahigh-resolution 3D human brain model. *Science (New York, N.Y.)* **340**, 1472–5. ISSN: 1095-9203 (June 2013).
10. Beliveau, V. *et al.* A high-resolution in vivo atlas of the human brain’s serotonin system. *Journal of Neuroscience* **37**, 120–128. ISSN: 15292401 (Jan. 2017).
12. Wienhard, K. *et al.* The ECAT HRRT: performance and first clinical application of the new high resolution research tomograph. *IEEE Transactions on Nuclear Science* **49**, 104–110. ISSN: 0018-9499 (Feb. 2002).
22. Reilhac, A. *et al.* PET-SORTEO: Validation and development of database of simulated PET volumes. *IEEE Transactions on Nuclear Science* **52**, 1321–1328. ISSN: 00189499 (Oct. 2005).
28. Zilles, K. *et al.* Architectonics of the human cerebral cortex and transmitter receptor fingerprints: Reconciling functional neuroanatomy and neurochemistry. *European Neuropsychopharmacology* **12**, 587–599. ISSN: 0924977X (2002).

29. Jan, S. *et al.* GATE: a simulation toolkit for PET and SPECT. *Physics in Medicine and Biology* **49**, 4543–4561. ISSN: 0031-9155 (2004).
39. Hoffman, E. J., Huang, S. C. & Phelps, M. E. *Quantitation in positron emission computed tomography: 1. Effect of object size.* 1979.
86. Avants, B. B., Epstein, C. L., Grossman, M. & Gee, J. C. Symmetric Diffeomorphic Image Registration with Cross-Correlation: Evaluating Automated Labeling of Elderly and Neurodegenerative Brain. *Medical image analysis* **12**, 26. ISSN: 1361-8423 (Feb. 2008).
91. Bataille, F., Comtat, C., Jan, S. & Trebossen, R. *Monte Carlo Simulation for the ECAT HRRT using GATE in IEEE Symposium Conference Record Nuclear Science 2004.* **4** (IEEE, 2004), 2570–2574. ISBN: 0-7803-8700-7. doi:10.1109/NSSMIC.2004.1462778. <http://ieeexplore.ieee.org/lpdocs/epic03/wrapper.htm?arnumber=1462778>.
121. Funk, T., Paquette, C., Evans, A. & Thiel, A. Surface-based partial-volume correction for high-resolution PET. *NeuroImage* **102**, 674–87. ISSN: 1095-9572 (Nov. 2014).
189. Toga, A. W., Thompson, P. M., Mori, S., Amunts, K. & Zilles, K. *Towards multimodal atlases of the human brain* Dec. 2006. doi:10.1038/nrn2012. <http://www.nature.com/articles/nrn2012>.
190. Olesen, O. *et al.* *Spatial resolution of the HRRT PET scanner using 3D-OSEM PSF reconstruction in 2009 IEEE Nuclear Science Symposium Conference Record (NSS/MIC)* (IEEE, Oct. 2009), 3789–3790. ISBN: 978-1-4244-3961-4.

- doi:10.1109/NSSMIC.2009.5401892. <http://ieeexplore.ieee.org/lpdocs/epic03/wrapper.htm?arnumber=5401892>.
191. Dubois, A., Dauguet, J. & Delzescaux, T. in *Small Animal Imaging: Basics and Practical Guide* 317–346 (Springer Berlin Heidelberg, Berlin, Heidelberg, 2011). ISBN: 9783642129445. doi:10.1007/978-3-642-12945-2_23. http://link.springer.com/10.1007/978-3-642-12945-2%7B%5C_%7D23.
 192. Pichat, J., Iglesias, J. E., Yousry, T., Ourselin, S. & Modat, M. A Survey of Methods for 3D Histology Reconstruction. *Medical Image Analysis* **46**, 73–105. ISSN: 13618415 (2018).
 193. Julien Dauguet. Three-dimensional histological imaging of primate brain and correlation with in vivo medical device images. *Revue de primatologie*. ISSN: 2077-3757. doi:10.4000/primatologie.546. <http://journals.openedition.org/primatologie/546> (Sept. 2010).
 194. Toga, A. W. & Arnica, T. L. Image analysis of brain physiology. *IEEE Computer Graphics and Applications* **5**, 20–25. ISSN: 02721716 (1985).
 195. Toga, A. W., Santori, E. M. & Samaie, M. Regional distribution of flunitrazepam binding constants: Visualizing K(d) and B(max) by digital image analysis. *Journal of Neuroscience* **6**, 2747–2756. ISSN: 02706474 (Sept. 1986).
 196. Toga, A. W. & Arnica-Sulze, T. L. Digital image reconstruction for the study of brain structure and function. *Journal of Neuroscience Methods* **20**, 7–21. ISSN: 01650270 (May 1987).

197. Kim, B., Boes, J. L., Frey, K. A. & Meyer, C. R. Mutual information for automated unwarping of rat brain autoradiographs. *NeuroImage* **5**, 31–40. ISSN: 10538119 (1997).
198. Gangolli, M. *et al.* Quantitative validation of a nonlinear histology-MRI coregistration method using generalized Q-sampling imaging in complex human cortical white matter. *NeuroImage* **153**, 152–167. ISSN: 10959572 (June 2017).
199. Hibbard, L. S. & Hawkins, R. A. Three-dimensional reconstruction of metabolic data from quantitative autoradiography of rat brain. *American Journal of Physiology - Endocrinology and Metabolism* **10**, E412–9. ISSN: 01931849 (Sept. 1984).
200. Hibbard, L. S. & Hawkins, R. A. Objective image alignment for three-dimensional reconstruction of digital autoradiograms. *Journal of Neuroscience Methods* **26**, 55–74. ISSN: 01650270 (Nov. 1988).
201. Toga, A. W. & Banerjee, P. K. Registration revisited. *Journal of Neuroscience Methods* **48**, 1–13. ISSN: 0165-0270 (June 1993).
202. Andreasen, A., Drewes, A. M., Assentoft, J. E. & Larsen, N. E. Computer-assisted alignment of standard serial sections without use of artificial landmarks. A practical approach to the utilization of incomplete information in 3-D reconstruction of the hippocampal region. *Journal of Neuroscience Methods* **45**, 199–207. ISSN: 01650270 (Dec. 1992).
203. Zhao, W., Young, T. Y. & Ginsberg, M. D. Registration and Three-Dimensional Reconstruction of Autoradiographic Images by the Disparity Analysis Method. *IEEE Transactions on Medical Imaging* **12**, 782–791. ISSN: 1558254X (1993).

204. Iglesias, J. E. *et al.* Joint registration and synthesis using a probabilistic model for alignment of MRI and histological sections. *Medical Image Analysis* **50**, 127–144. ISSN: 13618423 (Sept. 2018).
205. Ourselin, S., Roche, A., Subsol, G., Pennec, X. & Ayache, N. Reconstructing a 3D structure from serial histological sections. *Image and Vision Computing* **19**, 25–31. ISSN: 02628856 (Jan. 2001).
206. Chakravarty, M. M., Bertrand, G., Hodge, C. P., Sadikot, A. F. & Collins, D. L. The creation of a brain atlas for image guided neurosurgery using serial histological data. *NeuroImage* **30**, 359–376. ISSN: 10538119 (Apr. 2006).
207. Cifor, A., Bai, L. & Pitiot, A. Smoothness-guided 3-D reconstruction of 2-D histological images. *NeuroImage* **56**, 197–211. ISSN: 10538119 (May 2011).
208. Pichat, J., Modat, M., Yousry, T. & Ourselin, S. *A multi-path approach to histology volume reconstruction* in *2015 IEEE 12th International Symposium on Biomedical Imaging (ISBI)* (IEEE, Apr. 2015), 1280–1283. ISBN: 978-1-4799-2374-8. doi:10.1109/ISBI.2015.7164108. <http://ieeexplore.ieee.org/document/7164108/>.
209. Schormann, T., Dabringhaus, A. & Zilles, K. Statistics of Deformations in Histology and Application to Improved Alignment with MRI. *IEEE Transactions on Medical Imaging* **14**, 25–35. ISSN: 1558254X (Mar. 1995).
210. Dauguet, J. *et al.* Three-dimensional reconstruction of stained histological slices and 3D non-linear registration with in-vivo MRI for whole baboon brain. *Journal of Neuroscience Methods* **164**, 191–204. ISSN: 01650270 (Aug. 2007).

211. Schubert, N. *et al.* 3D reconstructed cyto-, muscarinic M2 receptor, and fiber architecture of the rat brain registered to the waxholm space atlas. *Frontiers in Neuroanatomy* **10**, 51. ISSN: 16625129 (May 2016).
212. Malandain, G., Bardinet, É., Nelissen, K. & Vanduffel, W. Fusion of autoradiographs with an MR volume using 2-D and 3-D linear transformations. *NeuroImage* **23**, 111–127. ISSN: 10538119 (Sept. 2004).
213. Yang, Z., Richards, K., Kurniawan, N. D., Petrou, S. & Reutens, D. C. MRI-guided volume reconstruction of mouse brain from histological sections. *Journal of Neuroscience Methods* **211**, 210–217. ISSN: 01650270 (Nov. 2012).
214. Iglesias, J. E. *et al.* Joint registration and synthesis using a probabilistic model for alignment of MRI and histological sections. *coRR* **abs/1801.0**. ISSN: 13618423. doi:10.1016/j.media.2018.09.002. arXiv: 1801.05284. <http://arxiv.org/abs/1801.05284> (Jan. 2018).
215. Ronneberger, O., Fischer, P. & Brox, T. U-net: Convolutional networks for biomedical image segmentation. *Lecture Notes in Computer Science (including subseries Lecture Notes in Artificial Intelligence and Lecture Notes in Bioinformatics)* **9351**, 234–241. ISSN: 16113349 (May 2015).
216. Otsu, N. Threshold Selection Method From Gray-Level Histograms. *IEEE Trans Syst Man Cybern* **SMC-9**, 62–66. ISSN: 00189472 (Jan. 1979).
217. Et al. Ad-Dab’bagh. *The CIVET image-processing environment: A Neuroimaging, fully automated comprehensive pipeline for anatomical Research* in *Proceedings of the 12th Annual Meeting of the Organization for Human Brain Mapping* (ed Corbetta) (Neuroimage, Florence, 2006).

218. Collins, D. L., Holmes, C. J., Peters, T. M. & Evans, A. C. Automatic 3-D model-based neuroanatomical segmentation. *Human Brain Mapping* **3**, 190–208. ISSN: 10659471 (Jan. 1995).
219. Lloyd, S. P. Least Squares Quantization in PCM. *IEEE Transactions on Information Theory* **28**, 129–137. ISSN: 15579654 (Mar. 1982).
220. Wagstyl, K., Paquola, C., Bethlehem, R., Evans, A. C. & Huth, A. *Equivolumetric layering for mesh surfaces* Oct. 2018. doi:10.5281/zenodo.1442584. <https://zenodo.org/record/1442584%7B%5C#%7D.XbxZbEX7SgQ%20https://doi.org/10.5281/zenodo.1442584>.
221. Jenkinson, M., Pechaud, M. & Smith, S. *BET2: MR-based estimation of brain, skull and scalp surfaces* in *Eleventh Annual Meeting of the Organization for Human Brain Mapping*, . (2005).
222. Kendall, M. G. A New Measure of Rank Correlation. *Biometrika* **30**, 81. ISSN: 00063444 (June 1938).
223. Wagstyl, K. *et al.* Mapping cortical laminar structure in the 3D bigbrain. *Cerebral Cortex* **28**, 2551–2562. ISSN: 14602199 (July 2018).
224. Whitehouse, P. J., Lynch, D. & Kuhar, M. J. Effects of Postmortem Delay and Temperature on Neurotransmitter Receptor Binding in a Rat Model of the Human Autopsy Process. *Journal of Neurochemistry* **43**, 553–559. ISSN: 14714159 (Aug. 1984).
225. Rodríguez-Puertas, R., Pascual, J. & Pazos, A. Effects of freezing storage time on the density of muscarinic receptors in the human postmortem brain: An

- autoradiographic study in control and Alzheimer's disease brain tissues. *Brain Research* **728**, 65–71. ISSN: 00068993 (July 1996).
226. Lloyd, K. G. & Dreksler, S. An analysis of [3H]gamma-aminobutyric acid (GABA) binding in the human brain. *Brain Research* **163**, 77–87. ISSN: 00068993 (Mar. 1979).
227. Faull, K. F. *et al.* Influence of freezer storage time on cerebral biogenic amine and metabolite concentrations and receptor ligand binding characteristics. *Brain Research* **450**, 225–230. ISSN: 00068993 (May 1988).
228. Kornhuber, J., Retz, W., Riederer, P., Heinsen, H. & Fritze, J. Effect of antemortem and postmortem factors on [3H]glutamate binding in the human brain. *Neuroscience Letters* **93**, 312–317. ISSN: 03043940 (Nov. 1988).
229. Burke, R. E. & Greenbaum, D. Effect of Postmortem Factors on Muscarinic Receptor Subtypes in Rat Brain. *Journal of Neurochemistry* **49**, 592–596. ISSN: 14714159 (Aug. 1987).
230. Kontur, P. J., Al-Tikriti, M., Innis, R. B. & Roth, R. H. Postmortem Stability of Monoamines, Their Metabolites, and Receptor Binding in Rat Brain Regions. *Journal of Neurochemistry* **62**, 282–290. ISSN: 14714159 (June 1994).
231. Gross-Isseroff, R., Salama, D., Israeli, M. & Biegon, A. Autoradiographic analysis of age-dependent changes in serotonin 5-HT₂ receptors of the human brain postmortem. *Brain Research* **519**, 223–227. ISSN: 00068993 (June 1990).
232. Gaudin, E. *et al.* Performance Simulation of an Ultrahigh Resolution Brain PET Scanner Using 1.2-mm Pixel Detectors. *IEEE Transactions on Radiation and Plasma Medical Sciences* **3**, 334–342. ISSN: 2469-7311 (May 2019).

233. Veronese, M. *et al.* *NRM2018 PET Grand Challenge dataset* 2018. doi:10.18112/openneuro.ds001705.v1.0.0. <https://openneuro.org/datasets/ds001705/versions/1.0.0>.

CHAPTER 7

Discussion

7.1 Discussion

Neurotransmitter receptor mapping can be performed in vivo with PET and post-mortem with receptor autoradiography. While autoradiography has the advantage of producing images at comparatively high resolution, $50 \mu\text{m}$, it is an expensive procedure and can only be performed post-mortem. Large scale neurotransmitter receptor mapping will therefore have to depend primarily on PET, but this requires overcoming important obstacles: PET spatial resolution and standardized PET processing software.

PET spatial resolution is a problem because it is not certain at exactly what scale PET can accurately measure receptor densities. While PVC algorithms may be able to increase PET spatial resolution, it is not clear exactly how reliable they are. In Chapter 3 we investigated neurotransmitter receptor mapping with PET in a clinical context. This experiment showed that PET can detect changes in $GABAA_{Benz.}$ receptor density, which serves as a proxy marker for neuronal density, at a spatial scale of 3 mm. An algorithm was also used to enhance the spatial resolution of PET and was found to lead to a larger measured change in $GABA_{Benz.}$ receptor density. The fact that a larger effect size of neuronal loss was larger with resolution

enhancement suggests that algorithms of this kind are effective in practice and can increase PET spatial resolution.

The fundamental limitation of practical investigation into PET resolution conducted in Chapter 3 is that the true $GABAA_{Benz.}$ receptor distribution is unknown. It is therefore impossible to determine with certitude the true spatial accuracy of PET and to assess exactly how much resolution enhancement algorithms can potentially improve spatial resolution. To address this limitation, we sought to use Monte-Carlo PET simulation as described in Chapter 6.

Neurotransmitter receptor atlases should be composed of enough subjects to capture the variability in receptor density in the target population. Existing brain atlases of neuroanatomy and serotonin neurotransmitter receptor densities, based on MRI and PET respectively, are composed of hundreds of individual scans [4, 10]. This suggests that continued neurotransmitter receptor mapping with PET will require hundreds of brain scans, possibly from multiple sites. Large-scale image processing with PET is difficult to perform reliably because it is susceptible to small but significant artefacts. Small differences in software implementation can also lead to different results [234].

A standard and open PET software package would be of great help to creating canonical neurotransmitter receptor atlases with PET. In Chapter 4 we presented a novel open-source software package for PET image analysis called APPIAN. This software package is freely available and can be easily extended to meet the needs of the PET research community. As a part of this software package, we sought to address the problem of processing error detection in automated PET analysis by

incorporating a novel algorithm for automated QC algorithm (discussed in Chapter 5). We used computational simulation to test the ability of this algorithm to detect the most common type of error in PET image analysis. Our results showed that this method could detect moderate to large errors in PET to MRI alignment.

An important assumption in our development of APPIAN was that PVC could in principle improve the resolution of PET and therefore constitutes a key processing step in PET image analysis. However, even if this may apply to analysis of individual PET scans, the role of PVC for improving spatial resolution of atlases derived from multiple PET images from different subjects onto a common template space remains to be demonstrated. While blurring induced by inter-subject averaging is no doubt an important factor, it would nonetheless be preferable to combine PET images at the highest resolution possible to limit the extent of this effect. An alternate approach to defining atlases on a single stereotaxic template has been to combine parcellations defined on a database of individual MRIs onto a target MRI [235]. Hence, instead of defining a unified PET atlas on a template brain, it may be preferable to warp PET images in a hypothetical atlas database onto individual target brains. While there are advantages to both approaches to building atlases, in both cases using PVC could improve the spatial resolution of PET atlases—assuming that PVC can be shown to be accurate and reliable.

APPIAN is currently publicly available. Our processing algorithms, implemented in APPIAN, have been used by others to measure neuronal density changes in patients with chronic pain [236, 237] and APPIAN is currently being used by PET researchers at several international sites. The main challenge with such a software

package is to make it more user-friendly for non-technical users and to ensure that it works reliably. To this end we are in the process of designing a new graphical user interface for APPIAN. We are also implementing automatic validation of the software using the simulated PET data released by Veronese et al.[233]. This will make it possible to compare the images produced by APPIAN to an objective benchmark and ensure that future changes to the code do not corrupt the outputs of the pipeline.

Additionally, APPIAN contains all the necessary steps to create new PET atlases in the manner of Beliveau et al [10]. We will therefore create a similar atlas based on $GABAA_{Benz.}$ receptor distribution using flumazenil PET.

Finally in Chapter 6 we presented an image processing pipeline for creating a high resolution 3D neurotransmitter receptor atlas based on 2D autoradiographs. The analyses using these autoradiographs were originally published by Zilles et al [28], but several technical obstacles and image artefacts prevented this data from being reconstructed into 3D until our work. Indeed, the reconstruction of these data has been envisioned since 2001 [238] but not been accomplished prior to this thesis work. The pipeline we designed attempts to systematically address these obstacles and produce a 3D reconstruction that is correctly aligned with the donor's brain. While only a single hemisphere and neurotransmitter receptor have been reconstructed to date, this pipeline will allow us to create a database of 3D neurotransmitter receptor atlases for 20 of the most common receptors for 3 donor brains.

While the reconstruction of the 2D autoradiographs has been much advanced by the work presented here, there are still important limitations to the reconstruction.

First, the initial rigid alignment of the autoradiographs does not always result in perfect alignment and this error can be propagated to subsequent sections. Another limitation is that the use of K-Means classification to derive a GM autoradiograph volume does not work equally well on all receptor types and thereby introduces significant noise in the derived GM volume. Both of these limitations in the reconstruction leads to a loss of smoothness in the reconstructed volume that may impact the non-linear alignment to the corresponding MRI. One approach to ameliorating this problem would be to use a more robust method for segmenting the GM in the autoradiographs, such as using deep learning. A secondary alignment of the autoradiographs after the initial rigid registration could also help increase the smoothness of the initial reconstructed autoradiograph volume.

Another major limitation is that the currently implemented method for interpolating missing sections assumes that the autoradiographs are sectioned orthogonally to the curvature of the cortex. Future work will attempt to overcome this limitation by developing an interpolation method that accounts for the laminar distribution of receptors across the cortex. This can be accomplished by only applying interpolation within layers. While the true receptor laminar distribution is unknown, except where orthogonally sectioned autoradiographs are available, a laminar model of the cortex can be derived from the surface meshes extracted from the donor's MRI. Thus a laminar representation of the cortex derived from the subject's MRI can be used to constrain interpolation of missing autoradiographs to occur only within these layers.

The reconstruction of the receptor atlases is part of a broader collaborative effort between McGill and Julich Forschungszentrum, the Helmholtz International BigBrain

Analytics Learning Laboratory (HIBALL), to create an ultra-high resolution atlas of the brain on which multiple layers for anatomic information can be superimposed. The fundamental scaffold for this multi-modal atlas is the Big Brain [9] and it will serve as the template to which the neurotransmitter atlases will be mapped. In addition, $1\mu\text{m}$ histology and white matter photon light imaging will be incorporated into an ultra-high resolution multi-modal brain atlas. Together these combined data will be used for computational modelling of neuronal and brain network dynamics. This of course poses the very significant challenge of how to solve the problem of inter-subject, multi-modal image alignment at $< 50 \mu\text{m}$. Future work will therefore also involve devising methods to optimally transform reconstructed receptor volumes to a common template, perhaps through the use of a method like Multi-modal Surface Matching [239].

To address the problem of PET spatial resolution raised in Chapter 3 and demonstrate one potential application of the reconstructed receptor volume, we used a reconstructed volume of $GABAA_{Benz.}$ receptor densities to perform Monte-Carlo PET simulation. The receptor densities were used to define radioactivity concentrations for the PET simulator to create a realistic simulated PET image. The simulated PET images illustrated that PET can, under ideal conditions, recover 71% of the underlying spatial pattern of radioactivity concentrations and reflects differences in laminar receptor density in the cortical GM. In the future additional simulations will be performed with more scanner geometries and based on additional neurotransmitter receptors.

Just as the 3D autoradiograph reconstruction will provide the research community with a database of high-resolution neurotransmitter receptor atlases, the PET simulation based on these atlases will provide a freely available dataset of simulated PET images. These will help inform the spatial accuracy of PET and help determine the smallest anatomic regions that can be visualized with PET. The work in Chapter 6 is therefore a continuation of the pioneering work of Hoffman, et al [39] and Mazziotta, et al. [40] who, in the early days of PET in the late 1970s and early 1980s, attempted to quantify the spatial resolution of PET scanners and the effect of brain anatomy on the quantitative accuracy of PET. In this work they used simple geometric phantoms to provide estimates of the quantitative accuracy of PET for many different anatomic regions. We hope that the simulated PET images produced using our method will similarly provide the PET research community with far more accurate measures of PET quantitative accuracy across a wide variety of radioligands, scanner geometries, and acquisition protocols.

Moreover, this database of simulated images will also serve to validate algorithms for analyzing or processing PET images. In this context we have already been contacted by several groups who wish to use the simulated images we will produce to validate their own PET atlases or evaluate novel scanner geometries.

7.2 Conclusion

The research project presented here has investigated the mapping of neurotransmitter receptor densities both in vivo with PET and in vitro with receptor autoradiography. This work has sought to create a high-resolution neurotransmitter

receptor atlas using autoradiography by developing a novel image processing pipeline that could reconstruct a 3D volume from 2D autoradiographs. At the same time, we have attempted to elucidate the spatial scale at which PET can accurately quantify neurotransmitter receptor densities and thereby be used to create in vivo neurotransmitter receptor atlases. We have thus helped provide a framework for future high-resolution neurotransmitter receptor mapping with PET.

Bibliography

1. Talairach, J. & Tournoux, P. Co-planar stereotaxic atlas of the human brain. *New York: Theime* (1988).
2. Collins, D. L., Neelin, P., Peters, T. & Evans, A. Automatic 3D intersubject Registration fo MR Volumetric Data in Standardized Talairach Space. *Journal of Computer Assisted Tomography* **10**, 192–205. ISSN: 10538119 (1994).
3. Holmes, C. J. *et al.* Enhancement of MR Images Using Registration for Signal Averaging. *Journal of Computer Assisted Tomography* **22**, 324–333. ISSN: 0363-8715 (Mar. 1998).
4. Mazziotta, J. *et al.* A probabilistic atlas and reference system for the human brain: International Consortium for Brain Mapping (ICBM). *Philosophical Transactions of the Royal Society B: Biological Sciences* **356**, 1293–1322. ISSN: 0962-8436 (Aug. 2001).
5. Brodmann, K. *Vergleichende Lokalisationslehre der Grosshirnrinde in ihren Prinzipien dargestellt auf Grund des Zellenbaues* (Barth, 1909).
6. Von Economo, C. & Koskinas, G. N. *Die Cytoarchitektonik der Hirnrinde des erwachsenen Menschen* **Pt 2**, 264 (J. Springer, 1927).
7. Amunts, K., Malikovic, a., Mohlberg, H., Schormann, T. & Zilles, K. Brodmann’s areas 17 and 18 brought into stereotaxic space-where and how variable? *NeuroImage* **11**, 66–84. ISSN: 1053-8119 (2000).

8. Amunts, K. *et al.* Cytoarchitectonic mapping of the human amygdala, hippocampal region and entorhinal cortex: intersubject variability and probability maps. *Anatomy and Embryology* **210**, 343–352. ISSN: 0340-2061 (Dec. 2005).
9. Amunts, K. *et al.* BigBrain: an ultrahigh-resolution 3D human brain model. *Science (New York, N.Y.)* **340**, 1472–5. ISSN: 1095-9203 (June 2013).
10. Beliveau, V. *et al.* A high-resolution in vivo atlas of the human brain’s serotonin system. *Journal of Neuroscience* **37**, 120–128. ISSN: 15292401 (Jan. 2017).
11. Young, A. B., Frey, K. A. & Agranoff, B. W. in *Positron Emission Tomography and Autoradiography: Principles and applications for Brain and Heart* (eds Phelps, M. E., Mazziotta, J. C. & Schelbert, H. R.) 197–236 (Raven Press, New York, 1986).
12. Wienhard, K. *et al.* The ECAT HRRT: performance and first clinical application of the new high resolution research tomograph. *IEEE Transactions on Nuclear Science* **49**, 104–110. ISSN: 0018-9499 (Feb. 2002).
13. Lecomte, R. *et al.* Progress in spatial resolution for imaging the human brain. *Journal of Cerebral Blood Flow & Metabolism* **39**, 524–608 (2019).
14. Hoffman, E. J. & Phelps, M. E. in *Positron Emission Tomography and Autoradiography: Principles and applications for Brain and Heart* (eds Phelps, M., Mazziotta, J. & Schelbert, H.) 237–286 (Raven Press, New York, 1986).
15. Alavi, A., Werner, T. J., Høilund-Carlsen, P. F. & Zaidi, H. Correction for Partial Volume Effect Is a Must, Not a Luxury, to Fully Exploit the Potential

- of Quantitative PET Imaging in Clinical Oncology. *Molecular Imaging and Biology* **20**, 1–3. ISSN: 18602002 (Feb. 2018).
16. Cysouw, M. C. F. *et al.* Accuracy and Precision of Partial-Volume Correction in Oncological PET/CT Studies. *Journal of Nuclear Medicine*. ISSN: 0161-5505. doi:10.2967/jnumed.116.173831 (2016).
 17. Hutton, B. F. *et al.* What approach to brain partial volume correction is best for PET/MRI? *Nuclear Instruments and Methods in Physics Research, Section A: Accelerators, Spectrometers, Detectors and Associated Equipment* **702**, 29–33. ISSN: 01689002 (Feb. 2013).
 18. Tohka, J. & Reilhac, A. Deconvolution-based partial volume correction in Raclopride-PET and Monte Carlo comparison to MR-based method. *NeuroImage* **39**, 1570–1584. ISSN: 10538119 (Feb. 2008).
 19. Greve, D. N. *et al.* Different partial volume correction methods lead to different conclusions: An 18F-FDG-PET study of aging. *NeuroImage* **132**, 334–343. ISSN: 10538119 (May 2016).
 20. Kwee, T. C., Cheng, G., Lam, M. G., Basu, S. & Alavi, A. SUVmax of 2.5 should not be embraced as a magic threshold for separating benign from malignant lesions. *European Journal of Nuclear Medicine and Molecular Imaging* **40**, 1475–1477. ISSN: 16197070 (Oct. 2013).
 21. Hoffman, E. J., Cutler, P. D., Digby, W. M. & Mazziotta, J. C. 3-D phantom to simulate cerebral blood flow and metabolic images for PET. *IEEE Transactions on Nuclear Science* **37**, 616–620. ISSN: 15581578 (Apr. 1990).

22. Reilhac, A. *et al.* PET-SORTEO: Validation and development of database of simulated PET volumes. *IEEE Transactions on Nuclear Science* **52**, 1321–1328. ISSN: 00189499 (Oct. 2005).
23. Baron, J.-C., Yamauchi, H., Fujioka, M. & Endres, M. Selective neuronal loss in ischemic stroke and cerebrovascular disease. *Journal of cerebral blood flow and metabolism : official journal of the International Society of Cerebral Blood Flow and Metabolism* **34**, 2–18. ISSN: 1559-7016 (2014).
24. Nedergaard, M., Astrup, J. & Klinken, L. Cell density and cortex thickness in the border zone surrounding old infarcts in the human brain. *Stroke; a journal of cerebral circulation* **15**, 1033–9. ISSN: 0039-2499 (Jan. 1984).
25. Nedergaard, M., Vorstrup, S. & Astrup, J. Cell density in the border zone around old small human brain infarcts. *Stroke* **17**, 1129–1137. ISSN: 0039-2499 (Nov. 1986).
26. Nedergaard, M. Neuronal injury in the infarct border: a neuropathological study in the rat. *Acta*, 267–274 (1987).
27. Torvik, A. & Svindland, A. Is there a transitional zone between brain infarcts and the surrounding brain? A histological study. *Acta neurologica Scandinavica* **74**, 365–370. ISSN: 0001-6314 (Nov. 1986).
28. Zilles, K. *et al.* Architectonics of the human cerebral cortex and transmitter receptor fingerprints: Reconciling functional neuroanatomy and neurochemistry. *European Neuropsychopharmacology* **12**, 587–599. ISSN: 0924977X (2002).
29. Jan, S. *et al.* GATE: a simulation toolkit for PET and SPECT. *Physics in Medicine and Biology* **49**, 4543–4561. ISSN: 0031-9155 (2004).

30. Beringer, R. & Montgomery, C. G. The Angular Distribution of Positron Annihilation Radiation. *Physical Review* **61**, 222–224. ISSN: 0031-899X (Mar. 1942).
31. Chawluk, J. B. *et al.* Positron emission tomography in aging and dementia: effect of cerebral atrophy. *Journal of nuclear medicine : official publication, Society of Nuclear Medicine* **28**, 431–7. ISSN: 0161-5505 (Apr. 1987).
32. Stewart, A. T. & March, R. H. Annihilation of positrons in LiH. *Physical Review* **122**, 75–76. ISSN: 0031899X (May 1961).
33. Lenard, P. Ueber die lichtelektrische Wirkung. *Annalen der Physik* **313**, 149–198. ISSN: 15213889 (Jan. 1902).
34. Compton, A. H. A Quantum Theory of the Scattering of X-rays by Light Elements. *Physical Review* **21**, 483–502. ISSN: 0031-899X (May 1923).
35. Zaidi, H. & Montandon, M. L. Scatter Compensation Techniques in PET. *PET Clinics* **2**, 219–234. ISSN: 15568598 (Apr. 2007).
36. Meikle, S. R. & Badawi, R. D. in *Positron Emission Tomography: Basic Sciences* (eds Bailey, D. L., Townsend, D. W., Valk, P. E. & Maisey, M. N.) 93–126 (Springer, 2005). doi:10.1007/1-84628-007-9_5.
37. Phelps, M. E., Hoffman, E. J., Mullani, N. A. & Ter-Pogossian, M. M. Coincidence detection to transaxial reconstruction reconstruction tomography. *Journal of Nuclear Medicine* **16**, 210–224 (1975).

38. Karp, J. S. & Daube-Witherspoon, M. E. Depth-of-interaction determination in NaI(Tl) and BGO scintillation crystals using a temperature gradient. *Nuclear Inst. and Methods in Physics Research, A* **260**, 509–517. ISSN: 01689002 (Oct. 1987).
39. Hoffman, E. J., Huang, S. C. & Phelps, M. E. *Quantitation in positron emission computed tomography: 1. Effect of object size*. 1979.
40. Mazziotta, J. C., Phelps, M. E., Plummer, D. & Kuhl, D. E. Quantitation in positron emission computed tomography: 5. physical-anatomical effects. *Journal of Computer Assisted Tomography* **5**, 734–743. ISSN: 15323145 (Oct. 1981).
41. Rousset, O., Rahmim, A., Alavi, A. & Zaidi, H. Partial Volume Correction Strategies in PET. *PET Clinics* **2**, 235–249. ISSN: 15568598 (Apr. 2007).
42. Astrup, J., Siesjo, B. & Symon, L. Thresholds in Cerebral Ischemia. *Stroke* **12**, 723–725 (1981).
43. Sette, G. *et al.* In vivo mapping of brain benzodiazepine receptor changes by positron emission tomography after focal ischemia in the anesthetized baboon. *Stroke; a journal of cerebral circulation* **24**, 2046–57, discussion 2057–8. ISSN: 0039-2499 (1993).
44. Möhler, H. GABA(A) receptor diversity and pharmacology. *Cell and tissue research* **326**, 505–16. ISSN: 0302-766X (Nov. 2006).
45. Hendry, S., Schwark, H., Jones, E. & Yan, J. Numbers and proportions of GABA-immunoreactive neurons in different areas of monkey cerebral cortex. *J. Neurosci.* **7**, 1503–1519 (May 1987).

46. Abadie, P. *et al.* Central benzodiazepine receptors in human brain: estimation of regional Bmax and KD values with positron emission tomography. *European Journal of Pharmacology* **213**, 107–115. ISSN: 00142999 (Mar. 1992).
47. La Fougère, C. *et al.* Where in-vivo imaging meets cytoarchitectonics: the relationship between cortical thickness and neuronal density measured with high-resolution [18F]flumazenil-PET. *NeuroImage* **56**, 951–60. ISSN: 1095-9572 (June 2011).
48. Heiss, W. D. *et al.* Repeat positron emission tomographic studies in transient middle cerebral artery occlusion in cats: residual perfusion and efficacy of postischemic reperfusion. *Journal of cerebral blood flow and metabolism : official journal of the International Society of Cerebral Blood Flow and Metabolism* **17**, 388–400. ISSN: 0271-678X (1997).
49. Watanabe, Y. *et al.* Detection of viable cortical neurons using benzodiazepine receptor imaging after reversible focal ischaemia in rats: comparison with regional cerebral blood flow. *European Journal of Nuclear Medicine and Molecular Imaging* **27**, 308–313. ISSN: 1619-7070 (Mar. 2000).
50. Katchanov, J. *et al.* Selective Neuronal Vulnerability Following Mild Focal Brain Ischemia in the Mouse. *Brain Pathology* **13**, 452–464. ISSN: 1015-6305 (Apr. 2006).
51. Fukumoto, D. *et al.* Multiparametric assessment of acute and subacute ischemic neuronal damage: A small animal positron emission tomography study with rat photochemically induced thrombosis model. *Synapse* **65**, 207–214. ISSN: 10982396 (Mar. 2011).

52. Rojas, S. *et al.* Positron emission tomography with ¹¹C-flumazenil in the rat shows preservation of binding sites during the acute phase after 2h-transient focal ischemia. *Neuroscience* **182**, 208–216. ISSN: 03064522 (May 2011).
53. Abe, K. *et al.* Discrepancy between cell injury and benzodiazepine receptor binding after transient middle cerebral artery occlusion in rats. *Synapse* **53**, 234–239. ISSN: 08874476 (Sept. 2004).
54. Nakagawara, J., Sperling, B. & Lassen, N. A. Incomplete Brain Infarction of Reperfused Cortex May Be Quantitated With Iomazenil. *Stroke* **28**, 124–132. ISSN: 0039-2499 (Jan. 1997).
55. Saur, D., Buchert, R., Knab, R., Weiller, C. & Röther, J. Iomazenil-single-photon emission computed tomography reveals selective neuronal loss in magnetic resonance-defined mismatch areas. *Stroke* **37**, 2713–2719. ISSN: 00392499 (2006).
56. Carrera, E. *et al.* Is neural activation within the rescued penumbra impeded by selective neuronal loss? *Brain* **136**, 1816–1829. ISSN: 00068950 (2013).
57. Guadagno, J. V. *et al.* Selective neuronal loss in rescued penumbra relates to initial hypoperfusion. *Brain : a journal of neurology* **131**, 2666–78. ISSN: 1460-2156 (Oct. 2008).
58. Zepper, P. *et al.* Imaging delayed cell death in subacute stroke with high-resolution ¹⁸F-Flumazenil. *Society of Nuclear Medicine Annual Meeting Abstracts* **53**, 37 (May 2012).

59. Müller-Gärtner, H. W. *et al.* Measurement of Radiotracer Concentration in Brain Gray Matter Using Positron Emission Tomography: MRI-Based Correction for Partial Volume Effects. *Journal of Cerebral Blood Flow & Metabolism* **12**, 571–583. ISSN: 0271-678X (July 1992).
60. Alicke, B. & Schwartz-Bloom, R. D. Rapid Down-Regulation of GABAA Receptors in the Gerbil Hippocampus Following Transient Cerebral Ischemia. *Journal of Neurochemistry* **65**, 2808–2811. ISSN: 14714159 (Nov. 1995).
61. Stein, G. H. & Yanishevsky, R. Autoradiography. *Methods in Enzymology* **58**, 279–292. ISSN: 15577988 (Jan. 1979).
62. Pert, C. B. & Snyder, S. H. Opiate receptor: demonstration in nervous tissue. *Science (New York, N.Y.)* **179**, 1011–4. ISSN: 0036-8075 (Mar. 1973).
63. Yamamura, H. I., Kuhar, M. J. & Snyder, S. H. In vivo identification of muscarinic cholinergic receptor binding in rat brain. *Brain Research* **80**, 170–176. ISSN: 0006-8993 (Nov. 1974).
64. Pert, C. B. & Snyder, S. H. Identification of opiate receptor binding in intact animals. *Life Sciences* **16**, 1623–1634. ISSN: 00243205 (May 1975).
65. Kuhar, M. J. & Yamamura, H. I. Light autoradiographic localisation of cholinergic muscarinic receptors in rat brain by specific binding of a potent antagonist. *Nature* **253**, 560–561. ISSN: 00280836 (Feb. 1975).
66. Kuhar, M. J. & Yamamura, H. I. Localization of cholinergic muscarinic receptors in rat brain by light microscopic radioautography. *Brain Research* **110**, 229–243. ISSN: 00068993 (July 1976).

67. Atweh, S. F. & Kuhar, M. J. Autoradiographic localization of opiate receptors in rat brain. I. Spinal cord and lower medulla. *Brain Research* **124**, 53–67. ISSN: 00068993 (Mar. 1977).
68. Wamsley, J. K., Zarbin, M. A., Birdsall, N. J. & Kuhar, M. J. Muscarinic cholinergic receptors: Autoradiographic localization of high and low affinity agonist binding sites. *Brain Research* **200**, 1–12. ISSN: 00068993 (Oct. 1980).
69. Scott Young, W. & Kuhar, M. J. A new method for receptor autoradiography: [3H]Opioid receptors in rat brain. *Brain Research* **179**, 255–270. ISSN: 00068993 (Dec. 1979).
70. Monaghan, D. T. & Cotman, C. W. The distribution of [3H]kainic acid binding sites in rat CNS as determined by autoradiography. *Brain Research* **252**, 91–100. ISSN: 00068993 (Dec. 1982).
71. Billard, W., Ruperto, V., Crosby, G., Iorio, L. C. & Barnett, A. Characterization of the binding of 3H-SCH 23390, a selective D-1 receptor antagonist ligand, in rat striatum. *Life Sciences* **35**, 1885–1893. ISSN: 00243205 (Oct. 1984).
72. Monaghan, D. T., Yao, D. & Cotman, C. W. Distribution of [3H]AMPA binding sites in rat brain as determined by quantitative autoradiography. *Brain Research* **324**, 160–164. ISSN: 00068993 (Dec. 1984).
73. Wong, E. H., Knight, A. R. & Woodruff, G. N. [3H]MK-801 Labels a Site on the N-Methyl-D-Aspartate Receptor Channel Complex in Rat Brain Membranes. *Journal of Neurochemistry* **50**, 274–281. ISSN: 14714159 (Jan. 1988).

74. Vilaró, M. T., Wiederhold, K. H., Palacios, J. M. & Mengod, G. Muscarinic M2 receptor mRNA expression and receptor binding in cholinergic and non-cholinergic cells in the rat brain: A correlative study using in situ hybridization histochemistry and receptor autoradiography. *Neuroscience* **47**, 367–393. ISSN: 03064522 (Mar. 1992).
75. Nénonéné, E. K., Radja, F., Carli, M., Grondin, L. & Reader, T. A. Heterogeneity of Cortical and Hippocampal 5-HT_{1A} Receptors: A Reappraisal of Homogeneous Binding with 8-[³H]Hydroxydipropylaminotetralin. *Journal of Neurochemistry* **62**, 1822–1834. ISSN: 14714159 (June 1994).
76. Rabow, L. E., Russek, S. J. & Farb, D. H. From ion currents to genomic analysis: Recent advances in GABA_A receptor research. *Synapse* **21**, 189–274. ISSN: 10982396 (Nov. 1995).
77. Marks, M. J., Smith, K. W. & Collins, A. C. Differential agonist inhibition identifies multiple epibatidine binding sites in mouse brain. *Journal of Pharmacology and Experimental Therapeutics* **285**, 377–386. ISSN: 00223565 (1998).
78. Zilles, K., Schleicher, A., Rath, M. & Bauer, A. Quantitative receptor autoradiography in the human brain - Methodical aspects. *Histochemistry* **90**, 129–137. ISSN: 03015564 (1988).
79. Lear, J. L. in *Positron Emission Tomography and Autoradiography: Principles and applications for Brain and Heart* (eds Phelps, M. E., Mazziotta, J. C. & Schelbert, H. R.) 197–235 (Raven Press, 1986). https://scholar.google.ca/scholar?hl=en&as%7B%5C_%7Dsdt=0%7B%5C%7D2C5%7B%5C%7Dq=Principles+of+Single+and+Multiple+Radionuclide+

Autoradiography%7B%5C%7DbtnG=%7B%5C%7Dd=gs%7B%5C_%7Dcit%7B%5C%7Du=%7B%5C%7D2Fscholar%7B%5C%7D3Fq%7B%5C%7D3Dinfo%7B%5C%7D3A7rfuPpb8vUAJ%7B%5C%7D3Ascholar.google.com%7B%5C%7D2F%7B%5C%7D26output%7B%5C%7D3Dcite%7B%5C%7D26scirp%7B%5C%7D3D0%7B%5C%7D26h1%7B%5C%7D3Den.

80. Schleicher, A. & Zilles, K. in *Molecular neuroanatomy* 147–157 (Elsevier Amsterdam, 1988). https://scholar.google.ca/scholar?hl=en%7B%5C%7Das%7B%5C_%7Dsd=0%7B%5C%7D2C5%7B%5C%7Dq=Schleicher%7B%5C%7D2C+A.%E2%80%A2+and+Zilles%7B%5C%7D2C+K.+%7B%5C%7D281988%7B%5C%7D29.+The+use+of+automated+image+analysis%7B%5C%7DbtnG=%7B%5C%7Dd=gs%7B%5C_%7Dcit%7B%5C%7Du=%7B%5C%7D2Fscholar%7B%5C%7D3Fq%7B%5C%7D3Dinfo%7B%5C%7D3ApTQ0fjZEKewJ%7B%5C%7D3Ascholar.google.com%7B%5C%7D2F%7B%5C%7D26output%7B%5C%7D3Dcite%7B%5C%7D26scirp%7B%5C%7D3D0%7B%5C%7D26h1%7B%5C%7D3Den.
81. Zilles, K. *et al.* Mapping of human and macaque sensorimotor areas by integrating architectonic, transmitter receptor, MRI and PET data. *Journal of anatomy* **187** (Pt 3, 515–537. ISSN: 0021-8782 (1995).
82. Adler, D. H. *et al.* Histology-derived volumetric annotation of the human hippocampal subfields in postmortem MRI. *NeuroImage* **84**, 505–523. ISSN: 1053-8119 (Jan. 2014).

83. Sotiras, A., Davatzikos, C. & Paragios, N. Deformable medical image registration: A survey. *IEEE Transactions on Medical Imaging* **32**, 1153–1190. ISSN: 02780062 (2013).
84. Klein, A. *et al.* Evaluation of 14 nonlinear deformation algorithms applied to human brain MRI registration. *NeuroImage* **46**, 786–802. ISSN: 10538119 (July 2009).
85. Beg, M. F., Miller, M. I., Trounevé, A. & Younes, L. Computing large deformation metric mappings via geodesic flows of diffeomorphisms. *International Journal of Computer Vision* **61**, 139–157. ISSN: 09205691 (Feb. 2005).
86. Avants, B. B., Epstein, C. L., Grossman, M. & Gee, J. C. Symmetric Diffeomorphic Image Registration with Cross-Correlation: Evaluating Automated Labeling of Elderly and Neurodegenerative Brain. *Medical image analysis* **12**, 26. ISSN: 1361-8423 (Feb. 2008).
87. Zaidi, H. Relevance of accurate Monte Carlo modeling in nuclear medical imaging. *Medical Physics* **26**, 574. ISSN: 00942405 (Apr. 1999).
88. Agostinelli, S. *et al.* Geant4—a simulation toolkit. *Nuclear Instruments and Methods in Physics Research Section A: Accelerators, Spectrometers, Detectors and Associated Equipment* **506**, 250–303. ISSN: 01689002 (July 2003).
89. Baró, J., Sempau, J., Fernández-Varea, J. & Salvat, F. PENELOPE: An algorithm for Monte Carlo simulation of the penetration and energy loss of electrons and positrons in matter. *Nuclear Instruments and Methods in Physics Research Section B: Beam Interactions with Materials and Atoms* **100**, 31–46. ISSN: 0168583X (May 1995).

90. España, S. *et al.* PeneloPET, a Monte Carlo PET simulation tool based on PENELOPE: features and validation. en. *Physics in medicine and biology* **54**, 1723–42. ISSN: 0031-9155 (Mar. 2009).
91. Bataille, F., Comtat, C., Jan, S. & Trebossen, R. *Monte Carlo Simulation for the ECAT HRRT using GATE* in *IEEE Symposium Conference Record Nuclear Science 2004*. **4** (IEEE, 2004), 2570–2574. ISBN: 0-7803-8700-7. doi:10.1109/NSSMIC.2004.1462778. <http://ieeexplore.ieee.org/lpdocs/epic03/wrapper.htm?arnumber=1462778>.
92. Jones, T. A. *et al.* Remodeling the brain with behavioral experience after stroke. *Stroke* **40**, S136–S139. ISSN: 00392499 (2009).
93. Nudo, R. J. Postinfarct cortical plasticity and behavioral recovery. *Stroke* **38**, 840–845. ISSN: 00392499 (2007).
94. Nudo, R. J. & Milliken, G. W. Reorganization of movement representations in primary motor cortex following focal ischemic infarcts in adult squirrel monkeys. *Journal of neurophysiology* **75**, 2144–2149. ISSN: 0022-3077 (1996).
95. Brown, C. E., Aminoltejari, K., Erb, H., Winship, I. R. & Murphy, T. H. In vivo voltage-sensitive dye imaging in adult mice reveals that somatosensory maps lost to stroke are replaced over weeks by new structural and functional circuits with prolonged modes of activation within both the peri-infarct zone and distant sites. *The Journal of neuroscience : the official journal of the Society for Neuroscience* **29**, 1719–1734. ISSN: 0270-6474 (2009).

96. Carmichael, S. T., Wei, L., Rovainen, C. M. & Woolsey, T. A. New patterns of intracortical projections after focal cortical stroke. *Neurobiology of disease* **8**, 910–922. ISSN: 0969-9961 (2001).
97. Florence, S. L., Taub, H. B. & Kaas, J. H. Large-scale sprouting of cortical connections after peripheral injury in adult macaque monkeys. *Science (New York, N.Y.)* **282**, 1117–1121. ISSN: 0036-8075 (1998).
98. Murphy, T. H. & Corbett, D. Plasticity during stroke recovery: from synapse to behaviour. *Nature reviews. Neuroscience* **10**, 861–872. ISSN: 1471-003X (2009).
99. Stroemer, R. P., Kent, T. a., Hulsebosch, C. E. & Feeney, D. M. Enhanced Neocortical Neural Sprouting, Synaptogenesis, and Behavioural Recovery With D -Amphetamine Therapy. *Stroke* **29**, 2381–2395 (1998).
100. Ueno, Y. *et al.* Axonal outgrowth and dendritic plasticity in the cortical peri-infarct area after experimental stroke. *Stroke* **43**, 2221–2228. ISSN: 00392499 (2012).
101. Carmichael, S. T. *et al.* Growth-associated gene expression after stroke: evidence for a growth-promoting region in peri-infarct cortex. *Experimental neurology* **193**, 291–311. ISSN: 0014-4886 (June 2005).
102. Gulyás, B. *et al.* Evolution of microglial activation in ischaemic core and peri-infarct regions after stroke: A PET study with the TSPO molecular imaging biomarker [11C]vinpocetine. *Journal of the Neurological Sciences* **320**, 110–117. ISSN: 0022510X (2012).

103. Price, C. J. S. *et al.* Intrinsic activated microglia map to the peri-infarct zone in the subacute phase of ischemic stroke. *Stroke* **37**, 1749–1753. ISSN: 00392499 (2006).
104. Schroeter, M. *et al.* Neuroinflammation extends brain tissue at risk to vital peri-infarct tissue: a double tracer [11C]PK11195- and [18F]FDG-PET study. *Journal of cerebral blood flow and metabolism : official journal of the International Society of Cerebral Blood Flow and Metabolism* **29**, 1216–1225. ISSN: 0271-678X (2009).
105. Ceulemans, A.-G. *et al.* The dual role of the neuroinflammatory response after ischemic stroke: modulatory effects of hypothermia. *Journal of neuroinflammation* **7**, 74. ISSN: 1742-2094 (Jan. 2010).
106. Thiel, A., Cechetto, D. F., Heiss, W. D., Hachinski, V. & Whitehead, S. N. Amyloid burden, neuroinflammation, and links to cognitive decline after ischemic stroke. *Stroke*, 2825–2829. ISSN: 00392499 (2014).
107. Fink, G. R., Herholz, K., Pietrzyk, U., Huber, M. & Heiss, W.-D. Peri-Infarct perfusion in human ischemia: Its relation to tissue metabolism, morphology, and clinical outcome. *Journal of Stroke and Cerebrovascular Diseases* **3**, 123–131. ISSN: 10523057 (1993).
108. Kim, Y. K., Yang, E. J., Cho, K., Lim, J. Y. & Paik, N.-J. Functional Recovery After Ischemic Stroke Is Associated With Reduced GABAergic Inhibition in the Cerebral Cortex: A GABA PET Study. *Neurorehabilitation and neural repair* **28**, 576–583. ISSN: 1552-6844 (2014).

109. Furlan, M., Marchal, G., Viader, F., Derlon, J. M. & Baron, J. C. Spontaneous neurological recovery after stroke and the fate of the ischemic penumbra. *Annals of neurology* **40**, 216–226. ISSN: 0364-5134 (1996).
110. Plautz, E. J. *et al.* Post-infarct cortical plasticity and behavioral recovery using concurrent cortical stimulation and rehabilitative training: A feasibility study in primates. *Neurological Research* **25**, 801–810. ISSN: 0161-6412 (Dec. 2003).
111. Cramer, S. C., Shah, R., Juranek, J., Crafton, K. R. & Le, V. Activity in the peri-infarct rim in relation to recovery from stroke. *Stroke* **37**, 111–115. ISSN: 00392499 (2006).
112. Heiss, W. D. *et al.* Progressive derangement of periinfarct viable tissue in ischemic stroke. *Journal of cerebral blood flow and metabolism : official journal of the International Society of Cerebral Blood Flow and Metabolism* **12**, 193–203. ISSN: 0271-678X (1992).
113. Markus, R. *et al.* Topography and Temporal Evolution of Hypoxic Viable Tissue Identified by ¹⁸F-Fluoromisonidazole Positron Emission Tomography in Humans After Ischemic Stroke. *Stroke* **34**, 2646–2652. ISSN: 00392499 (2003).
114. Carrera, E. *et al.* The vascular mean transit time: a surrogate for the penumbra flow threshold? *Journal of cerebral blood flow and metabolism : official journal of the International Society of Cerebral Blood Flow and Metabolism* **31**, 1027–35. ISSN: 1559-7016 (Apr. 2011).
115. Hatazawa, J. *et al.* Evaluation of cerebral infarction with iodine 123-iomazenil SPECT. *Journal of nuclear medicine : official publication, Society of Nuclear Medicine* **36**, 2154–2161. ISSN: 0161-5505 (1995).

116. Sasaki, M. *et al.* Benzodiazepine receptors in chronic cerebrovascular disease: comparison with blood flow and metabolism. *Journal of nuclear medicine : official publication, Society of Nuclear Medicine* **38**, 1693–1698. ISSN: 01615505 (1997).
117. Li, Q. *et al.* Cortical thickness estimation in longitudinal stroke studies: A comparison of 3 measurement methods. *NeuroImage: Clinical*. ISSN: 22131582. doi:10.1016/j.nicl.2014.08.017 (2014).
118. Sled, J. G., Zijdenbos, A. P. & Evans, A. C. A nonparametric method for automatic correction of intensity nonuniformity in MRI data. English. *IEEE transactions on medical imaging* **17**, 87–97. ISSN: 0278-0062 (Feb. 1998).
119. Zijdenbos, A. P., Forghani, R. & Evans, A. C. *Automatic Quantification of MS Lesions in 3D MRI Brain Data Sets: Validation of INSECT in MICCAI '98 Proceedings of the First International Conference on Medical Image Computing and Computer-Assisted Intervention* (Springer-Verlag, Oct. 1998), 439–448. ISBN: 3-540-65136-5. <http://dl.acm.org/citation.cfm?id=646921.709333>.
120. Tohka, J., Zijdenbos, A. & Evans, A. Fast and robust parameter estimation for statistical partial volume models in brain MRI. *NeuroImage* **23**, 84–97. ISSN: 1053-8119 (Sept. 2004).
121. Funck, T., Paquette, C., Evans, A. & Thiel, A. Surface-based partial-volume correction for high-resolution PET. *NeuroImage* **102**, 674–87. ISSN: 1095-9572 (Nov. 2014).

122. Lucy, L. B. An iterative technique for the rectification of observed distributions. en. *The Astronomical Journal* **79**, 745. ISSN: 00046256 (June 1974).
123. Richardson, W. H. Bayesian-Based Iterative Method of Image Restoration. EN. *Journal of the Optical Society of America* **62**, 55. ISSN: 0030-3941 (Jan. 1972).
124. Logan, J. *et al.* Distribution Volume Ratios Without Blood Sampling from Graphical Analysis of PET Data. *Journal of Cerebral Blood Flow & Metabolism* **16**, 834–840. ISSN: 0271-678X (Sept. 1996).
125. Savic, I. *et al.* in-Vivo Demonstration of Reduced Benzodiazepine Receptor Binding in Human Epileptic Foci. *The Lancet* **332**, 863–866. ISSN: 01406736 (Oct. 1988).
126. Salmi, E. *et al.* Measurement of GABAA receptor binding in vivo with [11C]flumazenil: a test-retest study in healthy subjects. *NeuroImage* **41**, 260–9. ISSN: 1053-8119 (June 2008).
127. Wilcoxon, F. Individual Comparisons by Ranking Methods. *Biometrics Bulletin* **1**, 80–83 (1945).
128. Hochberg, Y. A Sharper Bonferroni Procedure for Multiple Tests of Significance. *Biometrika* **75**, 800–802 (1988).
129. Heiss, W. D. *et al.* Permanent cortical damage detected by flumazenil positron emission tomography in acute stroke. *Stroke; a journal of cerebral circulation* **29**, 454–461. ISSN: 0039-2499 (1998).
130. Schaechter, J. D., Moore, C. I., Connell, B. D., Rosen, B. R. & Dijkhuizen, R. M. Structural and functional plasticity in the somatosensory cortex of

- chronic stroke patients. *Brain : a journal of neurology* **129**, 2722–2733. ISSN: 1460-2156 (Oct. 2006).
131. Brodtmann, A. *et al.* Changes in regional brain volume three months after stroke. *Journal of the Neurological Sciences* **322**, 122–128. ISSN: 0022510X (2012).
 132. Duering, M. *et al.* Incident subcortical infarcts induce focal thinning in connected cortical regions. *Neurology* **79**, 2025–2028. ISSN: 0028-3878 (Nov. 2012).
 133. Greve, D. N. *et al.* Cortical surface-based analysis reduces bias and variance in kinetic modeling of brain PET data. *NeuroImage* **92**, 225–236. ISSN: 10959572 (May 2014).
 134. Karjalainen, T. *et al.* Magia: Robust Automated Image Processing and Kinetic Modeling Toolbox for PET Neuroinformatics. *Frontiers in Neuroinformatics* **14**, 3. ISSN: 1662-5196 (Feb. 2020).
 135. Gorgolewski, K. *et al.* Nipype: A Flexible, Lightweight and Extensible Neuroimaging Data Processing Framework in Python. *Frontiers in Neuroinformatics* **5**, 13. ISSN: 1662-5196 (2011).
 136. Eskildsen, S. F. *et al.* BEaST: Brain extraction based on nonlocal segmentation technique. *NeuroImage* **59**, 2362–2373. ISSN: 10538119 (Feb. 2012).
 137. Avants, B. B. *et al.* A reproducible evaluation of ANTs similarity metric performance in brain image registration. *NeuroImage* **54**, 2033–2044. ISSN: 10538119 (2011).

138. Tzourio-Mazoyer, N. *et al.* Automated Anatomical Labeling of Activations in SPM Using a Macroscopic Anatomical Parcellation of the MNI MRI Single-Subject Brain. *NeuroImage* **15**, 273–289 (2002).
139. Thomas, B. A. *et al.* PETPVC: A toolbox for performing partial volume correction techniques in positron emission tomography. *Physics in Medicine and Biology* **61**, 7975–7993. ISSN: 13616560 (Nov. 2016).
140. Oikonen, V. *Software for positron emission tomography* 2017. http://www.turkupetcentre.net/petanalysis/sw%7B%5C_%7Dpet.html.
141. Logan, J. *et al.* Graphical analysis of reversible radioligand binding from time-activity measurements applied to [N-11C-methyl]-(-)-cocaine PET studies in human subjects. *Journal of cerebral blood flow and metabolism : official journal of the International Society of Cerebral Blood Flow and Metabolism* **10**, 740–7. ISSN: 0271-678X (Sept. 1990).
142. Gjedde, A. Calculation of cerebral glucose phosphorylation from brain uptake of glucose analogs in vivo: A re-examination. *Brain Research Reviews* **4**, 237–274. ISSN: 0165-0173 (June 1982).
143. Patlak, C. S., Blasberg, R. G. & Fenstermacher, J. D. Graphical evaluation of blood-to-brain transfer constants from multiple-time uptake data. *Journal of cerebral blood flow and metabolism : official journal of the International Society of Cerebral Blood Flow and Metabolism* **3**, 1–7. ISSN: 0271-678X (Mar. 1983).

144. Gunn, R. N., Lammertsma, A. A., Hume, S. P. & Cunningham, V. J. Parametric imaging of ligand-receptor binding in PET using a simplified reference region model. *NeuroImage* **6**, 279–287. ISSN: 10538119 (1997).
145. Sokoloff, L. *et al.* the [14C]Deoxyglucose Method for the Measurement of Local Cerebral Glucose Utilization: Theory, Procedure, and Normal Values in the Conscious and Anesthetized Albino Rat. *Journal of Neurochemistry* **28**, 897–916. ISSN: 14714159 (May 1977).
146. Pedregosa, F. *et al.* *Scikit-learn: Machine Learning in Python* 2825–2830. <http://dl.acm.org/citation.cfm?id=2078195> (MIT Press, 2001).
147. Sherif, T., Kassis, N., Rousseau, M.-E., Adalat, R. & Evans, A. C. Brain-Browser: distributed, web-based neurological data visualization. *Frontiers in Neuroinformatics* **8**, 89. ISSN: 1662-5196 (Jan. 2015).
148. Ge, Y. *et al.* Retrospective registration of pet and mr brain images: An algorithm and its stereotactic validation. *Journal of Computer Assisted Tomography* **18**, 800–810. ISSN: 15323145 (1994).
149. Andersson, J. L. R., Sundin, A. & Valind, S. A method for coregistration of PET and MR brain images. *Journal of Nuclear Medicine* **36**, 1307–1315. ISSN: 01615505 (July 1995).
150. Alpert, N., Berdichevsky, D., Levin, Z., Morris, E. & Fischman, A. Improved Methods for Image Registration. *NeuroImage* **3**, 10–18. ISSN: 1053-8119 (Feb. 1996).

151. Mutic, S. *et al.* Multimodality image registration quality assurance for conformal three-dimensional treatment planning. *International Journal of Radiation Oncology Biology Physics* **51**, 255–260. ISSN: 03603016 (Sept. 2001).
152. DeLorenzo, C. *et al.* A new method for assessing PET-MRI coregistration in *Proceedings of SPIE* (eds Plum, J. P. W. & Dawant, B. M.) **7259** (International Society for Optics and Photonics, Feb. 2009), 72592W–72592W–8. ISBN: 9780819475107. doi:10.1117/12.812170. <http://link.aip.org/link/PSISDG/v7259/i1/p72592W/s1%7B%5C%7DAgg=doi>.
153. Gorgolewski, K. J. *et al.* The brain imaging data structure, a format for organizing and describing outputs of neuroimaging experiments. *Scientific Data* **3**, 160044. ISSN: 20524463 (June 2016).
154. Adam, L.-E. *et al.* Performance evaluation of the whole-body PET scanner ECAT EXACT HR/sup +/- following the IEC standard. *IEEE Transactions on Nuclear Science* **44**, 1172–1179. ISSN: 00189499 (June 1997).
155. Rousset, O. G., Ma, Y. & Evans, A. C. Correction for partial volume effects in PET: Principle and validation. *Journal of Nuclear Medicine* **39**, 904–911. ISSN: 01615505 (May 1998).
156. Mikolajczyk, K., Szabatin, M., Rudnicki, P., Grodzki, M. & Burger, C. A JAVA environment for medical image data analysis: Initial application for brain PET quantitation in *Medical Informatics* **23** (Taylor & Francis, Jan. 1998), 207–214. doi:10.3109/14639239809001400. <http://www.tandfonline.com/doi/full/10.3109/14639239809001400>.

157. Bourgeat, P. *et al.* *Computational analysis of PET by AIBL (CapAIBL): a cloud-based processing pipeline for the quantification of PET images* in (eds Ourselin, S. & Styner, M. A.) (International Society for Optics and Photonics, Mar. 2015), 94132V. doi:10.1117/12.2082492. <http://proceedings.spiedigitallibrary.org/proceeding.aspx?doi=10.1117/12.2082492>.
158. Gunn, R. N., Coello, C. & Searle, G. E. Molecular Imaging And Kinetic Analysis Toolbox (MIAKAT) - A Quantitative Software Package for the Analysis of PET Neuroimaging Data. *Journal of Nuclear Medicine* **57**, 1928 (2016).
159. Savio, A. M., Schutte, M., Graña, M. & Yakushev, I. Pypes: Workflows for Processing Multimodal Neuroimaging Data. *Frontiers in Neuroinformatics* **11**, 25. ISSN: 1662-5196 (Apr. 2017).
160. Markiewicz, P. J. *et al.* NiftyPET: a High-throughput Software Platform for High Quantitative Accuracy and Precision PET Imaging and Analysis. *Neuroinformatics* **16**, 95–115. ISSN: 15392791 (Jan. 2018).
161. Dore, V. *et al.* in *Patch-Based Techniques in Medical Imaging: Second International Workshop, Patch-MI 2016, Held in Conjunction with MICCAI 2016, Athens, Greece, October 17, 2016, Proceedings* (eds Wu, G., Coupé, P., Zhan, Y., Munsell, B. C. & Rueckert, D.) 109–116 (Springer International Publishing, Cham, 2016). ISBN: 978-3-319-47118-1. doi:10.1007/978-3-319-47118-1_14. https://doi.org/10.1007/978-3-319-47118-1%7B%5C_%7D14.
162. Ashburner, J. *SPM: A history* Aug. 2012. doi:10.1016/j.neuroimage.2011.10.025. <https://www.sciencedirect.com/science/article/pii/S1053811911011888?via%7B%5C%7D3Dihub>.

163. Kriegeskorte, N. *et al.* Greater Neural Pattern Similarity Across Repetitions Is Associated with Better Memory {\textemdash} Greater Neural Pattern Similarity Across Repetitions Is Associated with Better Memory {\textemdash} Supporting Online Material. *NeuroImage* **10**, 97–102. ISSN: 10538119 (Aug. 2006).
164. Cox, R. W. *AFNI: What a long strange trip it's been* Aug. 2012. doi:10.1016/j.neuroimage.2011.08.056. <https://www.sciencedirect.com/science/article/pii/S1053811911009736?via%7B%5C%7D3Dihub>.
165. Searle, G., Coello, C. & Gunn, R. *Extension of the MIAKAT analysis software package to non-brain and pre-clinical PET analysis* **supplement 1**, 1305–1305. <http://jnm.snmjournals.org/content/58/supplement%7B%5C%7D1/1305.short> (Society of Nuclear Medicine, May 2017).
166. Yang, J., Huang, S. C., Mega, M. & Lin, K. P. Investigation of partial volume correction methods for brain fdg pet studies. *IEEE Transactions on Nuclear Science* **43**, 3322–3327. ISSN: 00189499 (1996).
167. Esteban, O. *et al.* MRIQC: Predicting Quality in Manual MRI Assessment Protocols Using No-Reference Image Quality Measures. *bioRxiv*. doi:10.1101/111294. <http://biorxiv.org/content/early/2017/02/24/111294> (2017).
168. Gedamu, E. L., Collins, D. & Arnold, D. L. Automated quality control of brain MR images. *Journal of Magnetic Resonance Imaging* **28**, 308–319. ISSN: 10531807 (Aug. 2008).

169. Oguz, I. *et al.* DTIPrep: quality control of diffusion-weighted images. doi:10.3389/fninf.2014.00004. <https://www.ncbi.nlm.nih.gov/pmc/articles/PMC3906573/pdf/fninf-08-00004.pdf> (2014).
170. Panta, S. R. *et al.* A Tool for Interactive Data Visualization: Application to Over 10,000 Brain Imaging and Phantom MRI Data Sets. *Frontiers in Neuroinformatics* **10**, 9. ISSN: 1662-5196 (Mar. 2016).
171. Christodoulou, A. G. *et al.* A quality control method for detecting and suppressing uncorrected residual motion in fMRI studies. *Magnetic Resonance Imaging* **31**, 707–717. ISSN: 0730725X (June 2013).
172. Frouin, V., Comtat, C., Reilhac, A. & Grégoire, M. C. Correction of partial-volume effect for PET striatal imaging: Fast implementation and study of robustness. *Journal of Nuclear Medicine* **43**, 1715–1726. ISSN: 01615505 (Dec. 2002).
173. Meltzer, C. C. *et al.* Comparative evaluation of MR-based partial-volume correction schemes for PET. *Journal of nuclear medicine : official publication, Society of Nuclear Medicine* **40**, 2053–65. ISSN: 0161-5505 (1999).
174. Quarantelli, M. *et al.* Integrated software for the analysis of brain PET/SPECT studies with partial-volume-effect correction. *Journal of Nuclear Medicine* **45**, 192–201. ISSN: 01615505 (Feb. 2004).
175. Funck, T. *et al.* Assessing neuronal density in peri-infarct cortex with PET: Effects of cortical topology and partial volume correction. *Human Brain Mapping* **38**, 326–338. ISSN: 10659471 (Jan. 2017).

176. Cox, S. M. *et al.* Striatal D1 and D2 signaling differentially predict learning from positive and negative outcomes. *NeuroImage* **109**, 95–101. ISSN: 10959572 (Apr. 2015).
177. Comtat, C. *et al.* *OSEM-3D reconstruction strategies for the ECAT HRRT in IEEE Symposium Conference Record Nuclear Science 2004*. **6** (IEEE, 2004), 3492–3496. ISBN: 0-7803-8701-5. doi:10.1109/NSSMIC.2004.1466639. <http://ieeexplore.ieee.org/document/1466639/>.
178. Collins, D. L. *et al.* in *Information Processing In Medical Imaging, Proceedings* 210–223 (Springer, Berlin, Heidelberg, 1999). ISBN: 978-3-540-66167-2. doi:10.1007/3-540-48714-X. <http://apps.webofknowledge.com/InboundService.do?SID=V1Mh6do0Hnf4594ppeI%7B%5C%7Dproduct=WOS%7B%5C%7DUT=000170515200016%7B%5C%7DsrcApp=Papers%7B%5C%7DDESTFail=http://www.webofknowledge.com%7B%5C%7DInit=Yes%7B%5C%7Daction=retrieve%7B%5C%7DFunc=Frame%7B%5C%7DcustomersID=mekentosj%7B%5C%7DsrcAuth=mekentosj%7B%5C%7DIsProductC%7B%5C%7D5Cnhttp://a>.
179. Collins, D. L. & Evans, A. C. Animal: Validation and Applications of Nonlinear Registration-Based Segmentation. *International Journal of Pattern Recognition and Artificial Intelligence* **11**, 1271–1294. ISSN: 0218-0014 (Dec. 1997).
180. Zijdenbos, A. *et al.* in *Lecture Notes in Computer Science (including subseries Lecture Notes in Artificial Intelligence and Lecture Notes in Bioinformatics)* 439–448 (Springer, Berlin, Heidelberg, 1996). ISBN: 3540616497. doi:10.1007/bfb0046984. <http://link.springer.com/10.1007/BFb0046984>.

181. Funck, T., Larcher, K., Toussaint, P. J., Evans, A. C. & Thiel, A. APPIAN: Automated Pipeline for PET Image Analysis. *Frontiers in Neuroinformatics* **12**. ISSN: 16625196. doi:10.3389/fninf.2018.00064. <https://www.frontiersin.org/article/10.3389/fninf.2018.00064/full> (Sept. 2018).
182. Studholme, C., Hill, D. L. & Hawkes, D. J. Automated three-dimensional registration of magnetic resonance and positron emission tomography brain images by multiresolution optimization of voxel similarity measures. *Medical Physics* **24**, 25–35. ISSN: 00942405 (Jan. 1997).
183. Strother, S. C. *et al.* Quantitative comparisons of image registration techniques based on high-resolution MRI of the brain. *Journal of computer assisted tomography* **18**, 954–62. ISSN: 0363-8715 (1994).
184. Ashburner, J. & Friston, K. Multimodal image coregistration and partitioning - A unified framework. *NeuroImage* **6**, 209–217. ISSN: 10538119 (Oct. 1997).
185. West, J. *et al.* Comparison and evaluation of retrospective intermodality brain image registration techniques. *Journal of Computer Assisted Tomography* **21**, 554–566. ISSN: 03638715 (1997).
186. Delbeke, D., Patton, J. A., Martin, W. H. & Sandler, M. P. FDG PET and dual-head gamma camera positron coincidence detection imaging of suspected malignancies and brain disorders. *Journal of Nuclear Medicine* **40**, 110–117. ISSN: 01615505 (Jan. 1999).
187. Nørgaard, M. *et al.* Optimization of preprocessing strategies in Positron Emission Tomography (PET) neuroimaging: A [11C]DASB PET study. *NeuroImage* **199**, 466–479. ISSN: 10959572 (Oct. 2019).

188. Rousset, O. & Zaidi, P. Correction for partial volume effects in emission tomography. *Quantitative Analysis in Nuclear Medicine ...* http://link.springer.com/chapter/10.1007/0-387-25444-7%7B%5C_%7D8 (2006).
189. Toga, A. W., Thompson, P. M., Mori, S., Amunts, K. & Zilles, K. *Towards multimodal atlases of the human brain* Dec. 2006. doi:10.1038/nrn2012. <http://www.nature.com/articles/nrn2012>.
190. Olesen, O. *et al.* *Spatial resolution of the HRRT PET scanner using 3D-OSEM PSF reconstruction in 2009 IEEE Nuclear Science Symposium Conference Record (NSS/MIC)* (IEEE, Oct. 2009), 3789–3790. ISBN: 978-1-4244-3961-4. doi:10.1109/NSSMIC.2009.5401892. <http://ieeexplore.ieee.org/lpdocs/epic03/wrapper.htm?arnumber=5401892>.
191. Dubois, A., Dauguet, J. & Delzescaux, T. in *Small Animal Imaging: Basics and Practical Guide* 317–346 (Springer Berlin Heidelberg, Berlin, Heidelberg, 2011). ISBN: 9783642129445. doi:10.1007/978-3-642-12945-2_23. http://link.springer.com/10.1007/978-3-642-12945-2%7B%5C_%7D23.
192. Pichat, J., Iglesias, J. E., Yousry, T., Ourselin, S. & Modat, M. A Survey of Methods for 3D Histology Reconstruction. *Medical Image Analysis* **46**, 73–105. ISSN: 13618415 (2018).
193. Julien Dauguet. Three-dimensional histological imaging of primate brain and correlation with in vivo medical device images. *Revue de primatologie*. ISSN: 2077-3757. doi:10.4000/primatologie.546. <http://journals.openedition.org/primatologie/546> (Sept. 2010).

194. Toga, A. W. & Arnicar, T. L. Image analysis of brain physiology. *IEEE Computer Graphics and Applications* **5**, 20–25. ISSN: 02721716 (1985).
195. Toga, A. W., Santori, E. M. & Samaie, M. Regional distribution of flunitrazepam binding constants: Visualizing K(d) and B(max) by digital image analysis. *Journal of Neuroscience* **6**, 2747–2756. ISSN: 02706474 (Sept. 1986).
196. Toga, A. W. & Arnicar-Sulze, T. L. Digital image reconstruction for the study of brain structure and function. *Journal of Neuroscience Methods* **20**, 7–21. ISSN: 01650270 (May 1987).
197. Kim, B., Boes, J. L., Frey, K. A. & Meyer, C. R. Mutual information for automated unwarping of rat brain autoradiographs. *NeuroImage* **5**, 31–40. ISSN: 10538119 (1997).
198. Gangolli, M. *et al.* Quantitative validation of a nonlinear histology-MRI coregistration method using generalized Q-sampling imaging in complex human cortical white matter. *NeuroImage* **153**, 152–167. ISSN: 10959572 (June 2017).
199. Hibbard, L. S. & Hawkins, R. A. Three-dimensional reconstruction of metabolic data from quantitative autoradiography of rat brain. *American Journal of Physiology - Endocrinology and Metabolism* **10**, E412–9. ISSN: 01931849 (Sept. 1984).
200. Hibbard, L. S. & Hawkins, R. A. Objective image alignment for three-dimensional reconstruction of digital autoradiograms. *Journal of Neuroscience Methods* **26**, 55–74. ISSN: 01650270 (Nov. 1988).
201. Toga, A. W. & Banerjee, P. K. Registration revisited. *Journal of Neuroscience Methods* **48**, 1–13. ISSN: 0165-0270 (June 1993).

202. Andreasen, A., Drewes, A. M., Assentoft, J. E. & Larsen, N. E. Computer-assisted alignment of standard serial sections without use of artificial landmarks. A practical approach to the utilization of incomplete information in 3-D reconstruction of the hippocampal region. *Journal of Neuroscience Methods* **45**, 199–207. ISSN: 01650270 (Dec. 1992).
203. Zhao, W., Young, T. Y. & Ginsberg, M. D. Registration and Three-Dimensional Reconstruction of Autoradiographic Images by the Disparity Analysis Method. *IEEE Transactions on Medical Imaging* **12**, 782–791. ISSN: 1558254X (1993).
204. Iglesias, J. E. *et al.* Joint registration and synthesis using a probabilistic model for alignment of MRI and histological sections. *Medical Image Analysis* **50**, 127–144. ISSN: 13618423 (Sept. 2018).
205. Ourselin, S., Roche, A., Subsol, G., Pennec, X. & Ayache, N. Reconstructing a 3D structure from serial histological sections. *Image and Vision Computing* **19**, 25–31. ISSN: 02628856 (Jan. 2001).
206. Chakravarty, M. M., Bertrand, G., Hodge, C. P., Sadikot, A. F. & Collins, D. L. The creation of a brain atlas for image guided neurosurgery using serial histological data. *NeuroImage* **30**, 359–376. ISSN: 10538119 (Apr. 2006).
207. Cifor, A., Bai, L. & Pitiot, A. Smoothness-guided 3-D reconstruction of 2-D histological images. *NeuroImage* **56**, 197–211. ISSN: 10538119 (May 2011).
208. Pichat, J., Modat, M., Yousry, T. & Ourselin, S. *A multi-path approach to histology volume reconstruction* in *2015 IEEE 12th International Symposium*

- on Biomedical Imaging (ISBI)* (IEEE, Apr. 2015), 1280–1283. ISBN: 978-1-4799-2374-8. doi:10.1109/ISBI.2015.7164108. <http://ieeexplore.ieee.org/document/7164108/>.
209. Schormann, T., Dabringhaus, A. & Zilles, K. Statistics of Deformations in Histology and Application to Improved Alignment with MRI. *IEEE Transactions on Medical Imaging* **14**, 25–35. ISSN: 1558254X (Mar. 1995).
210. Dauguet, J. *et al.* Three-dimensional reconstruction of stained histological slices and 3D non-linear registration with in-vivo MRI for whole baboon brain. *Journal of Neuroscience Methods* **164**, 191–204. ISSN: 01650270 (Aug. 2007).
211. Schubert, N. *et al.* 3D reconstructed cyto-, muscarinic M2 receptor, and fiber architecture of the rat brain registered to the waxholm space atlas. *Frontiers in Neuroanatomy* **10**, 51. ISSN: 16625129 (May 2016).
212. Malandain, G., Bardinet, É., Nelissen, K. & Vanduffel, W. Fusion of autoradiographs with an MR volume using 2-D and 3-D linear transformations. *NeuroImage* **23**, 111–127. ISSN: 10538119 (Sept. 2004).
213. Yang, Z., Richards, K., Kurniawan, N. D., Petrou, S. & Reutens, D. C. MRI-guided volume reconstruction of mouse brain from histological sections. *Journal of Neuroscience Methods* **211**, 210–217. ISSN: 01650270 (Nov. 2012).
214. Iglesias, J. E. *et al.* Joint registration and synthesis using a probabilistic model for alignment of MRI and histological sections. *coRR* **abs/1801.0**. ISSN: 13618423. doi:10.1016/j.media.2018.09.002. arXiv: 1801.05284. <http://arxiv.org/abs/1801.05284> (Jan. 2018).

215. Ronneberger, O., Fischer, P. & Brox, T. U-net: Convolutional networks for biomedical image segmentation. *Lecture Notes in Computer Science (including subseries Lecture Notes in Artificial Intelligence and Lecture Notes in Bioinformatics)* **9351**, 234–241. ISSN: 16113349 (May 2015).
216. Otsu, N. Threshold Selection Method From Gray-Level Histograms. *IEEE Trans Syst Man Cybern SMC-9*, 62–66. ISSN: 00189472 (Jan. 1979).
217. Et al. Ad-Dab’bagh. *The CIVET image-processing environment: A Neuroimaging, fully automated comprehensive pipeline for anatomical Research in Proceedings of the 12th Annual Meeting of the Organization for Human Brain Mapping* (ed Corbetta) (Neuroimage, Florence, 2006).
218. Collins, D. L., Holmes, C. J., Peters, T. M. & Evans, A. C. Automatic 3-D model-based neuroanatomical segmentation. *Human Brain Mapping* **3**, 190–208. ISSN: 10659471 (Jan. 1995).
219. Lloyd, S. P. Least Squares Quantization in PCM. *IEEE Transactions on Information Theory* **28**, 129–137. ISSN: 15579654 (Mar. 1982).
220. Wagstyl, K., Paquola, C., Bethlehem, R., Evans, A. C. & Huth, A. *Equivolumetric layering for mesh surfaces* Oct. 2018. doi:10.5281/zenodo.1442584. <https://zenodo.org/record/1442584%7B%5C#%7D.XbxZbEX7SgQ%20https://doi.org/10.5281/zenodo.1442584>.
221. Jenkinson, M., Pechaud, M. & Smith, S. *BET2: MR-based estimation of brain, skull and scalp surfaces in Eleventh Annual Meeting of the Organization for Human Brain Mapping, .* (2005).

222. Kendall, M. G. A New Measure of Rank Correlation. *Biometrika* **30**, 81. ISSN: 00063444 (June 1938).
223. Wagstyl, K. *et al.* Mapping cortical laminar structure in the 3D bigbrain. *Cerebral Cortex* **28**, 2551–2562. ISSN: 14602199 (July 2018).
224. Whitehouse, P. J., Lynch, D. & Kuhar, M. J. Effects of Postmortem Delay and Temperature on Neurotransmitter Receptor Binding in a Rat Model of the Human Autopsy Process. *Journal of Neurochemistry* **43**, 553–559. ISSN: 14714159 (Aug. 1984).
225. Rodríguez-Puertas, R., Pascual, J. & Pazos, A. Effects of freezing storage time on the density of muscarinic receptors in the human postmortem brain: An autoradiographic study in control and Alzheimer's disease brain tissues. *Brain Research* **728**, 65–71. ISSN: 00068993 (July 1996).
226. Lloyd, K. G. & Dreksler, S. An analysis of [3H]gamma-aminobutyric acid (GABA) binding in the human brain. *Brain Research* **163**, 77–87. ISSN: 00068993 (Mar. 1979).
227. Faull, K. F. *et al.* Influence of freezer storage time on cerebral biogenic amine and metabolite concentrations and receptor ligand binding characteristics. *Brain Research* **450**, 225–230. ISSN: 00068993 (May 1988).
228. Kornhuber, J., Retz, W., Riederer, P., Heinsen, H. & Fritze, J. Effect of antemortem and postmortem factors on [3H]glutamate binding in the human brain. *Neuroscience Letters* **93**, 312–317. ISSN: 03043940 (Nov. 1988).

229. Burke, R. E. & Greenbaum, D. Effect of Postmortem Factors on Muscarinic Receptor Subtypes in Rat Brain. *Journal of Neurochemistry* **49**, 592–596. ISSN: 14714159 (Aug. 1987).
230. Kontur, P. J., Al-Tikriti, M., Innis, R. B. & Roth, R. H. Postmortem Stability of Monoamines, Their Metabolites, and Receptor Binding in Rat Brain Regibns. *Journal of Neurochemistry* **62**, 282–290. ISSN: 14714159 (June 1994).
231. Gross-Isseroff, R., Salama, D., Israeli, M. & Biegon, A. Autoradiographic analysis of age-dependent changes in serotonin 5-HT₂ receptors of the human brain postmortem. *Brain Research* **519**, 223–227. ISSN: 00068993 (June 1990).
232. Gaudin, E. *et al.* Performance Simulation of an Ultrahigh Resolution Brain PET Scanner Using 1.2-mm Pixel Detectors. *IEEE Transactions on Radiation and Plasma Medical Sciences* **3**, 334–342. ISSN: 2469-7311 (May 2019).
233. Veronese, M. *et al.* *NRM2018 PET Grand Challenge dataset* 2018. doi:10.18112/openneuro.ds001705.v1.0.0. <https://openneuro.org/datasets/ds001705/versions/1.0.0>.
234. Kiar, G. *et al.* Comparing Perturbation Models for Evaluating Stability of Neuroimaging Pipelines. arXiv: 1908.10922. <https://arxiv.org/abs/1908.10922> <http://arxiv.org/abs/1908.10922> (Aug. 2019).
235. Svarer, C. *et al.* MR-based automatic delineation of volumes of interest in human brain PET images using probability maps. *NeuroImage* **24**, 969–979. ISSN: 10538119 (Feb. 2005).

236. Pomares, F. B. *et al.* Histological underpinnings of grey matter changes in fibromyalgia investigated using multimodal brain imaging. *Journal of Neuroscience* **37**, 1090–1101. ISSN: 15292401 (2017).
237. Pomares, F. B. *et al.* Up-regulation of cortical GABAA receptor concentration in fibromyalgia. *Pain*, 1. ISSN: 0304-3959 (Sept. 2019).
238. Toga, A. W. & Thompson, P. M. The role of image registration in brain mapping. *Image and Vision Computing* **19**, 3–24. ISSN: 02628856 (2001).
239. Robinson, E. C. *et al.* MSM: A new flexible framework for multimodal surface matching. *NeuroImage* **100**, 414–426. ISSN: 10959572 (Oct. 2014).